Title
In-situ Surface Enhanced Raman Spectroscopy Investigation of the Surface Films on Alloy 600 and Alloy 690 in Pressurized Water Reactor-Primary Water

Author
Wang, Feng

Publication Date
2012

Peer reviewed|Thesis/dissertation

In-situ Surface Enhanced Raman Spectroscopy Investigation of the Surface Films on Alloy 600 and Alloy 690 in Pressurized Water Reactor-Primary Water

By

Feng Wang

A dissertation submitted in partial satisfaction of the

requirements for the degree of

Doctor of Philosophy

in

Engineering-Materials Science and Mineral Engineering

in the

Graduate Division

of the

University of California, Berkeley

Committee in charge:

Professor Thomas M. Devine, Chair

Professor James W. Evans

Professor Paulo J. M. Monteiro

Fall 2012

In-situ Surface Enhanced Raman Spectroscopy Investigation of the Surface Films on Alloy 600 and Alloy 690 in Pressurized Water Reactor-Primary Water

Feng Wang

Abstract

In-situ Surface Enhanced Raman Spectroscopy Investigation of the Surface Films on Alloy 600 and Alloy 690 in Pressurized Water Reactor-Primary Water

by

Feng Wang

Doctor of Philosophy in Engineering-Materials Science and Mineral Engineering

University of California, Berkeley

Professor Thomas M. Devine, Chair

Alloy 600 is found to be susceptible to stress corrosion cracking (SCC) in Pressurized Water Reactor (PWR) primary water environment. In this study, in-situ Surface Enhanced Raman Spectroscopy (SERS) is used to characterize surface films formed on Alloy 600 and Alloy 690 in PWR PW at 320^{o}C. A simulated PWR PW system is constructed. In addition, a titanium autoclave is designed for high-temperature electrochemical tests.

In this study, we have also measured SERS spectra of surface films formed on unalloyed nickel, unalloyed chromium, Ni-5Cr-8Fe, Ni-10Cr-8Fe, Ni-10Cr and Ni-20Cr. The surface films were formed at different potentials, from -0.9V to -0.5V vs SHE.

A formation of NiO film is observed on the surface of nickel at -0.65V, which shows a Raman peak at 540 cm^{-1} due to crystal defects. For pure chromium, Cr_2O_3 passive film is formed on its surface. The Raman peaks are located at 540 cm^{-1} and 610 cm^{-1}. The thickness of Cr_2O_3 passive film is about several nanometers, depending on the growth time in PWR PW. A peak at 610 cm^{-1} would likely indicate Cr_2O_3 and the absence of this peak, in conjunction with a peak at 540 cm^{-1}, would indicate NiO. It is found that the surface films on Ni-5Cr-8Fe and Ni-10Cr-8Fe alloys are composed of Cr_2O_3 and $FeCr_2O_4$ spinel. No spinel oxide peak is observed in the SERS spectra for Ni-10Cr and Ni-20Cr binary alloys, and the surface film on both alloys is Cr_2O_3. An analysis of SERS spectra indicate that, as alloy's chromium concentration increases, the amount of Cr_2O_3 included in the alloy's surface film would increase.

The surface film of Alloy 600 is composed of Cr_2O_3 inner layer (IL) and $FeCr_2O_4$ outer layer (OL). For short-time growth (10 min), the inner Cr_2O_3 layer is about 2 - 4 nm thick, and the average size of $FeCr_2O_4$ crystallites is about 10 nm. The actual film thickness depends on the growth time and aqueous environment. The surface film formed on Alloy 600 in PWR PW has a minor change if the sample is removed from the autoclave and exposed to air. The surface film of Alloy 690 is entirely a single layer of Cr_2O_3 (~ 2 nm thick). According to Diffusion Path Analysis, the difference on surface films formed on Alloy 600 and Alloy 690 is a consequence of

a change in the relative diffusivity of O and Cr. Our in-situ SERS spectra measured for surface films on Alloy 600 and Alloy 690 are different with most of other people's findings. Three aspects have been considered and discussed. The first, there might be a difference between in-situ and ex-situ characterization techniques. The second, the film growth time in PWR PW is significantly different. The third, different autoclaves are used. The recirculating titanium autoclave is used in this study, while stainless steel autoclave is used in most of other studies, which might cause a change of the concentration of cations in the vicinity of metal surface and a precipitation of cations on the surface of oxides. It is found that the exposure time and testing autoclave might be responsible for the discrepancies between this study and the earlier studies.

By using in-situ Surface Enhance Raman Spectroscopy (SERS), we have investigated the surface oxides formed on Alloy 600, Alloy 690, Ni-Cr, and Ni-Cr-Fe alloys in PWR primary water at 320^{o}C. Our in-situ SERS spectra results suggest that SCC susceptibility of Ni-based alloys might be correlating with a formation of surface films formed in PWR primary water.

Table of Contents

List of Figures

Acknowledgments

First, I would like to thank my mentor, Professor Thomas M. Devine, for guidance, supporting, teaching, and love.

I would like to thank Dr. Peter Chou and Dr. Raj Pathania of Electric Power Research Institute, Palo Alto, CA, for their financial support and technical interest.

I would like to thank Dr. Peter Andresen of General Electric (GE) Global Research Center for providing alloys for testing and for valuable assistance with the design of the high temperature water loop and autoclave.

I would like to thank Dr. Christopher S. Kumai for much needed assistance in the construction of the water loop and autoclave and in the design and construction of the Raman spectrometer.

I would like to thank Devine Research group for many discussions and friendship.

Chapter 1

Introduction

1.1 Introduction of Alloy 600 and Alloy 690

Many, commercially available Ni-based alloys exhibit high mechanical strength (Yield strength: 500~800MPa) and high-temperature creep resistance [1-2]. An important characteristic of some Ni-based alloys is their excellent corrosion and oxidation resistance [3-5]. Ni-based alloys are commonly used in gas turbine engines [6], nuclear reactors [7-8], chemical processing vessels [9], and heat exchanger tubing [10].

Alloy 600 (UNS N06600) (nickel-chromium-iron alloy) is a standard engineering material for applications that require resistance to corrosion and heat [11]. With 72% minimum nickel content, Alloy 600 is resistant to corrosion in many organic and inorganic electrolytes and to reducing aqueous solutions [12-13]. The high nickel content also allows for good resistance to chloride-ion Stress-Corrosion Cracking (SCC) [14-15]. The 14-17% chromium content of the alloy provides corrosion resistance in mildly oxidizing conditions at high temperatures [16-17]. Alloy 600 has excellent mechanical properties and shows a desirable combination of high strength and good workability [18-19]. This alloy is extensively used in chemical and food processing [20], heat treating, acid vessels [21], jet engines [22], steam generators [23-24]. Alloy 600 is a standard material of construction for nuclear reactors [25-26].

Alloy 690 (UNS N06690) is another Ni-based alloy, which has a higher chromium content (27-31%Cr) than Alloy 600 (14-17%Cr). The alloy has high resistance to corrosion in many corrosive aqueous media and high temperature environments [27-29]. Alloy 690 has shown high creep-rupture strength [30], good metallurgical stability [31], good ductility [32] and favorable fabrication characteristics [33]. Alloy 690 has excellent resistance to stress-corrosion cracking in high-temperature water [34-35]. Thus, Alloy 690 is used for steam generator tubes, tubesheets, and other components in nuclear power plants [36-38].

1.2 Introduction of Stress Corrosion Cracking of Alloy 600 in PWR

During the past several decades, Alloy 600 has been the standard material used for steam generator tubes of Pressurized Water Reactors (PWRs) [39-40]. However, Alloy 600 was found to be susceptible to Stress Corrosion Cracking (SCC), which means that the material was prone to cracking when subjected to a combination of stress and a mildly corrosive environment [41-42]. SCC of Alloy 600 steam generator tube represents a serious safety problem to nuclear plants.

Stress corrosion cracking (SCC) is a complex phenomenon that is highly dependent on the temperature [43] and composition of the aqueous electrolyte [44] and the composition [45], microstructure [46], mechanical [47] and electrochemical properties [48] of the alloy. No single

chemical, electrochemical, metallurgical, or mechanical parameter can characterize the susceptibility of an alloy to SCC.

Most, if not all mechanisms of SCC indicate the important role of corrosion product films, such as passive films [49-51]. Depending on the particular theory, the specific property of the passive film that is associated with the film's role in SCC is related to the film's mechanical properties [52] (e.g., strain to failure), chemical properties [53] (e.g., aqueous solubility), or electrochemical properties [54] (e.g., ionic conductivity).

P.M. Scott was the first researcher to propose the internal oxidation mechanism for SCC of Alloy 600 steam generator tubes[55]. According to the internal oxidation mechanism, oxygen atoms dissolve into an alloy at the external oxide-metal interface and diffuse into the metal matrix to oxidize a more reactive alloying element than the solvent metal [55]. A pre-condition for SCC is that the solvent metal of the alloy must not participate significantly in the formation of a protective external oxide film. This conclusion is supported by the fact that the maximum sensitivity to Intergranular Stress Corrosion Cracking (IGSCC) of Alloy 600 is located at the Ni/NiO equilibrium potential [55].

Alloy 690 appears to be more resistant to IGSCC than Alloy 600 [56]. For example, while there have been a number of instances of IGSCC of Alloy 600 steam generator tubes in the heat exchangers of PWRs, to our knowledge there have been no reports of IGSCC of Alloy 690 steam generator tubes.

1.3 Correlation between SCC and the Formation of Surface Films

A hypothesis we are evaluating is that susceptibility of Alloy 600 to SCC in PWR primary water is possibly correlated with the formation of specific surface films on the alloy.

The idea that the susceptibility to SCC is dependent on the type of surface films is not original. J. Flis found that a high rate of SCC of mild steel in nitrate solution was connected with the formation of passive γ-Fe_2O_3 film and its sensitivity to the depassivating action of steel constituents, whereas SCC was hindered in the presence of Fe_3O_4 film by blockage of the cracks [57].

D. Cubicciotti studied the SCC of stainless steels of steam lines in Boiling Water Reactors (BWR). He found that a spinel oxide ($FeCr_2O_4$) was stable under the reducing conditions imposed by Hydrogen Water Chemistry (HWC), where SCC was mitigated [58]. However, a simple Cr-free oxide Fe_2O_3 was stable for the more oxidizing conditions of Normal Water Chemistry (NWC) (i.e., dissolved oxygen concentration of 0.2 ppm), where SCC occurred. The change of stability from $FeCr_2O_4$ to Fe_2O_3 occurred at the same potential as that for which SCC rate increased rapidly [58]. Cubicciotti pointed out that a change of the surface oxide was involved in the mechanism of stress corrosion cracking [58].

C.S. Kumai and T.M. Devine identified the films formed on Type304 stainless steel immersed in high-temperature (288°C), high-purity water. The films were a function of corrosion

potential, which was controlled by the water's dissolved oxygen concentration. Below -0.466V (vs. SHE), the surface film was composed of M_3O_4. At potentials above -0.466V, the film consisted of an inner layer M_3O_4 and an outer layer of γ-M_2O_3 (at lower potentials) or α-M_2O_3 (at higher potentials) [59]. Type 304 stainless steel was susceptible to IGSCC when a layer of α-M_2O_3 formed. IGSCC was not found at potentials below -0.466V, where only M_3O_4 oxide formed [59]. These results suggested that Hydrogen Water Chemistry (HWC) was effective in alleviating IGSCC of SS304 because HWC can lower the potential to values less than -0.466V [59].

In the current study, surface films formed on Alloy 600 and Alloy 690 in PWR primary water were investigated by using in-situ Surface Enhanced Raman Spectroscopy (SERS). Surface oxide films were grown at different electrochemical potentials, different pH values of solution, and different alloy compositions. The main goal of the research is to evaluate the validity of the hypothesis that the susceptibility of stress corrosion cracking has a correlation with a changing of surface films formed on alloys.

1.4 Previous Research on Surface Films of Alloy 600 and Alloy 690

It is helpful to make clear the operating conditions inside the primary water circuit of a PWR. The temperature ranges from 286°C in the reactor's cold leg to 322°C in the hot leg and 342 °C in the pressurizer [55, 60]. The pH value of primary coolant is fixed by boric acid and lithium hydroxide in a region between 6.8 and 7.4 at the operating temperature [55, 60]. Hydrogen is added to the primary coolant to avoid any net decomposition of water by radiolysis in the core [60]. The corrosion potential of Alloy 600 in primary water is very close to the Ni/NiO equilibrium potential (about -0.7V vs. SHE) [55]. From laboratory studies on Alloy 600 in PWR primary water, the maximum susceptibility to IGSCC is observed when the electrochemical potential is close to the Ni/NiO equilibrium potential and decreases at both higher and lower potentials within a band of about $\pm$ 80mV [55].

According to P. Combrade, the oxide layers formed on Alloy 600 and Alloy 690 in primary PWR water at 360^{o}C are similar in nature although quantitatively different [61]. The surface film is made of a Cr-rich inner layer and a Cr-free external layer. The Cr rich inner layer comprises two "sub-layers". On the metal side, the sublayer is made of Cr_2O_3 (or $(Cr,Fe)_2O_3$) oxide. On the solution side, the sublayer is Cr rich spinel type oxide, which is the main constituent of the inner layer. The Cr-free external layer consists of crystallites spread over the surface. This layer is almost (or possibly completely) Cr-free and contains only Fe and Ni [61]. Combrade et.al. pointed out that the external layer's composition strongly depend on the nature and surface condition of the base metal and also on the saturation of the aqueous environment in Fe and Ni cations. For Ni-based alloys it is generally made of $(Ni_xFe_{1-x})Fe_2O_4$ ferrite [61].

M. Sennour et. al. studied the oxide films at the surface of Alloy 690 in PWR primary coolant at 325^{o}C by Transmission Electron Microscopy (TEM) [62]. The oxide layer was divided in two parts. The internal layer was mainly composed of a continuous spinel layer, identified as $Ni_{(1-x)}Fe_xCr_2O_4$ [62]. Nodules of Cr_2O_3 were present at the interface between this

spinel and the alloy. The external layer is composed of large crystallites corresponding to a spinel structure rich in iron ($Ni_{(1-z)}Fe_{(2+z)}O_4$) resulting from precipitation phenomena [62].

From X-ray Photoelectron Spectroscopy (XPS) investigation, in the early stages (i.e., 0.4 - 4 minutes) of passivation of Alloy 600, the film consisted of an inner ultra-thin (1 nm thick) chromium oxide (Cr_2O_3) and an outer layer of $Cr(OH)_3$ with a very small amount of $Ni(OH)_2$ [63]. For longer exposures (4-8 minutes), the film had a relatively thick Cr_2O_3 inner layer (2 nm thick) and thin $Ni(OH)_2$ outer layer (less than 1 nm thick) [63]. Scanning Tunneling Microscopy (STM) data shown that Cr_2O_3 layer was crystalline and that the structure was consistent with the hexagonal structure of the oxygen sub-lattice in the (0001) orientation of α-Cr_2O_3 [63]. B.T. Ovanessian studied the structure of the oxide layer by using TEM and Secondary Ion Mass Spectrometry (SIMS) [64]. The outer scale was composed of two families of oxide grains, one in the form of discrete large crystallites ($NiFe_2O_4$ spinel oxides) and the other made of smaller grains of a mixed oxide of nickel, chromium and iron of average thickness of 50 nm. A thin, compact and continuous inner layer made of Cr rich spinel/Cr_2O_3 oxide was identified at the metal/oxide interface. In addition, a chromium depleted layer was present over a few tens nanometers in the alloy under the inner chromium rich oxide scale [64].

Experiments with markers and tracers were performed to understand the growth mechanism of surface oxide films [65]. It was confirmed that oxidation mechanism was via a process of oxygen diffusion along grain boundaries and oxygen diffusion coefficient was estimated to be in the range of 2×10^{-18}-1×10^{-17} ($cm^2 \bullet s^{-1}$) at 325^{o}C. Oxygen diffusion rates can be increased significantly at grain boundaries and by an applied stress, a porous structure, or vacancy injections [65]. Ovanessian considered the oxidation process to be related with a coupling transportation between vacancies and oxygen atoms [64]. Macroscopic energy spectra from photoelectrochemical (PEC) experiments had three contributions. The first one was the continuous inner layer of spinel phase $Ni_{1-x}Fe_xCr_2O_4$ with a band gap around 4.1– 4.5 eV [66]. The second was nodules of Cr_2O_3 quasi-uniformly dispersed along the alloy/oxide interface, which shown a band gap around 3.5eV. The last one was the external layer of nickel hydroxide and nickel ferrite heterogeneously dispersed on the surface, which had a band gap around 2.2eV [66].

1.5 The Current Challenges

One potential shortcoming of the earlier research is that the surface films of Alloy 600 and Alloy 690 were characterized by ex-situ techniques. Specifically, the surface films that are formed in PWR primary water at 320°C are examined in a vacuum at room temperature. The surface films might change during cooling to room temperature and upon air exposure or during the sample's preparation for characterization studies. In addition, no research has been conducted on the influence of the alloy's electrochemical potential and the water's pH on the identity of the surface oxide. Thus, in-situ characterization of the surface films formed over a range of conditions in PWR primary water is highly desired.

1.6 Our Research Objective

The objective of this research is to investigate the surface films formed on Alloy 600 and Alloy 690 in stimulated PWR primary water by in-situ Surface Enhanced Raman Spectroscopy (SERS).

1.7 Our Approach Methods

In order to achieve our goals, the following apparatus were constructed.

First, a simulated PWR primary water system was constructed in our lab. The temperature can be increased to a high value of $320^{o}C \sim 325^{o}C$. The hydrostatic pressure is able to reach 2000 psi. In order to minimize the thermal stress in the autoclave chamber, a pre-heater and a heat exchanger were required.

Second, a high-temperature, high-pressure autoclave was designed. Titanium was selected as the material for the autoclave because of titanium's resistance to corrosion in high-temperature water. A sapphire observation window was installed in the autoclave for the measurement of SERS spectra. Two important aspects were considered. One was to prevent creep at high temperatures of the various seals that were made of Teflon. Creeping of seals caused leaking of the autoclave at high temperatures. The other was to avoid cracking of the sapphire window in high-temperature and high-pressure water. The details for the design of autoclave are discussed later.

Third, a Raman spectroscopy characterization system, built by Dr. Chris Kumai, was employed. The light source is He-Ne laser (λ=632.8nm). Raman scattering radiation is dispersed and recorded by a Spex Model 500M spectrometer. Supplemental optics and computer-controlled software were also required for the Raman spectroscopy system.

Finally, our samples were provided by Dr. Peter Andresen of the General Electric Global Research Center (GE-GRC). A thin layer of gold nanoparticles is electrochemically deposited on the sample surface, for the purpose of increasing the Raman scattered intensity from the surface oxide. The details of gold nanoparticle deposition and SERS effect will be described later. The potentials of the samples were controled by using an external potentiostat. The variation of pH values is accomplished by changing the water's concentration of lithium hydroxide.

Chapter 2

Experimental Apparatus

2.1 Solution Chemistry

In Pressurized Water Reactor (PWR) primary water, boron is used to moderate the nuclear reaction. The reaction is $B_5^{10} + n_0^1 \rightarrow Li_3^7 + He_2^4 + \gamma$, where B is boron, n is neutron, Li is lithium, He is Helium, and γ is Gamma ray. Lithium hydroxide is added to adjust the pH value of solution, which suppresses bulk corrosion [55, 67]. The reason for selection of Li-7 is that Li-7 is produced by the reaction $^{10}B(n,\alpha)^7Li$. Further, Li-7 has a low neutron capture cross-section and does not form significant radioactive products [67]. Usually, the concentrations of boron and lithium are not constant values, and they may change through the operating life of the core [55, 67].

At operation temperatures, the pH value of primary coolant lies between 6.8 and 7.4 [55]. The electrochemical potential of the system is located at $E_{Ni/NiO} \pm 80mV$, where $E_{Ni/NiO}$ is the Ni/NiO equilibrium potential [55].

A simulated PWR primary-water system was built in our lab. In our tests, two solutions were prepared. The first was mixture solution of 1200 ppm H_3BO_3 + 2 ppm LiOH, and the second was mixture solution of 1200 ppm H_3BO_3 + 0.19 ppm LiOH. The pH value of solution was a function of temperature, pressure and dissociation of species in the solution. We did not measure the solution pH during tests. Instead, it was calculated using a model courtesy of Electric Power Research Institute (EPRI) (**EPRI Chem WORKS™**, 1013369, EPRI Primary System pH Calculator, PHC Version 3.1). For the solution 1200 ppm H_3BO_3 + 2 ppm LiOH, the calculated pH value at 320°C was 7.2. For the solution 1200 ppm H_3BO_3 + 0.19 ppm LiOH, the calculated pH value at 320°C was 6.2.

All components in our simulated PWR system were constructed of Grade 2 titanium, which prevented bulk corrosion of the apparatus at high temperatures. A good approximation was that there were no cations from autoclave or pipelines dissolving into the solution. The solution was saturated with 96% N_2+4% H_2 mixture gas for 24 hours before running high-temperature tests.

2.2 Titanium Autoclave

The cylindrical autoclave body was made of titanium, commercial purity grade 2. Titanium has a high corrosion resistance and it can form a thin protective layer of oxide film on its surface in an aqueous environment. The diameter of the cylindrical autoclave body is 102 mm and the length is 82 mm (As shown in Figure 1). A cavity was drilled out of the test chamber

(Diameter: 20 mm; Length: 60 mm). At the front surface of autoclave, a mouth of the chamber was fabricated (Diameter: 31mm; Depth: 11 mm). This mouth was designed to accommodate a sapphire observation window.

Generally, Teflon seals are prone to creep at 320 ^{o}C, which will cause water leaking from the autoclave. For the design of Working Electrode (Sample), the Teflon seals were moved far away from the high-temperature test chamber. On the back side of autoclave body, a hole was drilled. A titanium tube (Length: 220 mm; Diameter: 6 mm) was used to connect with that hole. At the end of titanium tube, Teflon seals were inserted into tube, and were tightened by titanium connectors and caps.

The water inlet of the system is 20 mm away from the back side of autoclave and the water outlet is at 25 mm away from the front side. When water is flowing slowly from the inlet to the outlet, water is gradually heated. A uniform temperature is beneficial for a minimization of thermal stress on the sapphire window at the front site of the autoclave.

2.3 Water Supply System

The water used in all experiments was double de-ionized by a Barnstead EASY UV deionizer with a Barnstead 0.2μm fiber filter. The water was contained in a vertical oriented borosilicate glass column (Diameter: 40mm; Length: 64inch). The water was bubbled with 96% N_2+4% H_2 mixture gas (Praxair Distribution Inc.). The gas bubbler is located at the bottom of the borosilicate glass column. Figure 2-1 is a sketch of simulated PWR primary-water supply system.

2.4 Pump

The pump used in the system was a NEPTUNE chemical pump (Model Number: 500-S-N3HP-T15; Series Number: 161235). The maximum capacity for each cycle is 1.0 GPH and maximum pressure is 3000 psi. This pump is made of 316 Stainless Steel and it was operated at a flow rate of 0.45 GPH. After exiting the pump, the pressurized water entered a two coaxial heat exchanger made of titanium.

2.5 Heat Exchanger

The heat exchanger is made of two coaxial titanium tubes. The diameter of the inner tube is 3 mm and the diameter of the outer tube is 6 mm. The cold water exiting the pump passed through the outer tube and entered into the autoclave through the water inlet. Water was heated up in the autoclave. The hot water exited out of autoclave from the water outlet, and then entered the inner tube of the heat exchanger.

The cold water in the outer titanium tube was warmed up by the hot water in the inner tube, likewise, the hot water in the inner tube was cooled by the cold water in the outer tube. The heat exchanger played two roles. The first, the water was pre-heated before it went into hot

autoclave body, which was beneficial to decrease the thermal stress on sapphire window. The second, the hot water from autoclave was cooled down before it went into the pressure regulator and pressure gauge.

2.6 Pre-Heater

In order to minimize the thermal stress, water was pre-heated before it goes into autoclave. The water was pre-heated along a 70cm-long titanium pipe at the entrance of the autoclave. The pre-heater was an extreme-temperature heat tape (6-feet length, 468Watts, 240VAC). The tape contained a ceramic fiber heater and wrapped around the titanium piping at the water inlet. We found that the sapphire window would crack at 320^{o}C if this heat tape was not used.

2.7 Backpressure Regulator

The pressure of the high-temperature system needs to be maintained at 1800 psi. A backpressure regulator was placed on the side of water outlet. Before the water passed through the pressure regulator, it was cooled by flowing through a loop of titanium pipe (Total length: ~ 17 feet). The backpressure regulator was purchased from Swagelok Company. A bleeder valve and a rupture disk were used in the line along with the backpressure regulator to prevent inadvertent overpressures. After the water exited the backpressure regulator, it entered back to the water column container.

2.8 Temperature Control

The temperature of the system was controlled by Watlow Series 96 PID controller. A temperature ramping program was written as following: step 1 (20^{o}C-150^{o}C, 1hour15min); step 2 (150^{o}C-200^{o}C, 40min); step 3 (200^{o}C-295^{o}C, 1hour25min); step 4 (295^{o}C-315^{o}C, 25min); step 5 (315^{o}C-320^{o}C, 10min); step 6 (HOLD). The heating rate can be changed by re-writing the temperature ramping program.

The heating elements were Watlow cartridge heaters (Length: 4-inch, Diameter: 9 mm, 240 V, 500 W). Four cartridge heaters were used to heat up the autoclave, and they were inserted into the four holes drilled throughout autoclave body. The four holes were uniformly distributed, so that during heating process the temperature of autoclave body was uniform. At higher temperatures, the heating rate was decreased in order to reduce the thermal stress and avoid the crack of the sapphire window.

An Omega titanium thermocouple was used to measure the temperature of autoclave. The thermocouple was inserted through the water outlet port and extended into the test chamber.

During tests, the autoclave was thermally insulated by ceramic fibers and ceramic blocks to reduce the heat loss and minimize temperature gradients. During cool-down, the temperature of autoclave was decreased at rate of 2^{o}C/min approximately.

2.9 Potential Control

In PWR primary water, the electrochemical potential is close to the Ni/NiO equilibrium potential [55]. The electrochemical potential can be changed by changing the concentration of hydrogen gas or oxygen gas in the solution. However, University safety requirements set a maximum on the amount of hydrogen content allowed for gas mixtures. In our experiments, the solution was saturated with 96% N_2 + 4% H_2 mixture gas, and oxygen gas was physically displaced from the solution. The potentials on samples were provided by using an external potentiostat (GAMRY instrument).

2.10 Sapphire Window

A sapphire window (the thickness: ~10 mm) was used for in-situ acquiring SERS spectra from samples inside the high-temperature autoclave. Single crystal sapphire was chosen because of its excellent optical transparency and high resistance to the attack of high-temperature solution.

Optical quality Hemlite CSI white purity sapphire window was purchased from Crystal Systems (Diameter: $30\text{mm} \pm 0.1\text{mm}$; Thickness: $10\text{mm} \pm 0.05\text{mm}$; Orientation: $(0001) \pm 2^{o}$; Surface finish:10/5 polish on faces, fine grind OD, light edge break).

At 320°C, sapphire window was prone to crack, which would cause water leaking from autoclave and damages of mirrors. Any non-uniform stresses should be avoided during autoclave sealing process. In addition, a gold-wire ring needs be used as a sealing between the sapphire window and the titanium autoclave chamber. A copper ring was placed between the sapphire window and the front cover plate, in order to prevent the cracking of sapphire window.

2.11 Reference Electrode

The Reference Electrode (RE) was pure platinum wire. In the test chamber, the platinum wire was coiled in order to increase its surface area. In the equilibrium state, the electrochemical reaction taking place at the reference electrode was written as: $2H^+ + 2e^- \leftrightarrow H_2$. The electrochemical potential at RE can be calculated by Nernst Equation: $\Delta\phi_e = \Delta\phi_e^0 - \frac{RT}{ZF} ln \frac{p_{H_2}}{[H^+]^2}$, where $\Delta\phi_e^0$ is the electrochemical potential at standard state; R is gas constant; T is the temperature; F is the Faraday constant; p_{H_2} is the partial pressure of hydrogen gas; H^+ is the concentration of hydrogen ions. The potential differences between samples and the platinum reference electrode were converted into the values relative to Standard Hydrogen Electrode (SHE).

2.12 Counter Electrode

The Counter Electrode (CE) was also made of platinum wire. In order to increase its surface area, the platinum wire was coiled. The surface area was about 1.2 cm^2. The distance between counter electrode and reference electrode was about 12 mm. The sample (working electrode) had the same distance with CE and RE, which was about 16 mm. The volume of autoclave test chamber was 17.6 cm^3.

2.13 Raman Spectroscopy

Raman-Stokes scattering component comes from the effect of inelastic scattering between an incident beam and molecules [68]. The major component of radiated light has the same frequency as the incident light, which is called elastic scattering [68]. The fact is that the molecules are always vibrating near their equilibrium positions and the change of polarizibility of the molecule might be a nonzero value for a certain vibration mode [68-69]. Under such circumstances, the radiated light will have a shifting in frequency with respect of the frequency of incident beam. The magnitude of Raman frequency shifting is dependent on the vibrational frequency of molecule. The condition for Raman-active vibration mode is that the polarizibility change for a vibration mode must be nonzero [68-69].

The vibration frequency of molecule is correlated with structure of molecule, effective mass, and bonding strength [68-69]. Therefore, Raman scattering spectra can be used to characterize film identity, crystal structure, and defects of material. Raman spectroscopy is based on the vibration of molecule, which can be used to study the passive films of metals formed in aqueous solutions [68-69].

Raman Spectroscopy system was equipped with light from Spectra-physics Model 127 35mW He-Ne laser (As shown in Figure 2-2). The wavelength of He-Ne laser was 632.8nm. After exiting the laser tube, laser passed through a Corion D1-633-R-T294 633nm plasma line filter. The laser was then directed by a Newport 05D20DM.4 632.8nm 12.7mm-diameter dielectric mirror and a Spindler & Hoyer 34 0444 DLHS 632.8nm 5mm-diameter dielectric mirror. A Newport plano-convex collection lens was used to focus the incident laser on the sample (BK 7; Diameter: 50.8 mm; Effective Focal Length: 75.6 mm; Wavelength Range: 430-700 nm). The back scattered light from the sample was then collected and collimated by the same Newport plano-convex lens. The collimated beam was passed through a HSNF-632.8-2.5 Holographic Super Notch Filter (Kaiser Optical Systems, Inc.) to remove the elastic component of the scattered light. After passing through the Holographic Notch Filter, the light was focused by a Sigma 70-210mm f/3.5-4.5 apochromatic macro zoom lens before entering into the slits of the spectrometer.

A Spex Model 500M spectrometer equipped with a 1200 groove/mm diffraction grating dispersed the Raman scattered radiation. The intensity of dispersed Raman radiation was recorded by a liquid-N_2-cooled charge-coupled device (CCD) camera at the exit of spectrometer. The temperature of CCD was maintained at 140K during measurements. The exposure time for

obtaining one Raman spectrum was set as 50sec. The entrance slit opening size of the spectrometer was 100μm×2mm. The effective bandwidth of spectrometer was 4.2cm^{-1}. The spectrometer was controlled by SPEX DM3000S spectrometer/camera drive software running on a generic 486 DOS PC. The original data obtained in the computer was SPT file, which was then transferred by using Galactic software to create a SPC file suitable for further data analysis.

2.14 Surface Enhanced Raman Spectroscopy (SERS)

The major problem of traditional Raman Spectroscopy is that Raman inelastic scattering signal is too weak [69]. In order to use Raman spectroscopy to investigate thin passive films, the inelastic scattering intensity has to be increased. One way to achieve this goal is to electrochemically deposit a thin layer of Au nanoparticles on metal surface (See Figure 2-3). With an illumination of incident laser, Surface Plasmons (SPs) are generated near the surface of these Au particles [70-71]. By satisfying the resonance condition, Surface Plasmon (SP) is coupled with the incident light, and there is a generation of Surface Plasmon Polariton (SPP) [72]. The local electrical field in the vicinity of Au surface is dramatically enhanced (about 10^3 times larger). The Raman intensity from the passive film is therefore increased by 10^6 times approximately [72-73].

The optimum size for Au nanoparticles to enhance the local electrical filed is about 50 nm [74]. In addition, the electrical field enhancement of SPP is dependent on the surrounding media and wavelength of incident light [72]. The enhanced electrical field has no influences on the electrochemical behavior of passive films because it is a time-varying electrical field with a very high frequency [74].

Gold particle is behaving as an inert Raman antenna, which is used to amplify the Raman scattering signal without affecting the electrochemical behavior of the passive film and materials [75]. There are two advantages for choosing Au as the deposited material. Firstly, Au does not produce galvanic effect on the sample if the potential on the sample is controlled by an external potentiostat. Second, Au is more thermodynamically stable in various aqueous solutions [75].

2.15 Gold Deposition

The gold deposition on each sample was carried out in a standard one liter electrochemical cell, which contained 0.5mM $AuCl_3$ dilute solution. The Gold(III) chloride power was purchased from Sigma-Aldrich (334049 - 99%). The solution was bubbled with pure nitrogen gas for one day before gold depositions. Electrochemical deposition of gold nanoparticles was accomplished with an EG&G Model 173 potentiostat, equipped with a digital coulometer (Princeton Applied Research). A glass body calomel electrode (Purchased from Fisher Scientific) served as Reference Electrode and two 2.5cm×2.5cm pieces of platinum mesh served as Counter Electrodes. All samples were thoroughly rinsed with double de-ionized water before gold plating.

During gold deposition process, Working Electrode (the sample) was cathodically polarized to -900mV vs. SCE (Saturated Calomel Electrode) for a certain time until an appropriate amount of charge was passed. The optimum size of deposited Au particles on the surface was about 50 nm (As shown in Figure 2-4). However, generally the gold particles exhibited a range of size, some as large as approximately 500 nm. After gold deposition, samples were rinsed with double de-ionized water.

2.16 Autoclave Sealing

In order to prevent sapphire window crack and water leaking at high temperatures, thermal stress and mechanical stress need to be minimized during the sealing of the autoclave. There was a countersunk mount designed for an accommodation of the sapphire window (Diameter: 31mm; Thickness: 11mm). The surface of countersunk mount was rough machined.

A gold-wire circle (Diameter: 25mm) was placed between the sapphire window and autoclave body. It acted as a seal. Gold wire was purchased from Alfa Aesar (0.5mm diameter; 99.95% metal basis). Gold was chosen because it was a ductile and inert metal. Gold-wire circle was mechanically deformed, and then formed a good seal in the periphery of sapphire window.

A Stainless Steel flange with a 4mm-thick round lip was used to hold the sapphire window. The lipped geometry was preferred over a flat flange in order to reduce non-uniform stresses. In addition, a copper O-ring was placed between the flange lip and sapphire window. Copper O-ring was annealed at 450^{o}C for 2 hours in furnace to increase its ductility, and subsequently polished to remove any copper oxides formed during heating. The copper ring protected the sapphire window from non-uniform stress distributions caused by thermal gradients and mechanical tightening.

The stainless steel flange had six holes fitting over six bolts extending from the autoclave body. The flange was tightened onto the autoclave body with nuts and washers. It clamped the copper ring and sapphire window to the autoclave, deformed the gold seal ring, and completed the pressure barrier of the test chamber. The nuts were tightened with a torque wrench to a torque of, initially 40 in-lb, 60, then 80,100,110, 120 in-lb, and to a final torque of 125 in-lb. The nuts were tightened in a star pattern to maintain a uniform stress on the sapphire window. Figure 2-5 was a photograph of autoclave after sealing.

2.17 Laser Alignment

The sealed autoclave was put on a Newport translation stage and placed in the front of Newport plano-convex collection lens. The autoclave was located at the position near the Focal Length of the lens. Before heating-up, the position of the autoclave was adjusted until the optimum Raman spectrum was obtained.

2.18 Data Analysis Software/Peak Subtraction/Peak Fitting

The SERS data obtained during measurements was SPT format file. It was then manually converted into SPC file by using GALACTIC software. Finally, all data were converted into OPJ file and analyzed by using ORIGINLAB software.

In the SERS spectra, there was a background included in the figure. In order to clearly reveal the peak features of the surface films on the sample, the background of spectra needs to be removed. One way was to subtract the SERS spectrum from a baseline spectrum. The background might be due to the PWR solution and the optical system. An ideal choice of the baseline spectrum was the SERS spectrum measured on the same sample under the same environment without a formation of surface films (for example: the sample was applied at a potential -1.8V vs. SHE). SERS spectra can be subtracted from this baseline spectrum (without formation of surface films). As a result, the plot obtained after subtraction represented the useful information about the surface films formed on the sample.

In some cases, the Raman peak was broad and may consist of several small peaks. This broad peak needs to be fitted. ORIGINLAB software was used to identify the multiple peaks by peak fitting. To fit the broad peak, Lorentzian-type function was chosen. The number of peaks was selected and input into the computer. Then, a value of Full Width Half Height (FWHH) was assigned to the ORIGINLAB software. The computer will run a peak fitting program and iterate these peaks until the best fitting is achieved. The statistics of peak fitting was recorded and the value of R^2 should be very close to 1 if it was a good peak fitting.

Chapter 3

Experimental Procedure

3.1 Samples

Dr. Peter Andresen of the General Electric Global Research Center (GE-GRC) provided a number of the alloys investigated in the present study. In particular, samples of Alloy 600 and Alloy 690 were obtained from commercial heats that were part of a GE research program. Two Ni-Cr binary alloys, Ni-10Cr and Ni-20Cr, and two Ni-Cr-Fe ternary alloys, Ni-5Cr-8Fe and Ni-10Cr-8Fe, were cast and thermomechanically processed at GE-GRC.

The chromium content of Alloy 600 makes it superior to pure nickel in many aqueous electrolytes [76]. High nickel content in Alloy 600 provides good corrosion resistance in reducing conditions and in alkaline solutions [76].

The compositional specification of Alloy 600 is shown in Table 1 [76].

TABLE 1. Chemical compositions of Alloy 600

ELEMENT	COMPOSITION (%)
Nickel	72.0min
Chromium	14.0-17.0
Copper	0.50max
Iron	6.0-10.0
Manganese	1.00max
Carbon	0.15max
Silicon	0.50max
Sulfur	0.015max

The typical mechanical properties of annealed Alloy 600 are shown in Table 2 [76].

TABLE 2. Mechanical properties of Alloy 600

Property	Value
Tensile Strength(MPa)	586-827
0.2% Yield Strength (Mpa)	205-345
% Elongation in 2"	50-30
%Reduction of Area	65-50
Rockwell Hardness	75-95B

Samples of Alloy 600 were cut into 6mm×5mm×1.5mm pieces. Each sample was polished by using 400 grit, 600 grit, 800 grit, and 1200 grit SiC paper. The sample (Working Electrode) was then tack welded to Alloy 600 wire (Diameter: 0.5mm; Length: 35cm) by using a welding equipment (UNITEK; WELDMATIC) operated at a power of 12 Watt Seconds. During tests conducted in the autoclave, the Alloy 600 wire served to electrically connect the sample to the potentiostat. After attaching with the metal wire, the sample was re-polished with 400, 600, 800, and 1200 grit SiC paper. Finally, the Alloy 600 sample with an attached wire was ultrasonically cleaned in Labtone detergent followed by double-deionized water.

The high chromium content of Alloy 690 provides excellent corrosion resistance in a broad range of aqueous environments. It is particularly resistant to high temperature solutions and many mildly oxidizing acids [77]. In addition, Alloy 690 has good strength and excellent metallurgical stability [77].

The compositional specification of Alloy 690 is shown in Table 3 [77].

TABLE 3. Chemical compositions of Alloy 690

ELEMENT	CHEMICAL COMPOSITION (%)
Nickel	58.0 min.
Chromium	27.0-31.0
Iron	7.0-11.0
Carbon	0.05 max.
Silicon	0.50 max.
Manganese	0.50 max.
Sulfur	0.015 max.
Copper	0.50 max.

To assist in assigning peaks in the SERS spectra of the oxides formed on Alloy 600 and Alloy 690, SERS spectra were also measured for the oxides formed on unalloyed nickel, unalloyed chromium, Ni-5Cr-8Fe, Ni-10Cr-8Fe, Ni-10Cr and Ni-20Cr samples. Unalloyed nickel and unalloyed chromium samples were purchased from Goodfellow Corporation. Ni-5Cr-8Fe, Ni-10Cr-8Fe, Ni-10Cr and Ni-20Cr samples were provided by GE-GRC.

The general information for Ni and Cr material is shown in Table 4.

TABLE 4. A list of samples of pure nickel and pure chromium

Material	Nickel	Chromium
Diameter	6mm	5mm
Length	100mm	100mm
Purity	99.99+%	99.7+%

A 1.5mm-thick piece of sample was cut from nickel rod and chromium rod respectively. These small samples were polished with 400, 600, 800, and 1200 grit SiC paper, and then thoroughly rinsed before all experiments.

3.2 Sample Loading

Only one sample was investigated per test run. As previously described, a long Alloy 600 wire was attached to each sample. The Alloy 600 wire was coated with Teflon tubing and double bore alumina rods, which are commonly used to hold thermocouple wires, in order to electrically isolate the wires from the titanium autoclave and piping. At the start of each test the sample was loaded into the autoclave and immersed in laboratory-simulated PWR primary water as it was deoxygenated for 24 h at room temperature. The wire that was attached to each sample and which was fed through the alumina tubes passed through a 220mm-long titanium tube with Teflon cap seals. Because the Teflon seals cannot properly function at the high test temperature of 320°C in the autoclave, they are off-set from the autoclave body by the 220 mm long titanium tube. The designs of Counter Electrode (CE) and Reference Electrode (RE) were similar as that of the Working Electrode (WE). Creep of Teflon seals was not found in any of the electrode seals while the autoclave was operating at 320 ^{o}C. Inside the autoclave the sample (working electrode) was displaced the same distance from the CE and RE, which was about 16 mm. The total volume of autoclave test chamber was 17.6 cm^3.

3.3 During heating-up

In addition to investigating the surface oxides that form on Alloy 600 and Alloy 690, tests were also conducted on laboratory heats of Ni-Cr-Fe alloys. The laboratory heats aided in identifying the phases those make up the oxides of Alloy 600 and Alloy 690. Obtaining the SER spectra of the oxides that form on nickel, chromium, and Ni-10Cr, Ni-20Cr, Ni- 5Cr-8Fe and Ni-10Cr-8Fe, began by immersing a sample in laboratory-simulated PWR primary water for a period of 24 h during which time the water was saturated with forming gas (mixture of 4% H_2 - balance N_2). Following 24 h of gas-saturation, one of two different procedures were employed as the water was heated at a rate of 1°C/min to the test temperatures of 320°C. In one method the sample was cathodically polarized at an applied potential of -1.8V vs SHE as the water was heated. In the second approach, the sample was unpolarized during the heat up.

3.4 Tests at 320°C

The potential on the sample was controlled by an external potentiostat (GAMRY instrument). At 320 °C the potential of all samples was stepped to -900 mV and thereafter, every 10 minutes the sample's potential was stepped in increments of 50 mV. Just prior to stepping the potential to the next higher value the SER spectrum of the sample's surface oxide was obtained.

3.5 Cool-down

The autoclave was cooled at rate of 2^{o}C/min approximately. During cool-down, the pump was kept running and the pressure maintained at 1800 psi so that water was still in a liquid phase. No steam was generated. When the temperature decreased below 100^{o}C, the pump was turned

off and the pressure was decreased to atmospheric. The temperature continued to decrease until it reached room temperature, at which point the SER spectrum of the oxide film was measured.

Then, the sample was removed from the autoclave and exposed to air for 10 min and the oxide's SER spectrum was measured. Finally, the sample was rinsed with pure water and dried by nitrogen gas, and the SERS spectrum was measured one more time.

Chapter 4

An Overview on the Experimental Results

4.1 Overview

In this study, in-situ Surface Enhanced Raman Spectroscopy (SERS) was employed to investigate the potential-driven changes in the surface films formed on Alloy 600 and Alloy 690 in laboratory-simulated PWR primary water at 320°C.

Assigning peaks in the SER spectra of the oxides that form on Alloy 600 and Alloy 690 was aided in the present investigation by first obtaining the SER spectra of the oxides that form on pure nickel, pure chromium, Ni-5Cr-8Fe, Ni-10Cr-8Fe, Ni-10Cr, and Ni-20Cr.

At 320°C, every 10 minutes the sample's potential was stepped in 50 mV increments from an initial value of -900 mV to a final value of -500 mV. Prior to stepping the potential to the next higher value, the sample was polarized at -1.8V for 10 min for a purpose of cathodically reducing (as much as possible) the oxide films formed at the previous potential. The 400 mV wide range of applied potential spans the alloys' corrosion potential of approximately -750 mV.

I would like to point out that each set of tests was repeated at least three times to check for reliability and reproducibility. If an unacceptable level of scatter was present among the first three tests, additional tests were conducted to achieve a satisfactorily reproducible result. Typically, it was never necessary to conduct more than five tests.. In this thesis, only one representative result is presented for each test condition.

4.2 IR Drop

Throughout the heat-up, the sample was subjected to an applied potential of -1.8V vs. SHE. The objective was to electrochemically reduce as much of the pre-existing surface oxide as possible and to minimize further oxidation of the sample. The uncompensated IR drop was largest during the end of the heat-up to 320 °C. The uncompensated IR drop was estimated as the product of the cell current and the electrolyte's resistance between sample and reference electrode. The product is most certainly larger than the true uncompensated IR drop so our estimate constitutes an upper limit.

The cell current associated with an applied potential of -1.8V increased monotonically from -40 μA at room temperature to -600 μA at 320 °C during the heat-up of one particular sample of Alloy 690 (Note: negative current indicates a net amount of electrochemical reduction on the surface of the sample). The electrolyte's resistance between sample and reference electrode was measured by electrochemical impedance spectroscopy. There was considerable

scatter in the measurements of resistance from test to test. The scatter was attributed to test-to-test variations in the position of the sample with respect to the reference electrode.

At frequencies ≥ 1 kohm, the impedance was approximately independent of frequency and exhibited values between 350 ohm and 1950 ohm. Again, the large variation is attributed to variations in the position of the reference electrode with respect to the sample. The reference electrode consisted of a thin platinum wire that was on occasion inadvertently bent on its insertion into the autoclave, which resulted in its non-reproducible positioning inside the autoclave.

Consequently, at an applied potential of -1.8 V, an upper-limit estimate of the maximum value (which occurred at 320 °C) of the uncompensated IR drop ranged from a high of 1.17 V to a low of 0.21 V. Presumably, the test-to-test variability of the uncompensated IR drop was responsible for the failure in some of the tests to completely reduce the spinel oxide on Alloy 600 during the heat-up of the autoclave.

Once the temperature of 320°C was reached, the applied potential was abruptly lowered from -1.8V to -0.9V and then raised in 50 mV increments every 10 minutes to a maximum value of -0.5V. During the polarization of the sample between -0.9V and -0.5V, the cell current ranged from a maximum value of 80 μA to a minimum value of 20 μA. At all values of applied potential ≥ -0.7V, the cell current was ≤ 50 μA. Consequently, for the case of the maximum observed value of resistance (1950 ohm) the uncompensated IR drop ranged from its high value of 0.156 V to its low value of 0.039 V as the applied potential was increased from -0.9V to -0.5V. At applied potentials ≥ -0.7V the IR drop was ≤ 0.098V in all cases. Over the same range of applied potential (-0.9V to -0.5V), for the case of the minimum observed value of resistance (350 ohm) the uncompensated IR drop decreased from 0.028 V to 0.007 V.

In summary, in all cases of polarization at potentials ≥ -0.700 V, the IR drop was less than 100 mV, and in approximately one-third of the tests, the IR drop was less than 25 mV at potentials ≥ -0.700 V.

The upper limit nature of the estimated uncompensated IR drop was confirmed by the SER spectra of the oxide film formed on nickel. The highest applied potential for which there was no peak attributed to NiO was -800 mV and the lowest potential at which the NiO peak appeared was -0.750 V. These results are in excellent agreement with the theoretical value of the electrochemical reduction potential of NiO in PWR primary water, which is -0.727 V, and suggests the uncompensated IR drop was less than 25 mV

4.3 Changes to the Surface Oxides during Heating from Room Temperature to 320°C

The SER spectrum of each sample's oxide film was measured at room temperature and thereafter at 50 °C intervals during the heat-up to the test temperature of 320 °C. Prior to the heat-up, the samples were cathodically polarized for 15 minutes at an applied potential of -1.8 V. During the heat-up to the test temperature two different procedures were employed. One group of samples was cathodically polarized with an applied potential of -1.8 V. The other group of samples was unpolarized during the heat-up.

There were two major differences between the oxide films formed on samples that were cathodically polarized during the heat-up and the oxides formed on samples that were not polarized during the heat-up. The first difference was in the thickness of the oxide film. The second distinction was in the phases that make up the oxide film.

The SERS results indicated that the main constituents of Alloy 600's oxide were Cr_2O_3 and $FeCr_2O_4$. During the heat-up the intensities of the SERS peaks assigned to Cr_2O_3 and $FeCr_2O_4$ increased with increasing temperature in 11 out of 14 unpolarized samples of Alloy 600, suggesting that the oxide films thickened but did not change their identity. In contrast, in 8 out of 10 samples of Alloy 600 that were cathodically polarized at an applied potential of -1.8V during the heat-up, the peak assigned to spinel oxide increased as the temperature was raised from room temperature reaching a maximum value at 100°C or 150°C. With further increases in temperature the intensity of the spinel oxide decreased to zero, suggesting that the spinel was cathodically reduced and that at temperatures $\geq 200^{o}$C - 250°C, the oxide consisted of a single species, Cr_2O_3.

The two sets of results are consistent with the higher potential of the unpolarized sample (approximately -0.7V vs. SHE) and the lower potential of the cathodically polarized sample (between -1.6V and -0.7V, depending on the magnitude of the IR drop) during cathodic polarization.

The results indicate (1) it is practically impossible to avoid film formation during heat up, and (2) a relatively simple film forms on cathodically polarized samples and a complex, multi-component oxide forms on unpolarized samples.

Additional SERS results indicate that in most tests Alloy 690's oxide consisted of only one species: Cr_2O_3. In two-thirds of the samples of Alloy 690 that were unpolarized during the heat-up, the intensity of the peaks assigned to Cr_2O_3 increased with increasing temperature, suggesting that the oxide thickened. In three out of seven samples that were cathodically polarized during the heat-up the film consisted of Cr_2O_3 and $FeCr_2O_4$. In the remaining four samples, the oxide consisted of only Cr_2O_3, which was not electrochemically reduced during the heat-up.

The presence/absence of $FeCr_2O_4$ in the oxide at 320 °C is largely determined by the large/small value, respectively, of the IR-drop during cathodic polarization. In this thesis only the oxides that were free of $FeCr_2O_4$ and consisted solely of Cr_2O_3 at -900 mV at 320 °C are discussed.

Once the test temperature was reached, all samples, whether cathodically polarized or unpolarized during the heat-up, were treated identically, starting with polarization at -900 mV for 10 minutes. Then the sample's potential was stepped every 10 minutes in 50 mV increments from an initial value of -900 mV to a final value of -500 mV.

Very few changes in the SER spectra of samples that were unpolarized during the heat-up occurred during polarization from -900 mV to -500 mV at 320 °C. In particular, the oxides formed on unpolarized samples of Alloy 600 during heat-up consisted of Cr_2O_3 and $FeCr_2O_4$ and were sufficiently thick to either mask or prevent changes to the oxide during polarization from -900 mV to -500 mV.

In contrast, the oxides of more than half of the samples of Alloy 600 that were cathodically polarized during heat-up consisted of just Cr_2O_3 and changes to these oxide films during polarization at 320 °C from -900 mV to -500 mV were detectable by SERS.

To focus on the oxides that form during polarization between -900 mV and -500 mV at 320 °C, this thesis includes the SER spectra obtained from only samples that were cathodically polarized during the heat-up from room temperature to 320 °C. The full sets of SERS spectra of Alloy 600 are shown in Appendix I and Appendix II. The full sets of SERS spectra of Alloy 690 are shown in Appendix III.

Chapter 5

In-situ SERS Investigation of the Surface Films on Pure Nickel, Pure Chromium, and Laboratory Heats of Ni-Cr and Ni-Cr-Fe Alloys

5.1 Pure Nickel

The growth and evolution with temperature and with applied potential of the oxides formed on pure nickel, pure chromium, Ni-10Cr, Ni-20Cr, Ni-5Cr-8Fe and Ni-10Cr-8Fe are not of primary interest in the present paper. Consequently, the full sets of SERS spectra are presented in the Appendix IV. Appendix V shows the SERS results after background subtraction and peak fitting. Suffice it to say, with regard to changes in the oxide during heat-up, the pre-existing oxide films, which were a consequence of air-exposure and immersion for 24 h in PWR PW during its deaeration, were never completely reduced. Specifically, Cr_2O_3 is a component of all pre-existing oxides (except in the case of pure nickel) and in all cases Cr_2O_3 was not electrochemically reduced during heat-up.

The current study uses only the minimum number of SER spectra of the films formed on nickel, chromium, and the four alloys that are needed to assist in assigning peaks in the SER spectra of the oxide films formed on Alloy 600 and Alloy 690. Specifically, only the SER spectra obtained at -0.65 V vs SHE of the oxides that form on nickel, chromium and the four Ni-Cr laboratory alloys are considered.

The SER spectra of the oxides formed on pure nickel and pure chromium at an applied potential of -0.65V and at a temperature of 320°C are presented in Figures 3-1 and Figure 3-2, respectively. To be clear, the samples were cathodically polarized at an applied potential of -1.8V during the heat-up to 320°C. At 320°C, the sample's potential was stepped in 50 mV increments from -900 mV to -650 mV. Before discussing the oxide films' spectra, note that there are two spectral features that are common to all of the measured SER spectra.

The peak at 415cm^{-1} is due to Raman scattering from the autoclave's sapphire window [78]. It was found that the intensity of the sapphire window's Raman peak was dependent on the distance between the window's inner surface and the sample inside the autoclave. If the sample was very close to the window's surface (<15mm), the Raman spectrum of the sapphire window would be very strong and outweigh the peaks in the spectrum of the sample's oxide film.

The well-defined peak at 880cm^{-1} is assigned to the A_1 totally symmetric stretch mode of aqueous borate ions [79,80,81]. The peak is attributed to borate ions in the bulk of the water and not to borate adsorbed on the surface of the samples [80]. If borate were adsorbed on the surface of the samples, the intensity of the peak and/or its location would likely shift with the sample's potential, which was not observed [80].

Given that all of the alloys that are of interest in the current study are nickel-base it is sensible to begin with the SER spectrum of the oxide film that forms on unalloyed nickel. The main objective of SERS measurements on pure nickel is to assist the analyses of SERS spectra of Ni-based alloys.

At E = -0.65V, there is a weak peak at about 540 cm^{-1} (as shown in Figure 3-1). The species that might form on nickel immersed in aqueous solutions are: NiO, $Ni(OH)_2$, and NiOOH. α-$Ni(OH)_2$ has strong Raman-active vibrational mode at 451 cm^{-1} and β-$Ni(OH)_2$ shows a strong peak at 449 cm^{-1} [75]. NiOOH has very strong peaks at 480 cm^{-1} and 550 cm^{-1} [75]. Therefore, the Raman peak at 540 cm^{-1} is unlikely due to either $Ni(OH)_2$ or NiOOH.

Comparison of the SER spectra to the Raman spectrum of nickel oxide indicates that the oxide formed on nickel at 320°C in PWR primary water is almost certainly NiO. NiO exhibits the Rock Salt structure (The oxygen ions form cubic close packed planes and all of the interstices are occupied by Ni^{2+}. The basic structural unit is the octahedron. All ions have octahedral coordination, so it doesn't matter if we consider the Ni^{2+} at the geometric center and in contact with the six oxygen ions located at the vertices, or vice-versa.). First order Raman scattering is symmetry forbidden for crystals with the Rock Salt structure [75].

That the NiO film on nickel exhibits weak SERS intensity, rather than zero intensity, is most likely a consequence of a high concentration of crystalline defects, such as a nano grain size as well as an overall film thickness of only several nanometers [75]. We assign the 540 cm^{-1} peak to "green" NiO. Green NiO is stoichiometric, while "black" NiO is off-stoichiometric and exhibits a relatively strong Raman peak at 490 cm^{-1} and a weak peak at 400 cm^{-1} [82]. Green NiO exhibits a relatively strong Raman peak at 535 cm^{-1} and weak peaks at 727 cm^{-1}, 913 cm^{-1}, and 1074 cm^{-1} [82]. The peaks at 490 cm^{-1} for black NiO and at 535 cm^{-1} for green NiO are attributed to disorder-allowed, first-order Raman scattering [75]. The weak peaks at 727 cm^{-1}, 913 cm^{-1} and 1074 cm^{-1} have been assigned to second-order Raman scattering [82]. Maslar et. al. identified by conventional Raman spectroscopy NiO in nickel coupons heated to 400 °C with a peak at 560 cm^{-1}. The NiO was also indicated by a weak peak at 910 cm^{-1}, which is attributed to second-order Raman scattering [83].

W.G. Cook et. al. developed the Pourbaix diagram for the nickel-water system at high temperatures. At potential above -0.7V (pH=7.2), the stable phase for Ni-H_2O system at 300°C was NiO [84]. It is consistent with our SERS results in which the NiO 540 cm^{-1} peak is absent below -0.75V, suggesting that the nickel metal phase is stable. Bhargava also found that NiO was formed at potentials greater than -0.7V (vs. SHE) in PWR primary water (288°C) by using Transmission Electron Microscopy (TEM). The thickness of NiO film is about 1~3nm [85].

$Ni(OH)_2$ exhibits the Brucite crystal structure, which consists of hexagonal close-packed OH^- with Ni^{2+} occupying one-half of the interstitial sites [75]. Close packed planes with fully occupied interstitial sites alternate with close packed planes with vacant interstitials. In the occupied planes, the octahedra share edges. An alternative description focuses on the octahedral structural unit, composed of Ni^{2+} at the center and one OH^- at each of the six vertices. The H ions are oriented into the tetrahedral interstices in between the layers and do not act as H bridges [75]. The octahedra are joined at their edges so that each OH^- is shared by three octahedra. The stoichiometry can be expressed as $Ni(OH)_{6/3}$.

For NiO, the position of the transverse optical (TO) phonon is at 440 cm^{-1} and the position of the longitudinal optical (LO) phonon is at 550 cm^{-1}. Increasing the amount of oxygen in the layers decreased the width of the LO mode and shifted its locations to a value of about 560 cm^{-1} [86]. This position characterizes the layers as a having a composition close to the Ni_2O_3 composition. Annealing causes a shift in the LO phonon mode from 510 cm^{-1}, which they assign to stoichiometric NiO, to 550 cm^{-1}, which corresponds to a significant excess of O (~Ni_2O_3) [86].

5.2 Pure Chromium

The addition of chromium can increase the corrosion resistance of nickel-based alloys by forming a thin, Cr-rich passive layer on the alloy's surface. In this study, SERS spectra of the oxide formed on pure chromium are measured. The main purpose is to help us to assign the Raman peaks of oxides formed on Alloys 600 and 690.

In all of the SERS spectra measured for the oxide formed on pure chromium, there is a strong peak at 540 cm^{-1} as well as a weaker peak at approximately 610 cm^{-1} (as shown in Figure 3-2). As was discussed further ahead, the peak at 610 cm^{-1} is important for distinguishing between NiO and Cr_2O_3. While both NiO and Cr_2O_3 exhibit a SERS peak at 540 cm^{-1}, only Cr_2O_3 exhibits peaks at both 540 cm^{-1} and 610 cm^{-1}. W.G. Cook has proposed a Pourbaix diagram for chromium-water system at 300 ^oC. The thermodynamic stable phase was Cr_2O_3 or $Cr(OH)_3$ at low potentials [87]. The strong SERS peak at 540 cm^{-1} could be assigned to $Cr(OH)_3$, CrOOH or Cr_2O_3, all of which have a strong Raman vibrational mode in the range of 530 cm^{-1} to 580 cm^{-1}. Determining the identity of the film formed on chromium must be based on the assignment of the weaker SERS peak located at 610 cm^{-1}, as well as the strong peak at 540 cm^{-1}. The SERS peak at 610 cm^{-1} excludes $Cr(OH)_3$, which has Raman peaks at 525 cm^{-1} [88], 530 cm^{-1} [88], and weak peaks in the range of 480-500 cm^{-1} and no peak in the vicinity of 610 cm^{-1} [88].

CrOOH and Cr_2O_3 exhibit similar structures, both are based on $Cr(III)O_6$ octahedra. Their similar structures predict both would exhibit similar Raman spectra. Indeed, CrOOH exhibits a strong Raman peak at 525 cm^{-1} and a less intense peak at 610 cm^{-1} [89]. α-CrOOH has Raman peaks at 345 cm^{-1}, 475 cm^{-1}, and several peaks in the region of 530 cm^{-1}-640 cm^{-1}, and 545 cm^{-1} - 610 cm^{-1} [90]. J.E. Maslar assigned the Raman peak at 580 cm^{-1} to α-CrOOH, which formed on chromium in high temperature, pressurized water [90]. As discussed in the following paragraph, a number of investigations have reported the most intense Raman peak of Cr_2O_3 occurs at 550 cm^{-1} along with a weaker peak at 610 cm^{-1} (as well as several other weak peaks).

The Raman spectrum of single crystal Cr_2O_3, with the corundum structure, is well established. According to P. Fabis et. al, Cr_2O_3 has a strong vibrational mode at 540 cm^{-1}, and less intense peaks at 300 cm^{-1}, 350 cm^{-1} [91]. D. Thicrry found that Cr_2O_3 shows a strong Raman peak at 306 cm^{-1}, weak peaks at 342cm^{-1}, 541 cm^{-1} and 602 cm^{-1} [92]. I.R. Beattie assigned the strong peaks at 303cm^{-1}, 551 cm^{-1} and weak peaks at 351 cm^{-1}, 397 cm^{-1}, 530 $cm^{-}1$ and 609 cm^{-1} to the Raman-active vibrational modes of Cr_2O_3 [93].

Thus, based on its SERS spectrum, the oxide formed on chromium at 300°C in PWR primary water could be either CrOOH or Cr_2O_3, or even a mixture of the two. For the sake of

ease in discussing the structures of the more complex oxides that form on Alloy 600, and other alloys investigated in the present study, we will assign the SERS peaks at 540 cm^{-1} and 610 cm^{-1} to Cr_2O_3 since these two peaks are closer to the 550 cm^{-1} and 610 cm^{-1} Raman peaks of Cr_2O_3 than to the 525 cm^{-1} and 610 cm^{-1} peaks of CrOOH.

In addition to the Raman spectrum of Cr_2O_3 providing a slightly better fit than that of CrOOH to the SERS spectrum of the oxide formed on Cr in PWR primary water at 300°C, most thermodynamic calculations indicate Cr_2O_3 is the thermodynamically stable phase.

Cr_2O_3 is stable under very reducing conditions, which might explain its resistance to electrochemical reduction when samples were being heated in the autoclave to 320°C.

The oxidation of Cr to Cr_2O_3:

$$(1) 2Cr + 3H_2O \rightarrow Cr_2O_3 + 6H^+ + 6e^-$$

$$(2) \Delta\emptyset_e = \Delta\emptyset_e^0 - \frac{RT}{ZF} ln \frac{[Cr]^2[H_2O]}{[Cr_2O_3][H^+]^6}$$

Where the $\Delta\emptyset_e$ is the Cr/Cr_2O_3 equilibrium potential, and $\Delta\emptyset_e^0$ is Cr/Cr_2O_3 equilibrium potential at standard state. R is the gas constant, F is Faraday constant and T is the temperature. The activity of Cr and H_2O can be taken as unity, and the Cr/Cr_2O_3 equilibrium potential is determined by the activity of Cr_2O_3 species and hydrogen ion concentration.

$$(3) \quad \Delta\emptyset_e = \Delta\emptyset_e^0 - \frac{RT}{ZF} ln \frac{1}{[Cr_2O_3][H^+]^6}$$

The value of the equilibrium potential at pH 7.2 and 300°C is about -1.475V vs.SHE. It is well below the equilibrium potential of $H_2O + e^- \Leftrightarrow ½ H_2 + OH^-$ (about -0.814V), which represents the lower potential limit of the stability of H_2O. That is, Cr_2O_3 is stable at potentials below the stability range of water. The thermodynamic stability of Cr_2O_3 relative to that of H_2O at very reducing potentials probably accounts for our inability to electrochemically reduce Cr_2O_3 by cathodic polarization during the heat-up to 300°C of chromium and various Ni-Cr alloys immersed in de-oxygenated PWR primary water.

At 300°C, Pourbaix diagram shows a wide stable phase region for Cr_2O_3, where the potential range is from -1.2V to 0V (for pH=7.0), and pH ranges from 2.5 to 11 [87]. D. Cubicciotti has calculated the Potential-pH diagram for the $Cr-H_2O$ system at 298K and 562K [94]. In both cases, Cr_2O_3 is the stable phase below 0.1V approximately [94]. Therefore, the SERS peaks at 540 cm^{-1} and 610 cm^{-1} are assigned to Cr_2O_3.

In summary, it is possible that the passive film on pure chromium consists entirely of Cr_2O_3, or of α-CrOOH, or a mixture of Cr_2O_3 and α-CrOOH, but the strength of the evidence sloightly favors Cr_2O_3 as the dominant species in the passive film formed on chromium in PWR primary water at 300°C. As summarized in the following two paragraphs, thermodynamic data also support the assignment of chromium's passive film to Cr_2O_3.

5.3 Comparison of the SER Spectra of Films Formed on Chromium and Nickel

The SER spectra of the films formed on nickel and chromium both exhibit a peak of significant intensity located at 540 cm^{-1}. Consequently, a peak located at 540 cm^{-1} in spectra will be difficult to unambiguously assign. It's possible to confuse NiO for α-Cr_2O_3, and vice-versa, in the surface films formed on Ni-Cr alloys.

One set of the spectra obtained from the surface film of Cr exhibited fairly high intensity for the peak at 540 cm^{-1} but the other set exhibited a relatively weak peak (i.e., relative to the intensity of the peak at 880 cm^{-1}, which is assigned to borate ions in the bulk solution), just as was the case for the four spectra of NiO. Consequently, it's not possible to distinguish between NiO and Cr_2O_3 solely on the basis of the intensity of the 540 cm^{-1} peak.

The best way of distinguishing between NiO and Cr_2O_3 is the presence/absence of a peak at 610 cm^{-1}. A peak at 610 cm^{-1} would likely indicate Cr_2O_3 and the absence of this peak, in conjunction with a peak at 540 cm^{-1}, might suggest NiO. The absence of a peak at 610 cm^{-1} cannot rule out Cr_2O_3 because the intensity of a relatively weak peak such as that at 610 cm^{-1} is often not detectable from very small samples, such as thin surface oxides. Generally, small samples are identified by the presence/absence of the strongest peak of their Raman spectra. Distinguishing between thin films of NiO and Cr_2O_3 is particularly challenging because their most intense Raman peaks are both located at 540 cm^{-1}.

In our approach, the combination of a strong peak at 540 cm^{-1} and a weak peak at 610 cm^{-1} is assigned to Cr_2O_3, but we cannot exclude the possibility that NiO contributes, most likely in a small way, if at all, to the intensity of the peak at 540 cm^{-1}. The presence of a peak at 540 cm^{-1} without a peak at 610 cm^{-1}, might be assigned to NiO. However, Raman activity of the vibrational mode of NiO in the range of 500-540 cm^{-1} is symmetry forbidden, so, in our opinion, even in the absence of a peak at 610 cm^{-1}, a Raman peak at 540 cm^{-1} in the spectrum of an oxide formed on a Ni-Cr alloy is best assigned to Cr_2O_3.

5.4 Ni-5Cr-8Fe

The SER spectrum of the oxides formed on Ni-5Cr-8Fe at -0.65 V is presented in Figure 3-3(a). Figure 3-3b presents the SER spectrum following background subtraction. In addition, the SERS peak is deconvoluted and shown to consist of three overlapping peaks.

The most intense peak of the spectrum is located at 540 cm^{-1}. Because 540 cm^{-1} is the strongest peak in the Raman spectra of both NiO and α-Cr_2O_3, it is difficult to assign this peak in the SER spectra of the film formed on Ni-5Cr-8Fe. Obviously, it might be tempting to assign the peak to NiO rather than to α-Cr_2O_3 because of the alloy's small concentration of chromium.

There are three points that argue against such an assignment. First, at least part of the sample's film was formed at room temperature before the sample was inserted into the autoclave. SERS during heating of the autoclave indicates that cathodic polarization did not completely remove the prior-formed film, which suggests it is Cr_2O_3 because Cr_2O_3 is more resistant than NiO to electrochemical reduction. Second, thermodynamic calculations by L. Kaufman indicate

the portion of the 320°C film formed at potentials below approximately -800 mV will not contain any nickel [95]. Third, it is kinetically possible for an element that is relatively reactive and fast diffusing to form a continuous corrosion product on the alloy's surface. Examples include the formation of continuous Al_2O_3 films during high temperature gaseous oxidation of superalloys that contain only a few atomic percent of aluminum, and the formation of continuous chromium oxide films during room temperature aqueous corrosion of iron-chromium alloys that contain approximately 12 atomic percent of chromium.

As we have discussed, the key to assigning with high confidence the peak at 540 cm^{-1} to Cr_2O_3 is the presence of a peak at 610 cm^{-1}.

In three out of the three sets of spectra measured in 0.19 ppm Li + 1200 ppm B a peak at 610 cm^{-1} was present. In some cases (such as in Figure 3-3b), the 610 cm^{-1} peak overlapped with higher wavenumber peaks (discussed below) and was not as distinct as it was in the case of the spectra of α-Cr_2O_3.

The 610 cm^{-1} was not detected in approximately one-half of the second set of spectra measured in 2.0 ppm Li + 1200 ppm B. Those spectra in which the peak at 610 cm^{-1} was missing also exhibited a weak peak at 540 cm^{-1} and the missing peak at 610 cm^{-1} could be explained by the weakness of the SERS signal.

Thus, the combination of a strong peak at 540 cm^{-1} and a second peak at 610 cm-1 indicates the film most likely contains α-Cr_2O_3. It's also possible that the film contains a small amount of NiO since the SER spectra of nickel's passive film consists almost entirely of a single peak at 540 cm^{-1}, and the strongest Raman peak in spectra of standards of NiO is at or very close to 540 cm^{-1}. However, the dominant species must be Cr_2O_3.

As shown in Figure 3-3b, there is one other peak present in the SER spectra of the films formed on Ni-5Cr-8Fe and this peak is not present in any of the spectra measured for nickel and chromium. The peak in question is located in the vicinity of 670 cm^{-1} and is assigned to a spinel compound. The Raman spectra of spinels contain a number of peaks but the most intense peak (A_{1g}) is located at approximately 670 cm^{-1} [96,97,98].

The spinel peak is either absent or is very weak in the spectra measured during heating of the water to 320°C. In almost all cases the spinel peak grows significantly during the sample's polarization from -900 mV to -400 mV at 320°C.

There are several possible identities of the spinel oxide formed on Ni-5Cr-8Fe. $NiFe_2O_4$ is thermodynamically stable at potentials $\geq$ -0.787 V [95]. $FeCr_2O_4$ is thermodynamically stable at potentials $\geq$ -0.954 V [95]. While $NiCr_2O_4$ is not thermodynamically stable on Ni-Cr-8Fe alloys [95] it could be present as a consequence of kinetic factors. To distinguish between $NiFe_2O_4$, $FeCr_2O_4$ and $NiCr_2O_4$, SER spectra were collected from the oxides that form on Ni-10Cr and Ni-20Cr. As illustrated in Figures 3-4 and 3-5, the SER spectra at -0.65 V consist of peaks at 540 cm^{-1} and 610 cm^{-1} with either very little or no evidence of a peak at 670 cm^{-1}. Thus, the spinel that forms on Ni-5Cr-8Fe is most likely $FeCr_2O_4$.

It is possible that there are additional cations in the oxides we have identified as Cr_2O_3 and $FeCr_2O_4$. For example, the spinel that we have identified as $FeCr_2O_4$ might best be

represented as chromium-rich $(Fe,Ni)(Cr,Fe)_2O_4$. In addition, Cr_2O_3 might contain some iron and therefore should be described by $(Cr,Fe)_2O_3$. In this context it is worth noting that Hamilton and Anderson detected $(Cr,Fe)_2O_3$ as the chromia film that formed during thermal air oxidation of Fe-18Cr-2Mo [99].

In brief, the surface film of Ni-5Cr-8Fe alloy consists of Cr_2O_3, $FeCr_2O_4$ spinel and possibly NiO.

5.5 Ni-10Cr-8Fe

The SER spectrum of the oxides formed on Ni-10Cr-8Fe at -0.65 V is shown in Figure 3-6.

The spectrum contains a strong peak at 540 cm^{-1} and a weaker peak at 610 cm^{-1}, which overlaps and forms a shoulder on the 540 cm^{-1} peak. The peak at 610 cm^{-1} is easier to discern than in the spectra of Ni-5Cr-8Fe's film. This difference might be due to larger amounts of α-Cr_2O_3 formed on the 10 Cr alloy than for films formed on the 5 Cr alloy.

As is the case for the films formed on Ni-5Cr-8Fe, deconvolution of the SER peak as shown in Figure 3-6b indicates $FeCr_2O_4$ spinel phase is also formed in the surface film of Ni-10Cr-8Fe.

There are no qualitative differences in the SER spectra of the films formed on Ni-10Cr-8Fe and Ni-5Cr-8Fe. The surface films of both alloys contain Cr_2O_3, $FeCr_2O_4$, and possibly NiO.

Note in each spectrum that the intensity of the peak at 540 cm^{-1} relative to the intensity of the borate peak at 880 cm^{-1} in Figures 3-1 – Figure 3-4 increases monotonically as the chromium concentration is increased from 0 (unalloyed nickel), to 5%, 10% and unalloyed chromium. The trend of increasing intensity of the 540 cm^{-1} peak with increasing chromium concentration of the alloy further supports the assignment of the strong 540 cm^{-1} peak in the SER spectra of the oxides formed on Ni-5Cr-8Fe and Ni-10Cr-8Fe to Cr_2O_3.

Succinctly stated, the surface oxide films formed on Ni-5Cr-8Fe and Ni-10Cr-8Fe alloys in PWR primary water at 320°C are composed of Cr_2O_3 and $FeCr_2O_4$ spinel.

5.6 Ni-10Cr and Ni-20Cr

The SER spectra of the oxides formed on Ni-10Cr and Ni-20Cr binary alloys at -0.65 V are presented in Figures 3-4 and 3-5. As already mentioned, these spectra were used to help identify the spinel oxide that forms on Ni-5Fe-8Cr and Ni-10Cr-8Fe.

SERS spectra of the oxides formed on both Ni-10Cr and Ni-20Cr contain a strong peak at 540 cm^{-1} and a peak at 610 cm^{-1}. The spectra indicate that Cr_2O_3 film is formed on the surface of Ni-10Cr and Ni-20Cr. The intensity of the Cr_2O_3 peak relative to the intensity of the borate peak at 880 cm^{-1} increases as the chromium composition increases from 10% to 20%.

No spinel oxide peak exists in the SERS spectra for Ni-10Cr and Ni-20Cr binary alloys.

Therefore, the surface film of Ni-10Cr and Ni-20Cr alloys is Cr_2O_3. Again, the possible small contribution of NiO to the intensity of the peak at 540 cm^{-1} cannot be ruled out.

5.7 Comparison of the SER Spectra of Films Formed on Chromium, Nickel, Ni-5Cr-8Fe, Ni-10Cr-8Fe, Ni-10Cr and Ni-20Cr

The key to the analyses of the present results is the use of a secondary peak in the Raman spectrum of Cr_2O_3 in order to distinguish between Cr_2O_3 and NiO, which are the two species associated with the most intense peak, located at 540 cm^{-1}, in the spectra of all of the oxides formed on the metals and alloys investigated in the present study. The second-most strong peak in the Raman spectrum of Cr_2O_3 is located at 610 cm^{-1}. The presence of the peak at 610 cm^{-1} confirmed the presence of Cr_2O_3 in the films that form on chromium, Ni-5Cr-8Fe, Ni-10Cr-8Fe, Ni-10Cr and Ni-20Cr.

As we have discussed, the 880cm^{-1} peak is assigned to the totally symmetric stretch mode of borate ions dissolved in the bulk of the electrolyte, and its intensity and position would not change with the sample's potential [79,80,81]. As a result, normalizations of the intensity of 610 cm^{-1} peak by dividing by the intensity of the peak at 880 cm^{-1} would provide approximate information on the relative amounts of Cr_2O_3 in the films that form on the samples. The approximate nature of the information obtained about the relative amounts of Cr_2O_3 needs to be emphasized. Even after normalizing all of the spectra to account for differences in incident intensity of the laser, the relative intensities of the peak at 610 cm^{-1} cannot rigorously determine the relative amounts of Cr_2O_3 because of the possibility that the magnitude of the SERS enhancement differs from sample to sample.

The chromium concentration of the samples investigated increased from 0% (unalloyed nickel), to 5% Cr (Ni-5Cr-8Fe), 10%Cr (Ni-10Cr-8Fe), 15%Cr (Alloy 600), 20%Cr (Ni-20Cr), 30%Cr (Alloy 690), and 100%Cr (unalloyed chromium). A detailed, evaluation of SERS results is presented in the following section of this thesis. The quantitative analysis shows that the integrated intensity (i.e. the area under the curve of Raman peak) ratio between 610 cm^{-1} peak and 880 cm^{-1} peak increases with the chromium concentrations in the samples. It indicates that the amount of Cr_2O_3 in the surface films increases with the alloy's chromium concentration.

As already mentioned, NiO has a Raman peak at 540 cm^{-1}, which is the same position as the most intense Raman peak of Cr_2O_3. Therefore, the 540 cm^{-1} peak is possibly due to two species, NiO and Cr_2O_3. Clearly, in the SERS spectrum of the oxide formed on unalloyed chromium, the 540 cm^{-1} peak is entirely due to Cr_2O_3. As the chromium concentration decreases and the nickel concentration increases, the integrated intensity ratio between 610 cm^{-1} peak and 540 cm^{-1} peak in the SERS spectra of the oxides formed on Ni-Cr and Ni-Cr-Fe alloys decreases. Therefore, the integrated intensity ratio reaches a maximum value for unalloyed chromium. The quantitative analysis (in section 5.8) demonstrates that, any values less than the maximum value suggests that a NiO film contributes to 540 cm^{-1} peak. As the chromium composition increases from 0% (unalloyed nickel), to 5% Cr (Ni-5Cr-8Fe), 10%Cr (Ni-10Cr-8Fe), 15%Cr (Alloy 600), 20%Cr (Ni-20Cr), 30%Cr (Alloy 690), and 100%Cr (unalloyed chromium), the intensity ratio

between 610 cm^{-1} peak and 540 cm^{-1} peak increases from 0 to its maximum constant value, and the composition of NiO in the surface films ($NiO+Cr_2O_3$) decreases from 100% (unalloyed nickel) to 0 (unalloyed chromium).

The third phase detected in some of the surface oxides is a spinel oxide. It is found in the surface films of Ni-5Cr-8Fe and Ni-10Cr-8Fe. Typically, the most intense peak of the spinel phase is located between 650 cm^{-1} and 690 cm^{-1}. No spinel Raman peak is found for the oxides of Ni-10Cr or Ni-20Cr binary alloys. As we have extensively discussed, the spinel responsible for the peak at 670 cm^{-1} is $FeCr_2O_4$. We have found that the integrated intensity of the spinel peak increases with sample's potential.

5.8 Quantitative Analysis

The full sets of SERS spectra results of Ni, Cr, Ni-5Cr-8Fe, Ni-10Cr-8Fe, Ni-10Cr and Ni-20Cr, are presented in the Appendix IV and Appendix V. The spectra presented in the body of the thesis are representative of all of the measured spectra and were subjected to quantitative analysis. The objective was to extract additional information about the identities of the oxide films formed on the different alloys by comparing the relative intensities of selected peaks in each spectrum.

The protocol for analyzing the SERS spectra is as follows. For all SERS spectra, there is a strong background, which must be subtracted in order to calculate the intensity of Raman peaks. As is the case for conventional Raman scattering, stray light due to Rayleigh scattering constitutes a major component of the background, especially at low values of Raman shift (e.g., $\leq$ 300 cm^{-1}). The Rayleigh component of the background is generally modeled by an appropriate polynomial function. The portion of the spectrum of interest in the current research is located in the range of 500-700 cm^{-1} where the background is conveniently represented by a straight line [100, 101].

After background subtraction, the number, location, size and shape of the Raman peaks were identified. Spectral features composed of multiple overlapping peaks were deconvoluted with computer assistance (Origin™ software). Typically, only two or three overlapping Lorentzian peaks were required to duplicate the measured feature. The location, height and integrated intensity were determined for each of the overlapping peaks. A peak's integrated intensity was the output of the peak fitting. The SERS results after background subtraction and peak fitting are shown in Appendix V.

The integrated intensity ratio between film's peak and the borate's peak (880 cm^{-1} peak) were calculated to normalize our SERS results for test-to-test variations in the incident laser intensity.

Figure 3-7 plots the ratio of the integrated intensity of the peak at 610 cm^{-1} to the integrated intensity of the peak at 880 cm^{-1} as a function of applied potential. For any given alloy, the variation in intensity of the peak at 610 cm^{-1} with increasing potential is non-monotonic. We attribute the non-monotonic potential dependency to changes in the area of the sample analyzed at one value of potential to the next. Shifts in the spot that is analyzed were not deliberate and

were due to relatively small movements of the sample. The differences in intensity of the peak at 610 cm^{-1} from one site on the sample to another are due to at least two effects: (1) changes in the thickness of the oxide film with increasing potential, and (2) changes in the enhancement of the Raman spectrum due to differences in the number and geometry of the gold particles that magnify the optical field of the laser. The nature and magnitude of the potential dependency strongly suggest that the dominant effect is the latter.

Despite the potential-to-potential scatter in the intensity of the peak at 610 cm^{-1} there is a rough correlation between the amount of chromium in the alloy and the intensity of the 610 cm^{-1} peak. For nickel, no peak at 610 cm^{-1} exists at any potential. As the chromium concentrations of the Ni-Cr binary and Ni-Cr-Fe ternary alloys increase, the integrated intensity ratio of 610 cm^{-1}/ 880 cm^{-1} increases. Evidence for the increase in intensity with increasing chromium concentration of the alloy is enhanced by the data for Alloy 600 and Alloy 690, which are introduced further ahead in this thesis.

The decreasing intensity of the 610 cm^{-1} peak of chromium's oxide with increasing potential is both surprising and reproducible. The results of similar tests conducted on two other samples of chromium revealed the same effect of potential. The results suggest that the oxide formed on chromium decreases with increasing potential, which seems unlikely to be the case. One possible explanation is a change in the identity of chromium's oxide film from CrOOH to Cr_2O_3 as the potential is increased. We have already mentioned that it is difficult for most techniques of chemical analysis, including Raman spectroscopy, to distinguish between CrOOH and Cr_2O_3. Studies of passive films at room temperature have suggested that some films are dehydrogenated as the sample's potential is increased. The more positive potential drives H^+ out of the film. In the present study, CrOOH might form at low potentials and convert to Cr_2O_3 at higher potentials. The very similar structures of CrOOH and Cr_2O_3 would generate very similar Raman spectra, and if the Raman scattering cross-section of Cr_2O_3 is lower than that of CrOOH, the intensity of the spectrum would decrease as the potential is raised and CrOOH is converted to Cr_2O_3. At this time it is not known if the Raman scattering cross sections are different and our proposed explanation remains an untested hypothesis.

The effect of the alloy's chromium concentration on the intensity of the peak at 610 cm^{-1} is made more apparent in Figure 3-8, which presents the ratio of the intensities of the 610 cm^{-1} and 880 cm^{-1} peaks at potentials of -0.7V, -0.6V and -0.5V. The results are the same as those presented in Figure 3-7. The influence of the alloy's chromium concentration is brought out by re-plotting Figure 3-7's results as a function of chromium concentration. The results strongly suggest that the amount of Cr_2O_3 formed increases with the alloy's chromium concentration.

From the general observation that the protectiveness of a surface oxide is inversely proportional to its thickness (i.e., a thicker oxide suggests a greater amount of oxidation) the increasing amount of Cr_2O_3 with increasing potential is surprising. However, the results might be explained by an opposing tendency in which the tendency to form Cr_2O_3 (as opposed to another oxide, such as a spinel) scales with the alloy's chromium concentration. It would appear that the latter effect is dominant. Thus, it might be the case that the corrosion resistance of the alloys increases with the alloy's chromium concentration and that the total amount of corrosion product, which includes all oxides and not just Cr_2O_3, decreases with the alloy's chromium concentration.

The hypothesis that oxides other than Cr_2O_3 are formed in quantities inversely proportional to the alloy's chromium concentration is supported by the data presented in Figures 3-9 and 3-10. Figure 3-9 plots the ratio of the integrated intensities of the peaks at 610 cm^{-1} and 540 cm^{-1} as a function of the alloy's chromium concentration. The data were obtained from the spectrum of each alloy at an applied potential of -0.65 V. Since Cr_2O_3 is the only oxide formed on unalloyed chromium, the ratio of 2.28 obtained for chromium's oxide film can be compared to the values of the ratio obtained for the other alloys in order to estimate the amount of NiO that forms in addition to Cr_2O_3 (Recall that NiO is the only other species that is likely to contribute to the SERS peak at 540 cm^{-1}). Thus, the results indicate that a significant amount of NiO forms on the alloys and the amount are inversely proportional to the alloy's chromium concentration.

The results presented in Figure 3-10 indicate that spinal $FeCr_2O_4$ forms as well as NiO and Cr_2O_3 on alloys of Ni-5Cr-8Fe and Ni-10Cr-8Fe. The spinel phase forms at potentials slightly greater than the equilibrium potential of $FeCr_2O_4$ and the amount of spinel increases with increasing potential.

The formation of NiO and $FeCr_2O_4$, in addition to Cr_2O_3 on alloys of Ni-Cr and Ni-Cr-Fe, and in amounts that vary inversely proportional to the alloy's chromium concentration suggests that the protectiveness against corrosion of the alloy's Cr_2O_3 depends on the alloy's chromium concentration. The correlation between Cr_2O_3's protectiveness and the alloy's chromium concentration might be due to two effects: an increasing amount of Cr_2O_3, which the data clearly indicates occurs with increasing chromium concentration of the alloy, and a difference in the properties of the alloy's Cr_2O_3. The increasing amount of Cr_2O_3 might affect the protection afforded by Cr_2O_3 because the breadth/continuity of coverage might increase with the alloy's chromium concentration, as well as the thickness of a continuous layer of Cr_2O_3. The properties of Cr_2O_3 might change with the alloy's chromium concentration because higher amounts of iron, and possibly nickel, are included in alloys of relatively low chromium concentration. For example, the presence of substitutional impurities of Fe^{+2} and Ni^{+2} in Cr_2O_3 would increase the oxygen ion vacancy concentration in order to maintain charge neutrality. The higher rate of oxygen ion transport that accompanies a high vacancy concentration might increase the alloy's oxidation. .

Chapter 6

In-situ SERS Spectra of the Oxide Films Formed on Alloy 600 and Alloy 690 in PWR Primary Water at 320°C

6.1 SERS Results of Surface Films Formed on Alloy 600 and Alloy 690

Figure 4-1 ~ 4-9 show the SERS results for Alloy 600 at potentials from -0.9V to -0.5V. At all potentials, there is a peak at 540cm^{-1}, a peak at 610 cm^{-1} and a peak at 670cm^{-1}.

As we have extensively discussed in Chapter 5, the peak at 540 cm^{-1} and the peak at 610 cm^{-1} are assigned to Cr_2O_3 film on the surface of Alloy 600. The peak at 670cm^{-1} is due to the formation of $FeCr_2O_4$ spinel.

The presence of Cr_2O_3 on the surface film of Alloy 600 is in agreement with ex situ analyses conducted by other researchers. A. Machet et. al. used XPS and STM to study the growth and structure of passive films on Alloy 600 in high temperature water. An inner layer of Cr_2O_3 was identified, and it was very thin and protective [63]. L. Marchetti has identified the nodules of Cr_2O_3 quasi-uniformly dispersed along the alloy/oxide interface by TEM [66].

The formation of spinel outer layer on the surface of Ni-based alloys is also supported by other research work. J. Panter proposed that the discrete spinel $Ni(Cr,Fe)_2O_4$ crystallites as the outer layer [102]. J.H. Kim detected the formation of $Ni(Fe)Cr_2O_4$ and $NiFe_2O_4$ spinels [103]. L. Marchetti used micro-photoelectrochemical technique to identify the spinel as $Ni_{1-x}Fe_xCr_2O_4$ [66].

Figure 4-10 ~ 4-18 are the SERS results for Alloy 690 at potentials from -0.9V to -0.5V.

There is a peak at 540cm^{-1} and a peak at 610cm^{-1}. At all potentials, there is no significant change on the SERS spectra.

The peak at 540 cm^{-1} and the peak at 610 cm^{-1} are due to the formation of Cr_2O_3. There is no any other peak observed in the SERS spectra, so the surface film formed on Alloy 690 is entirely Cr_2O_3.

6.2 Quantitative Analyses of the *in situ* SERS Spectra of the Oxides Formed on Alloy 600 and Alloy 690 in PWR PW at 320°C

Quantitative analysis of the SERS spectra of Alloy 600 was conducted and the results are summarized in Figures 5-1 – 5-5. The ratio of the integrated intensities of the peaks at 610 cm^{-1} and 880 cm^{-1} increased as the applied potential increased from -0.9V to -0.5V. The non-monotonic nature of the potential dependency presented in Figure 5-1 was also observed in the data for the laboratory heats of Ni-Cr and Ni-Fe-Cr alloys and its cause is thought to be the same.

Namely, the area analyzed changes as the sample's position shifts with time. As shown in Figure 5-2, the ratio of the integrated intensities of the peaks at 540 cm^{-1} and 880 cm^{-1} exhibited a similar dependency on potential.

As previously mentioned several times, both Cr_2O_3 and NiO exhibit Raman active modes at 540 cm^{-1}. Their relative contributions to the measured intensity of the peak at 540 cm^{-1} are inferred from the ratio of the integrated intensities of the peaks at 610 cm^{-1} and 540 cm^{-1}, which is presented in Figure 5-3. The results indicate that the ratio is independent of potential and has a value of 1.36 with a standard deviation of 0.22. The potential independence of the ratio indicates that Cr_2O_3 is the only species responsible for the 540 cm^{-1} peak in the SERS spectra of Alloy 600's oxide film.

Although NiO is not a part of Alloy 600's oxide, the results presented in Figure 5-4 indicate that a spinel oxide forms and increases with increasing potential. For reasons presented in Chapter 5, the spinel oxide is most likely $FeCr_2O_4$.

Identical analyses were performed on the SERS spectra of the surface oxide formed on Alloy 690 in PWR PW at 320°C and the results are presented in Figures 5-5 – 5-7. The ratios of the integrated intensities of the peaks at 610 cm^{-1} and 880 cm^{-1}, and the peaks at 540 cm^{-1} and 880 cm^{-1} are presented on Figures 5-5 and 5-6, respectively. Once again there is a non-monotonic variation in the ratios with increasing potential. As before, the non-monotonic trend is attributed to the position of the sample shifting with time. Despite the scatter due to changes in the sample's position, both ratios appear to decrease with increasing potential. This effect was previously observed for the oxide formed on unalloyed chromium. The decrease in intensity with increasing potential is unexpected as was mentioned in Chapter 4. Typically, oxide films thicken as the potential increases.

The similar influence of potential on the two ratios for both chromium and Alloy 690 suggests that the oxides formed on the two metals are very similar. As hypothesized in Chapter 5, at low potentials the oxide might be CrOOH, which converts to Cr_2O_3 at higher potentials. The conversion of CrOOH to Cr_2O_3 is proposed to be responsible for the decrease in intensity with increasing potential.

As summarized in Figure 5-7, the ratio of the integrated intensities of the peaks at 610 cm^{-1} and 540 cm^{-1} is independent of potential and exhibits a mean value of 1.80 with a standard deviation of 0.20. Thus, the only species thought to contribute to the peak at 540 cm^{-1} in the SERS spectra of Alloy 690's oxide in Cr_2O_3 and NiO is not formed, as was also true for Alloy 600. However, unlike the case for Alloy 600's oxide no spinel is formed on Alloy 690. While Alloy 600's oxide is composed of Cr_2O_3 and $FeCr_2O_4$, Alloy 690's oxide consists solely of Cr_2O_3.

It is instructive to add the data for Alloy 600's oxide and Alloy 690's oxide to the data for the oxides formed on Ni, Cr, and the Ni-Cr binary and Ni-Cr-Fe ternary alloys, which were presented in Figures 3-8 and 3-9. To that end, all of the data are presented in Figures 5-8 and 5-9. The results in Figure 5-8 show that the data for the oxides formed on Alloy 600 and Alloy 690 support the trend of increasing amount of Cr_2O_3 as the alloy's chromium concentration increases. And the results in Figure 5-9 are consistent with the view that the amount of NiO in the alloy's oxide decreases as the alloy's chromium concentration increases.

Chapter 7

Influence of Cooling to Room Temperature and Air-Exposure on SERS of Oxides Formed on Alloy 600 and Alloy 690 in PWR PW at 320°C

After the tests at 320°C were finished, the autoclave was cooled to room temperature, at which point the SER spectrum of the oxide film was measured. Finally, the sample was removed from the autoclave and exposed to air and the oxide's SER spectrum was measured one more time. Representative spectra are presented in Figures 6-1 ~ 6-4. Comparing the spectra (1) at 320°C, (2) at room temperature, and (3) after exposure to air at room temperature indicates there are changes in the oxide films.

Only one small change occurred to the oxide's spectrum upon cooling to room temperature, namely, the height of the 580 cm^{-1} peak increased relative to the height of the 540 cm^{-1} peak. The peak at 580 cm^{-1} can be assigned to α-CrOOH or $Cr(OH)_3$.

On exposure to air, the intensity of the entire spectrum was increased as a consequence of the removal of the sapphire window and aqueous solution from the optical path. In addition, a peak at approximately 700 cm^{-1} was prominent. It was unclear whether the 700 cm^{-1} peak was a completely new spectral feature or was the result of a shift in the position of the 670 cm^{-1} spinel peak.

Consider the possibility that the location of the spinel peak shifts from 670 cm^{-1} at 320°C to 700 cm^{-1} at room temperature. Maslar et al. identified $NiFe_2O_4$ as the dominant component in the oxide formed on Alloy 600 at 543°C in high purity air-saturated water and reported that the location of the A_1 mode shifted to higher wavenumbers as the temperature decreased [90]. The A_1 mode of $NiFe_2O_4$ was centered at approximately 690 cm^{-1} at 543°C and shifted to higher values as the temperature was lowered, reaching a value of approximately 705 cm^{-1} at room temperature. The temperature dependence of the location of the A_1 mode of $NiFe_2O_4$ as reported by Maslar et al. indicate that our chromite spinel's peak might also shift with decreasing temperature. Thus, the peak at 700 cm^{-1} in the room temperature SER spectrum might be due to the temperature dependency of the peak's location and not due to a change in the oxide's identity.

Parenthetically, the overriding presence of $NiFe_2O_4$ in the results of Maslar et al. is not in conflict with the present results, in which the spinel phase is most likely a chromite. The results of Maslar et al. are explained by the high value of Alloy 600's corrosion potential in their tests, which were conducted in air-saturated water.

In brief, the SER spectrum of the oxide formed on Alloy 600 in PWR primary water at 320°C changes slightly on cooling to room temperature (perhaps associated with conversion of some Cr_2O_3 to α-CrOOH or $Cr(OH)_3$). On exposure to air at room temperature, the relative intensity of the spinel peak increases.

The SER spectra presented in Figures 7-1 – 7-4 illustrate the influence of (1) cooling from 320°C to room temperature, and (2) removal of the sample from the aqueous solution and

exposure to air, on the SER spectrum of the oxide film formed on Alloy 690 at a potential of -0.5V and at a temperature of 320°C. At 320°C, the oxide consists of only one species, namely Cr_2O_3. Upon cooling to room temperature and exposing to air, the oxide is unchanged. The only significant change in the SERS spectrum is an overall increase in intensity, which is attributed to the removal of the sapphire window and the aqueous solution from the optical path. The higher overall intensity of light at the sample makes the weaker peak at 610 cm^{-1} more obvious.

The comparison of the in situ SERS spectra of the oxides of Alloy 600 and Alloy 690 at 320°C to their in situ spectra at room temperature and their ex-situ spectra following air-exposure at room temperature addresses the issue of differences between in-situ characterization and ex-situ characterization of surface oxide films formed in high temperature, pressurized water. The present results indicate that no significant changes occur to the oxide of Alloy 690 and only slight changes to the oxide of Alloy 600 are possible: partial conversion of Cr_2O_3 to α-CrOOH of $Cr(OH)_3$ on cooling to room temperature, and small increase in the relative amount of spinel upon exposure to air at room temperature.

Chapter 8

Comparison of Results of In-Situ SERS Investigation to Results of Ex-Situ Investigations of Oxides formed on Alloy 600 and Alloy 690 in PWR PW at 320°C

As discussed in Chapter 7, cooling to room temperature and exposing to air the oxides formed on Alloy 600 and Alloy 690 in PWR PW at 320°C had little substantive effect on the oxides' identities as judged by their SERS spectra. Consequently, one should expect reasonable agreement between the results of the present investigation and the results of earlier, ex-situ investigations conducted by other researchers. In fact, as the following discussion indicates, there is significant disagreement between our results and those of other researchers regarding the identities of the oxides that form on Alloy 600 and Alloy 690 in high-temperature PWR PW. After first summarizing the results of other researchers, possible reasons for the discrepancies are considered.

Before describing the results of other researchers who investigated the compositions and microstructures of the oxides formed on Alloy 600 and Alloy 690, it is worth recognizing that the oxide films of interest are relatively thin, which contributes to the technical challenge of investigating their identity and properties. In general, the thickness of surface oxide films grown on metals immersed in aqueous solutions is a strong function of potential. Typically, the thickness increases linearly with applied potential. In addition, the thickness of the oxide film is dependent on time at potential. Typically the growth rate decreases with time. For example, in some cases the growth rate varies as $t^{-1/2}$ and in some cases the growth rate varies as $exp^{-a \cdot t}$, where a is a constant.

Most researchers report the oxides formed on Alloy 600 and Alloy 690 in PWR PW exhibit a duplex structure. Typically, the inner layer is relatively thin and continuous and the outer layer is thicker and more irregular in shape as it consists of relatively large crystals that have grown at different rates. The inner layer (IL) is thought to be more important than the outer layer (OL) and to be responsible for the corrosion resistance of the alloy.

A. Machet et al. has determined the thickness of the film formed on Alloy 600, which was exposed in 325°C water for short time periods (0.4-8.2 min) [63]. From 0.4 min to 4 min, Cr_2O_3 oxide layer was about 1nm and it was thick enough to form a continuous surface layer. After 8 min of passivation, the continuous layer of Cr_2O_3 was about 2 nm thick [63]. However, if Alloy 600 is exposed in PWR primary water for a very long time (e.g. 1000 h), the Cr_2O_3 oxide layer can reach a thickness of 10 nm [64]. In brief, Machet et al. found the IL of Cr_2O_3 to be thin, compact, and continuous. It was suggested that the Cr_2O_3 acted as a barrier to limit further oxidation [63].

There is good agreement that the outer layer consists of spinel oxides. P. Combrade stated that the outer layer is composed of smaller grain-size $(Fe,Ni)(Fe,Cr)_2O_4$ crystallites with larger grain-size $(Ni,Fe)Fe_2O_4$ crystallites [61]. The size of small crystallites was about 50 nm and the larger crystallites had a size in a range of 300-700 nm [61]. J. Panter proposed that the larger

crystallite is $NiFe_2O_4$ and the smaller crystallite is $Ni(Cr,Fe)_2O_4$ [102]. From our SERS results, the outer spinel layer was identified as $FeCr_2O_4$. Kim's SERS spectrum shown that the spinel oxide was $(Ni,Fe)Cr_2O_4$ [103].

For clarity, the results discussed above as well as the results of a few other researchers are summarized in Table A. The consensus is that the surface oxide formed on Alloy 600 consists of two layers. The IL is always identified as a chromium-rich oxide. Based on compositional analyses several of the studies indicate the IL is most likely Cr_2O_3, possibly mixed with a chromite spinel, e.g., $(Fe,Ni)Cr_2O_4$. The majority of the studies suggest, based again on compositional analyses, that the IL is a single phase consisting of $(Fe,Ni)Cr_2O_4$. To our knowledge only the investigation of Morton et al. included electron diffraction analysis of the IL, which indicated the IL was indeed a spinel [104]. In combination with their compositional analysis, Morton et al identified the IL as chromium-rich $Ni(Cr,Fe)_2O_4$ [104]. There is also reasonable agreement among all of the studies conducted by other researchers that the OL contains rather large (hundreds of nm diameter) crystals of $NiFe_2O_4$. The majority of the studies also indicate the presence in the OL of smaller grains of $(Ni,Fe)(Cr,Fe)_2O_4$, which contain significantly less chromium than the IL.

Therefore, the general picture that emerges from the collected results of other researchers of the surface oxide formed on Alloy 600 is of a duplex structure composed of a continuous IL of chromium-rich oxide, most likely $(Ni,Fe)Cr_2O_4$, and an OL that consists of relatively small grains of $(Ni,Fe)(Cr,Fe)_2O_4$ and relatively large grains of $NiFe_2O_4$. The results are in clear disagreement with our SERS investigation that reports an IL of Cr_2O_3 and an OL of spinel. Before discussing possible reasons for the discrepancy, the results of our SERS investigation of Alloy 690's oxide film will be compared to the results of other researchers.

The results of four investigations of the cation concentrations in oxide films formed on samples of Alloy 690 in simulated PWR PW are summarized in Table B.

There is very good qualitative agreement between the results of all four investigations. Each investigation reported significant compositional differences through the thickness of the film, suggesting the presence of two distinct layers. The average of six measurements presented in the four investigations is presented in the bottom row of Table B. On average, the IL had more than twice as much chromium as the outer layer. While the OL had almost three times as much Fe as the IL. The nickel content of the OL was 1.5 times greater than that of the IL.

In addition to the compositional measurements of the oxides formed on Alloy 690, several of the studies discussed above also investigated the phases that make up Alloy 690's oxide. The structure of the surface film formed on Alloy 690 in simulated PWR PW is schematically illustrated in Figure 8-1 and Figure 8-2. The film structure sketched in Figure 8-1 is largely based on the TEM investigations of Sennour [105,62], which present similar sketches. Figure 8-2 presents a slightly modified version of Figure 8-1 and is based on the film's description provided by Delabrouillel [106]. The key difference between the two oxides is their microstructures – the distribution of Cr_2O_3. Both of the proposed film structures are consistent with the results of several other studies in which the films were investigated by *ex-situ* TEM, GIXRD, SIMS, EDS, and XPS [107, 65, 66].

Thus, while our in-situ SERS results identify Alloy 690's oxide as a monolithic film of Cr_2O_3, the results of other researchers indicate the oxide exhibits a duplex structure in which the IL consists of two phases. One phase is Cr_2O_3, which exhibits one of two morphologies: either discrete particles of Cr_2O_3 that are approximately 10 nm in diameter, or an extremely thin but continuous layer of Cr_2O_3. The second phase is the dominant species of the IL and consists of $(Ni,Fe)Cr_2O_4$. The OL is similar to that described above for Alloy 600's oxide.

There are at least two possible explanations for the discrepancies in the identities of the surface oxides as found in the present study versus those reported by other researchers. First, there is s significant difference in the times of oxidation, and second, there is a difference in the materials of construction for the autoclaves and the high temperature, high pressure water loops. In our view, either of these two differences provides credible explanations for the differences in results.

Most of the earlier tests were conducted using much longer oxidation times (typically 48 h or longer) than were employed in the present study, in which the time at each potential was 10 minutes and the total time at 320°C was 1.5 h. It's possible that the inner layer of Cr_2O_3 found in the present study would transform over longer times to the thermodynamically stable iron chromite, which is the thermodynamically stable oxide of Alloy 600 [95]. The study by Machet et al. [63] employed even shorter times (0.4-8min) than were used in the current study and found that the inner layer oxide of Alloy 600 was chromium-rich and much like Cr_2O_3 according to the Cr 2p3/2 core level spectrum. Thus, an inner layer of Cr_2O_3 might be characteristic of the early stages of oxidation of Alloy 600 at 320°C. Consistent with the idea of a time evolution of the inner layer from Cr_2O_3 to spinel chromite are results like those of Combrade et al. [61] that report very thin inner layers of Cr_2O_3 between the alloy and chromite spinel, which is the surface film's dominant species. That is, the results of Machet et al. and the present results, along with the results of long time oxidation tests of Combrade et al. are consistent with the view that Cr_2O_3 forms at very short oxidation times due to kinetic factors (e.g., faster rate of oxidation of chromium compared to iron) and that over long periods of time the Cr_2O_3 transforms to the thermodynamically stable $FeCr_2O_4$. Thus, collectively the present results and those of earlier studies suggest a continuous, decreasing thickness of the inner layer of Cr_2O_3 as the oxidation time at 320°C increases from several minutes (relatively thick Cr_2O_3), to several hours (relatively thick Cr_2O_3), to hundreds of hours (relatively thin Cr_2O_3), to thousands of hours (no Cr_2O_3).

The differences in the oxides formed in the present study and in earlier studies might also be explained by differences in the concentrations of aqueous metal cations. Most, if not all, of the earlier tests were conducted in stainless steel autoclaves and high temperature water loops, suggesting that the water was saturated with Fe^{2+} and Ni^{2+}. The water's metal ion concentration is expected to result in the adsorption of the aqueous cations onto the oxide/water interface. The adsorption of aqueous Fe^{2+} and Ni^{2+} on the oxide surface is driven by a combination of chemical and electrostatic forces. The early work of James and Healy indicates that hydrolysable cations, such as Fe^{2+} and Ni^{2+}, adsorb on an oxide's surface with increasing pH of the water, eventually leading at sufficiently high pH (in the range of mildly acidic to mildly alkaline, depending on the identities of the oxide and the aqueous cations) to the complete precipitation of the aqueous cations as an oxide [108]. Thus, it is possible that the saturation concentrations of aqueous Fe^{2+} and Ni^{2+} in tests conducted in stainless steel autoclaves and water loops result in cation

adsorption and, given the mildly alkaline pH of the water, precipitation on the oxide's surface resulting in a chromite spinel oxide rather than Cr_2O_3.

In principle, the PWR PW employed in our studies should be saturated with titanium cations, which might affect the compositions of the oxides formed on Alloy 600 and Alloy 690 just as we have hypothesized saturation concentrations of aqueous cations Ni^{+2} and Fe^{+2} affect the identities of the oxides formed on samples of Alloy 600 and Alloy 690. However, Mintz and Devine used Auger electron spectroscopy to investigate the chemistry of the oxide formed on Alloy 600 in PWR PW in tests conducted in our all-titanium system [109]. No evidence of titanium in the oxide was found. Presumably some combination of a low concentration of titanium cations in the water and unfavorable conditions (electrostatic and/or chemical) for titanium ion adsorption on the oxide is responsible for the absence of titanium in the films formed on Alloy 600 (and presumably, Alloy 690).

It is worth noting that several earlier studies reported the effect of aqueous Ni^{+2} and Fe^{+2} on the chemistry of the OL of oxides formed on Alloy 600 and Alloy 690. To our knowledge, ours is the first study to (possibly) demonstrate the effect of aqueous Ni^{+2} and Fe^{+2} on the identity of the IL of oxides formed on Alloy 600 and Alloy 690. Since the IL is responsible for the alloys' corrosion resistances, recognizing the possible importance of aqueous cations on the composition and structure of the IL is very important.

The previously cited study by Machet et al., which reported an inner layer oxide of Cr_2O_3 following exposure to 320°C water for very short times of 0.4-8 min., was conducted in a titanium autoclave (although the water's holding tank was made of stainless steel). Thus, the two studies (namely, that of Machet et al. and the present study) that report an inner layer of Cr_2O_3 were both conducted in titanium autoclaves and for short oxidation times. Either or both factors could be responsible for the formation of an inner layer of Cr_2O_3 rather than an inner layer of spinel chromite, such as was observed in most other investigations (which were conducted for longer times of corrosion and in stainless steel autoclaves).

The same two factors of oxidation time and aqueous cations of Fe^{+2} and Ni^{+2} can also account for the differences in oxide films formed on Alloy 690 as observed in the present study versus the results of earlier studies.

We are currently conducting tests in our all-titanium autoclave and water loop in which the water is doped with aqueous Fe^{++} and Ni^{++} in an effort to determine the relative influence of oxidation time and aqueous cations on the identity of the inner layer of the oxide that forms on Alloy 600 in PWR PW at 320°C.

Table A

Alloy 600's Passive Film Formed at ≥300°C in PWR PW

Titanium Autoclave and Stainless Steel Water Supply Tank

Inner layer	**Outer Layer**	**Time of Oxidation**	**Reference**
Cr_2O_3	$Ni(OH)_2$	4-8 min	[63]

Stainless Steel Autoclaves

Inner layer	**Outer Layer**	**Time of Oxidation**	**Ref.**
$(Ni_{0.7}Fe_{0.3})(Fe_{0.3}Cr_{0.7})_{23}O_4$	$(Ni_{0.9}Fe_{0.1})(Fe_{0.85}Cr_{0.15})_2O_4$	260°C 1,000-10,000h	[110]
Cr-rich oxide	(Ni,Cr,Fe)-spinel $NiFe_2O_4$	1000h/320°C	[111]
Cr-rich oxide	$Ni(Cr,Fe)_2O_4$	360°C/300h	[102]
Cr_2O_3/$(Fe,Ni)Cr_2O_4$	$NiFe_2O_4$	360°C/300h	[61]
$Ni(Cr,Fe)_2O_4$	$NiFe_2O_4$	338°C/4,000h	[104]

High Purity water (buffered to neutral pH at 338°C) with 60 cc/KgH_2.

Cr-rich oxide	$NiFe_2O_4$	360°C/1000h	[106]

Alloy 690 Autoclave; Alloy 600 Tubing

Inner layer	**Outer Layer**	**Time of Oxidation**	[103]
CrOOH Cr-oxide	$NiCr_2O_4$ NiO	70h/350°C	

Table B

TEM Compositional Analyses of Oxides Formed on Samples of Alloy 690 Tested in Stainless Steel Water Loops and Autoclaves Containing Simulated PWR PW

	Cr(IL)	Cr(OL)	Fe(IL)	Fe(OL)	Ni(IL)	Ni(OL)	Ref
	68	42	14	35	18	23	[106]
	56	44.6	6.7	13	37.3	32.1	[105]
	64	36.1	10.5	14.8	25.6	49.2	
	72	9.4	17	54.7	10	35.9	
690TEM	32	11	19	37	39	49	[107]
CombScMrc	65	0	17	67	18	33	[61]
AVG	59.5	23.9	13.8	36.9	24.7	37.0	

Chapter 9

Conclusion

In this study, we have acquired the first *in situ* vibrational spectra of oxides formed on Alloy 600 and Alloy 690 at 320°C in laboratory simulated Primary Water (PW) of Pressurized Water Reactors (PWR). The vibrational spectra were measured by surface enhanced Raman spectroscopy (SERS). In-situ SERS is the appropriate technique to characterize thin surface films formed in aqueous environment. It is a convenient, low-cost, and time-saving technique.

The oxides' spectra were measured at 320°C as a function of applied potential, from -0.9V to -0.5V vs SHE. In addition, the spectra were measured following cooling of the PWR PW to room temperature and after the samples were removed from the PWR PW and exposed to air. Our results indicate only minor changes occurred upon cooling to room temperature and upon exposure to air. The results prove for the first time that using *ex situ* techniques to analyze the surface oxides formed on Alloy 600 and Alloy 690 is valid.

To assist our analyses of the SERS of Alloy 600's oxide and Alloy 690's oxide, SERS was also conducted on the oxides formed in PWR PW at 320°C on unalloyed nickel, unalloyed chromium, Ni-10Cr, Ni-20Cr, Ni-5Cr-8Fe, and Ni-10Cr-8Fe.

SERS spectrum of nickel shows a weak Raman peak at 540 cm^{-1}, which is associated with NiO film. Although the crystal structure for NiO is symmetry forbidden for first-order Raman scattering, a high concentration of crystalline defects, such as a nano grain size as well as an overall film thickness of only several nanometers is likely to contribute to the Raman-active mode.

A thin and protective Cr_2O_3 film is formed on the surface of pure chromium, which exhibits a Raman mode at 540 cm^{-1} and a mode at 610 cm^{-1}.

In Ni-Cr alloys, the way to distinguish between NiO 540 cm^{-1} peak and Cr_2O_3 540 cm^{-1} peak is to observe the presence/absence of a peak at 610 cm^{-1}. The absence of a peak at 610 cm^{-1} in combination with a peak at 540 cm^{-1} would indicate NiO. The presence of a peak at 610 cm^{-1} in combination with a peak at 540 cm^{-1} would indicate Cr_2O_3 is present but it cannot exclude the possible presence of NiO.

SERS spectra measured for Ni-5Cr-8Fe and Ni-10Cr-8Fe indicate that the surface films of both alloys are similar. The film has an inner layer (IL) of Cr_2O_3 and an outer layer (OL) of $FeCr_2O_4$. The surface film of Ni-10Cr and Ni-20Cr alloys is entirely Cr_2O_3.

The oxide film of Alloy 600 consists of Cr_2O_3 inner layer (IL) and $FeCr_2O_4$ outer layer (OL). The thickness of the surface oxide is dependent on the film growth time and aqueous environment. For short-time growth ($\leq$10 min), the inner Cr_2O_3 layer is about 2 - 4 nm thick, and the average size of $FeCr_2O_4$ crystallites is about 10 nm.

A single layer of Cr_2O_3 is the surface film of Alloy 690 formed in PWR PW at 320°C.

Our results conflict with the results of earlier studies by other investigators. Two possible explanations of the discrepancies have been proposed: (1) our use of shorter oxidation times (several hrs) compared to longer oxidation times (hundreds to thousands of hrs) employed by other investigators; (2) our use of an all-titanium autoclave and water loop is in contrast with other researchers who employed all-stainless steel systems, which saturate the water with nickel ions and iron ions. The saturated concentrations of nickel ions and iron ions are hypothesized to affect the chemistries and structures of the oxides that form on Ni-Fe-Cr alloys.

That different oxides form on Alloy 600 and Alloy 690 might help to explain the different resistances of the two alloys to stress corrosion cracking in PWR PW, and to the different amount of adsorption/absorption of aqueous radioactive cobalt and nickel ions in the oxides formed on the two alloys. However, the results are unable to explain the influence of potential on the susceptibility of Alloy 600 to IGSCC. This finding might be accounted for in several ways. First, the results indicate no correlation between the potential dependency of the oxides that form on the free surface of Alloy 600 and the potential dependency of the alloy's susceptibility to IGSCC. It might be that the oxide that forms at the tip of a stress corrosion crack controls the alloy's susceptibility to IGSCC. The condition at the tip of a crack might be different from the conditions outside the crack, resulting in different oxides at a free surface and at the tip of a crack. The chemistry of the water at a crack tip can be different from the chemistry of the bulk water. In addition, the potential at a crack tip can also be different from the potential of the alloy outside the crack. Both the local chemistry and local potential control the reactions occurring at a crack tip, including the oxide-film formation reaction. Second, the key characteristics of a film can change with potential even though the oxide's identity remains unchanged. For example, the oxide's thickness and rate of thickening are often strong functions of potential and both could affect the alloy's resistance to stress corrosion cracking.

Chapter 10

Reference

[1]. M. Sundararaman and J.B. Singh, Transactions of the Indian Institute of Metals, 2010, Vol.63, No.2-3, page(313-319)

[2]. X. Wang, Q.H. Ni, H. Zhou and Q.P. Kong, Materials Science and Engineering A, 1990, Vol.123, No.2, page(207-211)

[3]. M. Kondo, T. Nagasaka, T. Muroga, A. Sagara, Q. Xu, D. Ninomiya, N. Masaru, A. Suzuki and T. Terai, Fusion Science and Technology, 2009, Vol.56, No.1, page(190-194)

[4]. V.V. Ignat'ev, A.I.Surenkov, I.P. Gnidoi, V.I. Fedulov, V.S. Uglovi, A.V. Panov, V.V. Sagaradze, et.al., Atomic Energy, 2006, Vol.101, No.4, page(730-738)

[5]. I.B. Singh, British Corrosion Journal, Vol.33, No.1, page(67-70)

[6]. M.B. Henderson, D. Arrell, R. Larsson, M. Heobel and G. Marchant, Science and Technology of Welding and Joining, 2004, Vol.9, No.1, page(13-21)

[7]. F. Delabrouille, B. Viguier, L. Legras and E. Andrieu, Materials at High Temperatures, 2005, Vol.22, No.3-4, page(287-292)

[8]. M. Khalifa, F. Khan and M. Haddara, Reliability Engineering & System Safety, 2010, Vol.95, No.5, page(494-498)

[9]. K.E. Perumal, Transactions of the Indian Institute of Metals, 2003, Vol.56, No.3, page(287-296)

[10]. T. Matsuo, M. Ueki, M. Takeyama and R. Tanaka, Journal of Materials Science, 1987, Vol.22, No.6, page(1901-1907)

[11]. P. Hernalsteen, Nuclear Engineering and Design, 1993, Vol.143, No.2-3, page(131-142)

[12]. M. Vishnudevan, G. Venkatachari, S. Muralidharan and N.S. Rengaswamy, Anti-Corrosion Methods and Materials, 1998, Vol.45, No.4, page(248-251)

[13]. J.M. Abels and H.H. Strehblow, Corrosion Science, 1997, Vol39, No.1, page(115-132)

[14]. E.A. Ashour, F. Schneider and K. Mummert, Materials and Corrosion, 1997, Vol.48, No.7, page(409-413)

[15]. I.S. Hwang and I.-G. Park, Corrosion, 1999, Vol.55, No.6, page(616-625)

[16]. P. Combrade, M. Foucault, D. Vancon, P. Marcus, J.M. Grimal and A. Gelpi, Memoires Et Etudes Scientifiques De La Revue De Metallurgie, 1990, Vol.87, No.7-8, page(429-442)

[17]. R. Bandy and R.L. Sabatini, Corrosion, 1985, Vol.41, No.4, page(242-244)

[18]. "INCONEL alloy 600", Technical Bulletin, Special Metals Corporation, 2008

[19]. R. Kilian and A. Roth, Materials and Corrosion, 2002, Vol.53, No.10, page(727-739)

[20]. K.S. Al-Rubaie, L.B. Godefroid and J.A.M. Lopes, International Journal of Fatigue, 2007, Vol.29, No.5, page(931-940)

[21]. B. Junker, Bioprocess and Biosystems Engineering, 2009, Vol.32, No.1, page(1-29)

[22]. R.J. Smith, G.J. Lewis and D.H. Yates, Aircraft Engineering and Aerospace Technology, 2001, Vol.73, No.2, page(138-146)

[23]. R.W. Staehle and J.A. Gorman, Corrosion, 2004, Vol.60, No.2, page(115-180)

[24]. D.H. Hur, M.S. Choi, D.H. Lee, M.H. Song, S.J. Kim, J.H.Han, Nuclear Engineering and Design, 2004, Vol.227, page(155-160)

[25]. R.B. Rebak and Z.S. Smialowska, Corrosion, 1994, Vol.50, No.5, page(378-393)

[26]. B. Gronwall, L. Ljungberg, W. Hubner and W. Stuart, Nuclear Engineering and Design, 1967, Vol.6, page(383-390)

[27]. R.S. Dutta, R. Tewari and P.K. De, Corrosion Science, 2007, Vol.49, No.2, page(303-318)

[28]. H.P. Kim, S.S. Hwang, Y.S. Lim, I.H. Kuk and J.S.. Kim, Key Engineering Materials, 2000, Vol.183-187, page(707-712)

[29]. Y.Y. Chen, L.B. Chou and H.C. Shih, Materials Chemistry and Physics, 2006, Vol.97, page(37-49)

[30]. C.J. Boehlert, Materials Science and Engineering A, 2008, Vol.473, No.1-2, page(233-237)

[31]. F.F.II. Noecker, J.N. DuPont, Welding Journal, 2009, Vol.88, No.1, page(7S-20S)

[32]. P. Diano, A. Muggeo, J.C. Vanduysen and M. Guttmann, Journal of Nuclear Materials, 1989, Vol.168, No.3, page(290-294)

[33]. "INCONEL alloy 690", Technical Bulletin, Special Metals Corporation, 2009

[34]. M. Casales, V.M. Salinas-Bravo, A. Martinez-Villafane and J.G. Gonzalez-Rodriguez, Materials Science and Engineering A, 2002, Vol.332, No.1-2, page(223-230)

[35]. J.M. Boursier, F. Vaillant, P. Saulay, Y. Brechet and G. Zacharie, 11th International Symposium on Environmental Degradation of Materials in Nuclear Power Systems—Water Reactors, 2003, page(199-207)

[36]. B.A. Young, X.S. Gao, T.S. Srivatsan and P.J. King, Materials and Design, 2007, Vol.28, No.2, page(373-379)

[37]. G.P. Airey, A.R. Vaia and R.G. Aspden, Nuclear Technology, 1981, Vol.55, No.2, page(436-448)

[38]. J.K. Hong and I.S. Kim, C.Y. Park and E.S. Kim, Wear, 2005, Vol.259, No.1-6, page(349-355)

[39]. G. Frederick and P. Hernalsteen, International Journal of Pressure Vessels and Piping, 1986, Vol.25, page(47-67)

[40]. I.G. Park, Nuclear Engineering and Design, 2002, Vol.212, page(395-399)

[41]. P.H. Hoang, A. Gangadharan, S.C. Ramalingam, Nuclear Engineering and Design, 1998, Vol.181, page(209-219)

[42]. J. Congleton, E.A. Charles and G.Sui, Corrosion Science, 2001, Vol.43, page(2265-2279)

[43]. K. Arioka, T. Yamada, T. Terachi and G.Chiba, Corrosion, 2007, Vol.63, No.12, page (1114-1123)

[44]. A.C.C. Tseung, T. Sriskandarajah and H.C. Chan, Corrosion Science, 1985, Vol.25, No.6, page(383-393)

[45]. R.R. Boyer and W.F. Spurr, Metallurgical Transaction A, 1978, Vol.9A, page(1443-1448)

[46]. N. Saito, S. Tanaka and H. Sakamoto, Corrosion, 2003, Vol.59, No.12, page(1064-1074)

[47]. T. Sriskandarajah, H.C. Chan and A.C.C. Tseung, Corrosion Science, 1985, Vol.25, No.6, page(395-414)

[48]. R.C. Newman and K. Sieradzki, Corrosion Science, 1983, Vol.23, No.4, page(363-378)

[49]. F.P. Ford, P.L. Andresen, 3rd International Symposium on Environmental Degradation of Materials in Nuclear Power Systems—Water Reactors, 1988, page(789-796)

[50]. R.B. Rebak and Z.Szklarska-smialowska, Corrosion Science, 1996, Vol.38, No.6, page(971-988)

[51]. J.C. Scully, Corrosion Science, 1967, Vol.7, page(197-207)

[52]. M.M. Hall Jr., Corrosion Science, 2009, Vol.51, page(225-233)

[53]. J. Gluszek and K. Nitsch, Corrosion Science, 1982, Vol.22, No.11, page(1067-1078)

[54]. J.S. Baek, J.G. Kim, D.H. Hur, J.S. Kim, Corrosion Science, 2003, Vol.45, page(983-994)

[55]. P.M. Scott, Ninth International Symposium on Environmental Degradation of Materials in Nuclear Power Systems—Water Reactors, 1999, page(3-14)

[56]. H.P. Kim, S.S. Hwang, Y.S. Lim, I.H. Kuk and J.S. Kim, Key Engineering Materials, 2000, Vols.183-187, page(707-712)

[57]. J. Flis, Corrosion Science, 1975, Vol.15, page(553-564)

[58]. D. Cubicciotti, Journal of Nuclear Materials, 1989, Vol.167, page(241-248)

[59]. C.S. Kumai, Ph.D thesis, University of California, Berkeley, 2000

[60]. A. Turnbull and M.P. Dombrowski, Corrosion Science, 1992, Vol.33, No.12, page(1925-1966)

[61]. P. Combrade, P.M. Scott, M. Foucault, E. Andrieu and P. Marcus, Proceedings of the 12th International Conference on Environmental Degradation of Materials in Nuclear Power System – Water Reactors, 2005, page(883-890)

[62]. M. Sennour, L.Marchetti, F. Martin, S. Perrin, R. Molins and M. Pijolat, Journal of Nuclear Materials, 2010, Vol.402, page(147-156)

[63]. A. Machet, A. Galtayries, S. Zanna, L. Klein, V. Maurice, P. Jolivet, M. Foucault, P. Combrade, P. Scott and P. Marcus, Electrochimica Acta, 2004, Vol.49, page(3957-3964)

[64]. B.T. Ovanessian, J. Deleume, J.M. Cloué, E. Andrieu, Materials Science Forum, 2008, Vols.595-598, page(449-462)

[65]. L. Marchetti, S. Perrin, O. Raquet and M. Pijolat, Materials Science Forum, 2008, Vols.585-598, page(529-537)

[66]. L. Marchetti, S. Perrin, Y. Wouters and M. Pijolat, Electrochimica Acta, 2010, Vol.55, No.19, page(5384-5392)

[67]. Y. Solomon, "An overview of water chemistry for pressurized water nuclear reactors", Westinghouse Electric Corporation, Pennsylvania, page(101-112)

[68]. W.H. Weber, R. Merlin, “Raman scattering in materials science”, Springer, 2000

[69]. J.R. Ferraro and K. Nakamoto, "Introductory Raman Spectroscopy", 2nd Edition, Elsevier, 1994

[70]. P.L. Stiles, J.A. Dieringer, N.C. Shah and R.P.V. Duyne, Annual Review of Analytical Chemistry, 2008, Vol.1, page(601-626)

[71]. K. Ikeda, S. Suzuki and K. Uosaki, Nano Letters, 2011, Vol.11, page(1716-1722)

[72]. L. Novotny, B. Hecht, "Principles of Nano-optics", Chapter 12-Surface plasmons, Cambridge University Press, 2006, page(407-450)

[73]. K. Kneipp, M. Moskovits, H. Kneipp, "Surface-Enhanced Raman Scattering: Physics and Applications", Springer, 2010, page(67-86)

[74]. J. Gui, and T. M. Devine, J. Electrochem. Soc., 1991, Vol. 138, No. 5, page(1376-1384)

[75]. L.J. Oblonsky and T.M. Devine, Journal of The Electrochemical Society, 1995, Vol.142, No.11, page(3677-3682)

[76]. "INCONEL alloy 600", Technical Bulletin, Special Metals Corporation, 2008

[77]. "INCONEL alloy 690", Technical Bulletin, Special Metals Corporation, 2009

[78]. M. kadleikova, J. Breza and M. Vesely, 2001, Microelectronics Journal, Vol.32, page(955-958)

[79]. J. Gui and T. M. Devine, Corrosion Science,1991, Vol. 32, No. 10, page(1105-1124)

[80]. F. Wang, S. Harrington and T.M. Devine, Electrochemical Society Transactions, 2007, Vol.3, No.31, page(39-57)

[81]. L.J. Oblonsky and T.M. Devine, Corrosion Science, 1995, Vol.37, No.1, page(17-41)

[82]. R.E. Dietz, G.I. Parisot and A.E. Meixner, Physical Review B, 1971, Vol.4, No.7, page(2302-2310)

[83]. J.E. Maslar, W.S. Hurst, W.J. Bowers, Jr., J.H. Hendricks and M.I. Aquino, Corrosion, 2002, Vol.58, No.3, page(225-231)

[84]. W.G. Cook and R.P. Olive, Corrosion Science, 2012, Vol.58, page(284-290)

[85]. Y.V.Bhargava., Ph.D thesis, University of California, Berkeley, 2008

[86]. R. Srnbnek, I. Hotovy, V. Malcher, A. Vincze, D. McPhail and S. Littlewood, 3rd International EuroConference on Advanced Semiconductor Devices and Microsystems, 2000, page(303-306)

[87]. W.G. Cook and R.P. Olive, Corrosion Science, 2012, Vol.58, page(291-298)

[88]. C.A. Melendres, M. Pankuch, Y.S. Li and R.L. Knight, Electrochmica Acta, 1992, Vol.37, No.15, page(2747-2754)

[89]. R.G. Snyder and J.A. Ibers, The Journal of Chemical Physics, 1962, Vol.36, No.6, page(1356-1360)

[90]. J.E. Maslar, W.S. Hurst, W.J. Bowers, Jr., J.H. Hendricks, M.I. Aquino and I. Levin, Applied Surface Science, 2001, Vol.180, page(102-118)

[91]. P. Fabis, R. Heidersbach, C. Brown and T. Rockett, Corrosion, 1981, Vol.37, page(700-712)

[92]. D. Thicrry, D. Persson, C. Leygraf, D. Delichere, S. Joiret, C. Pallotta and A. Hugot-Le Goff, Journal of The Electrochemical Society, 1988, Vol.135, No.2, page(305-310)

[93]. I.R. Beattie and T.R. Gilson, Journal of the Chemical Society (A), 1970, page(980-986)

[94]. D. Cubicciotti, Journal of Nuclear Materials, 1993, Vol.201, page(176-183)

[95]. L. Kaufman, Figures associated with EPRI Report that considers the Thermodynamically Stable Oxidation Products of Alloy 600 and Alloy 690, 2008

[96]. R.L. Farrow, R.E. Benner, A.S. Nagelberg and P.L. Mattern, Thin Solid Films, 1980, Vol.73, page(353-358)

[97]. B.D. Hosterman, Ph.D dissertation, University of Nevada, Las Vegas, August, 2011

[98]. M. Chen, J.F. Shu, X.D. Xie and H.K. Mao, Geochimica et Cosmochimica Acta, 2003, Vol.67, No.20, page(3937-3942)

[99]. J.C. Hamilton and R.J. Andersen, Journal of The Electrochemical Society, 1985, Vol.132, No.7, page(1753-1757)

[100]. K. Nakamura, S. Era, Y. Ozaki, M. Sogami, T. Hayashi, M. Murakami, FEBS Letters, 1997, Vol.417, No.3, page(375-378)

[101]. J.L. Lippert, D. Tyminski and P.J. Desmeules, Journal of the American Chemical Society, 1976, Vol.98, No.22, page(7075-7080)

[102]. J. Panter, B. Viguier, J.-M. Cloue´, M. Foucault, P. Combrade and E. Andrieu, Journal of Nuclear Materials, 2006, Vol.348, page(213-221)

[103]. J.H. Kim, and II.S. Hwang, 11th Int. Conf. Environmental Degradation of Materials in Nuclear Systems, Stevenson, WA, Aug. 10-14, 2003

[104]. D Morton, N Lewis, M Hanson, S Rice, P Sanders, "Nickel Alloy Primary Water Bulk Surface and SCC Corrosion Film Analytical Characterization and SCC Mechanistic Implications," LockheedMartin Report #07K022 April 18, 2007

[105]. M. Sennour, L. Marchetti, S. Perrin, R. Molins, M. Pijolat and O. Raquet, Materials Science Forum, 2008, Vols.595-598, page(539-547)

[106]. F. Delabrouille1, L. Legras, F. Vaillant, P. Scott, B.Viguier and E. Andrieu, Proceedings of the 12th International Conference on Environmental Degradation of Materials in Nuclear Power System – Water Reactors, 2005, page(903-911)

[107]. F. Carrette, M.C. Lafont, G. Chatainier, L. Guinard and B. Pieraggi, Surface and Interface Analysis, 2002, Vol.34, page(135-138)

[108]. R.O. James and T.W. Healy, Journal of Colloid and Interface Svlence, 1972, Vol.40, No.1, page(42-64)

[109]. T.S. Mintz and T.M. Devine, Key Engineering Materials, 2004, Vols.261-263, page(875-884)

[110]. S.E. Ziemniak and M. Hanson, Corrosion Science, 2006, Vol.48, page(498-521)

[111]. T. Terachi, N. Totsuka, T. Yamada, T. Nakagawa, H. Deguchi, M. Horiuchi and M. Oshitani, of Nuclear Science and Technology, 2003, Vol.40, No.7, page(509-516)

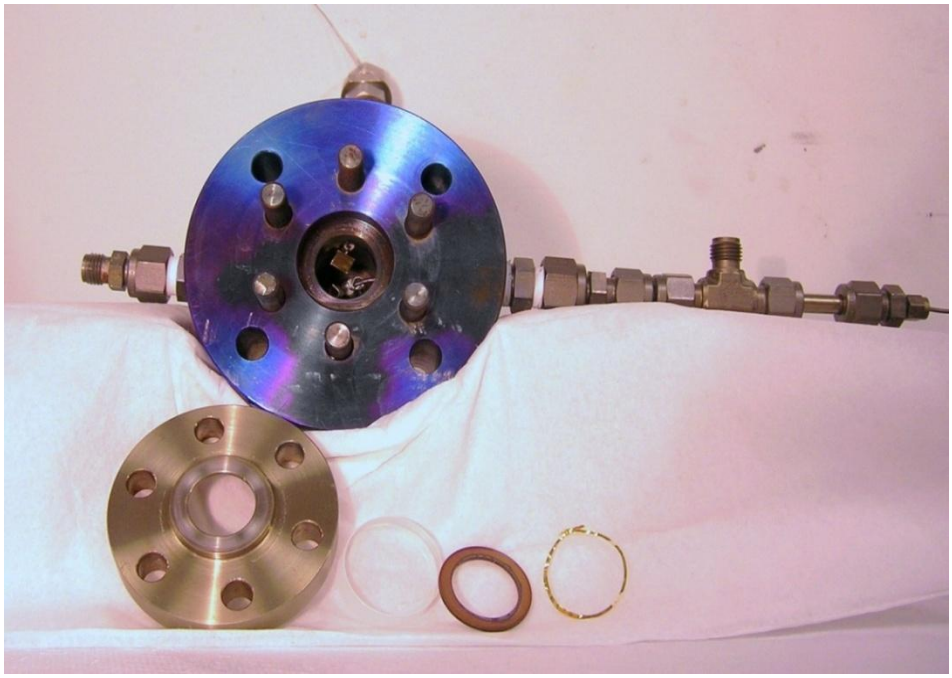

Figure 1. A photo of titanium autoclave parts

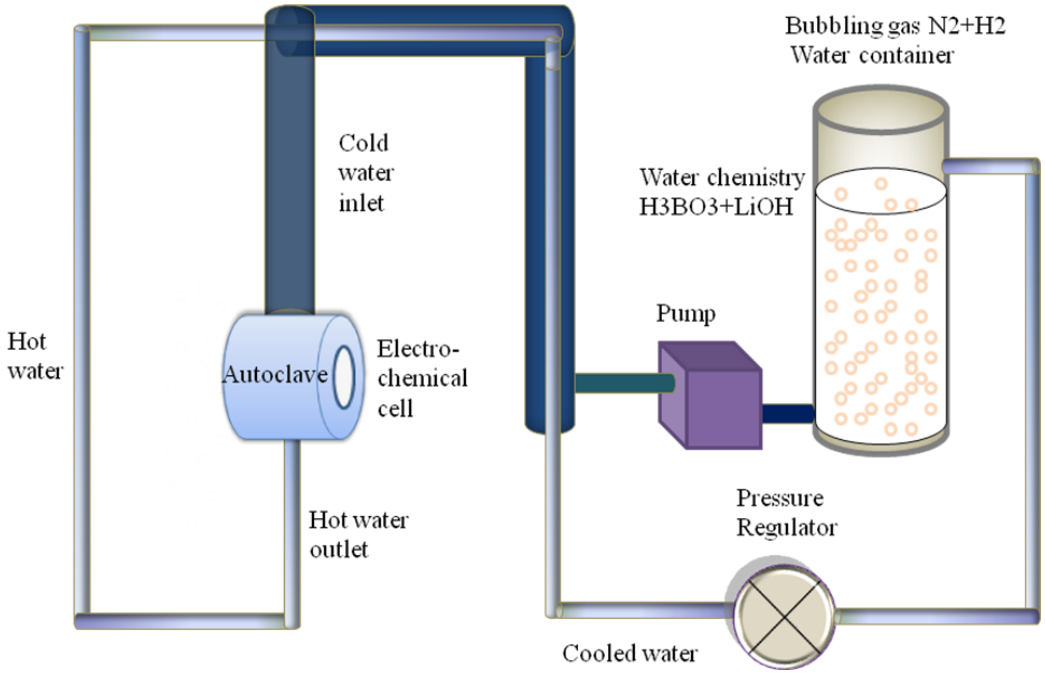

Figure 2-1. A sketch of water loop system

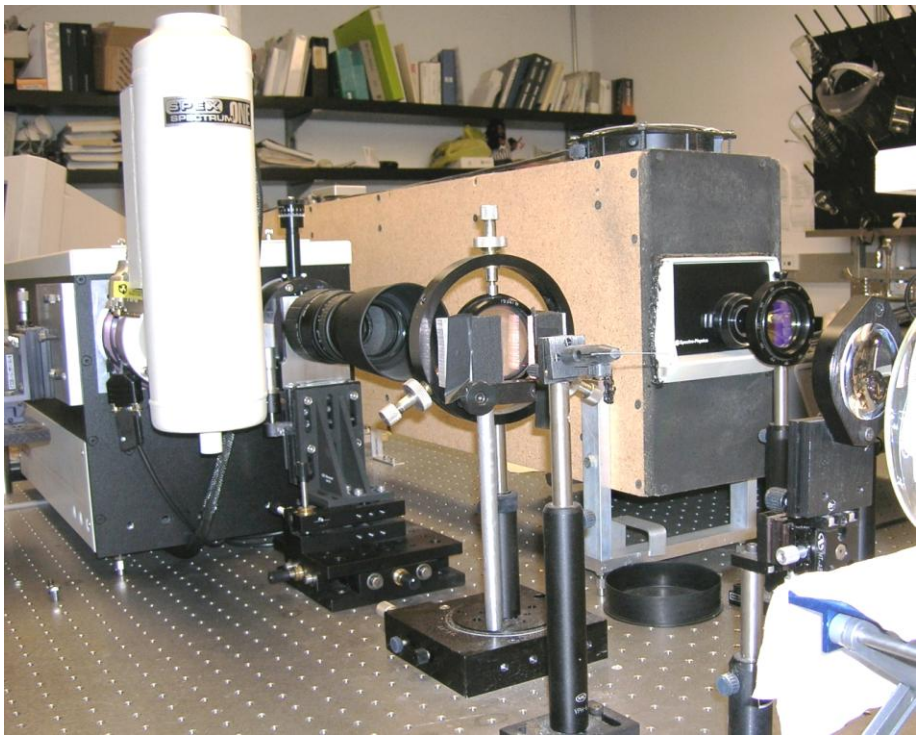

Figure 2-2. A photo of Raman Spectroscopy system

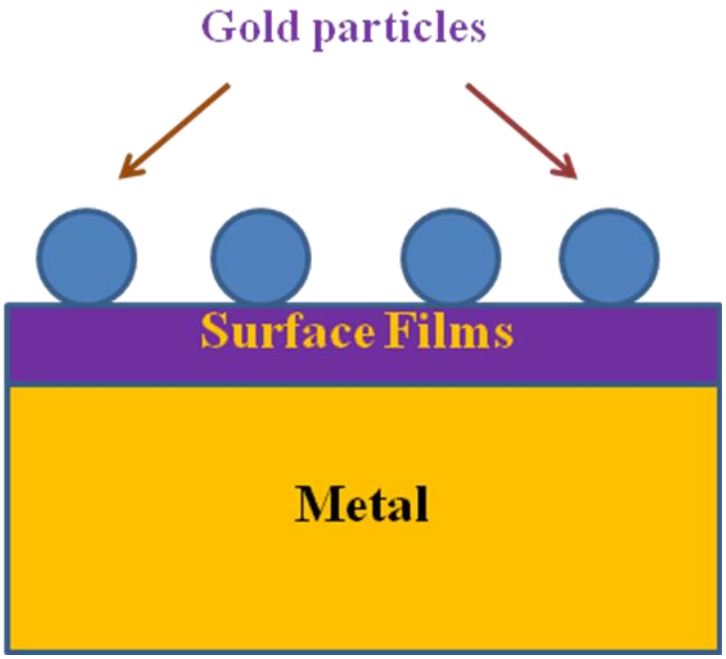

Figure 2-3. A sketch of SERS-Gold nanoparticle

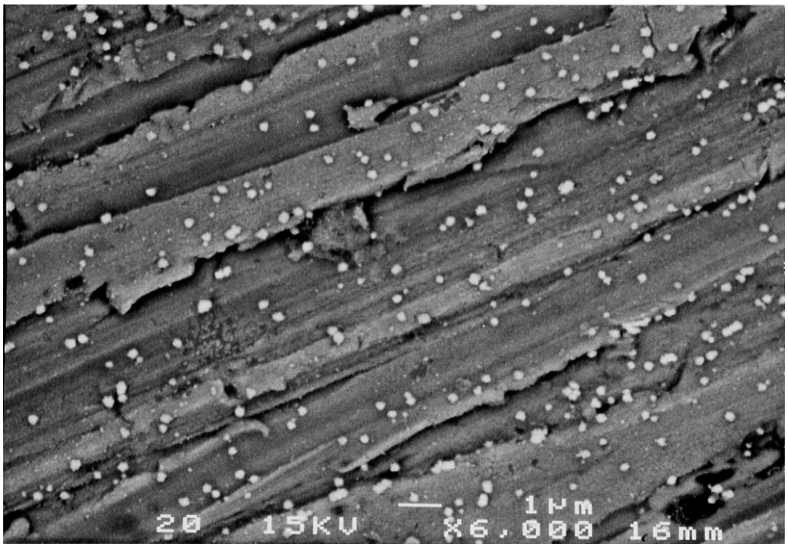

Figure 2-4. A SEM image of gold nanoparticles deposited on metal surface (Todd Mintz)

Figure 2-5. A photo of sealed autoclave

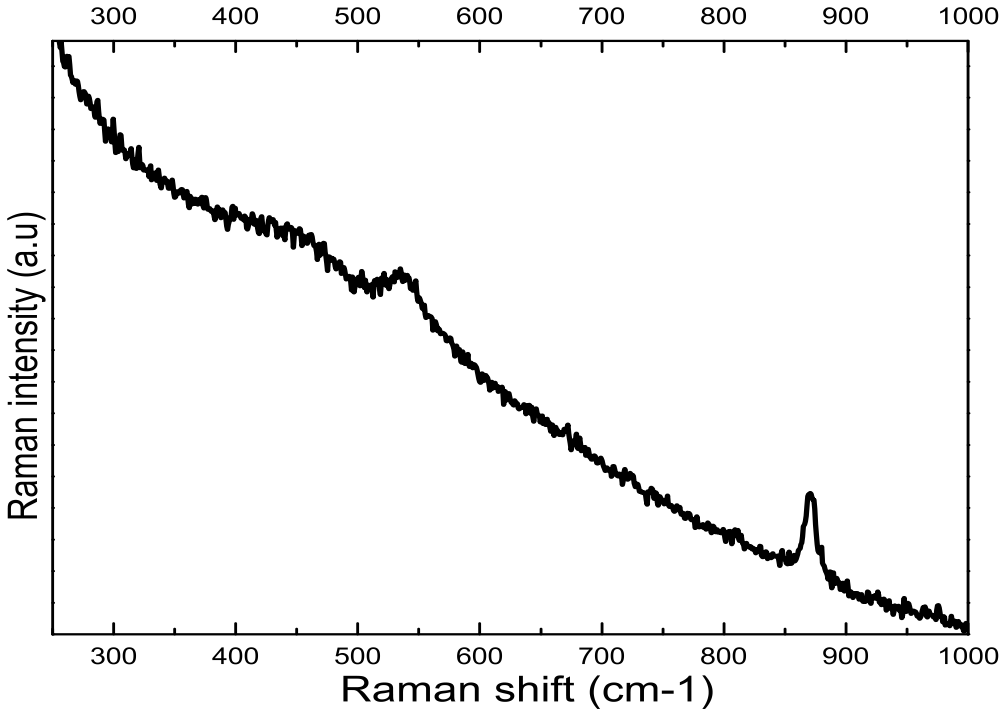

Figure 3-1a. SERS Spectrum measured for Nickel at E = -0.65V

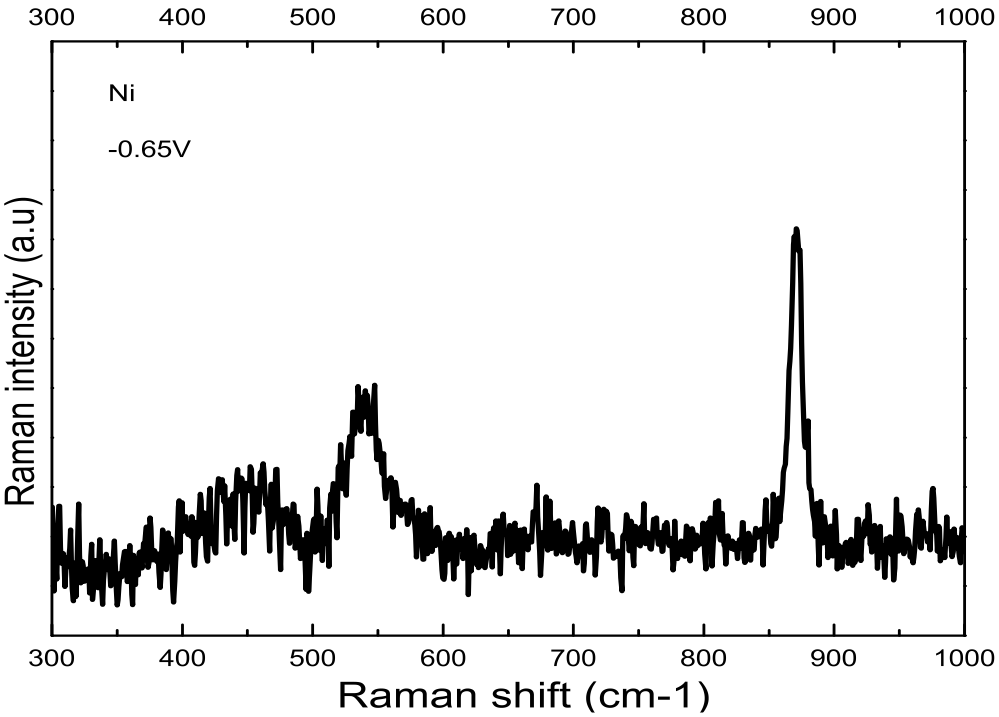

Figure 3-1b. SERS Result for Nickel at E = -0.65V
(After Background Subtraction)

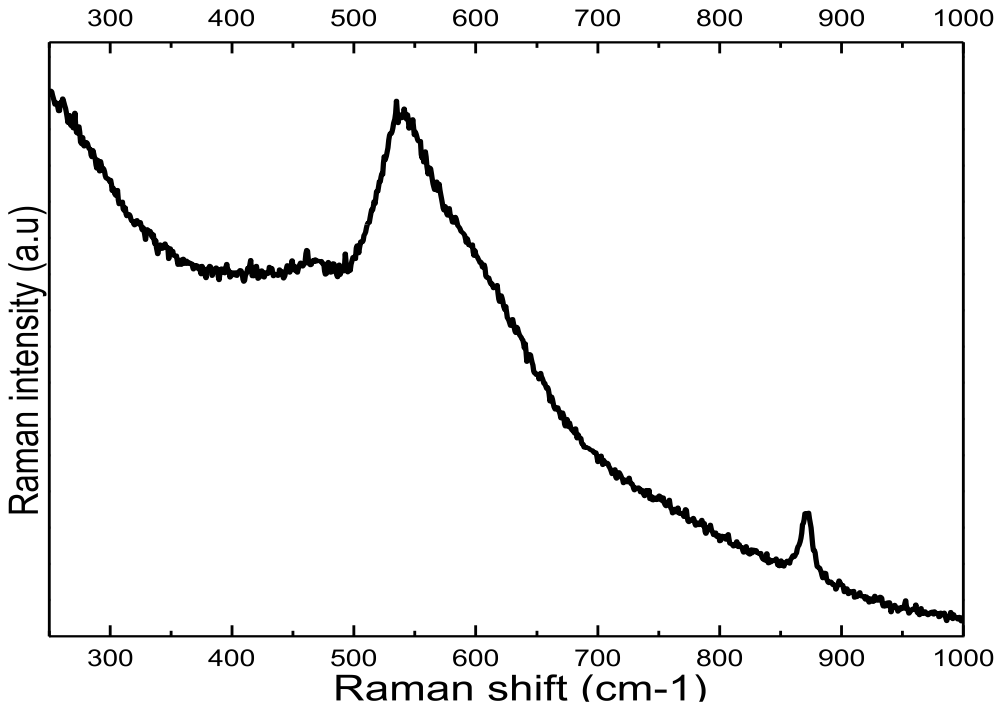

Figure 3-2a. SERS Spectrum measured for Chromium at E = -0.65V

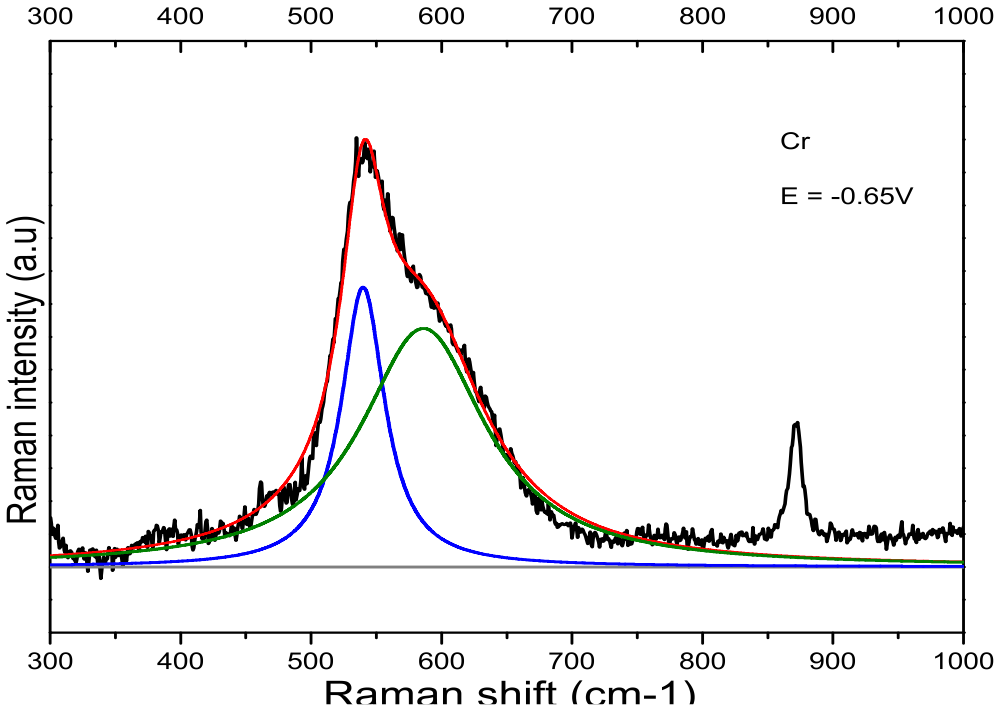

Figure 3-2b. SERS Result for Chromium at E = -0.65V
(After Background Subtraction and Peak Fitting)

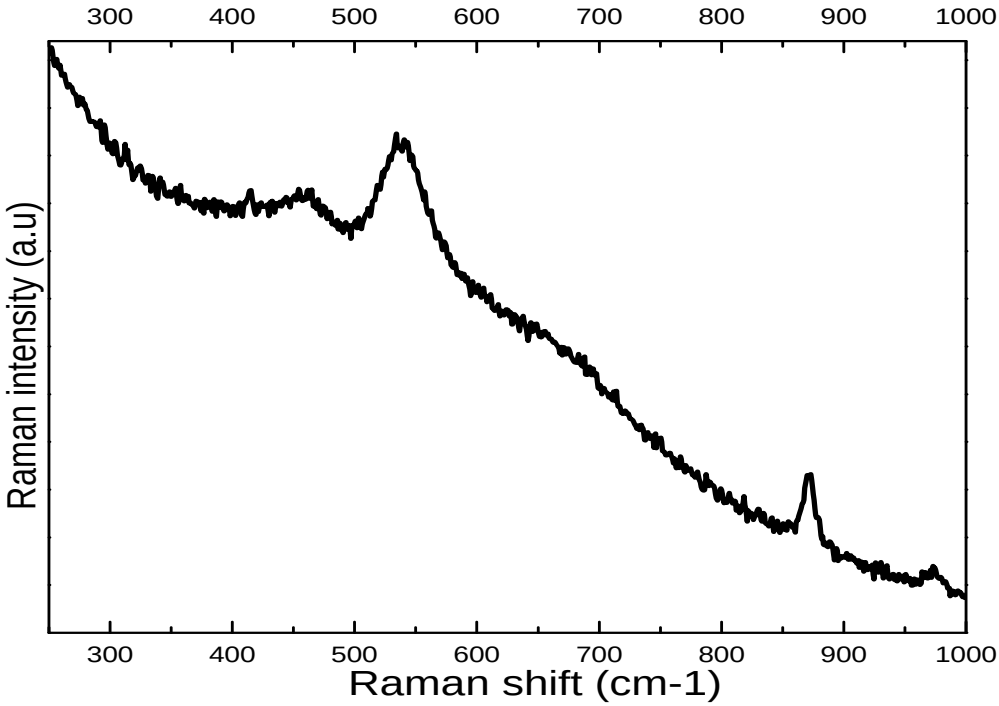

Figure 3-3a. SERS Spectrum measured for Ni-5Cr-8Fe at E = -0.65V

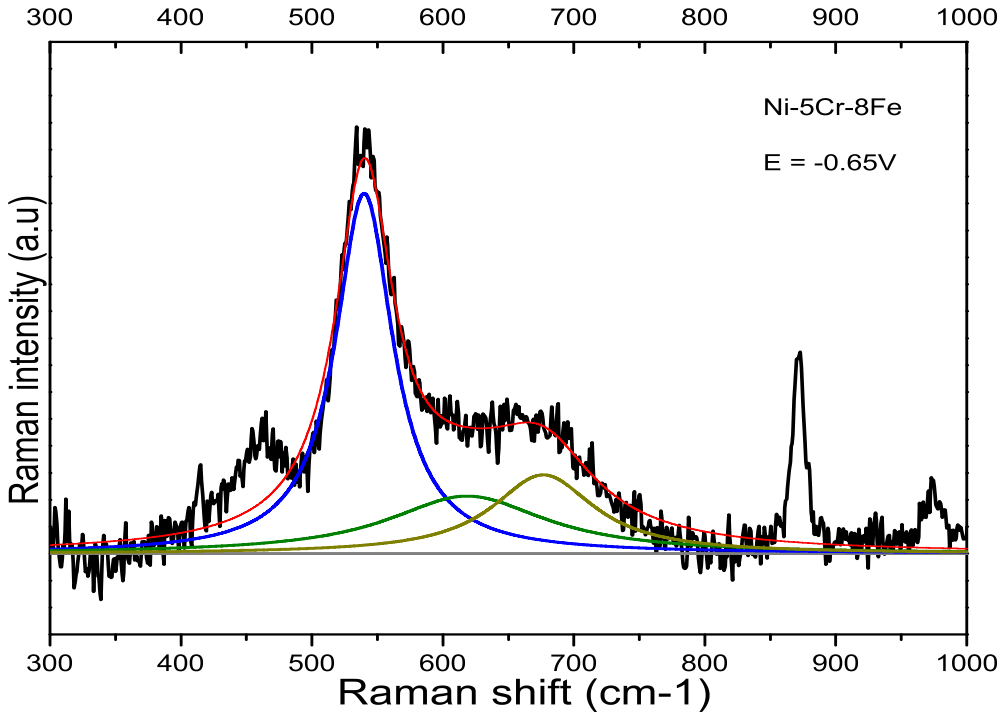

Figure 3-3b. SERS Result for Ni-5Cr-8Fe at E = -0.65V
(After Background Subtraction and Peak Fitting)

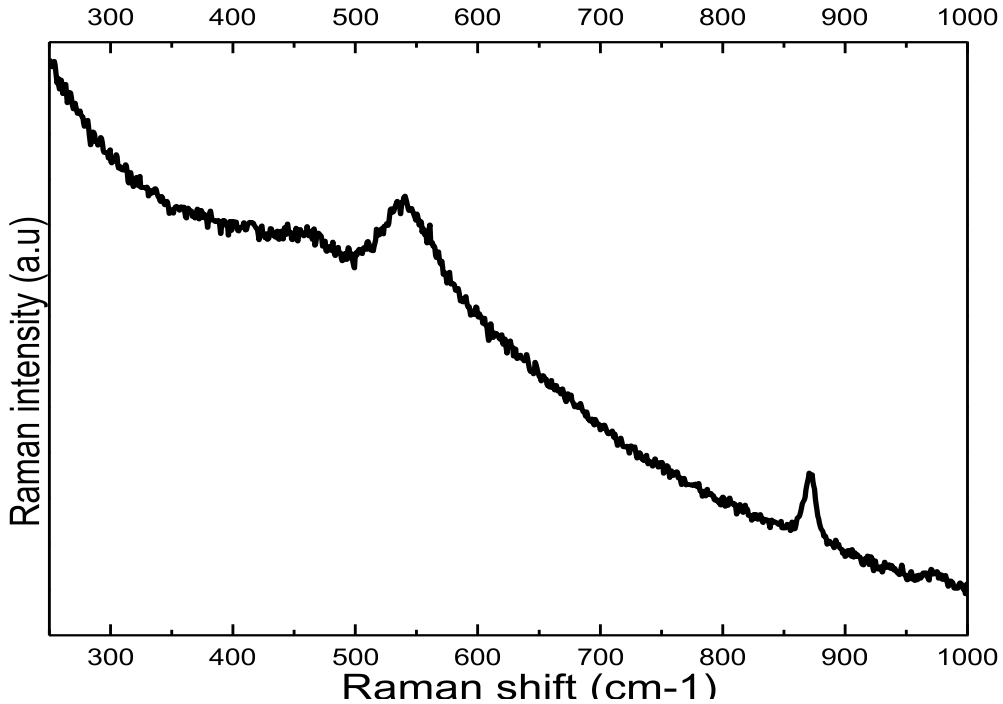

Figure 3-4a. SERS Spectrum measured for Ni-10Cr at E = -0.65V

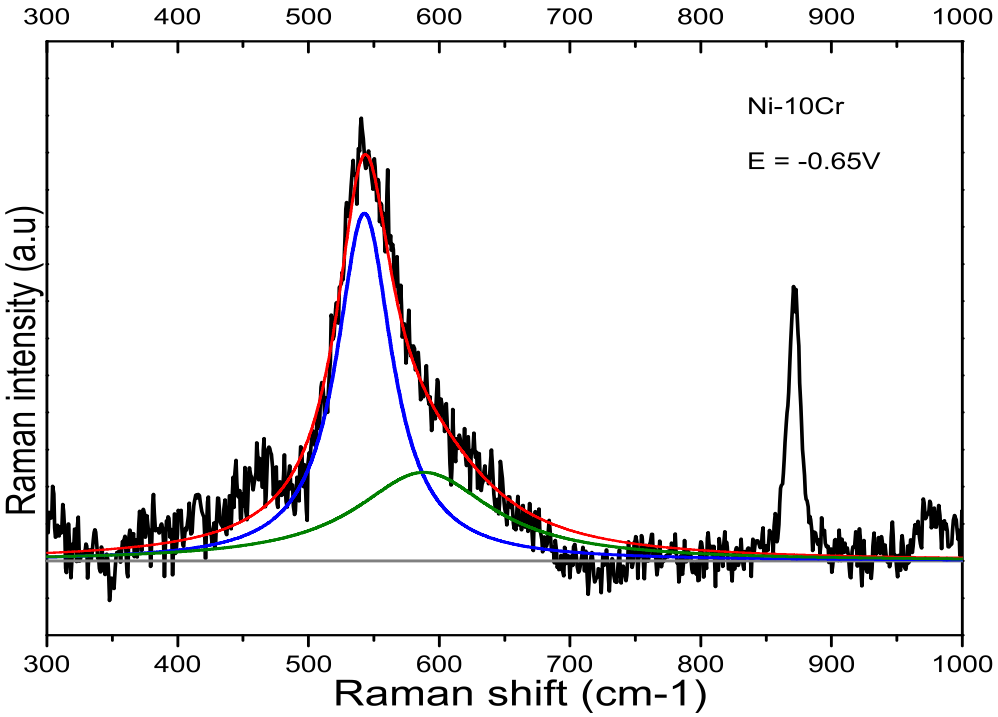

Figure 3-4b. SERS Result for Ni-10Cr at E = -0.65V
(After Background Subtraction and Peak Fitting)

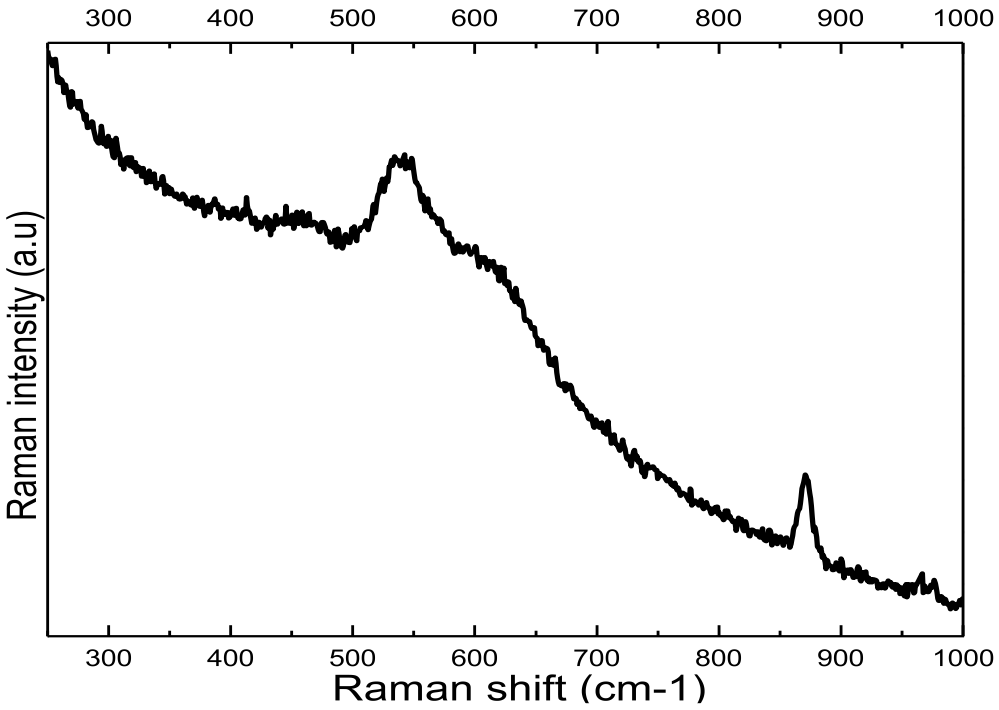

Figure 3-5a. SERS Spectrum measured for Ni-20Cr at E = -0.65V

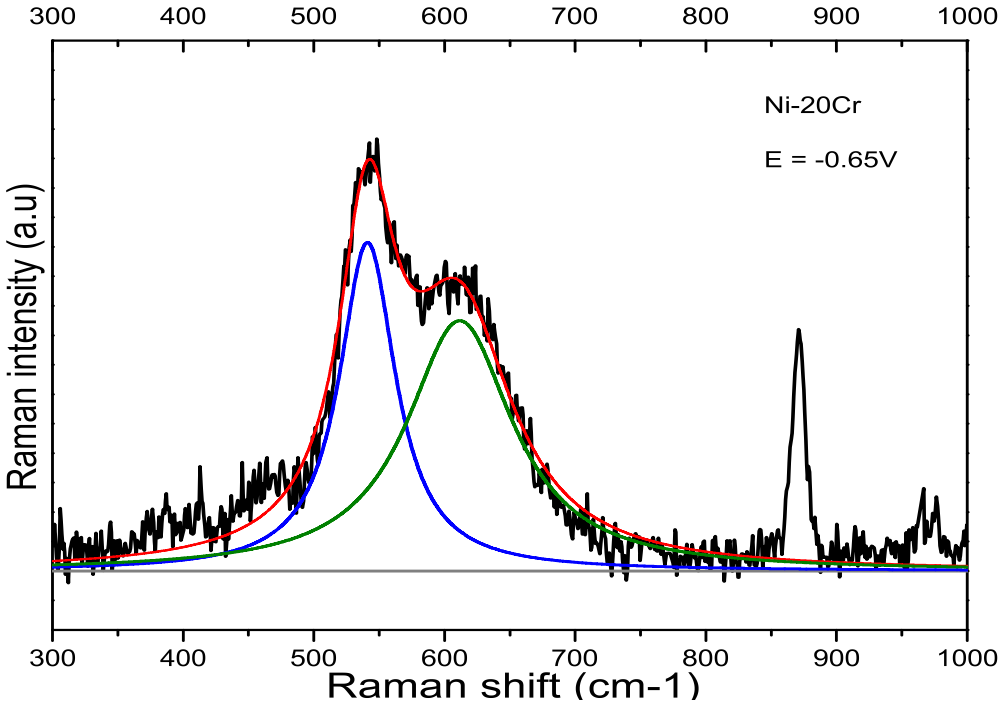

Figure 3-5b. SERS Result for Ni-20Cr at E = -0.65V
(After Background Subtraction and Peak Fitting)

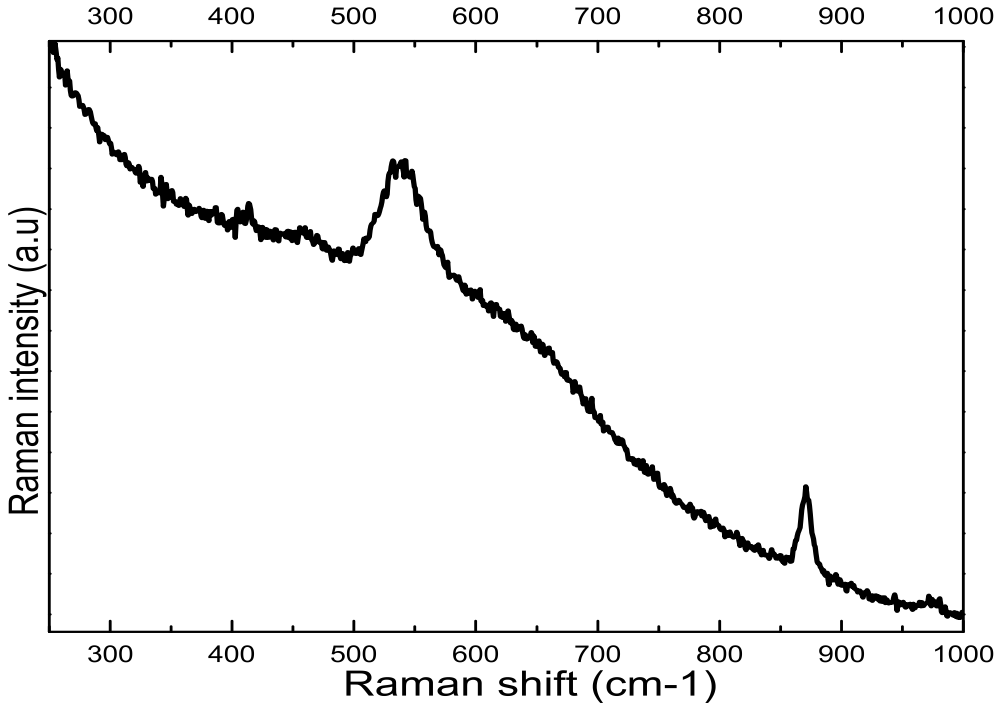

Figure 3-6a. SERS Spectrum measured for Ni-10Cr-8Fe at E = -0.65V

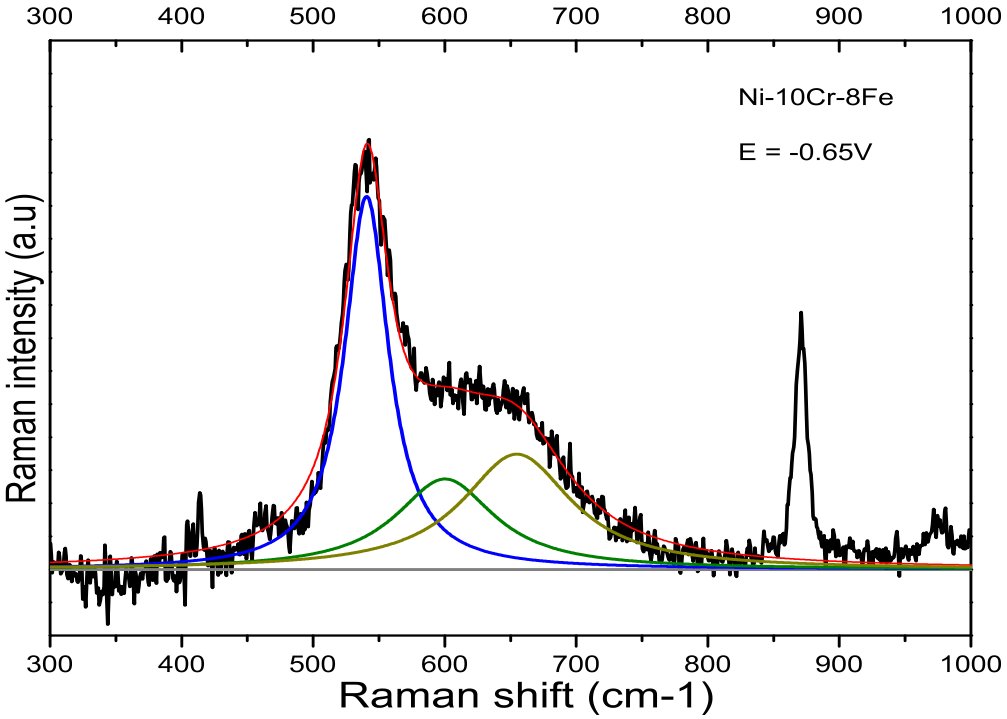

Figure 3-6b. SERS Result for Ni-10Cr-8Fe at E = -0.65V
(After Background Subtraction and Peak Fitting)

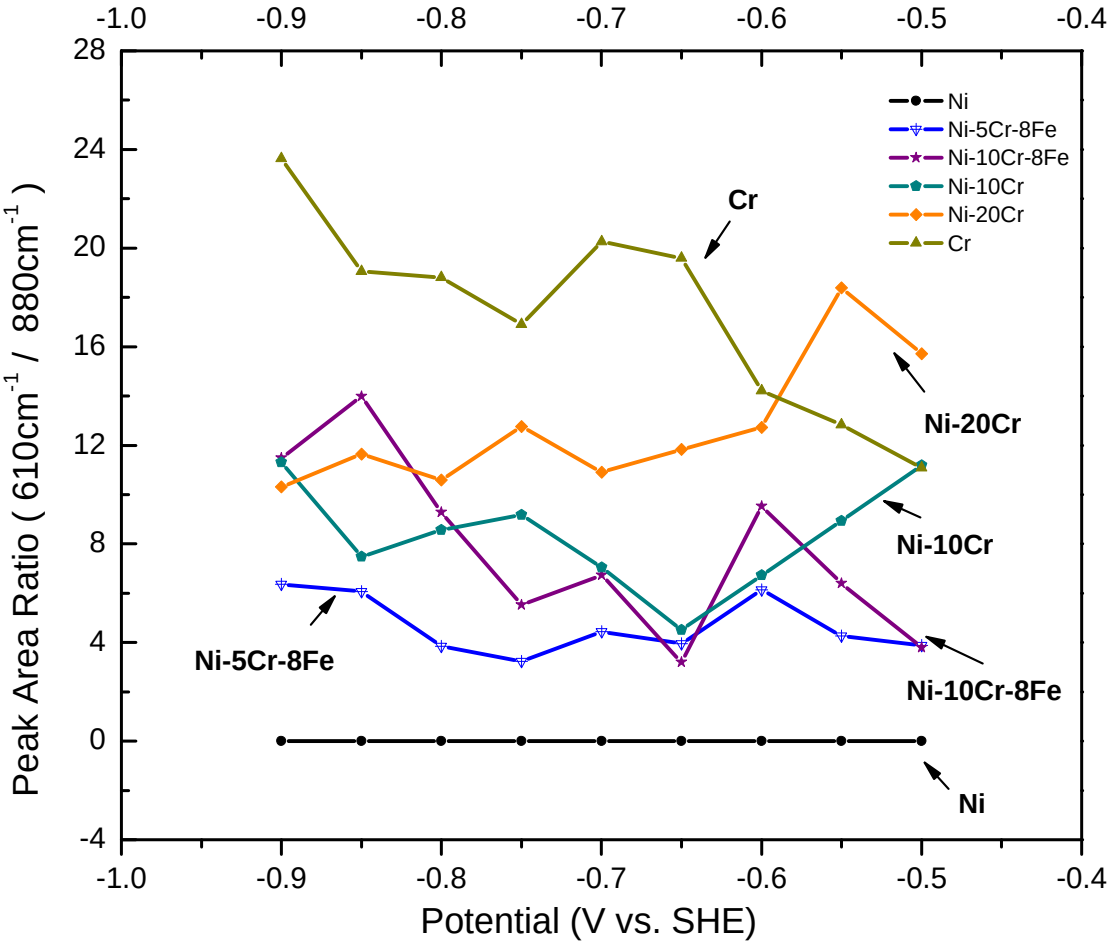

Figure 3-7. The ratio of integrated intensity of the peak at 610 cm^{-1} to the peak at 880 cm^{-1} as a function of applied potential

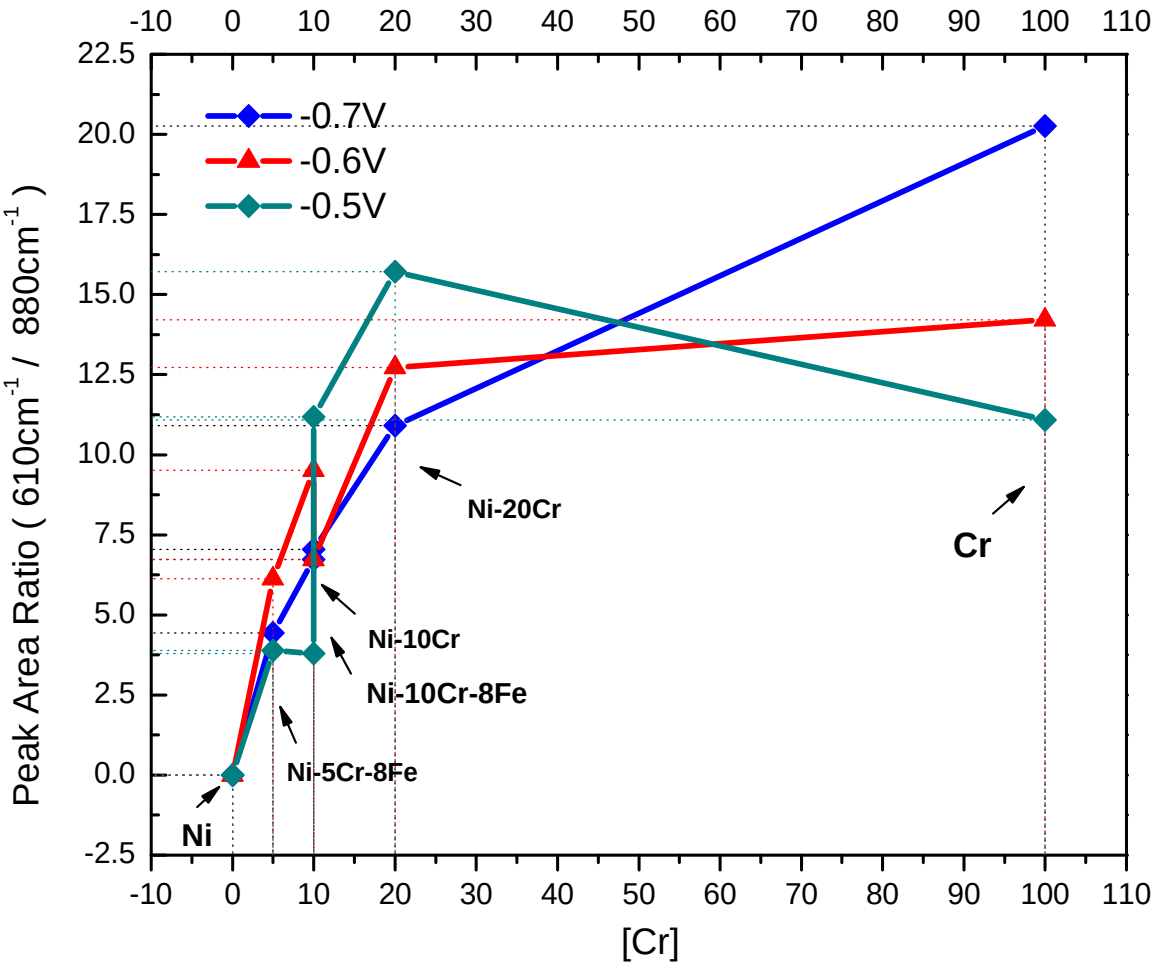

Figure 3-8. The integrated intensity ratio of 610 cm^{-1}/ 880 cm^{-1} as a function of chromium composition

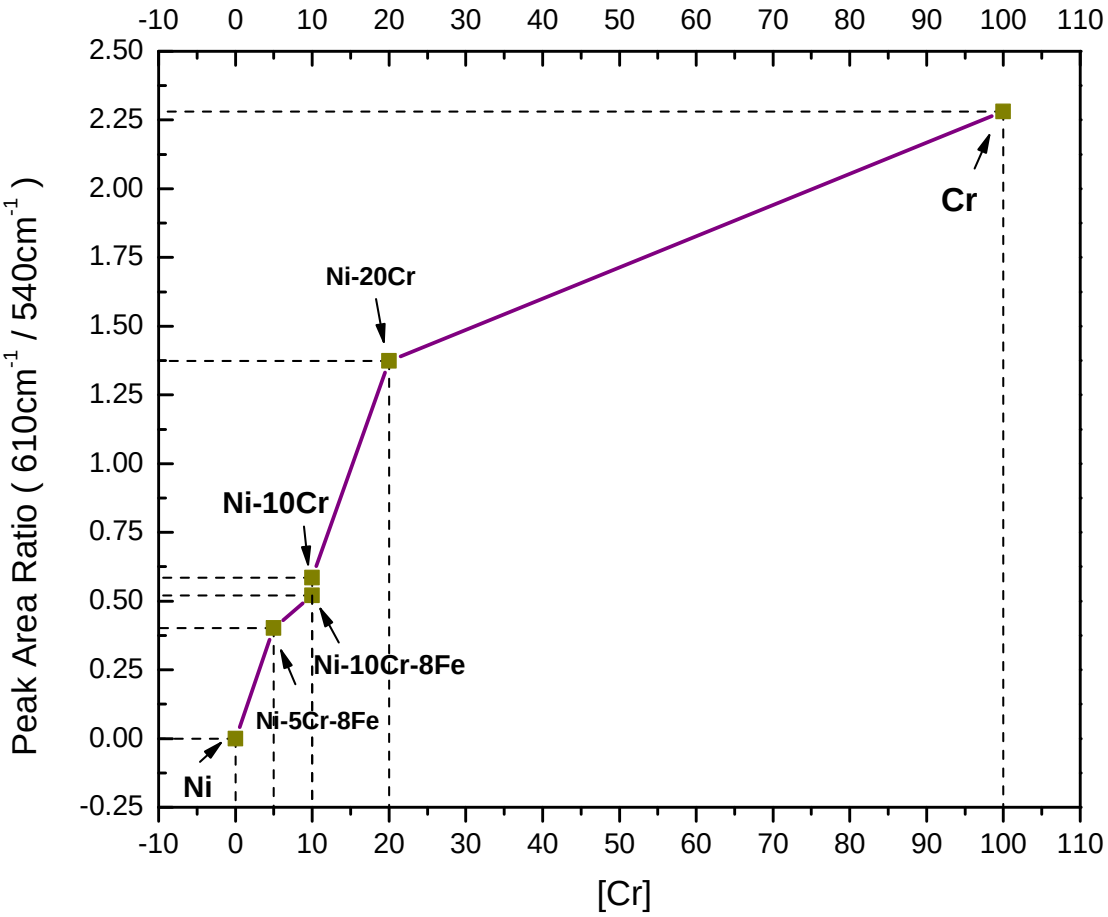

Figure 3-9. The integrated intensity ratio of 610 cm^{-1}/ 540 cm^{-1} as a function of chromium composition

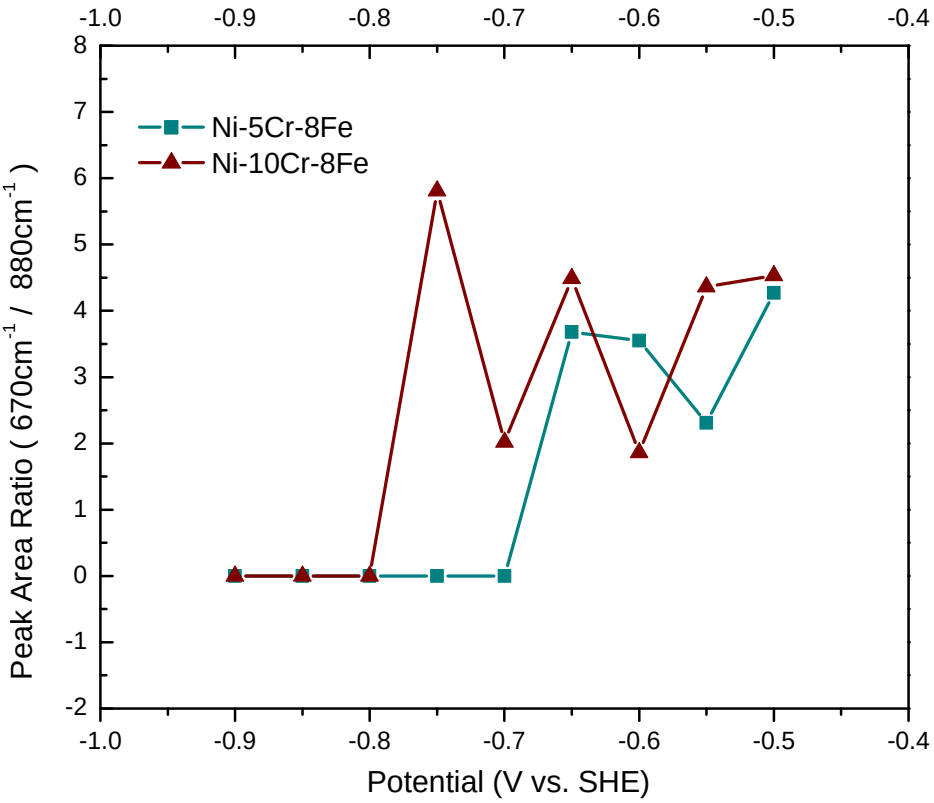

Figure 3-10. The integrated intensity ratio of 670 cm^{-1}/ 880 cm^{-1} as a function of potential

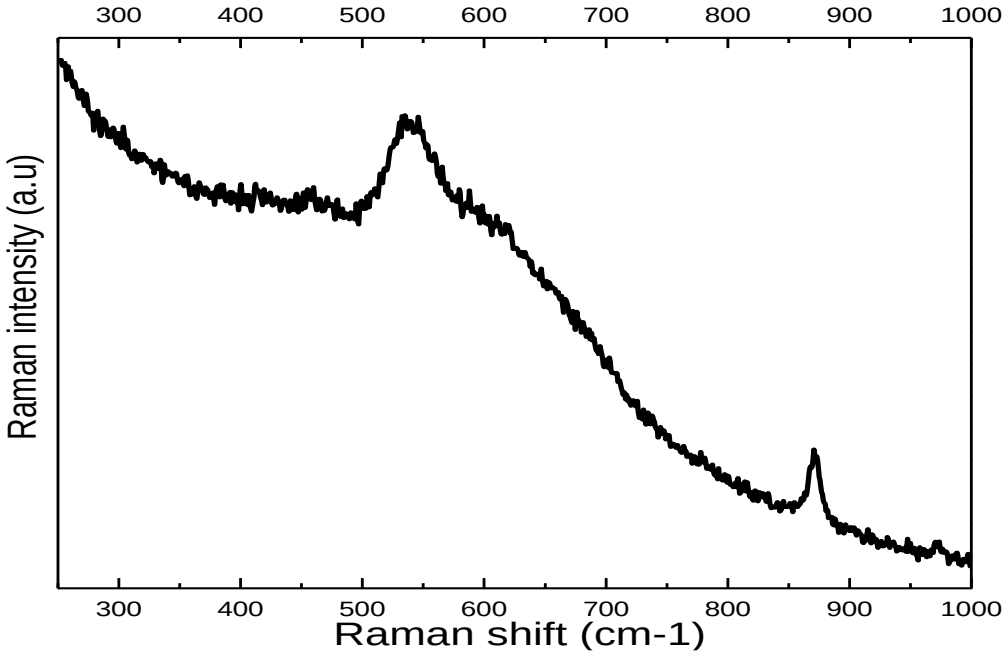

Figure 4-1a. SERS Spectrum measured for Alloy 600 at E = -0.9V

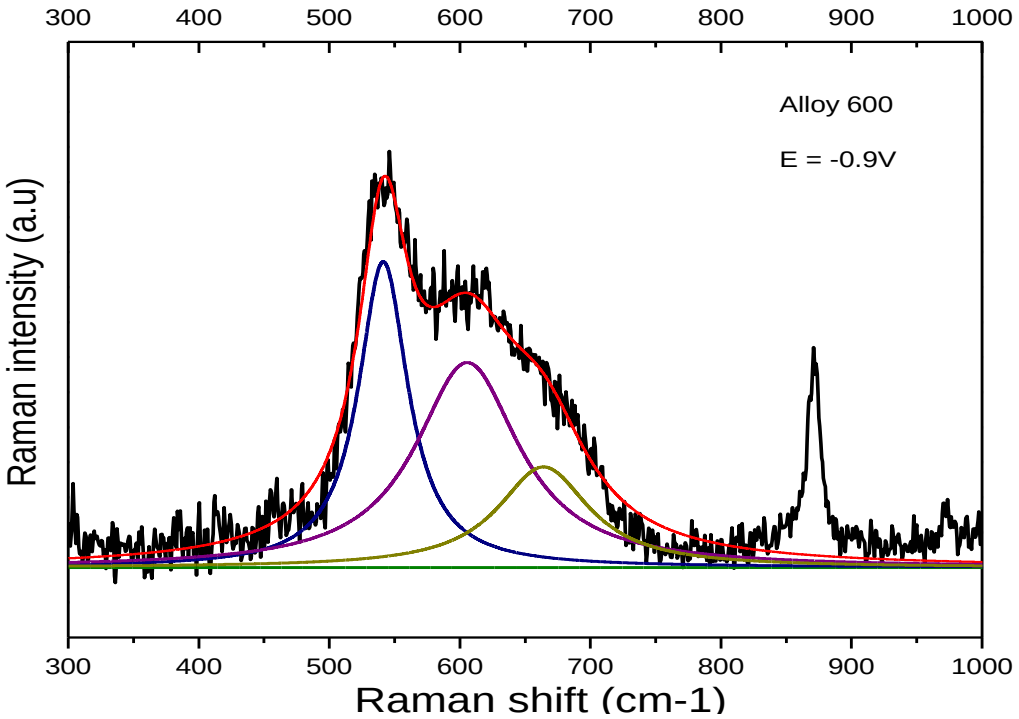

Figure 4-1b. SERS Result for Alloy 600 at E = -0.9V
(After Background Subtraction and Peak Fitting)

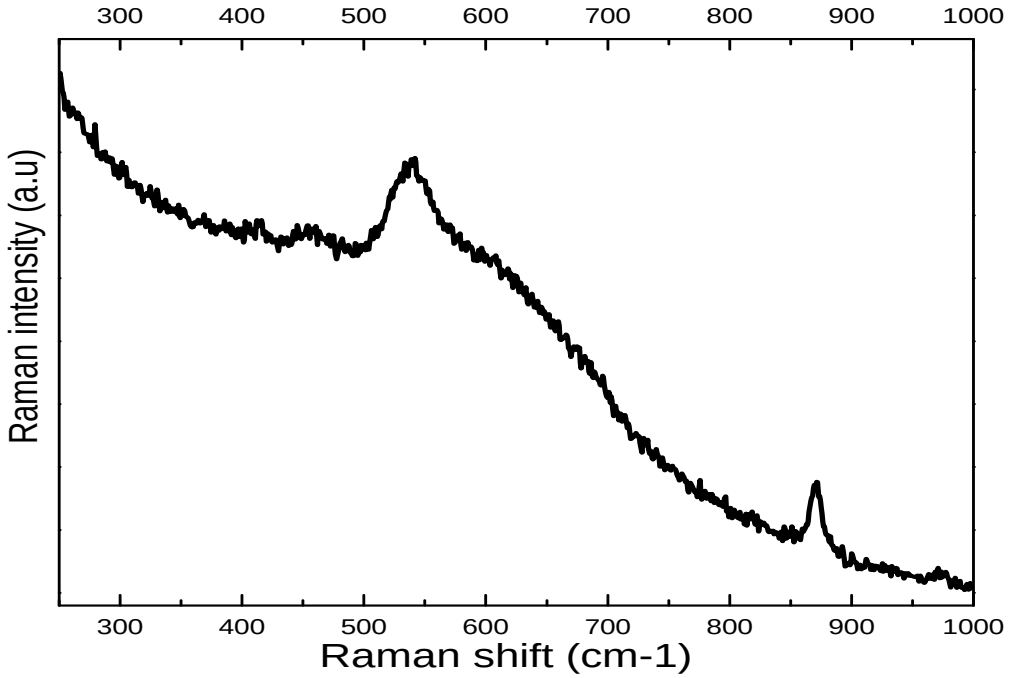

Figure 4-2a. SERS Spectrum measured for Alloy 600 at E = -0.85V

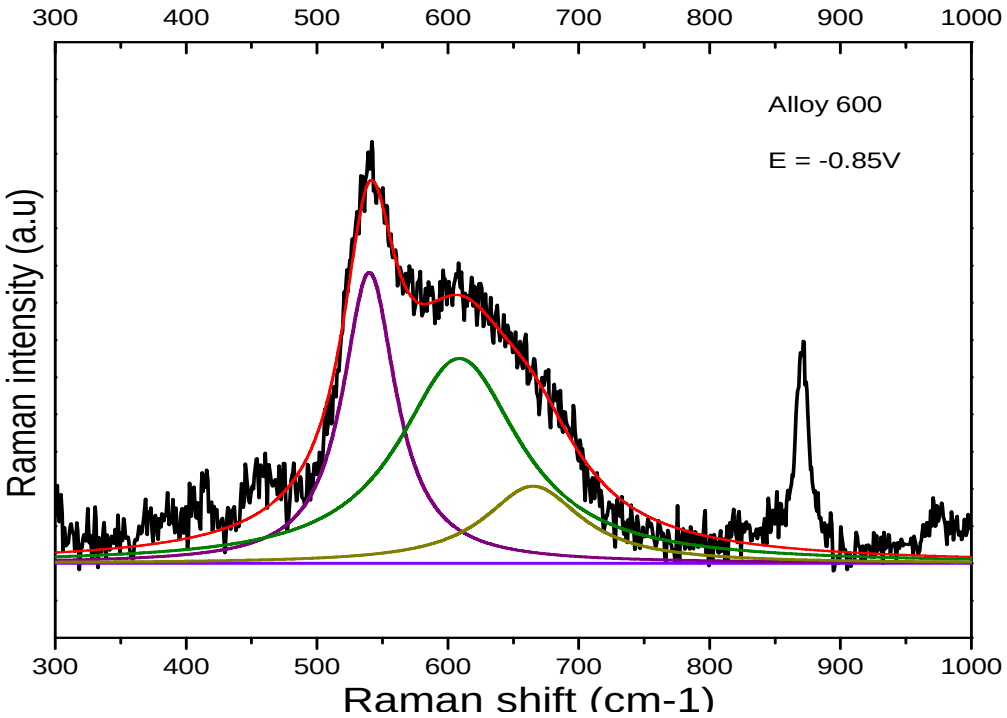

Figure 4-2b. SERS Result for Alloy 600 at E = -0.85V
(After Background Subtraction and Peak Fitting)

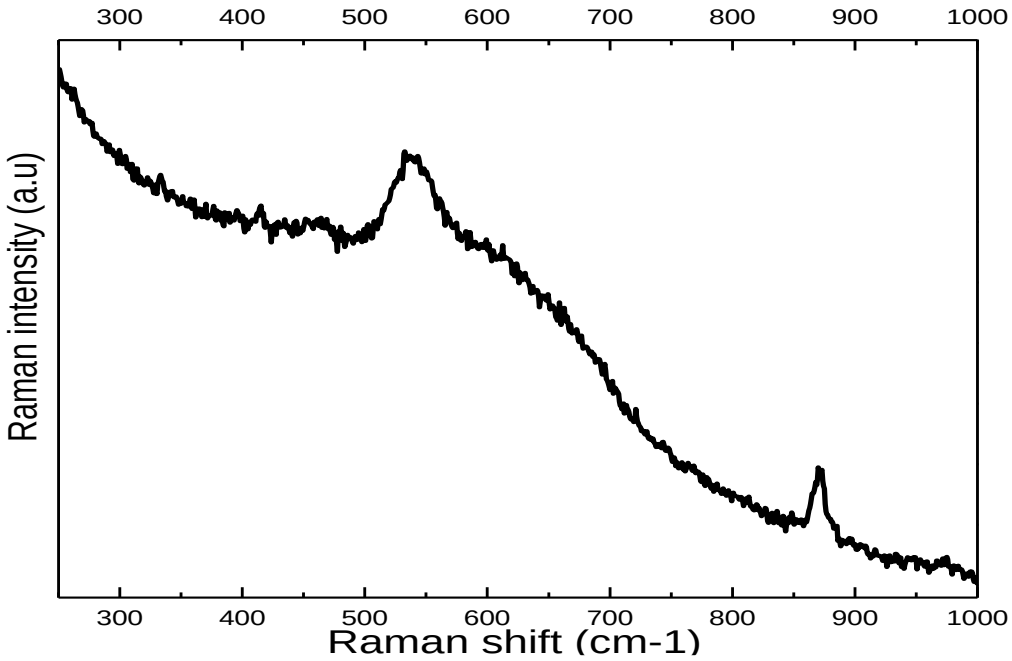

Figure 4-3a. SERS Spectrum measured for Alloy 600 at E = -0.8V

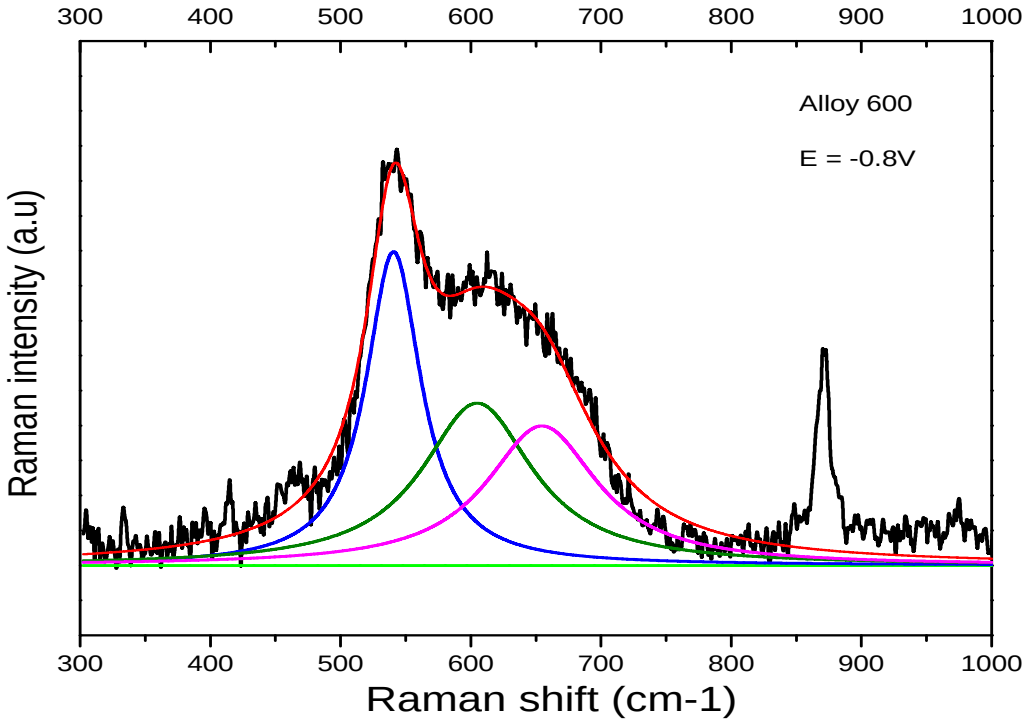

Figure 4-3b. SERS Result for Alloy 600 at E = -0.8V
(After Background Subtraction and Peak Fitting)

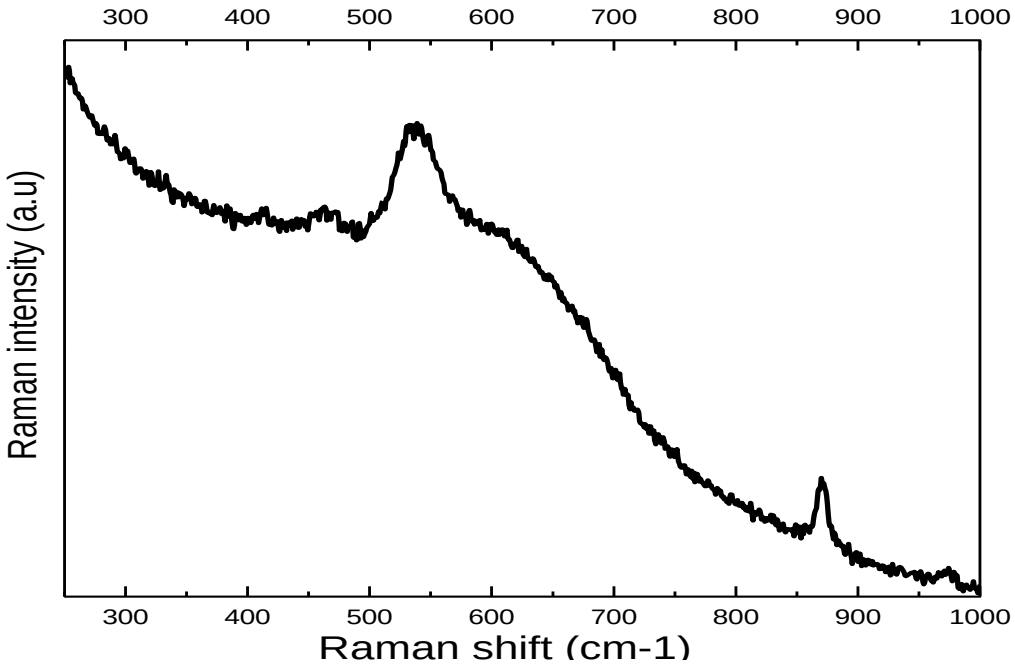

Figure 4-4a. SERS Spectrum measured for Alloy 600 at E = -0.75V

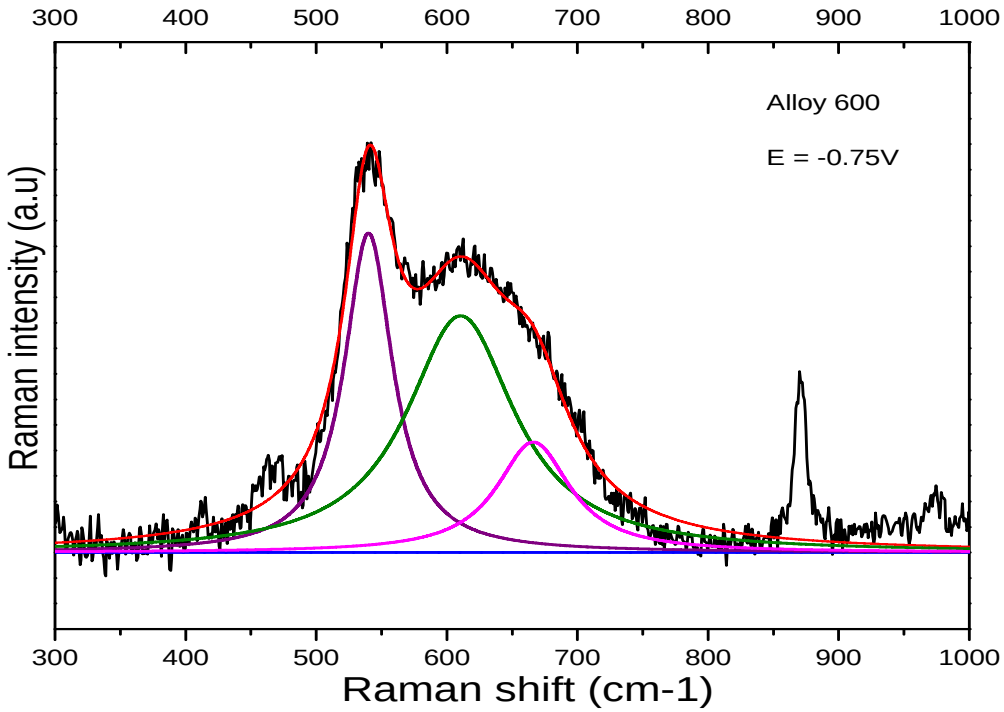

Figure 4-4b. SERS Result for Alloy 600 at E = -0.75V
(After Background Subtraction and Peak Fitting)

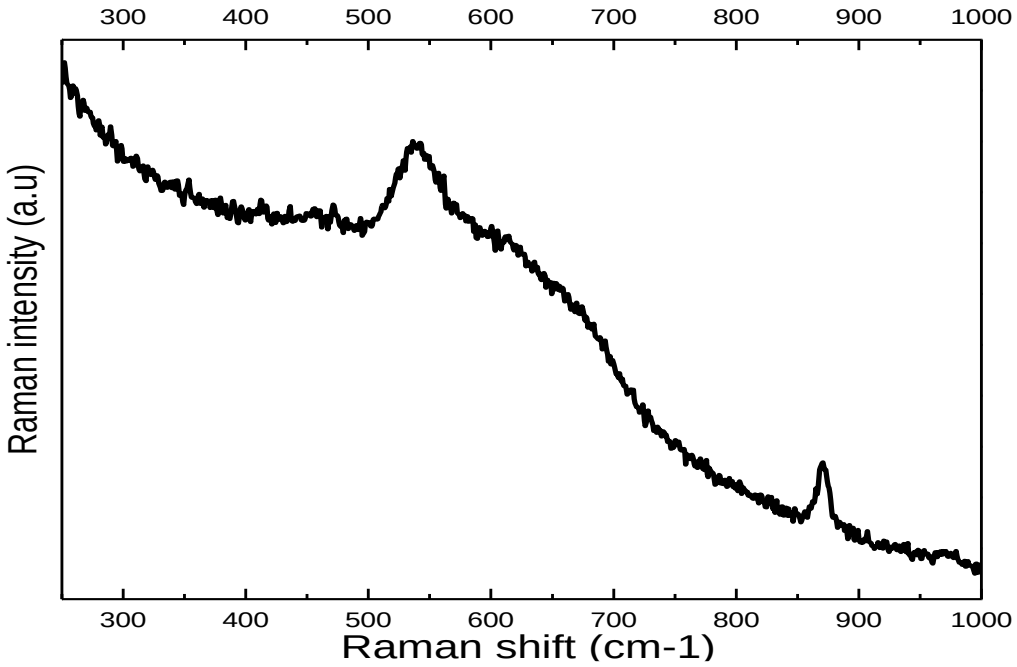

Figure 4-5a. SERS Spectrum measured for Alloy 600 at E = -0.7V

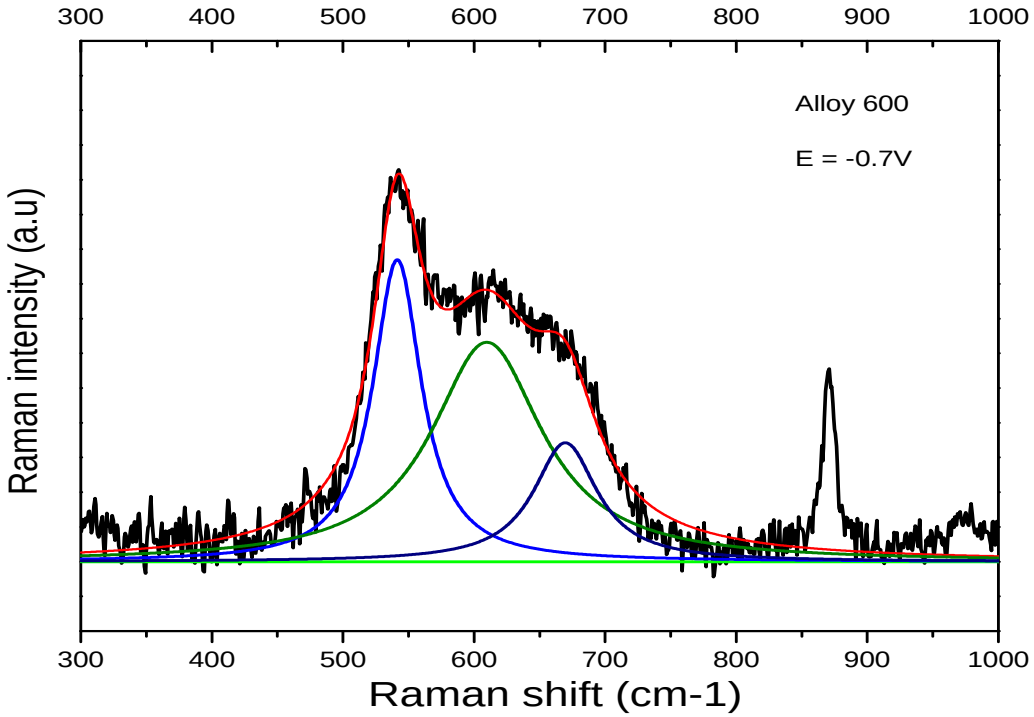

Figure 4-5b. SERS Result for Alloy 600 at E = -0.7V
(After Background Subtraction and Peak Fitting)

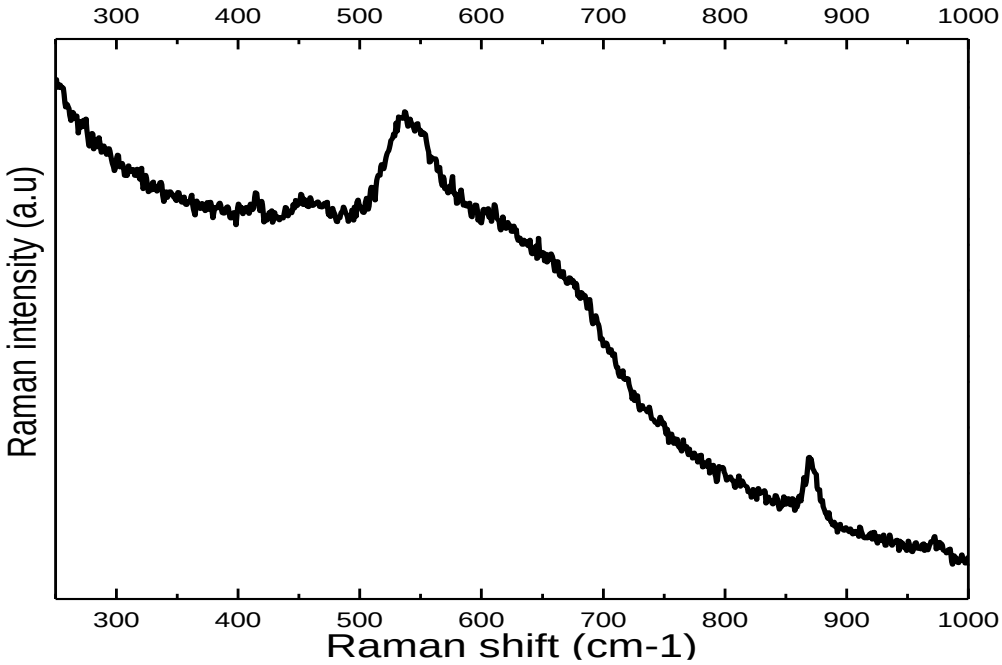

Figure 4-6a. SERS Spectrum measured for Alloy 600 at E = -0.65V

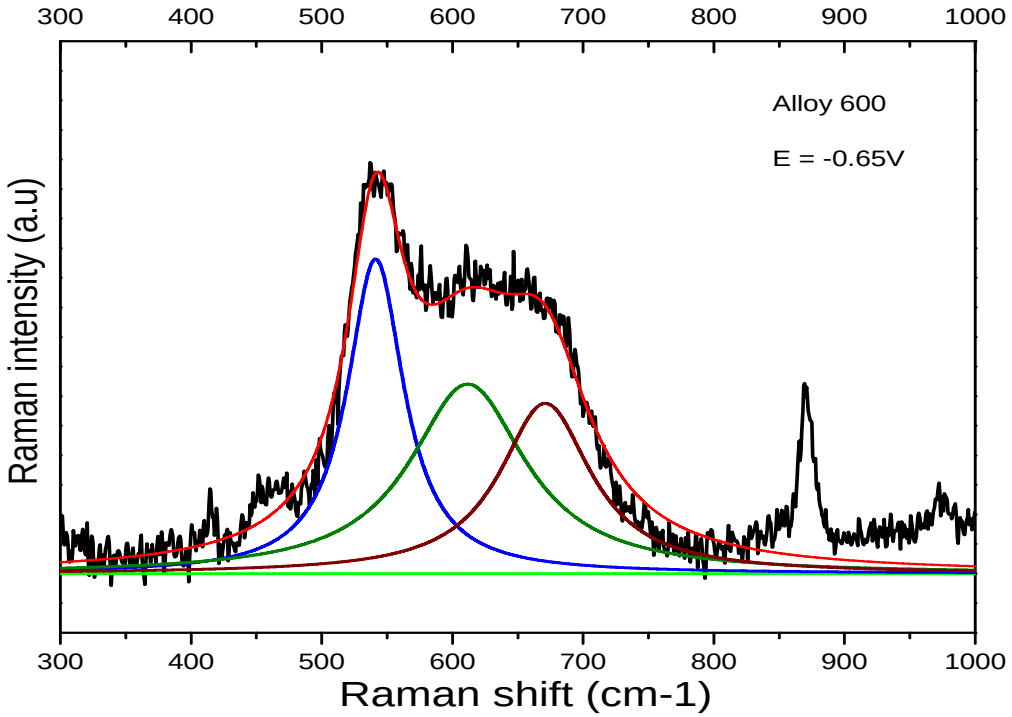

Figure 4-6b. SERS Result for Alloy 600 at E = -0.65V
(After Background Subtraction and Peak Fitting)

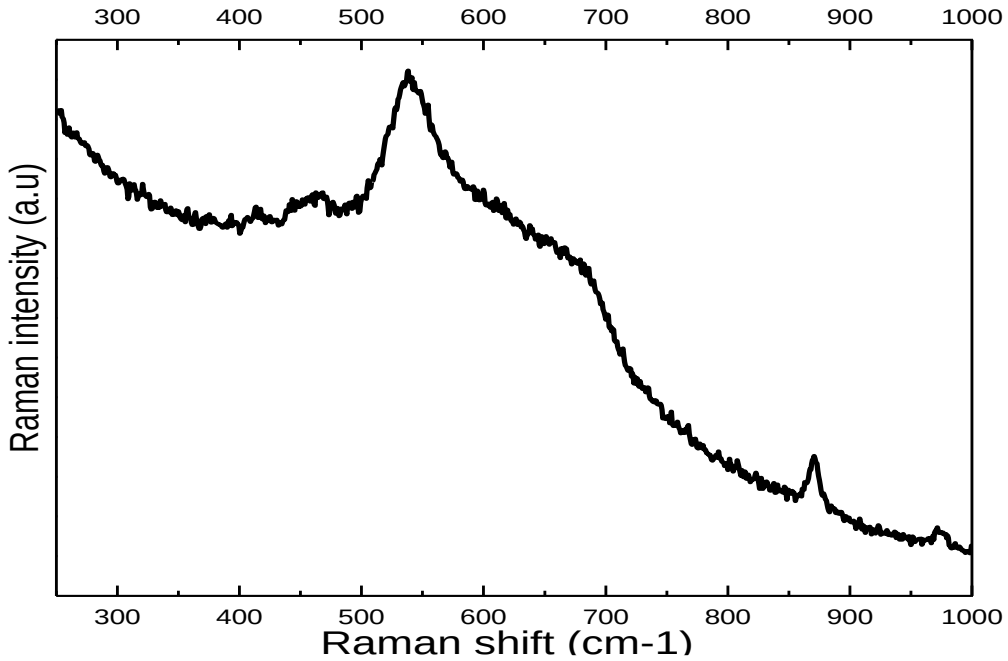

Figure 4-7a. SERS Spectrum measured for Alloy 600 at E = -0.6V

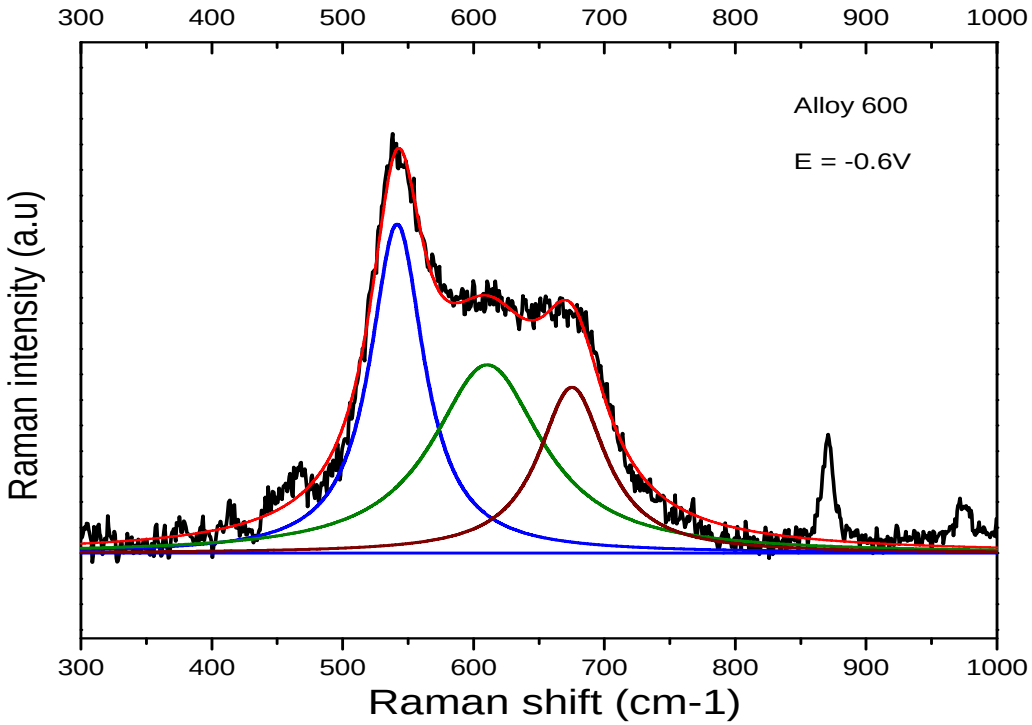

Figure 4-7b. SERS Result for Alloy 600 at E = -0.6V
(After Background Subtraction and Peak Fitting)

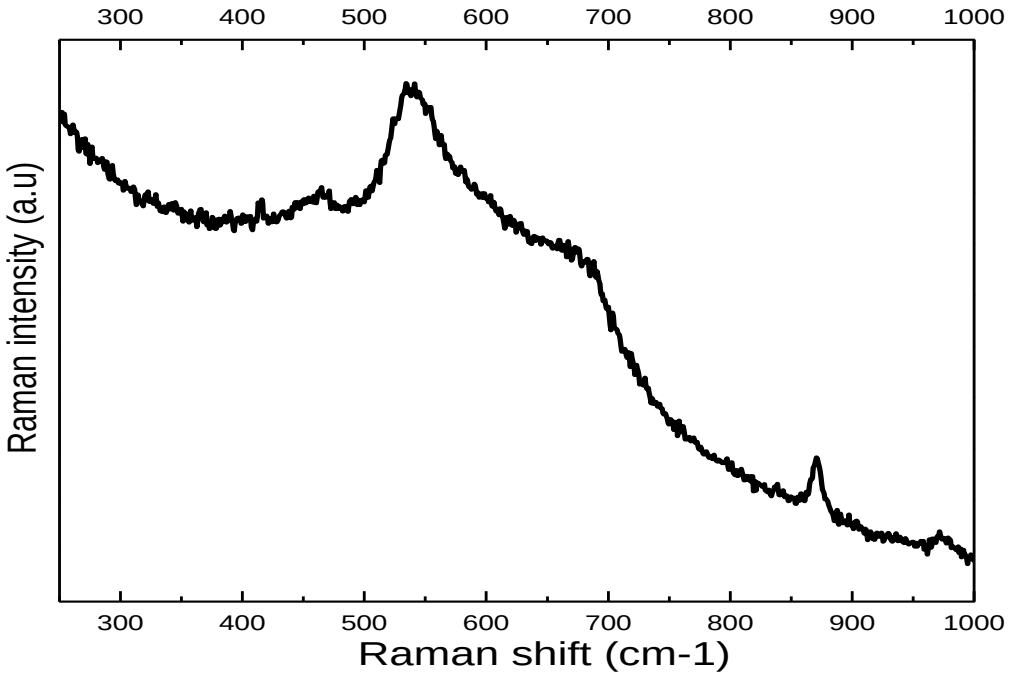

Figure 4-8a. SERS Spectrum measured for Alloy 600 at E = -0.55V

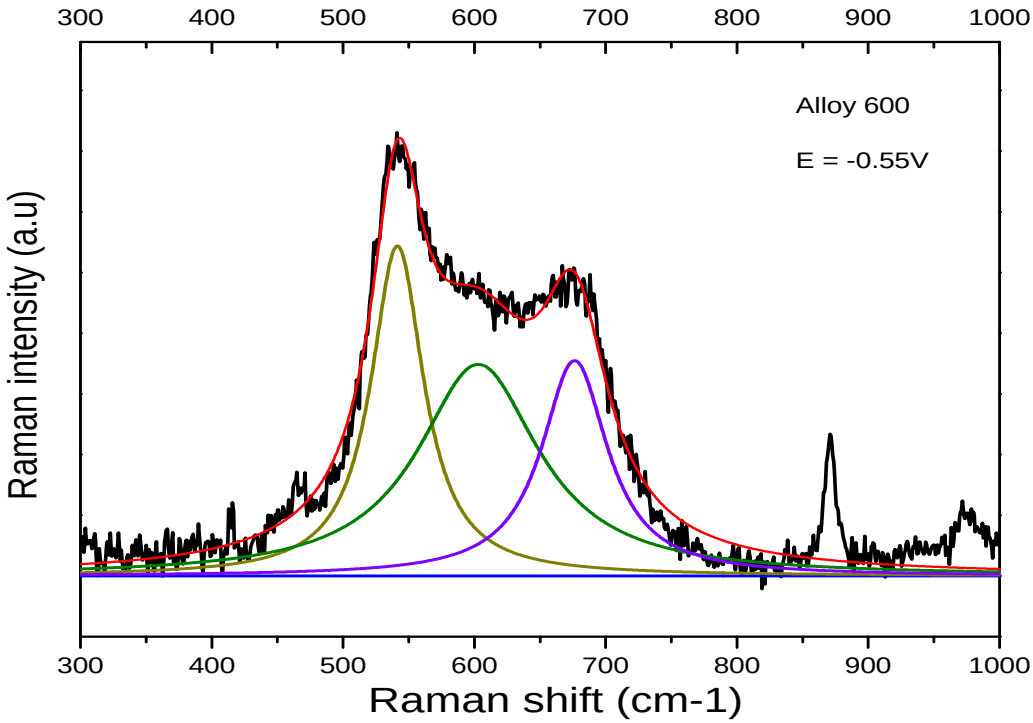

Figure 4-8b. SERS Result for Alloy 600 at E = -0.55V
(After Background Subtraction and Peak Fitting)

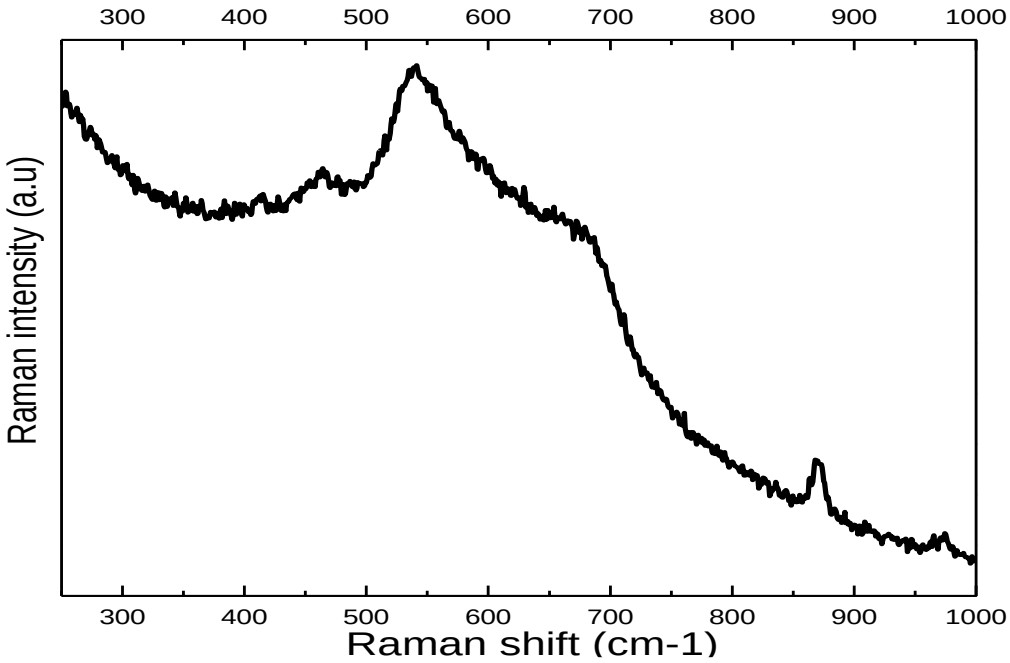

Figure 4-9a. SERS Spectrum measured for Alloy 600 at E = -0.5V

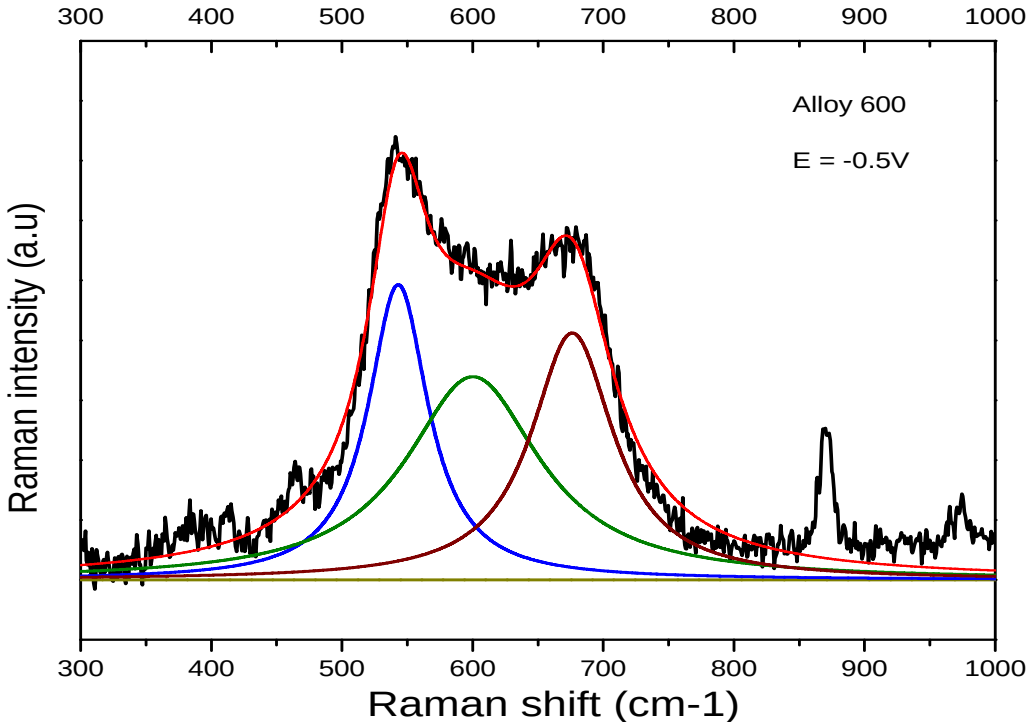

Figure 4-9b. SERS Result for Alloy 600 at E = -0.5V
(After Background Subtraction and Peak Fitting)

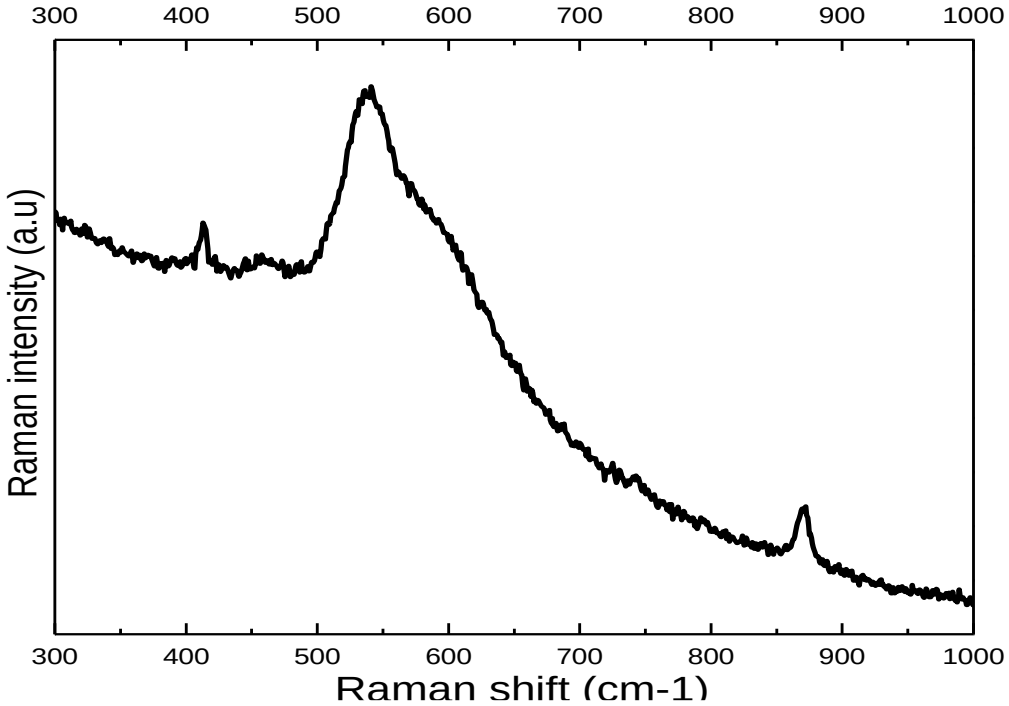

Figure 4-10a. SERS Spectrum measured for Alloy 690 at E = -0.9V

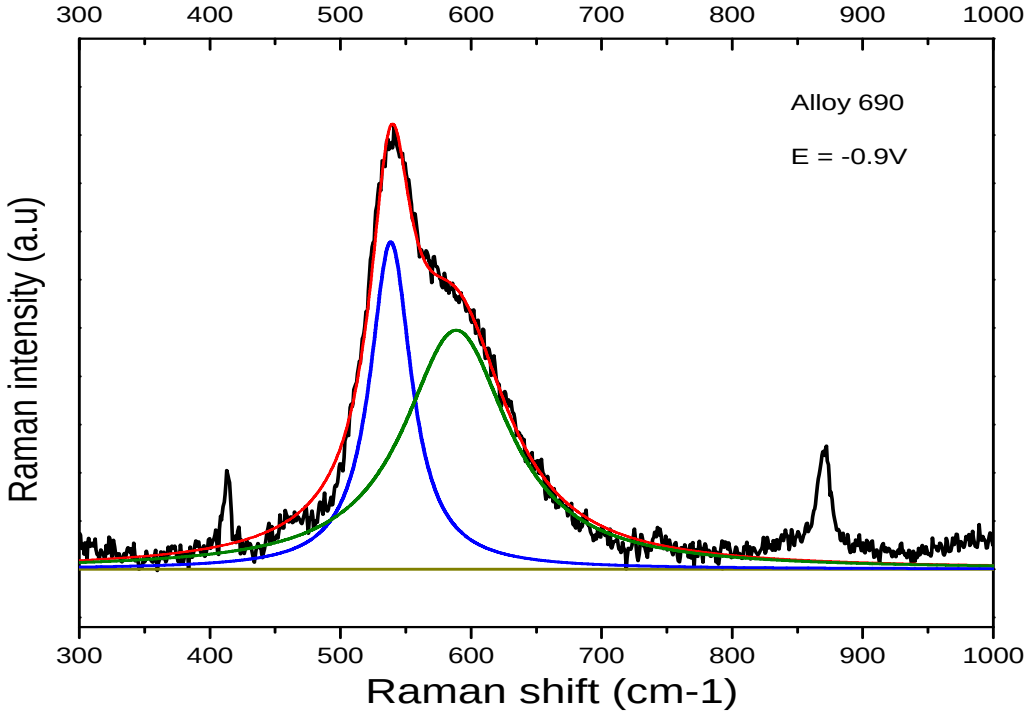

Figure 4-10b. SERS Result for Alloy 690 at E = -0.9V
(After Background Subtraction and Peak Fitting)

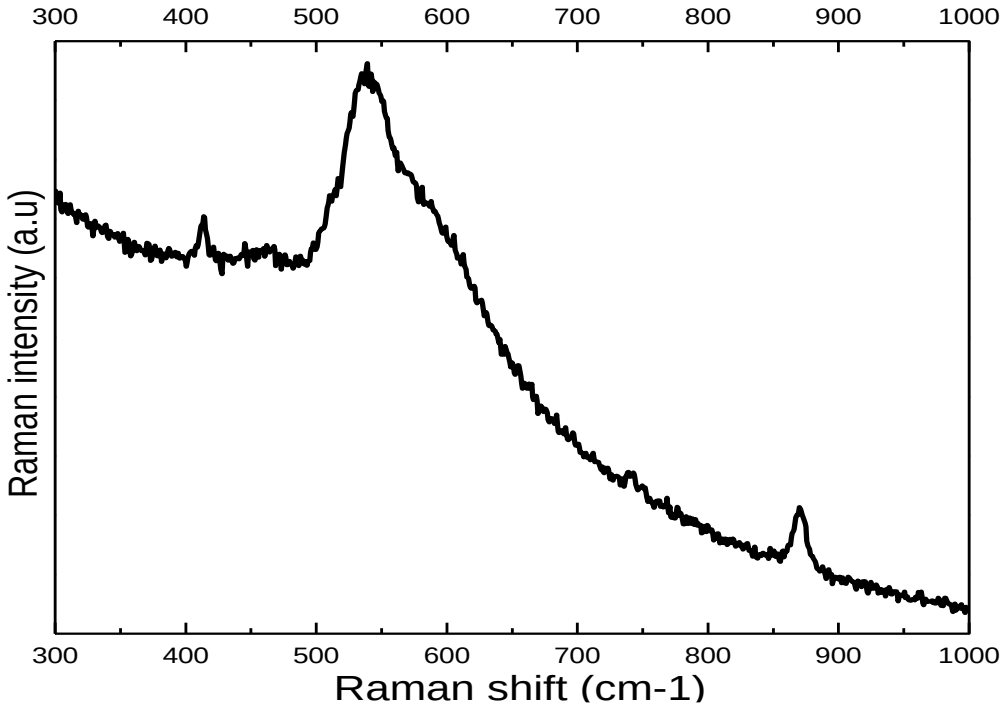

Figure 4-11a. SERS Spectrum measured for Alloy 690 at E = -0.85V

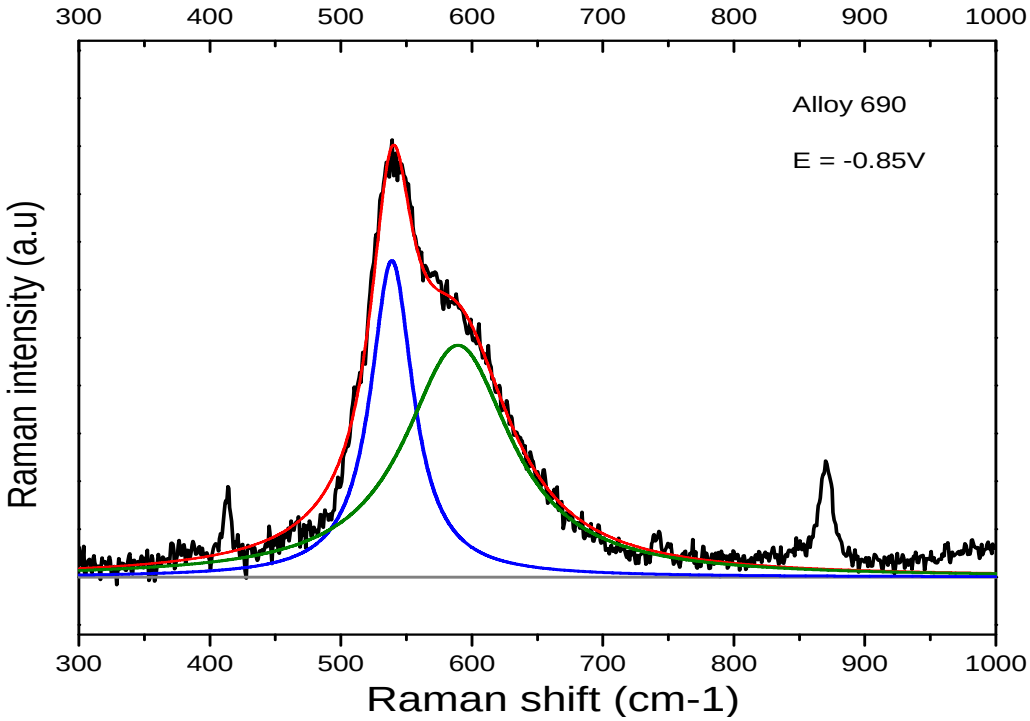

Figure 4-11b. SERS Result for Alloy 690 at E = -0.85V
(After Background Subtraction and Peak Fitting)

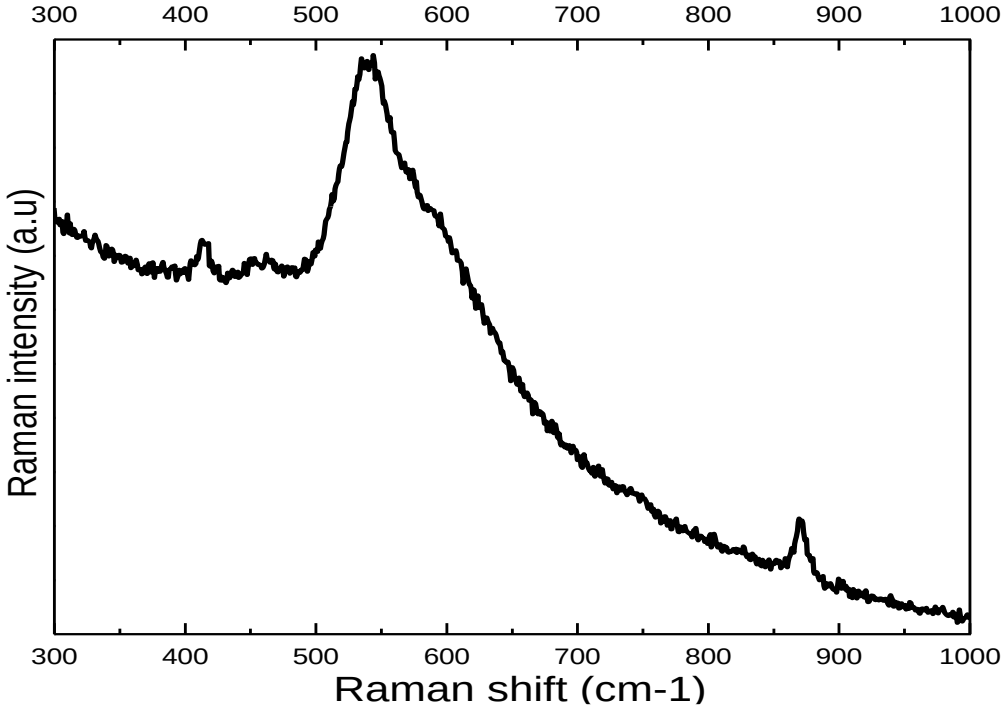

Figure 4-12a. SERS Spectrum measured for Alloy 690 at E = -0.8V

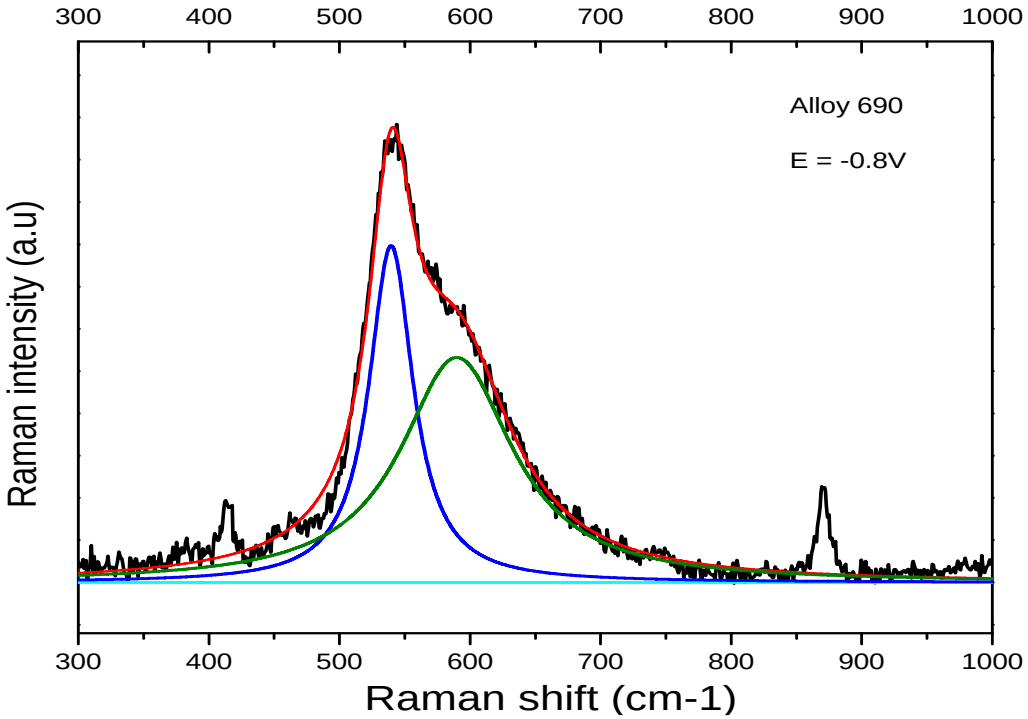

Figure 4-12b. SERS Result for Alloy 690 at E = -0.8V
(After Background Subtraction and Peak Fitting)

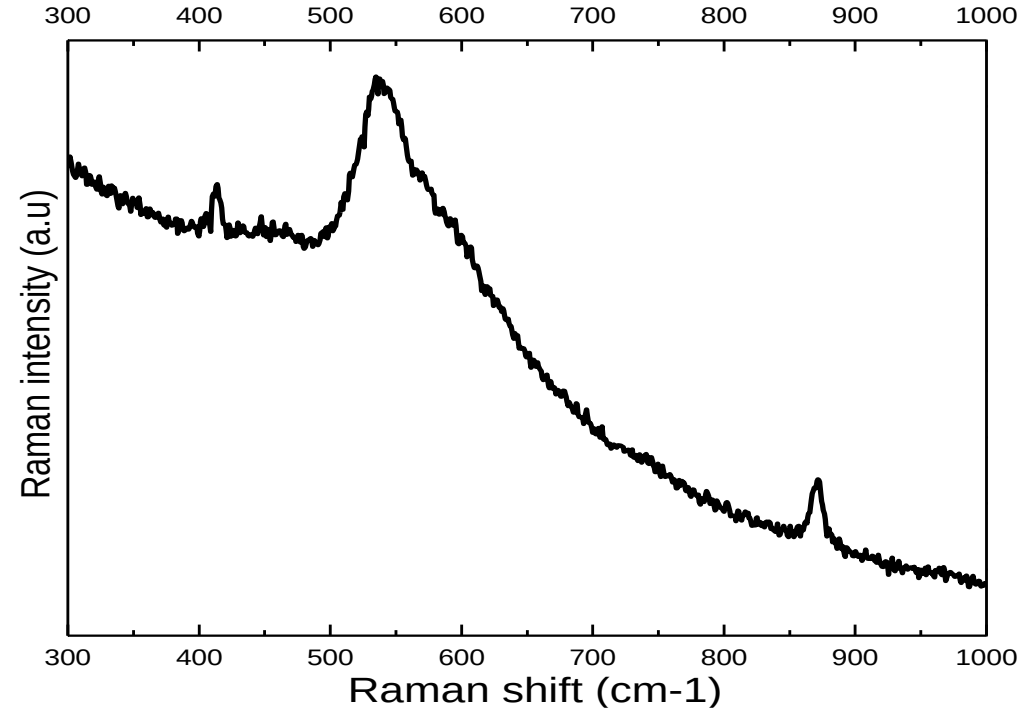

Figure 4-13a. SERS Spectrum measured for Alloy 690 at E = -0.75V

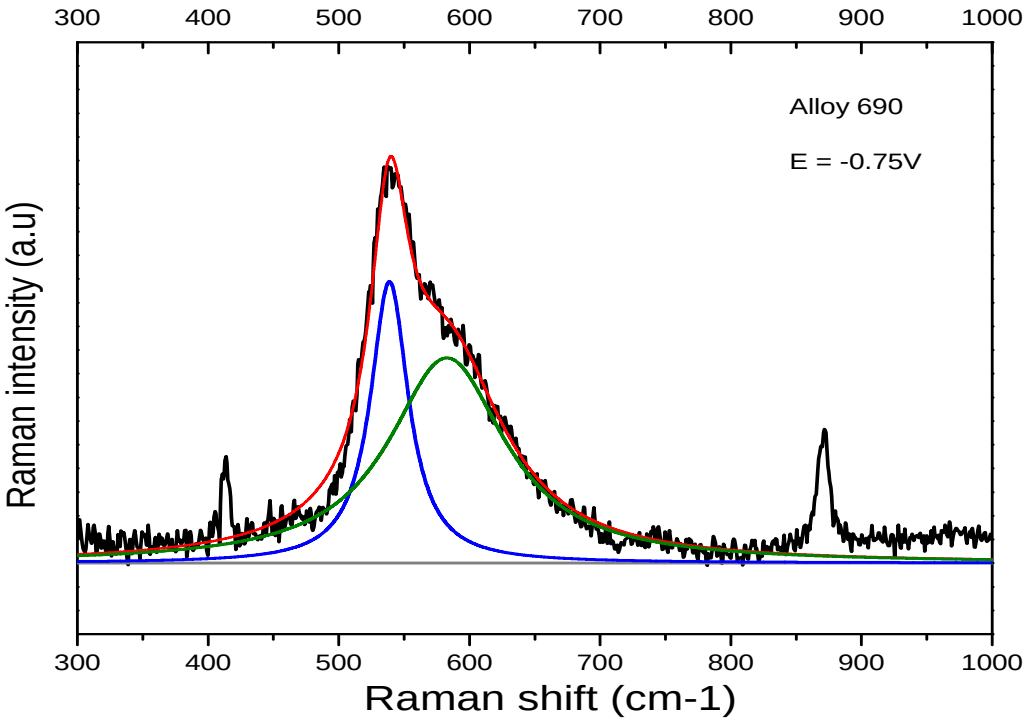

Figure 4-13b. SERS Result for Alloy 690 at E = -0.75V
(After Background Subtraction and Peak Fitting)

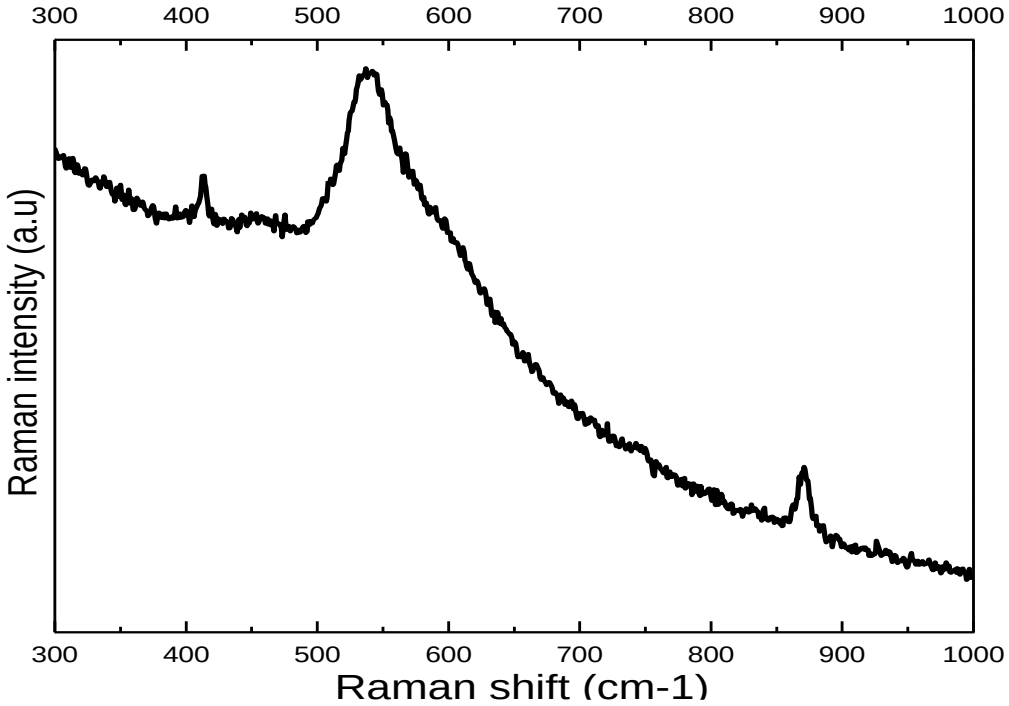

Figure 4-14a. SERS Spectrum measured for Alloy 690 at E = -0.7V

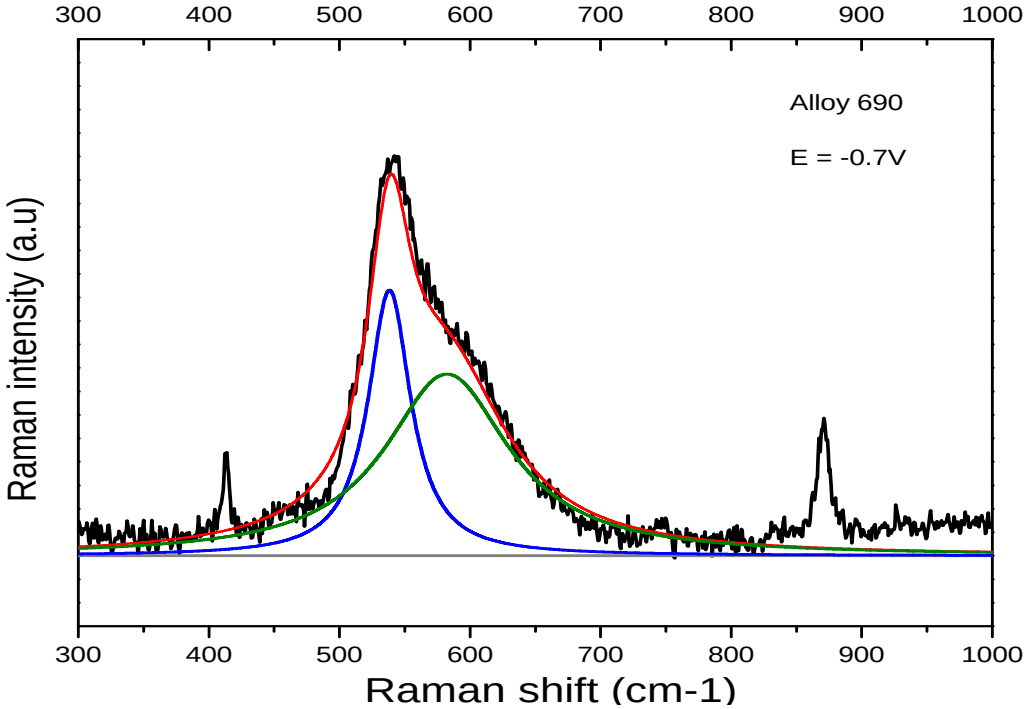

Figure 4-14b. SERS Result for Alloy 690 at E = -0.7V
(After Background Subtraction and Peak Fitting)

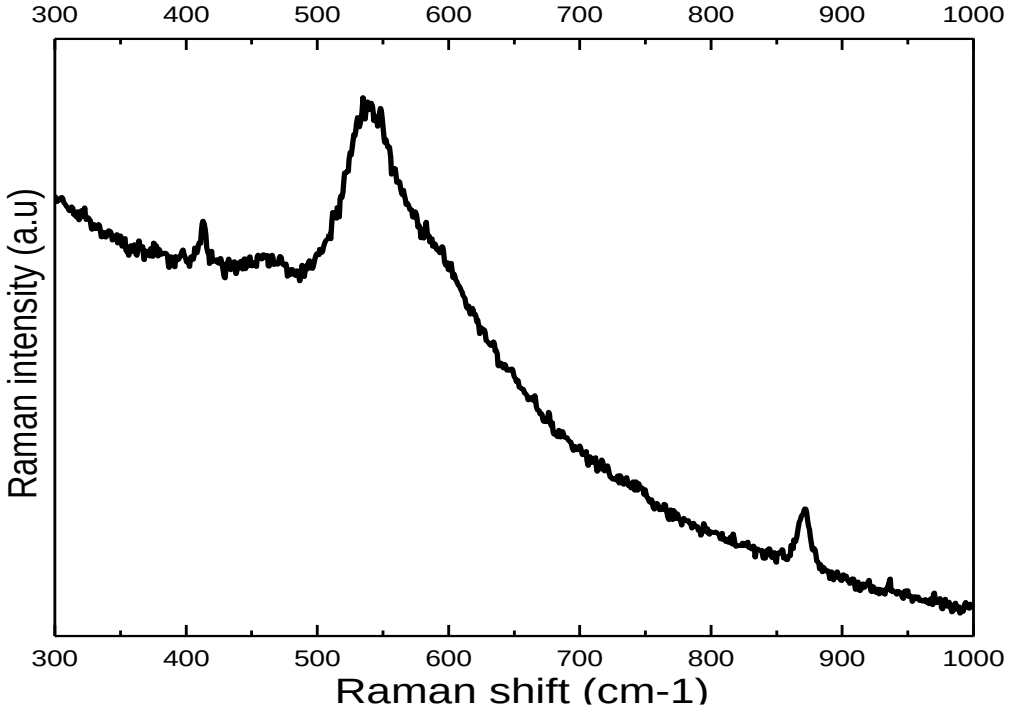

Figure 4-15a. SERS Spectrum measured for Alloy 690 at E = -0.65V

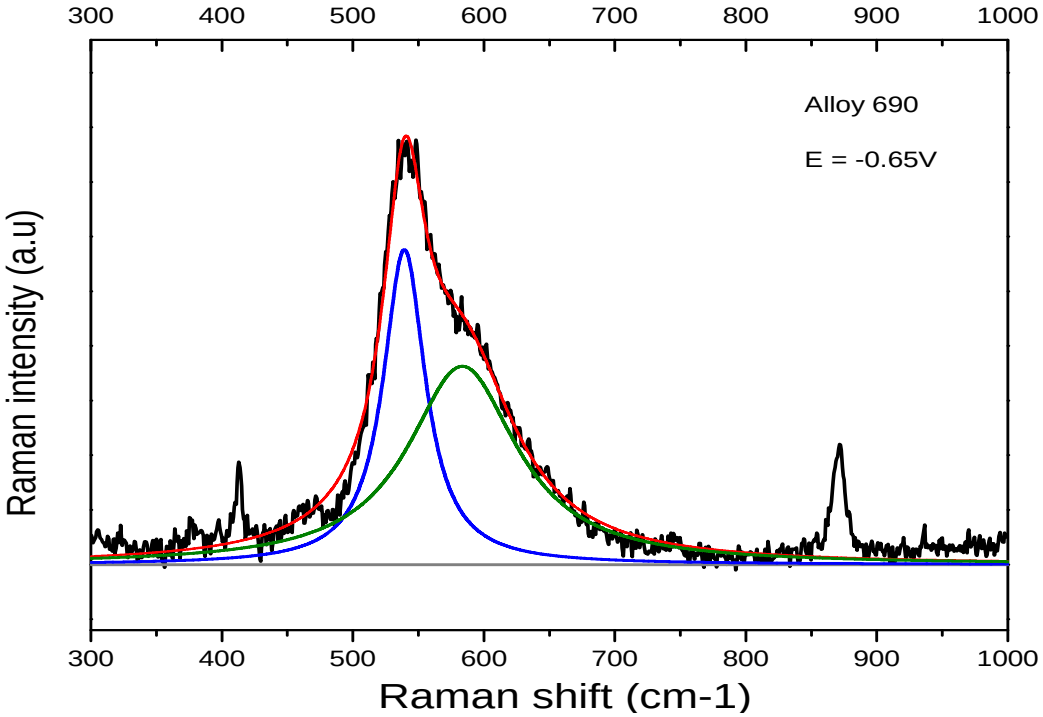

Figure 4-15b. SERS Result for Alloy 690 at E = -0.65V
(After Background Subtraction and Peak Fitting)

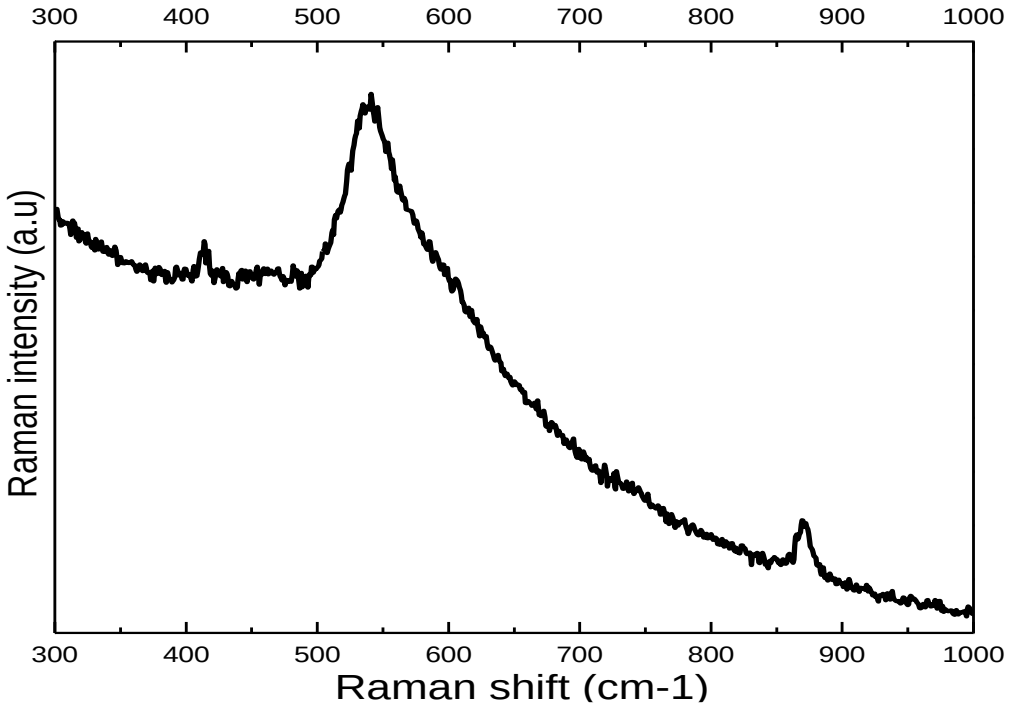

Figure 4-16a. SERS Spectrum measured for Alloy 690 at E = -0.6V

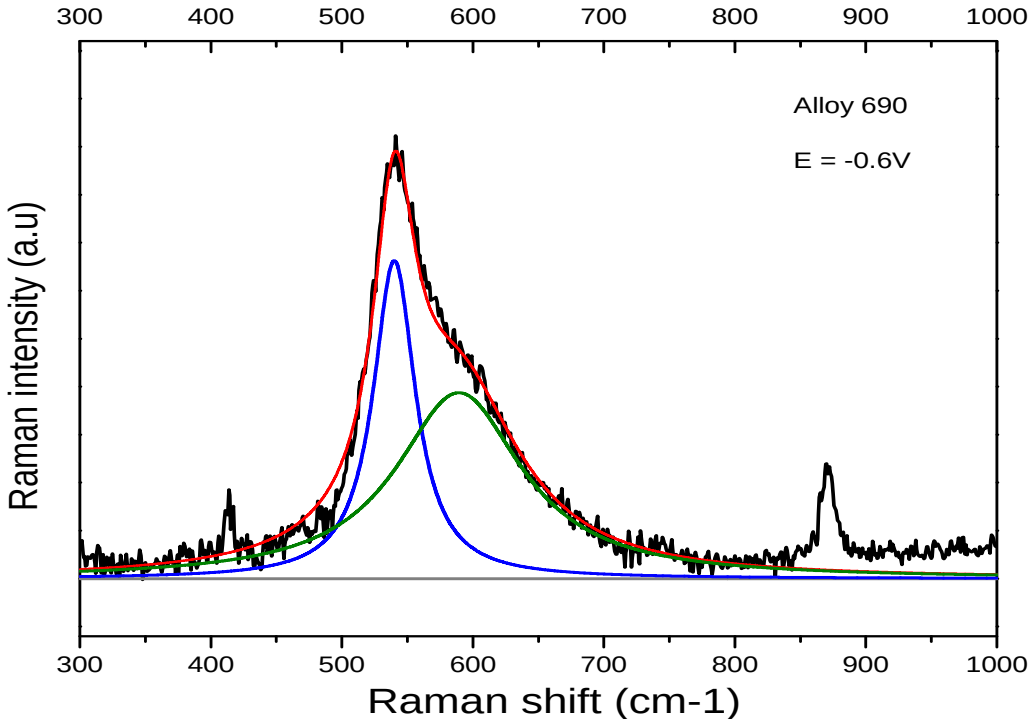

Figure 4-16b. SERS Result for Alloy 690 at E = -0.6V
(After Background Subtraction and Peak Fitting)

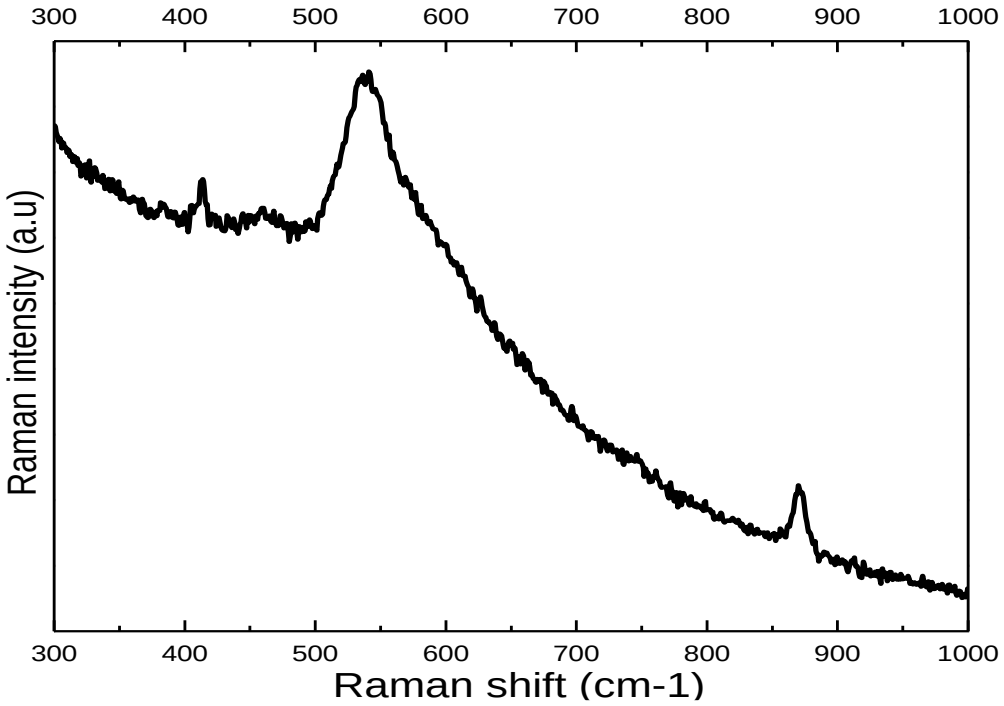

Figure 4-17a. SERS Spectrum measured for Alloy 690 at E = -0.55V

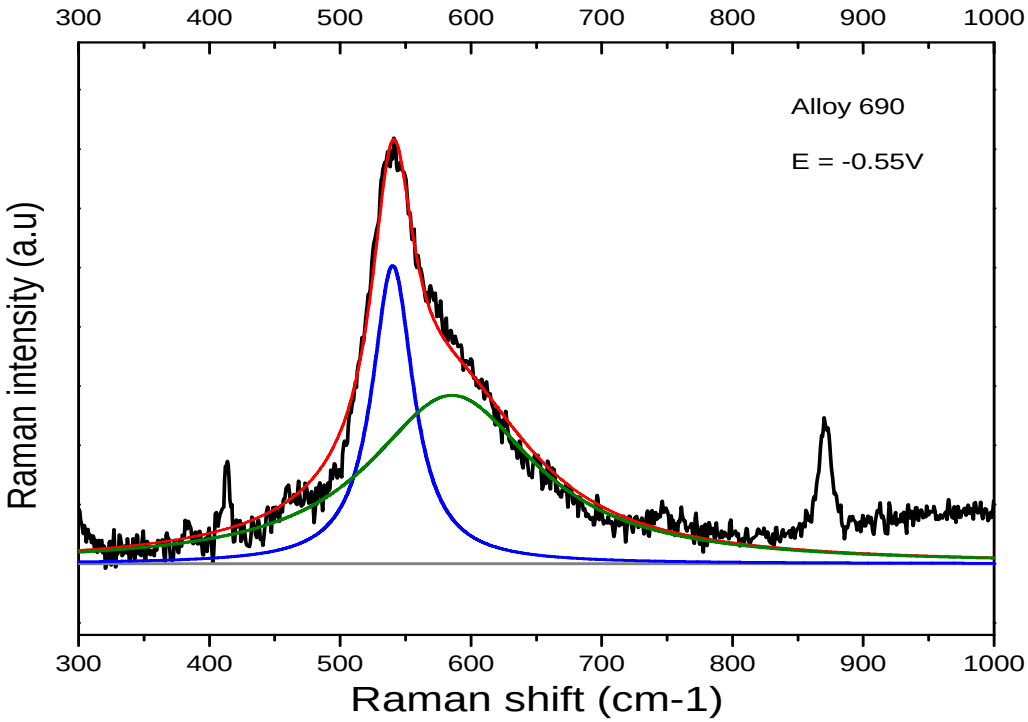

Figure 4-17b. SERS Result for Alloy 690 at E = -0.55V
(After Background Subtraction and Peak Fitting)

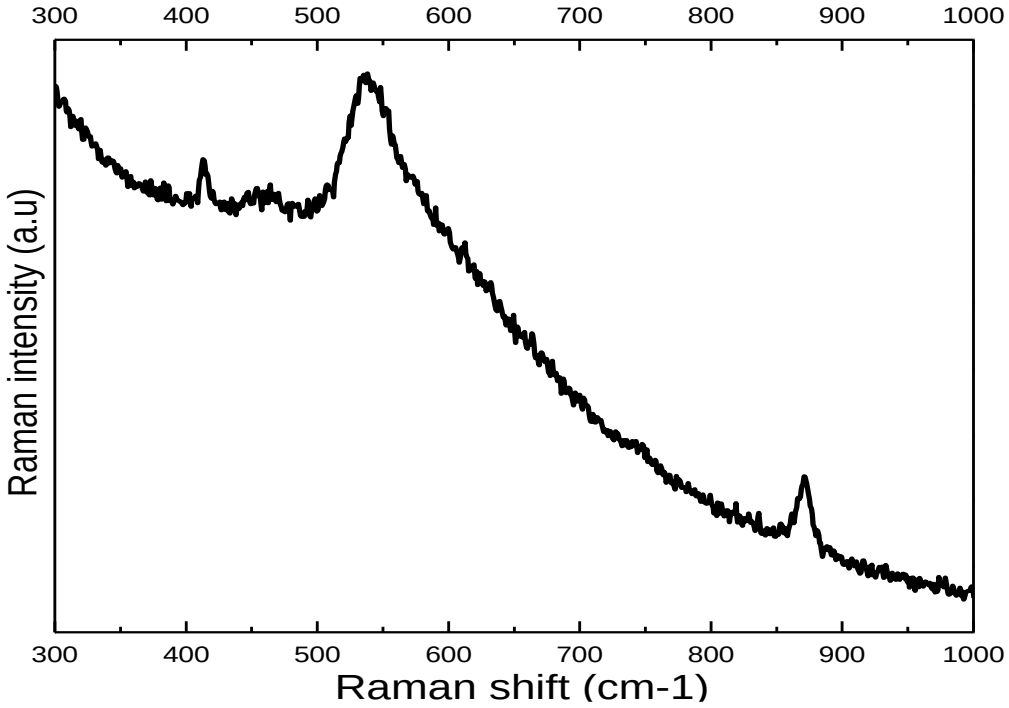

Figure 4-18a. SERS Spectrum measured for Alloy 690 at E = -0.5V

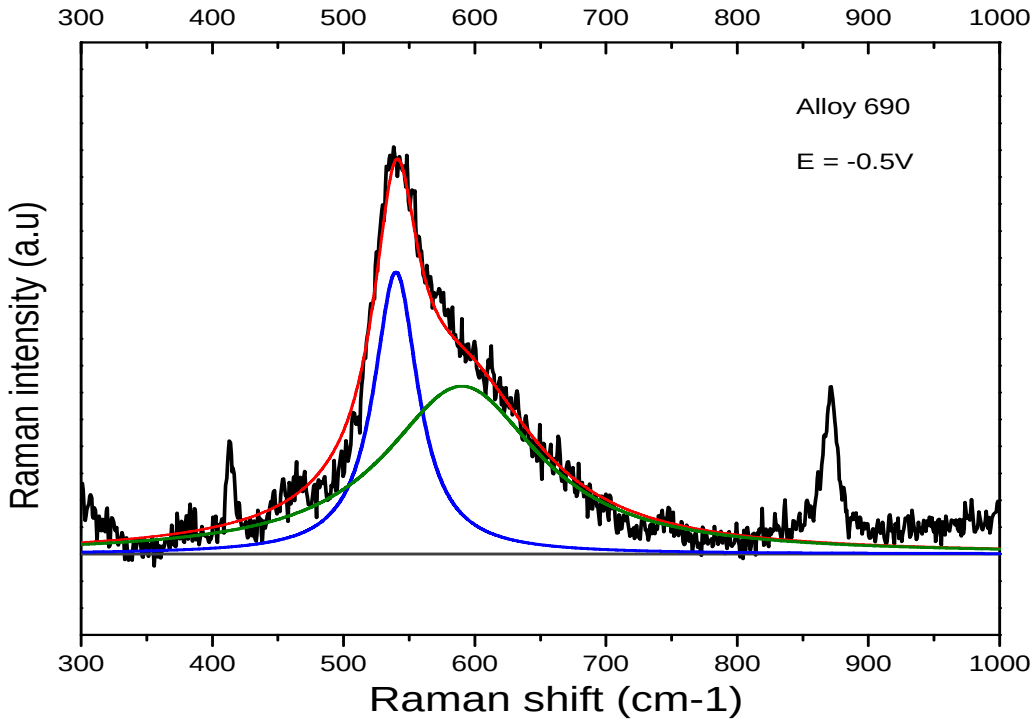

Figure 4-18b. SERS Result for Alloy 690 at E = -0.5V
(After Background Subtraction and Peak Fitting)

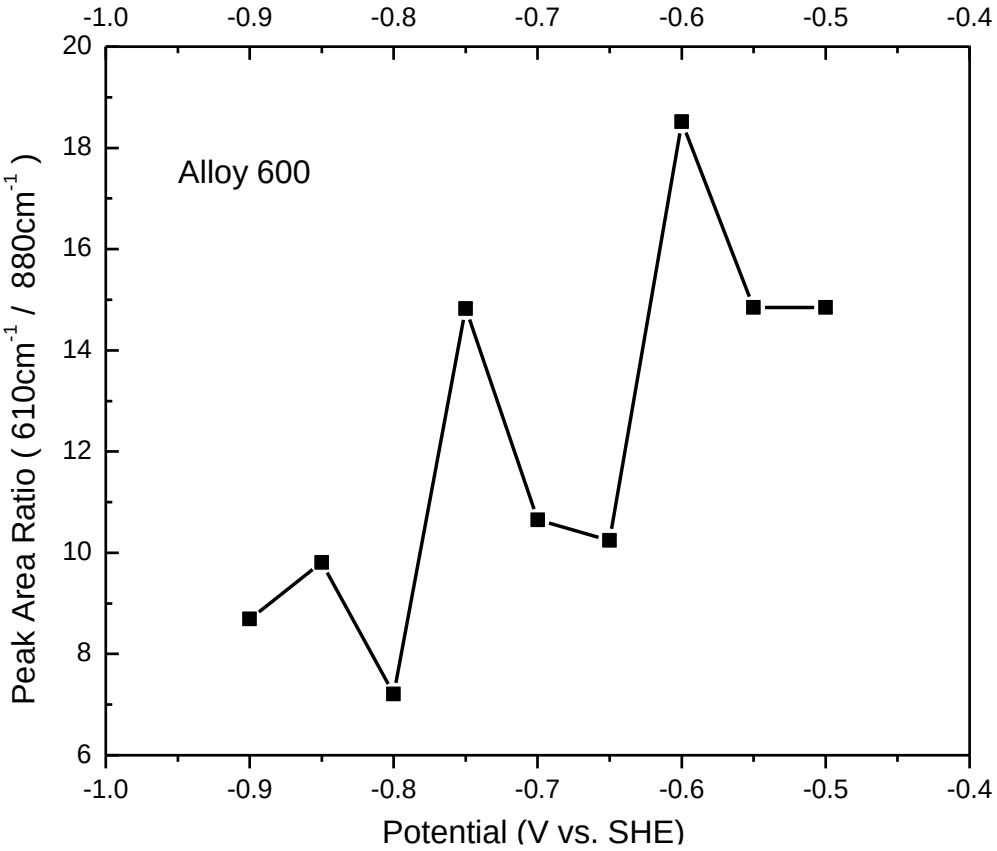

Figure 5-1. The integrated intensity ratio of 610 cm^{-1}/ 880 cm^{-1} for Alloy 600 as a function of applied potential

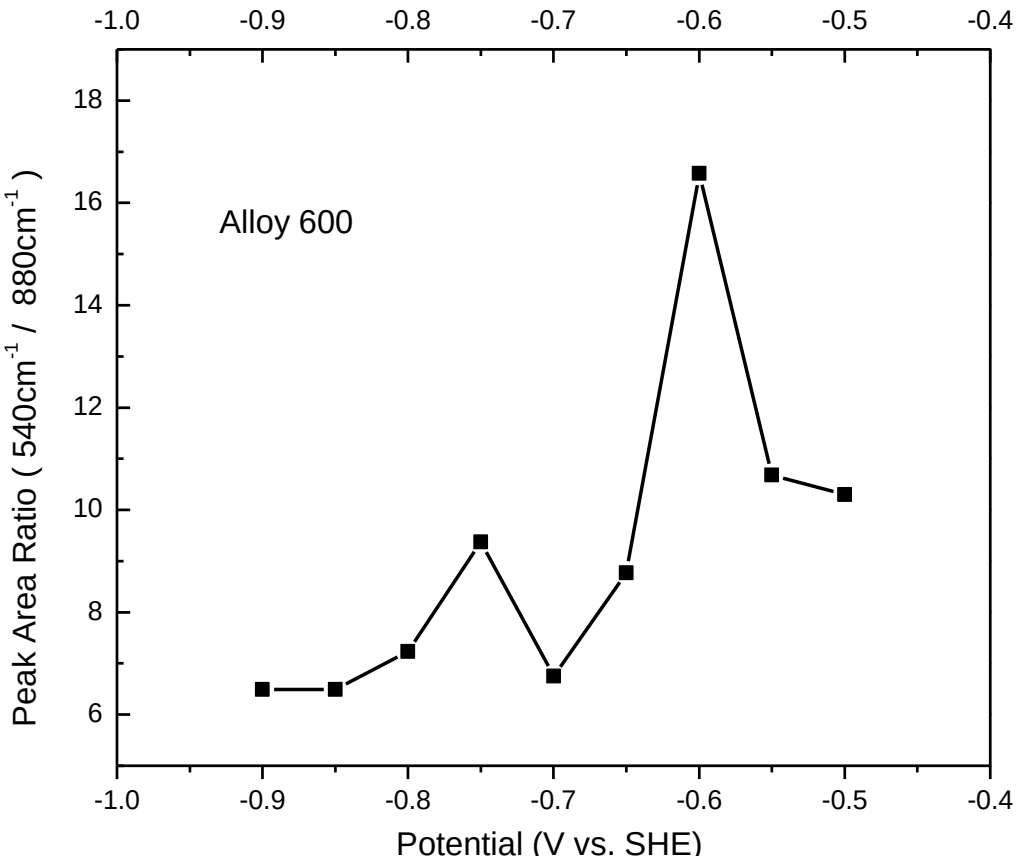

Figure 5-2. The integrated intensity ratio of 540 cm^{-1}/ 880 cm^{-1} for Alloy 600 as a function of applied potential

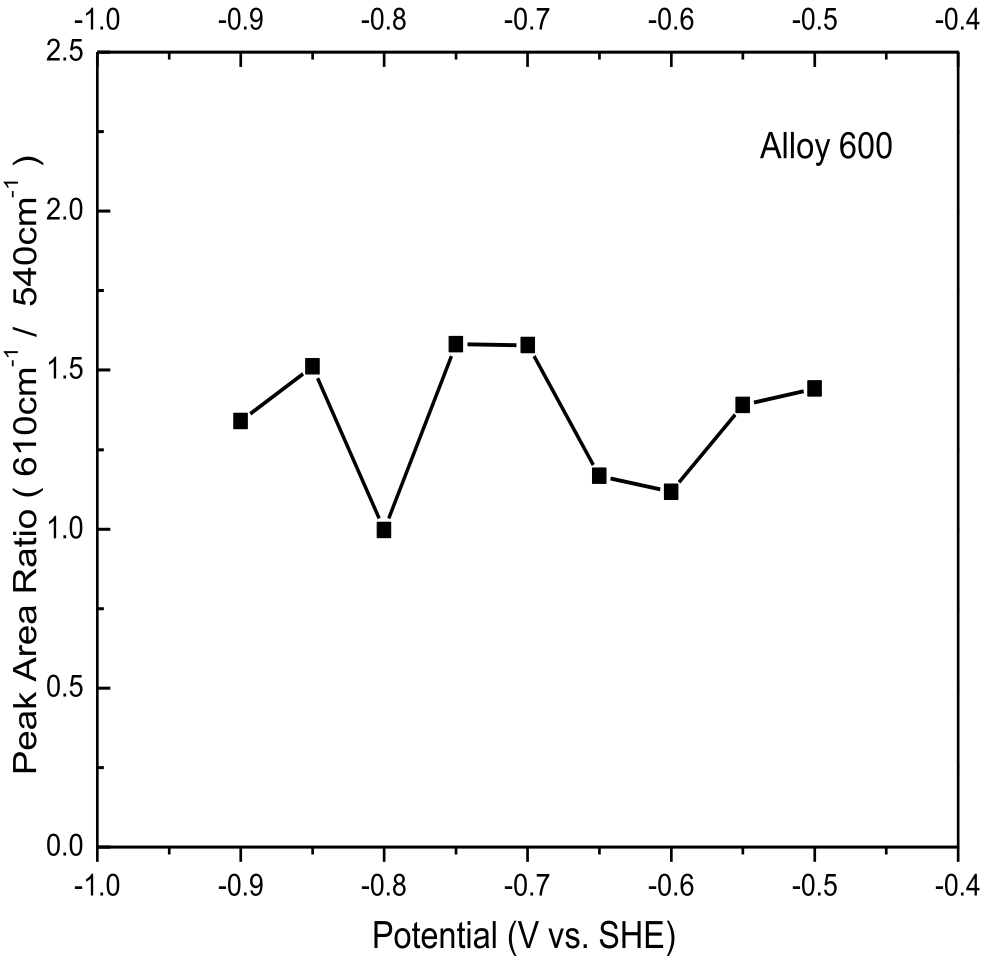

Figure 5-3. The integrated intensity ratio of 610 cm^{-1}/ 540 cm^{-1} for Alloy 600 as a function of applied potential

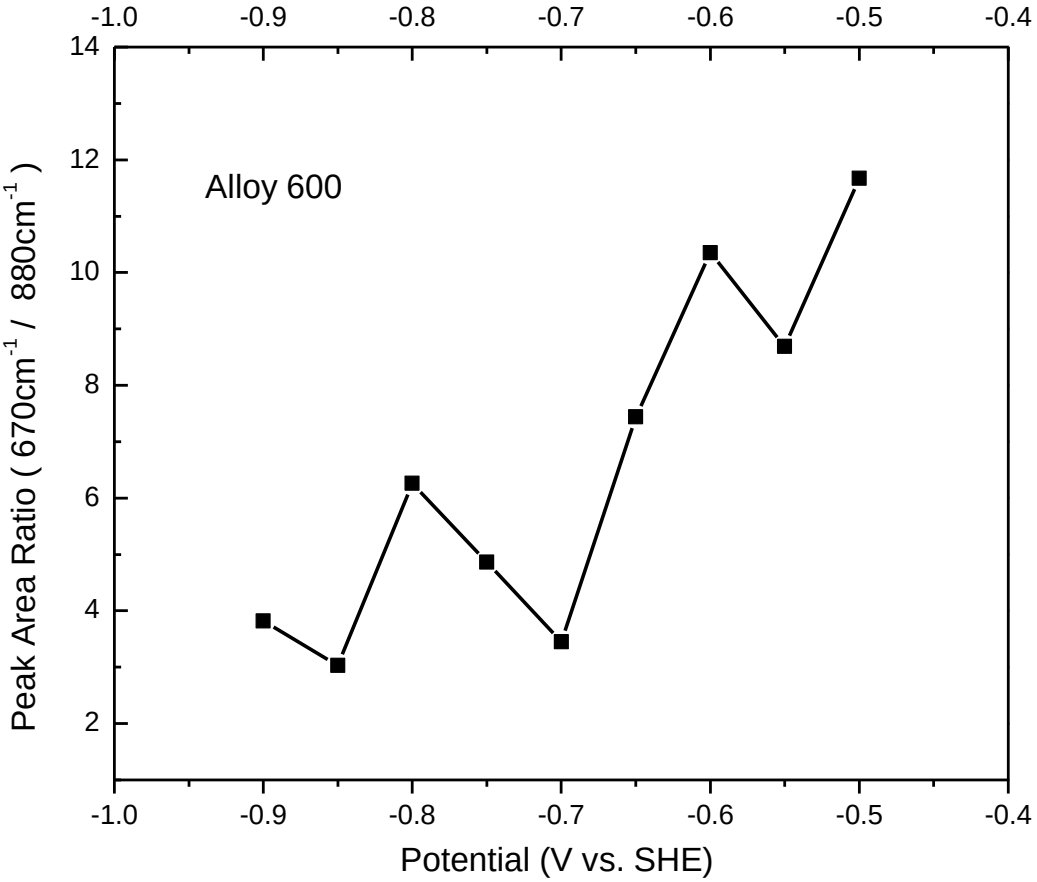

Figure 5-4. The integrated intensity ratio of 670 cm^{-1}/ 880 cm^{-1} for Alloy 600 as a function of applied potential

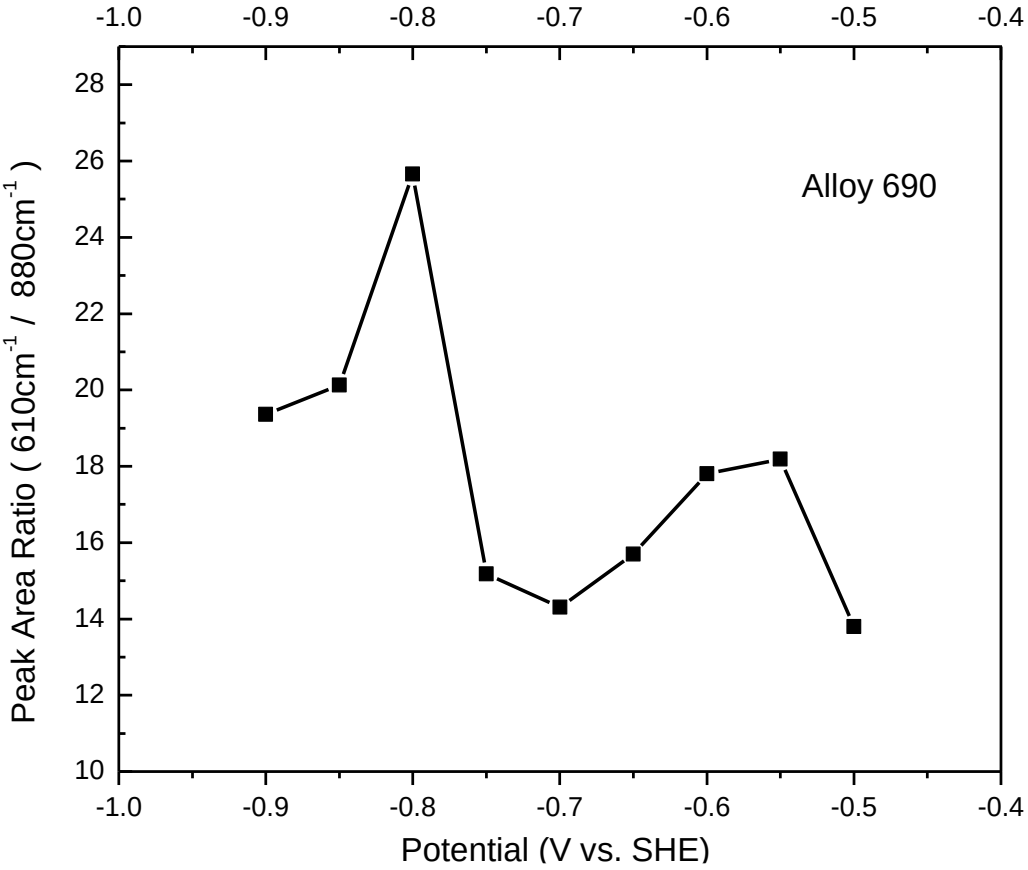

Figure 5-5. The integrated intensity ratio of 610 cm^{-1}/ 880 cm^{-1} for Alloy 690 as a function of applied potential

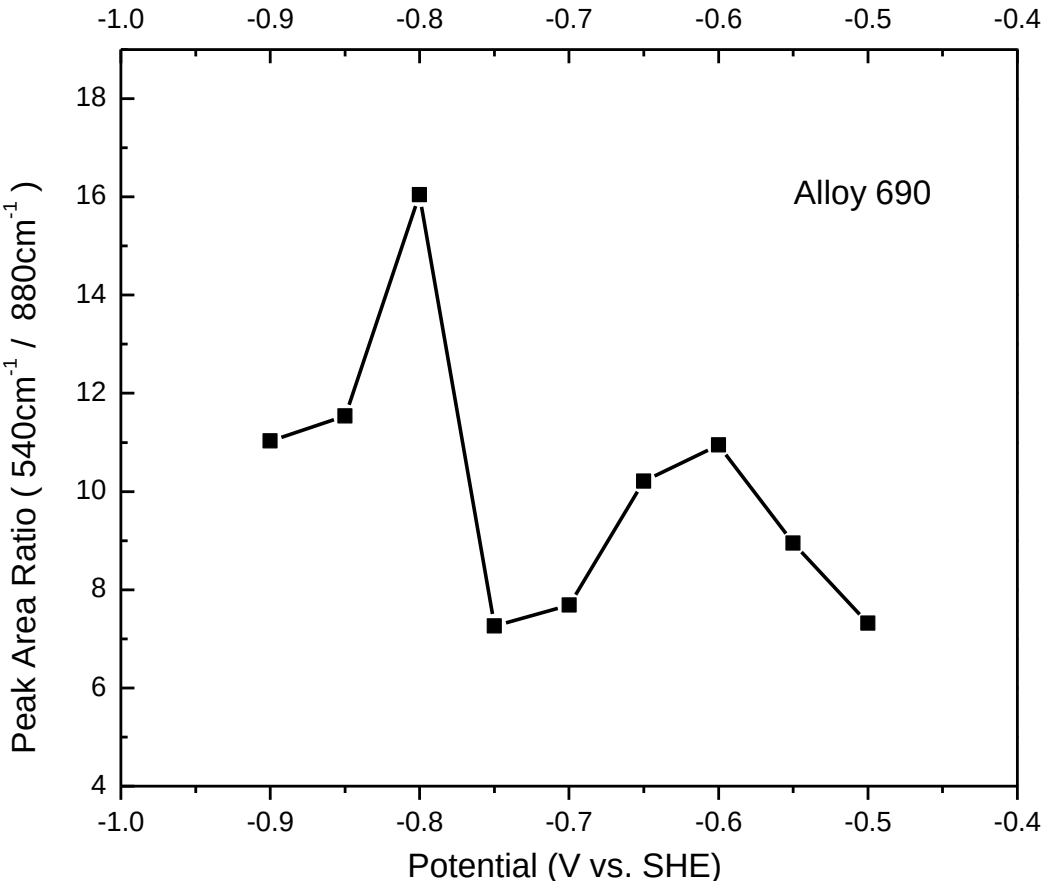

Figure 5-6. The integrated intensity ratio of 540 cm^{-1}/ 880 cm^{-1} for Alloy 690 as a function of applied potential

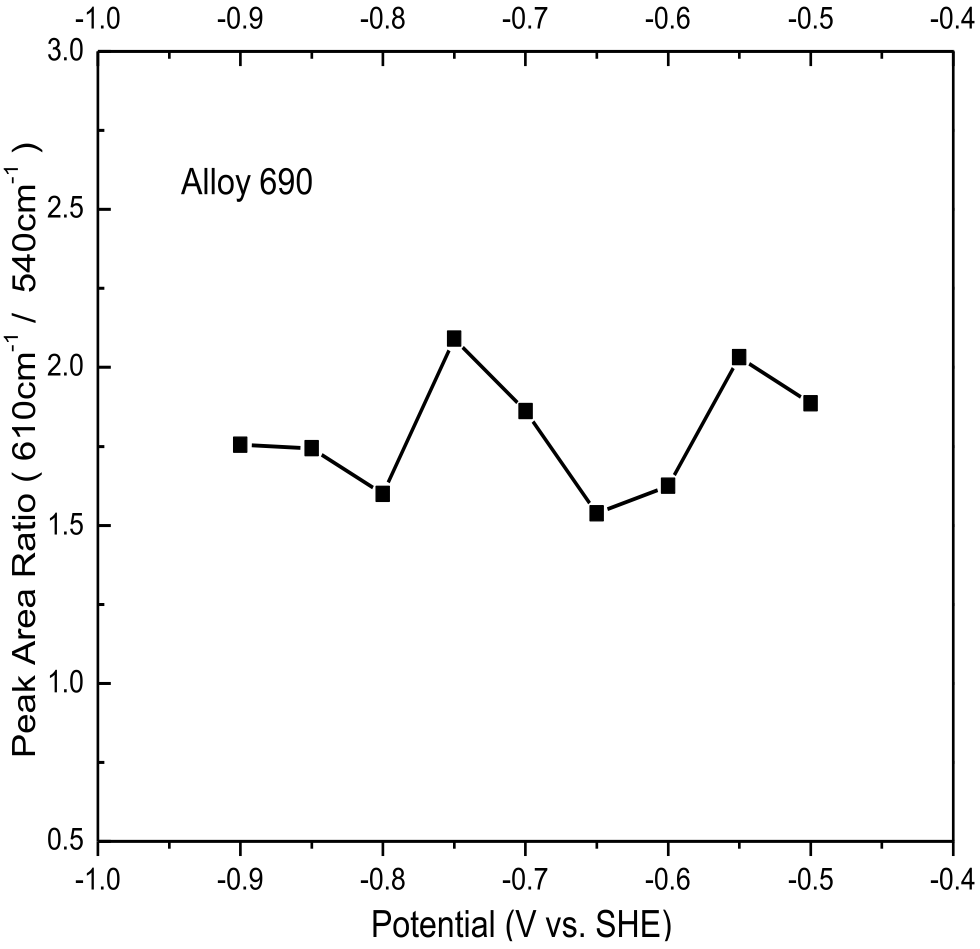

Figure 5-7. The integrated intensity ratio of 610 cm^{-1}/ 540 cm^{-1} for Alloy 690 as a function of applied potential

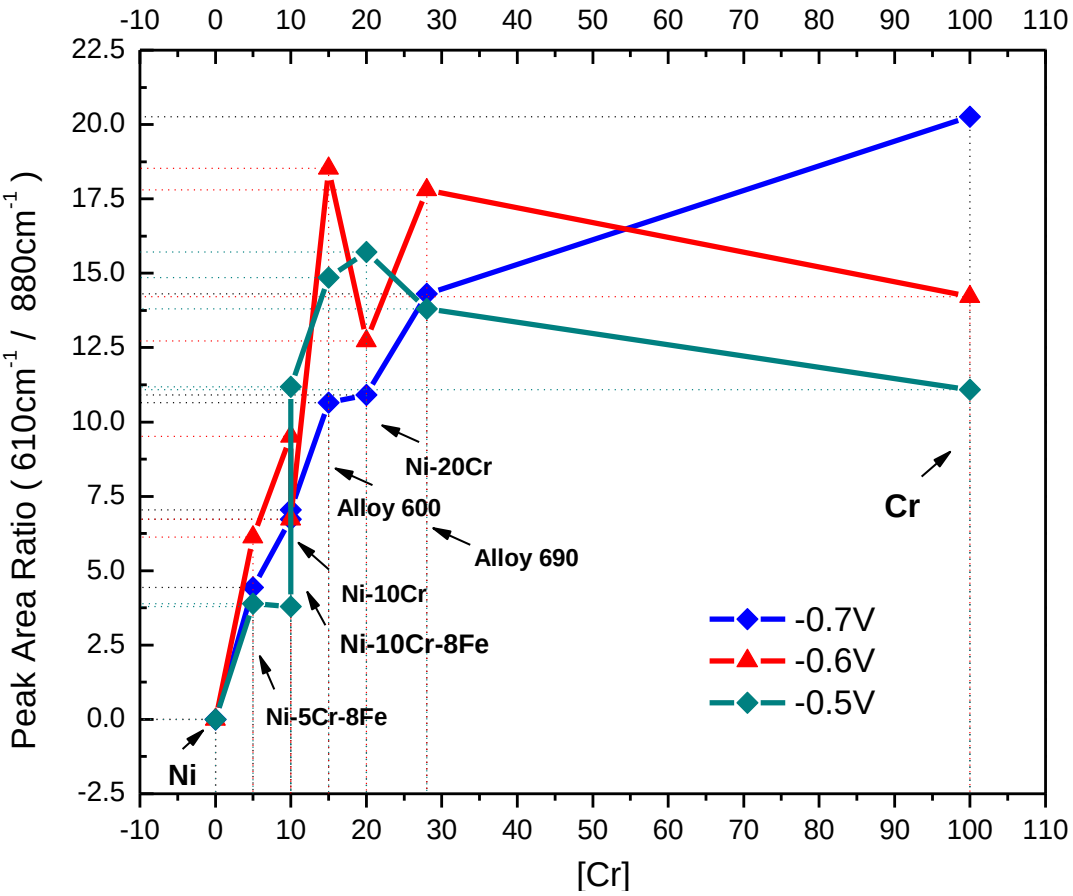

Figure 5-8. The integrated intensity ratio of 610 cm^{-1}/ 880 cm^{-1} as a function of chromium composition

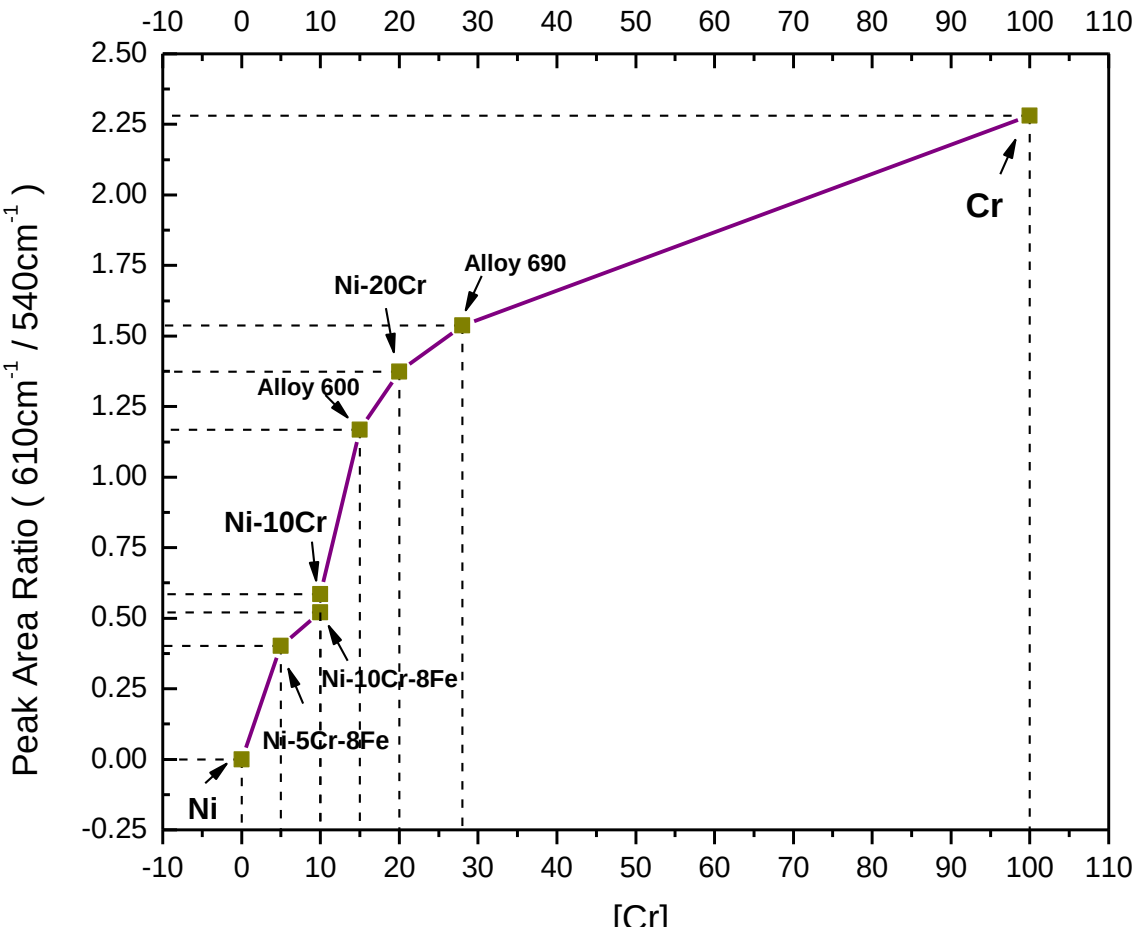

Figure 5-9. The integrated intensity ratio of 610 cm^{-1}/ 540 cm^{-1} as a function of chromium composition

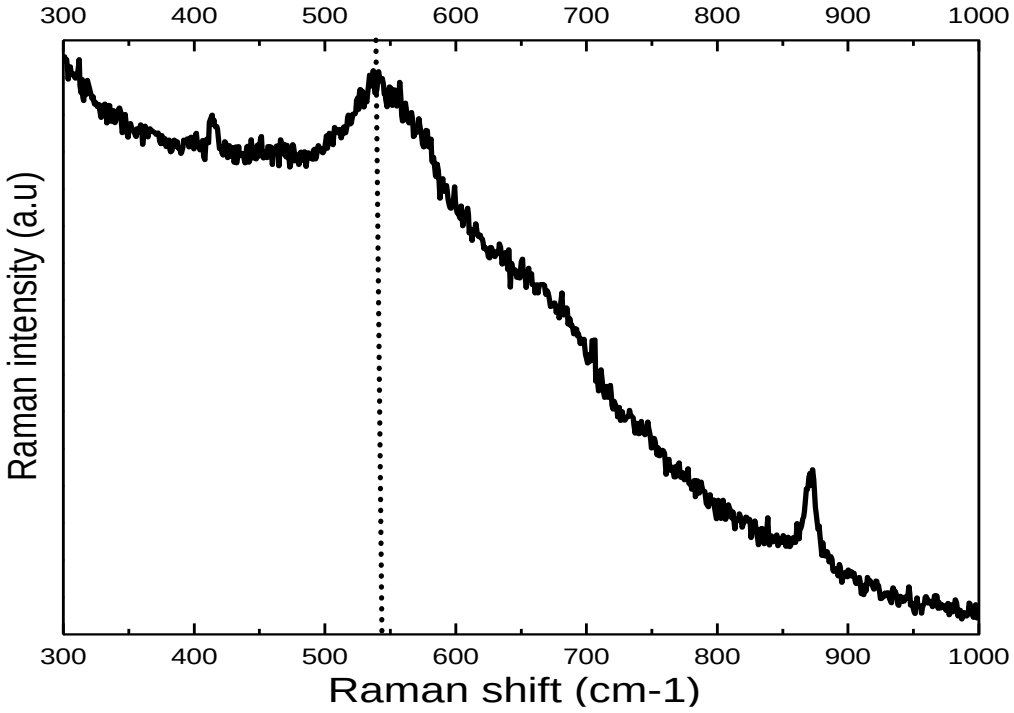

Figure 6-1. SERS result for Alloy 600 at E = -0.5V

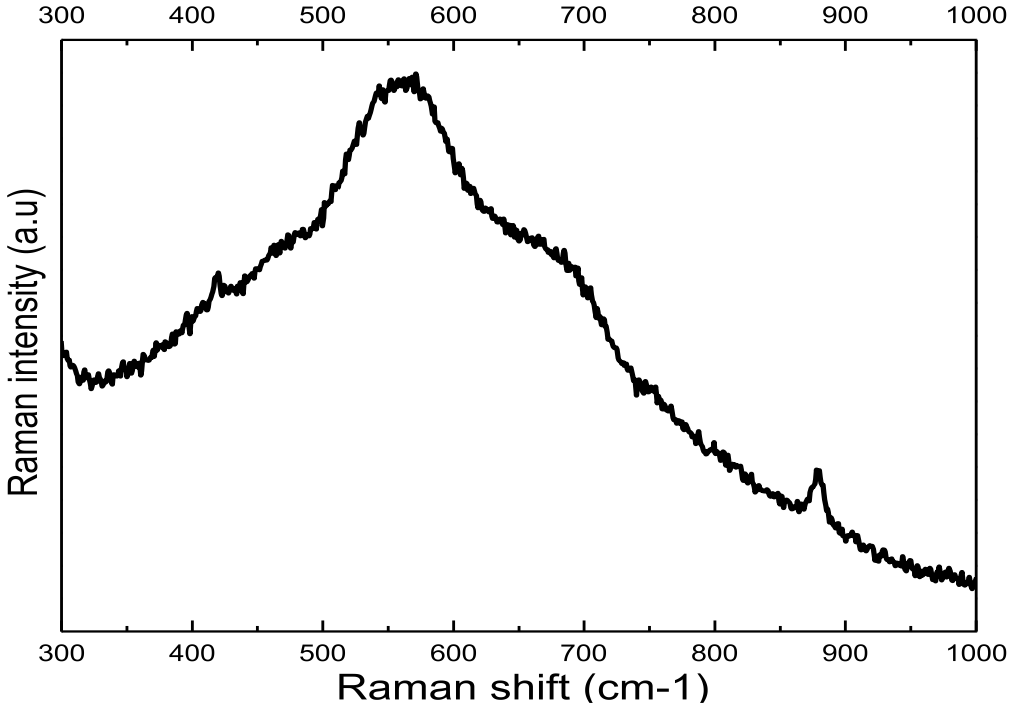

Figure 6-2. SERS result for Alloy 600; Cooling to room temperature

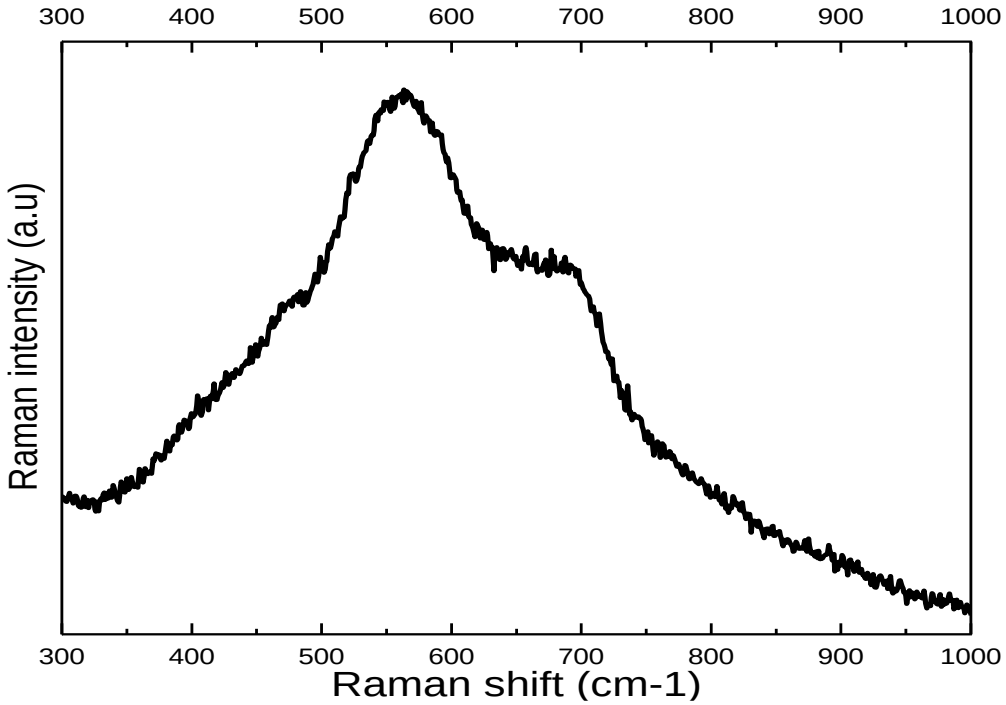

Figure 6-3. SERS result for Alloy 600; Exposed in the air for 10 min

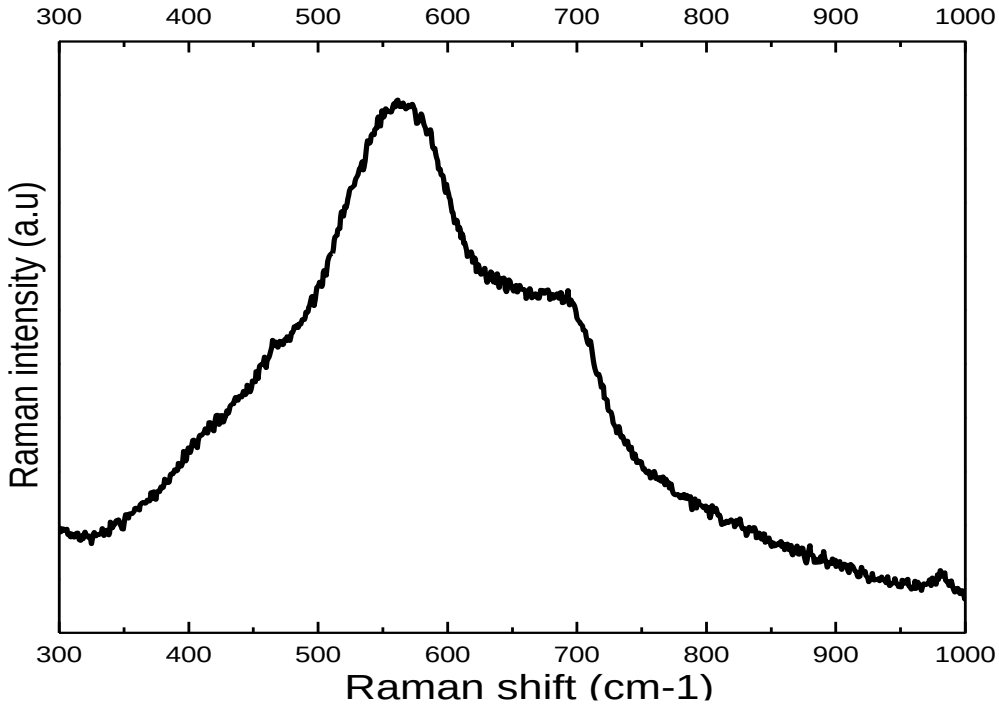

Figure 6-4. SERS result for Alloy 600; After water rinsed and dried

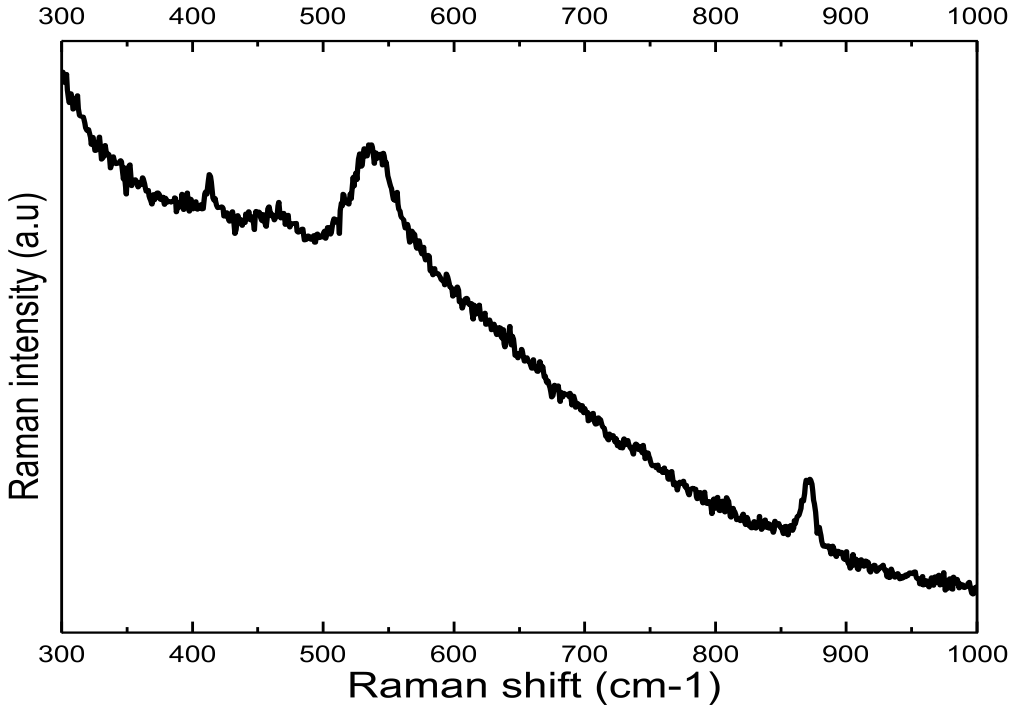

Figure 7-1. SERS result for Alloy 690 at E = -0.5V

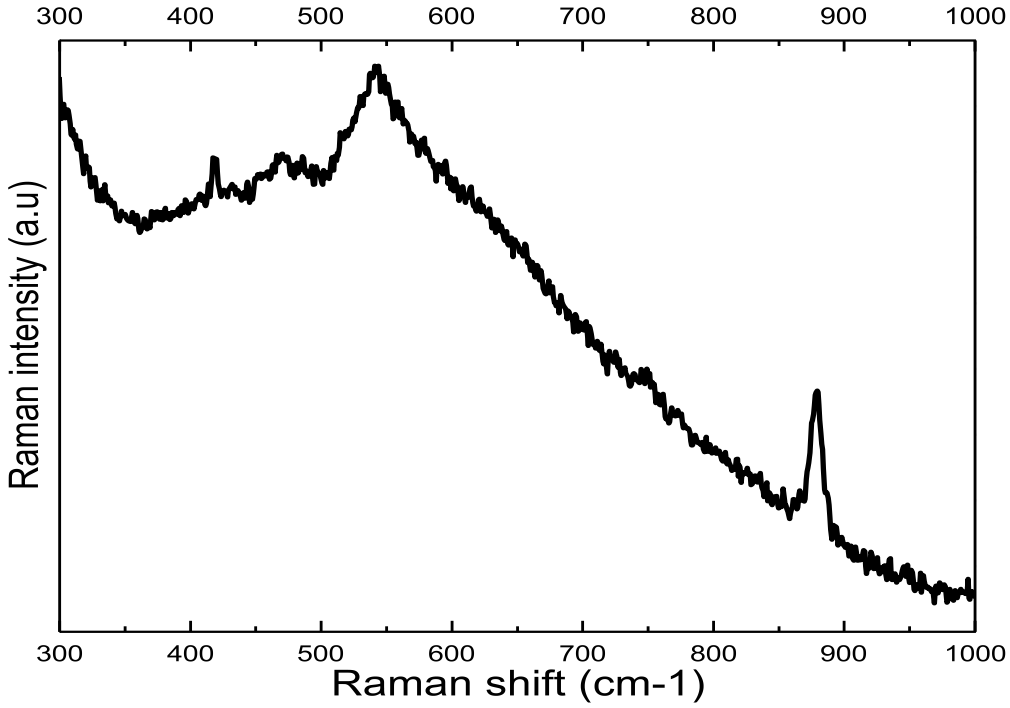

Figure 7-2. SERS result for Alloy 690; Cooling to room temperature

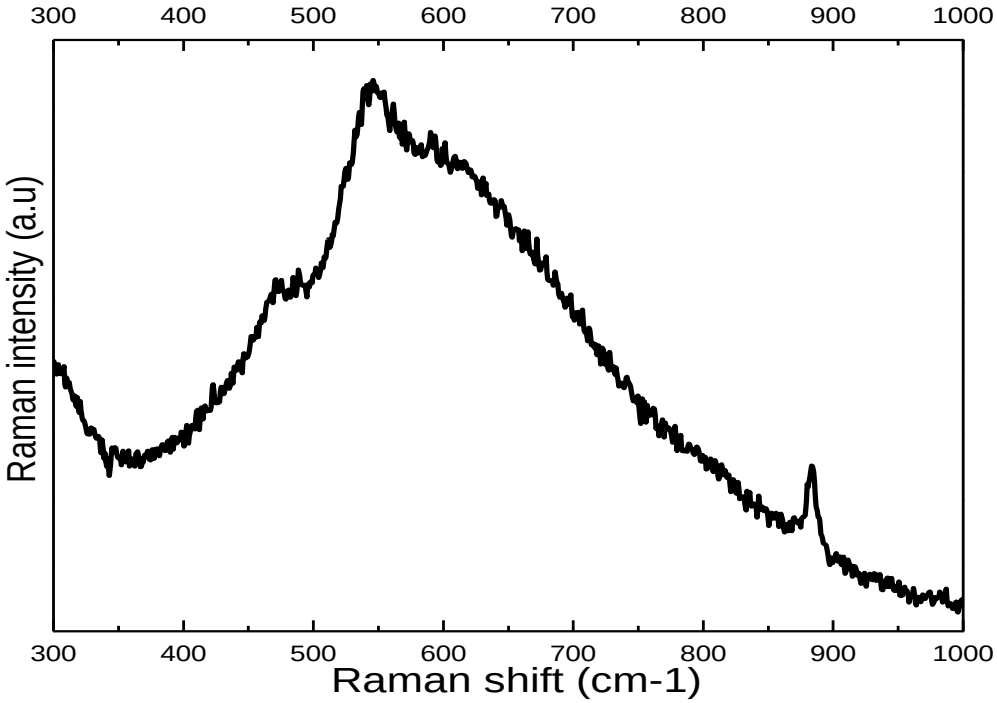

Figure 7-3. SERS result for Alloy 690; Exposed in the air for 10 min

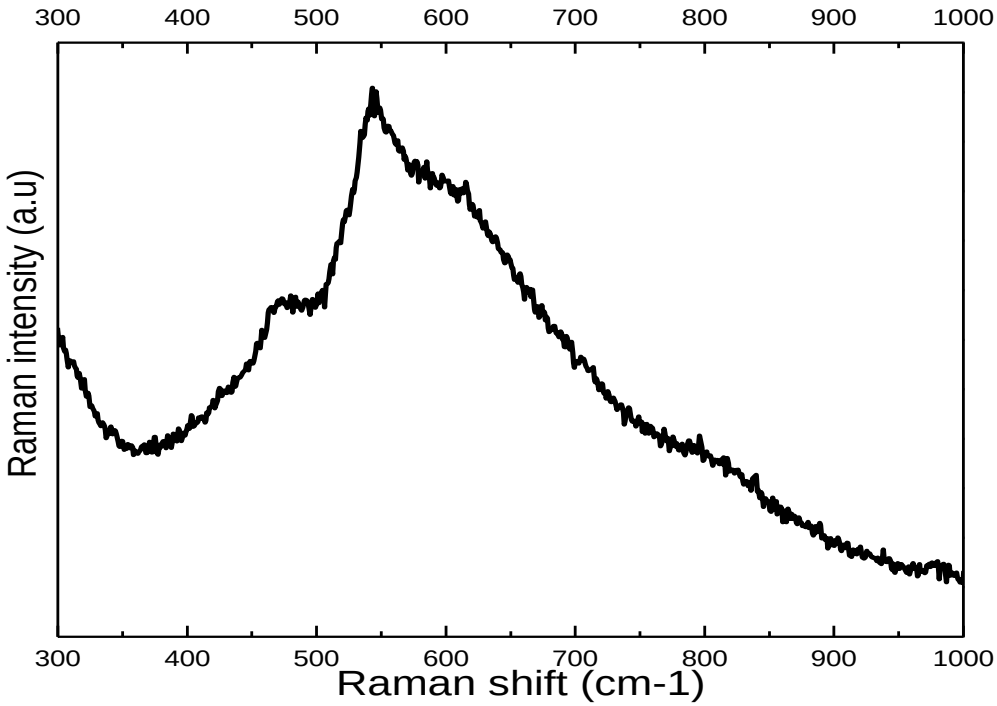

Figure 7-4. SERS result for Alloy 690; after water rinsed and dried

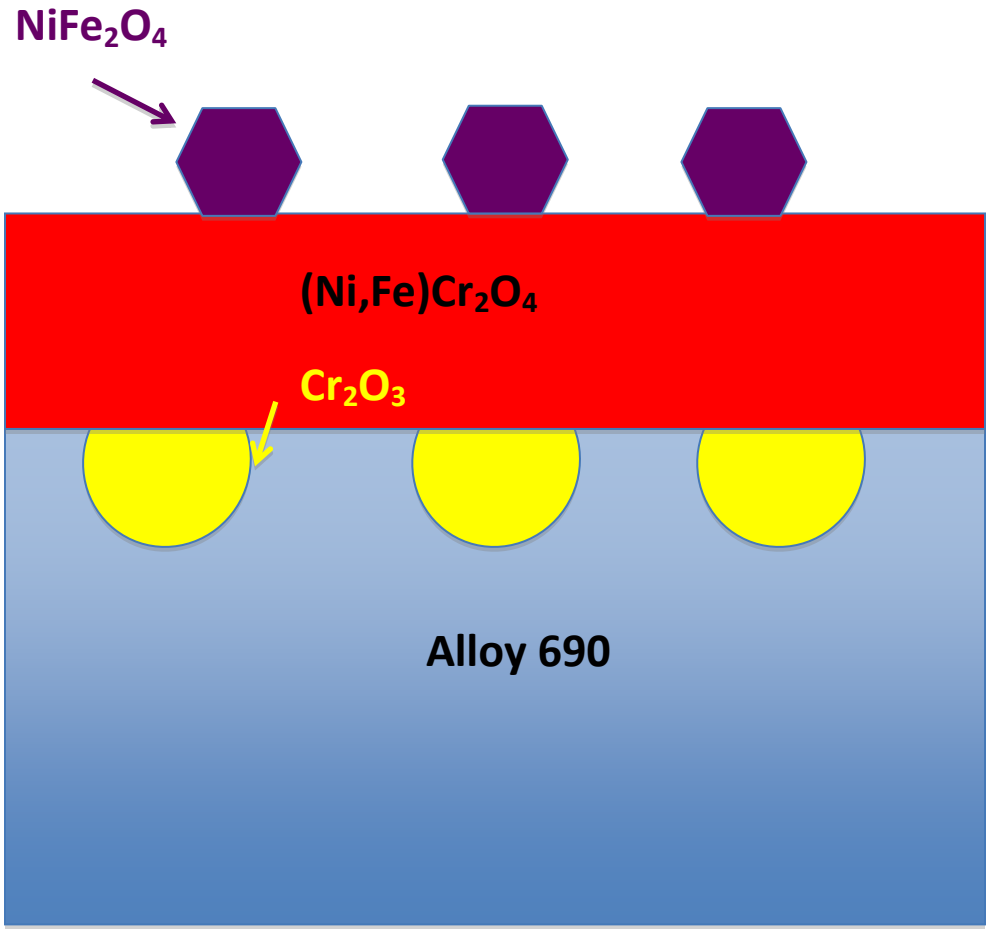

Figure 8-1. Schematic cross-section of oxide film (with discontinuous Cr_2O_3) formed on Alloy 690 in PWR primary water saturated with Ni^{++} and Fe^{+z}.

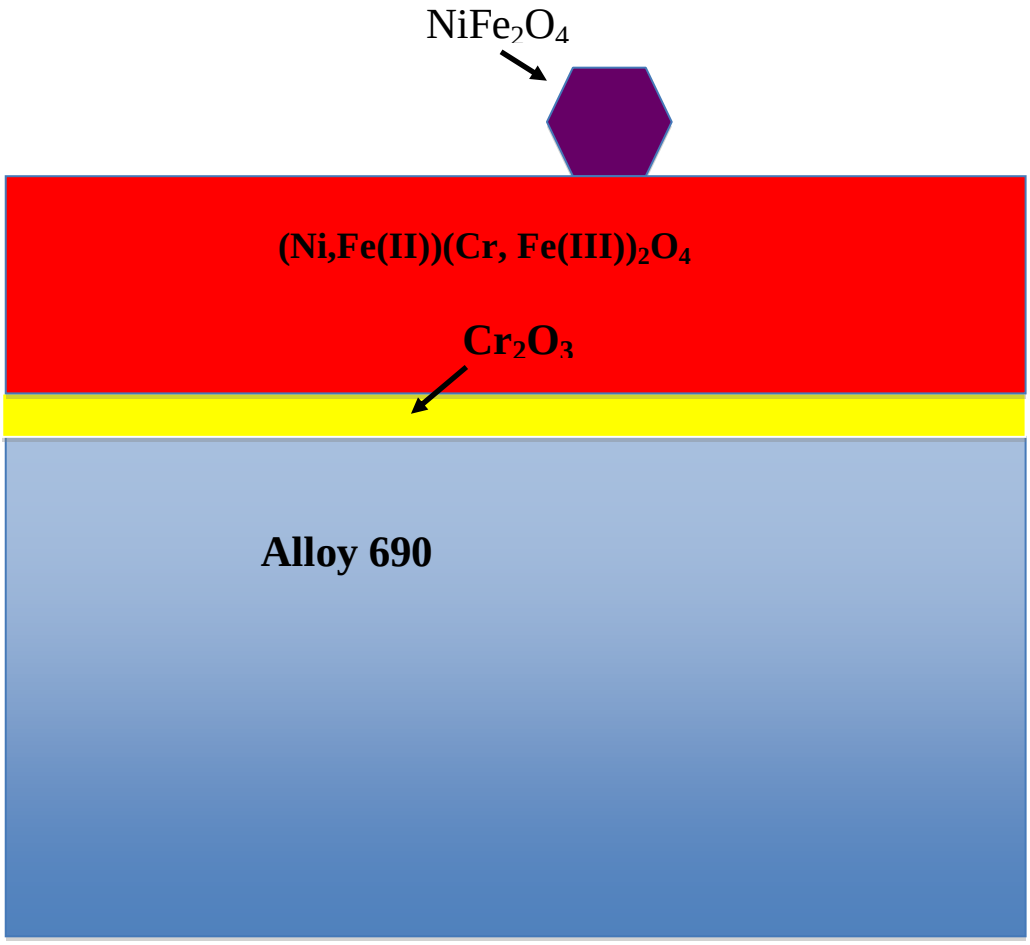

Figure 8-2. Schematic cross-section of oxide film (with continuous Cr_2O_3) formed on Alloy 690 in PWR primary water saturated with Ni^{++} and Fe^{+z}.

Appendix I. SERS spectra of Alloy 600 that were unpolarized during the heat-up from room temperature to 320 °C

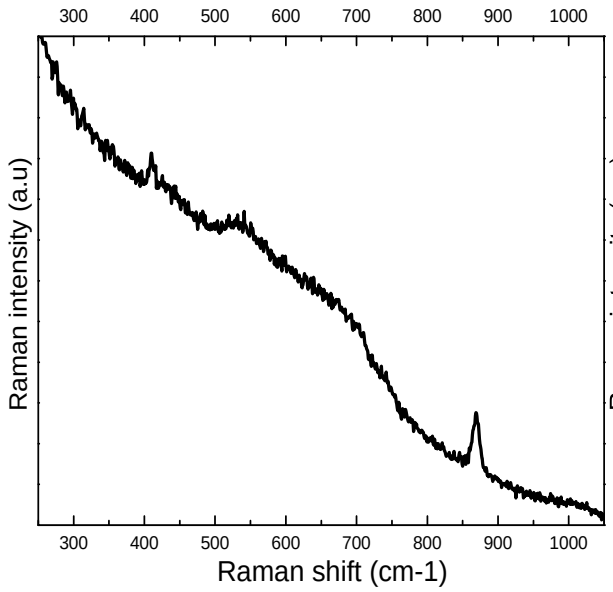

SERS Spectrum for Alloy 600
At E = -0.9V and pH=7.2

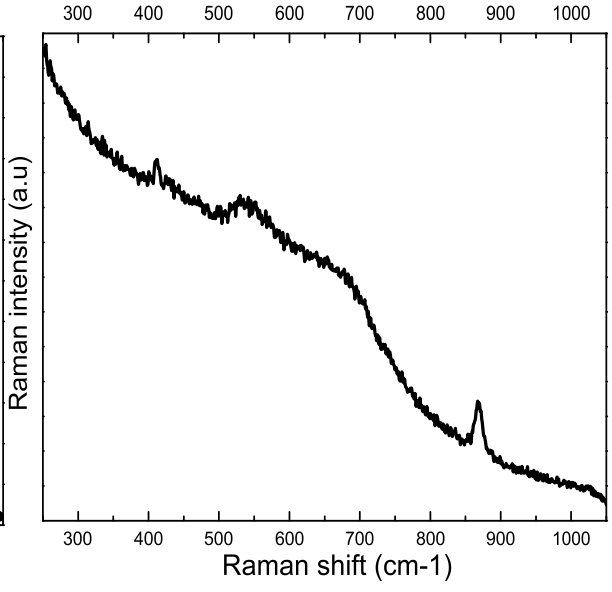

SERS Spectrum for Alloy 600
At E = -0.85V and pH=7.2

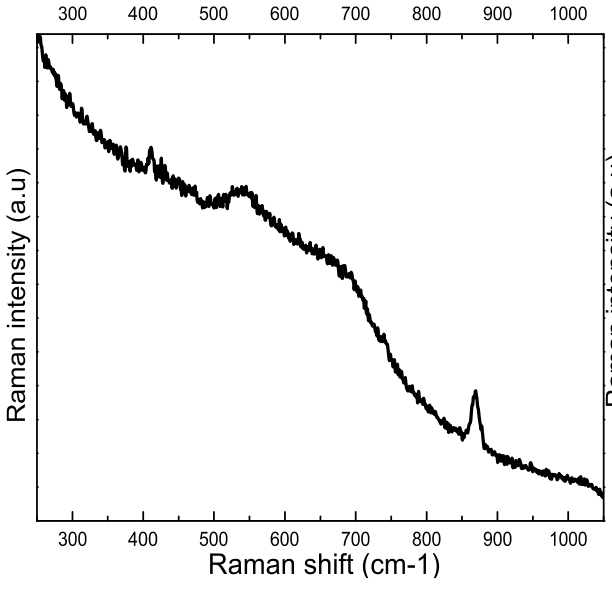

SERS Spectrum for Alloy 600
At E = -0.8V and pH=7.2

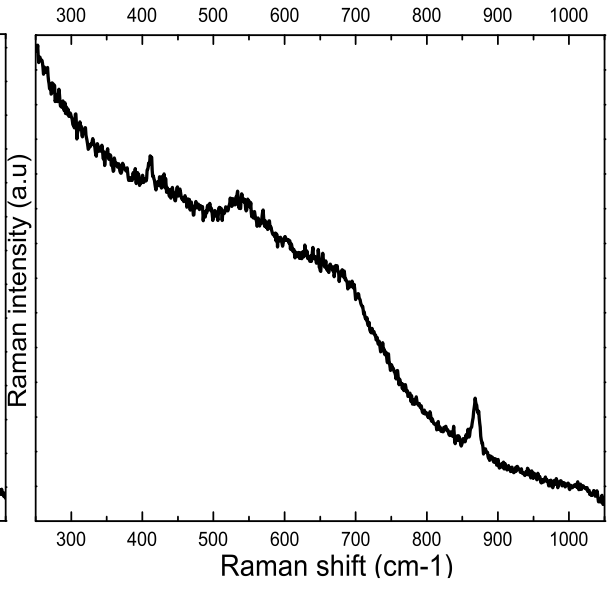

SERS Spectrum for Alloy 600
At E = -0.75V and pH=7.2

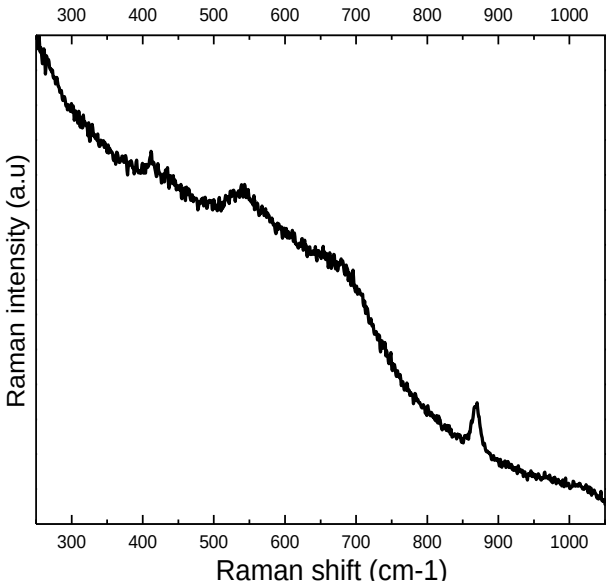

SERS Spectrum for Alloy 600
At E = -0.7V and pH=7.2

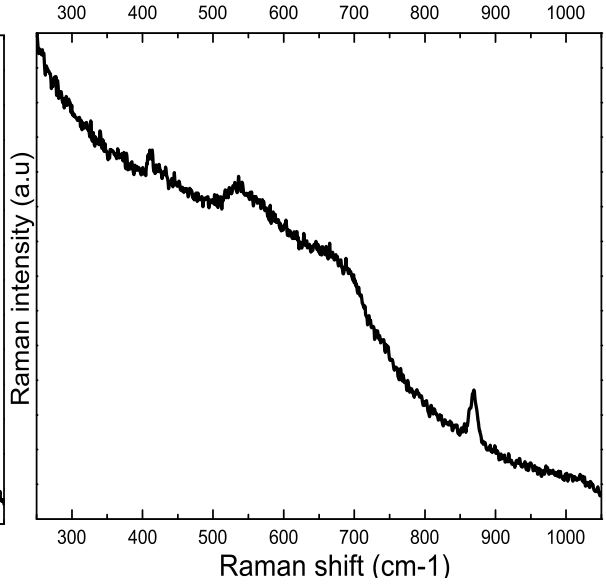

SERS Spectrum for Alloy 600
At E = -0.65V and pH=7.2

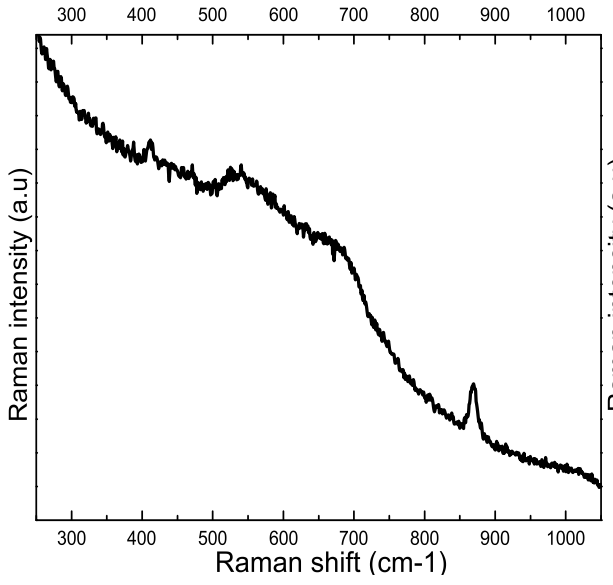

SERS Spectrum for Alloy 600
At E = -0.6V and pH=7.2

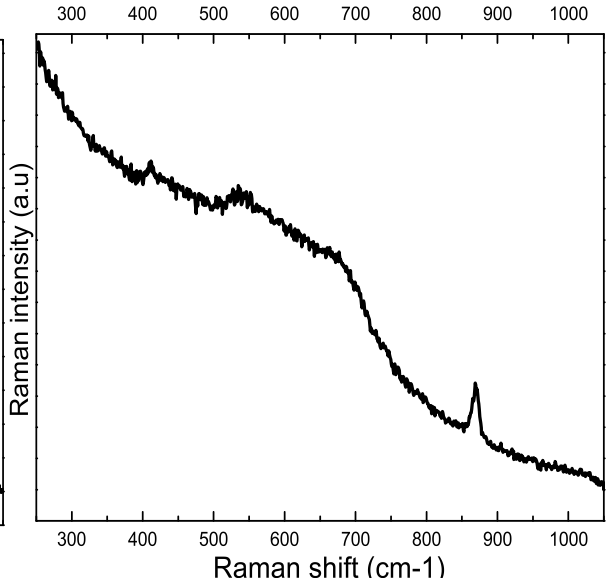

SERS Spectrum for Alloy 600
At E = -0.55V and pH=7.2

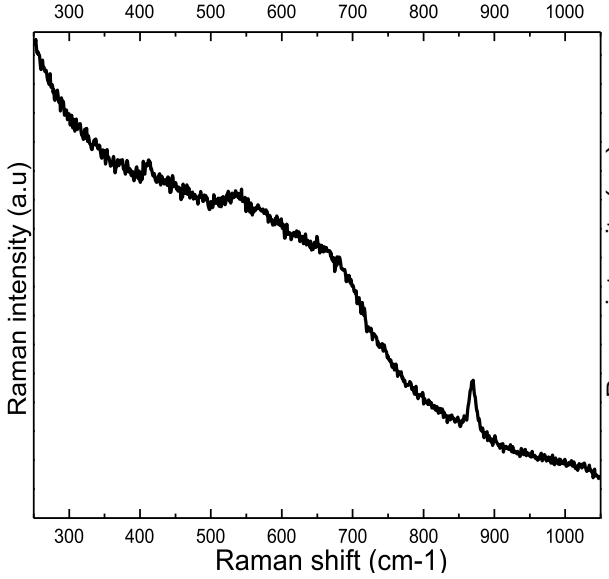

SERS Spectrum for Alloy 600
At E = -0.5V and pH=7.2

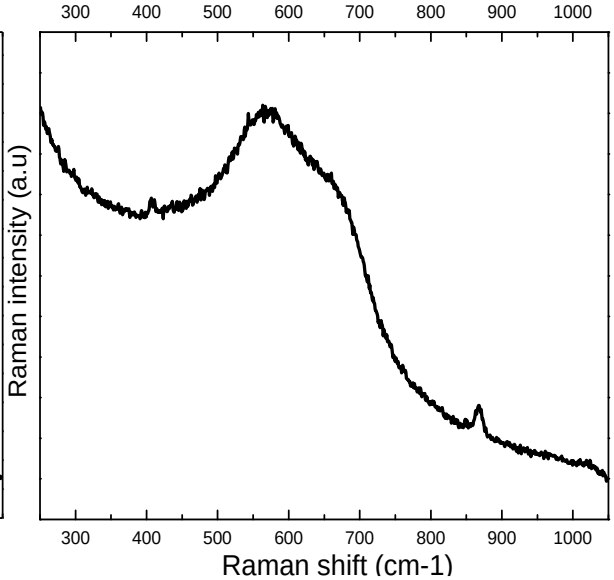

SERS Spectrum for Alloy 600
At E = -0.9V and pH=6.2

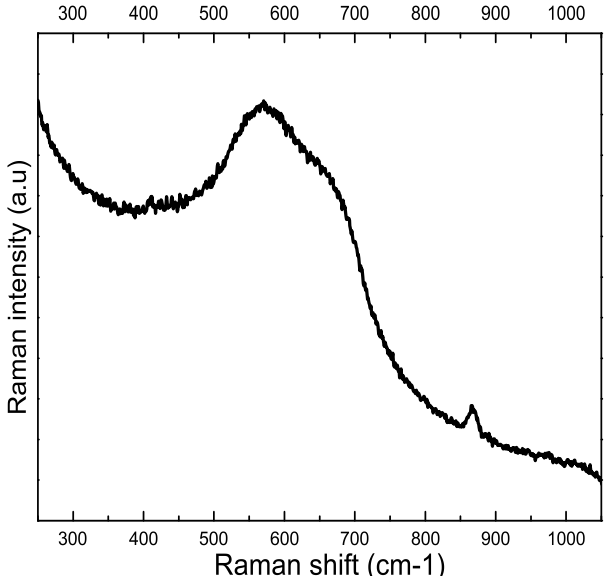

SERS Spectrum for Alloy 600
At E = -0.85V and pH=6.2

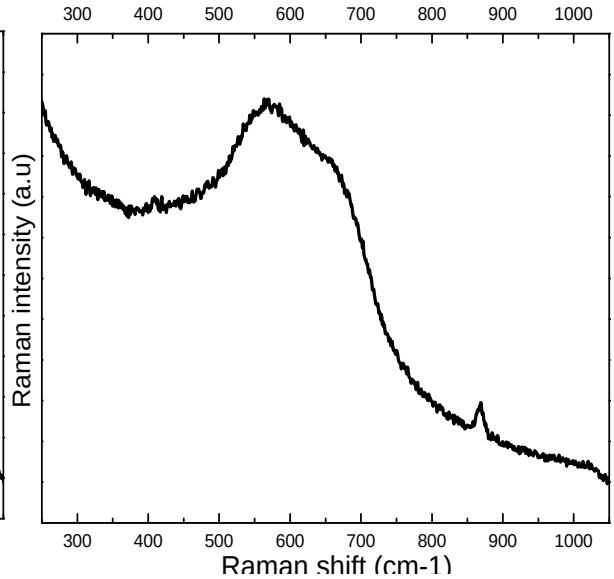

SERS Spectrum for Alloy 600
At E = -0.8V and pH=6.2

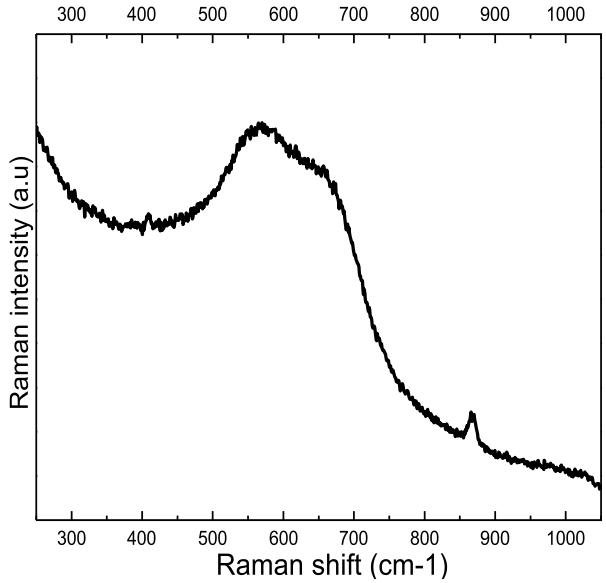

SERS Spectrum for Alloy 600
At E = -0.75V and pH=6.2

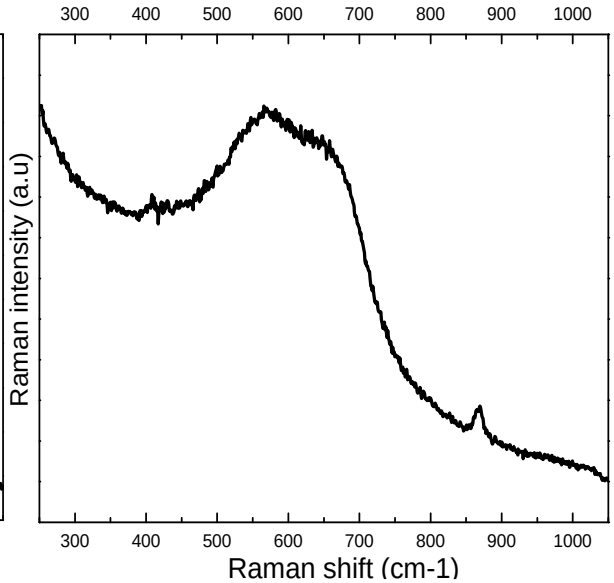

SERS Spectrum for Alloy 600
At E = -0.7V and pH=6.2

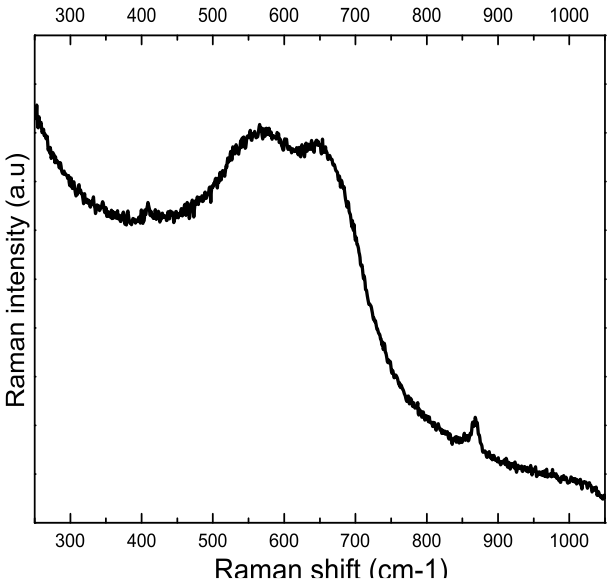

SERS Spectrum for Alloy 600
At E = -0.65V and pH=6.2

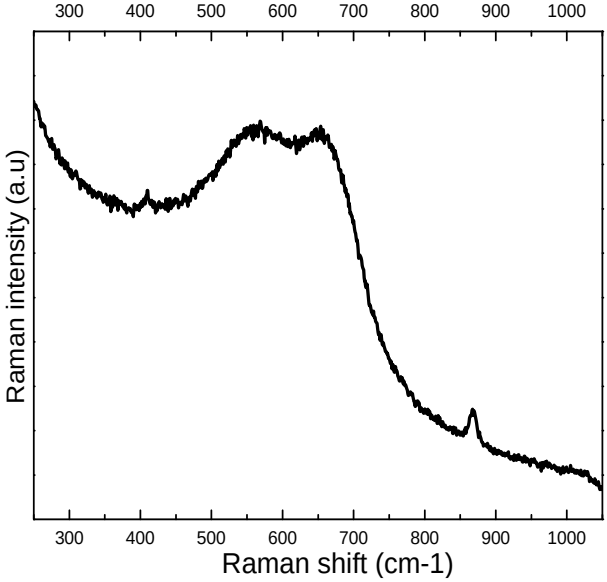

SERS Spectrum for Alloy 600
At E = -0.6V and pH=6.2

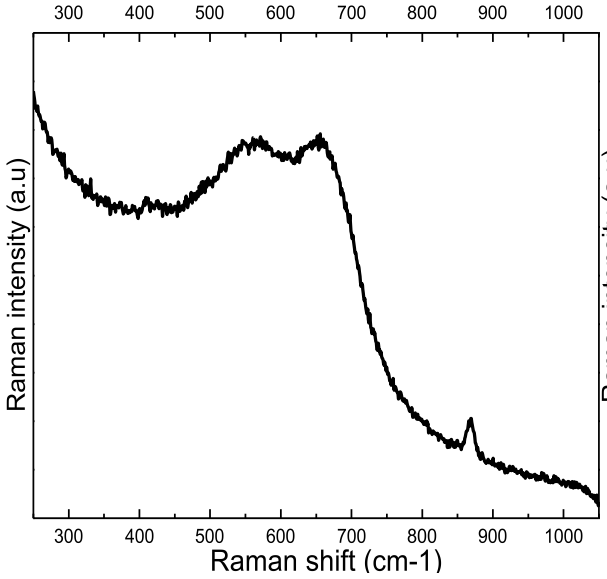

SERS Spectrum for Alloy 600
At E = -0.55V and pH=6.2

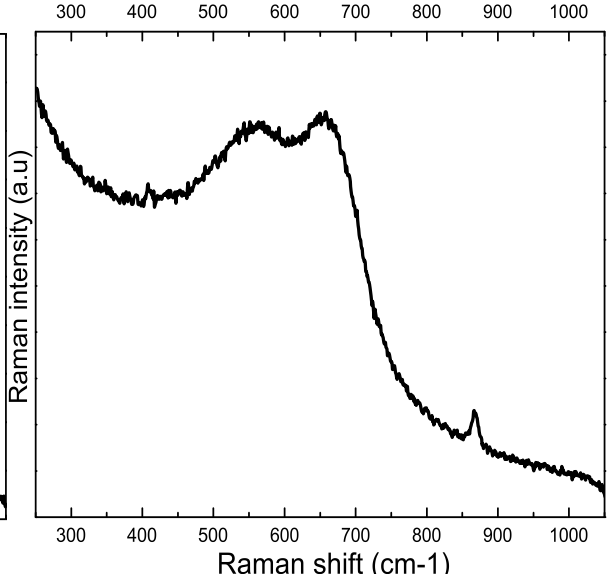

SERS Spectrum for Alloy 600
At E = -0.5V and pH=6.2

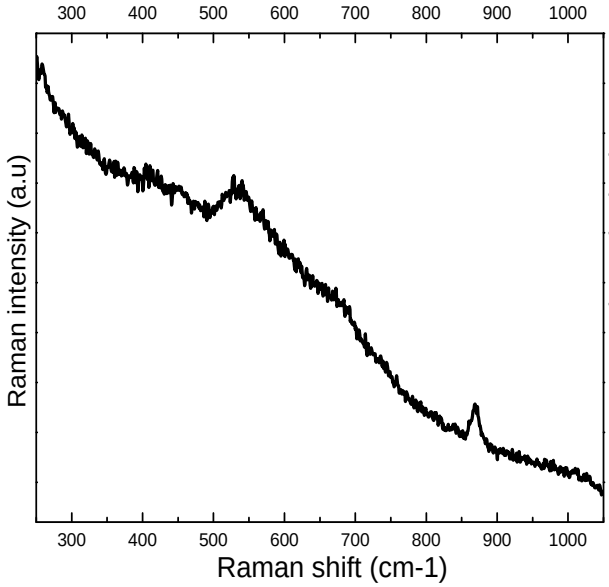

SERS Spectrum for Alloy 600
At E = -0.9V and pH=7.2

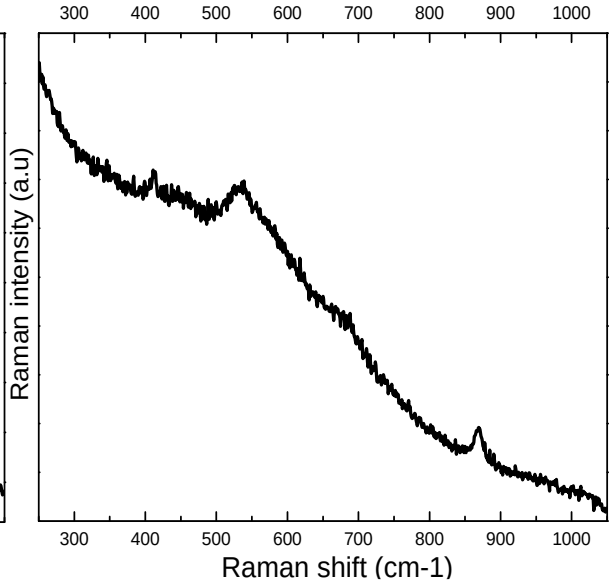

SERS Spectrum for Alloy 600
At E = -0.85V and pH=7.2

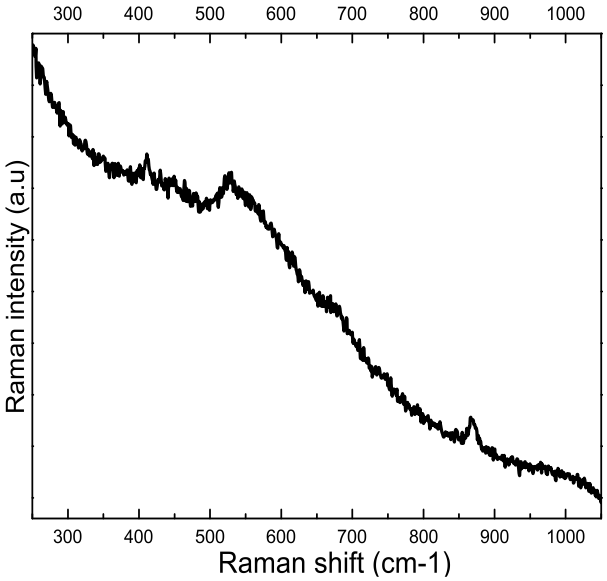

SERS Spectrum for Alloy 600
At E = -0.8V and pH=7.2

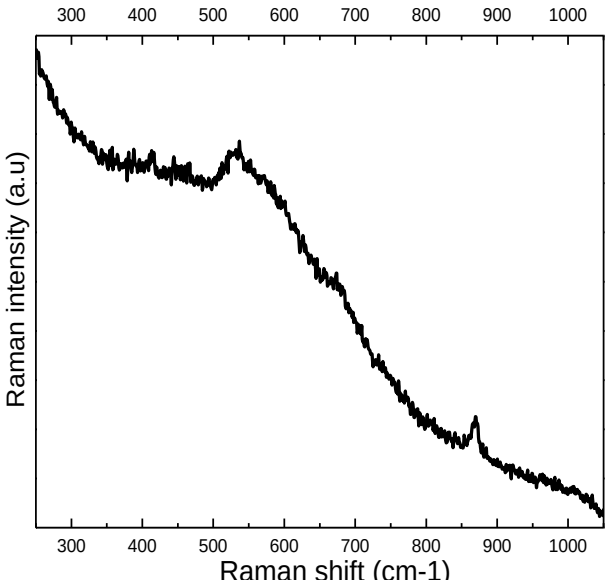

SERS Spectrum for Alloy 600
At E = -0.75V and pH=7.2

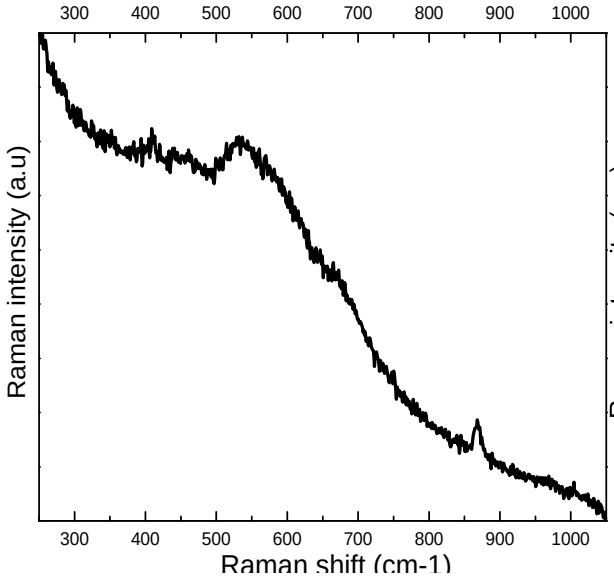

SERS Spectrum for Alloy 600
At E = -0.7V and pH=7.2

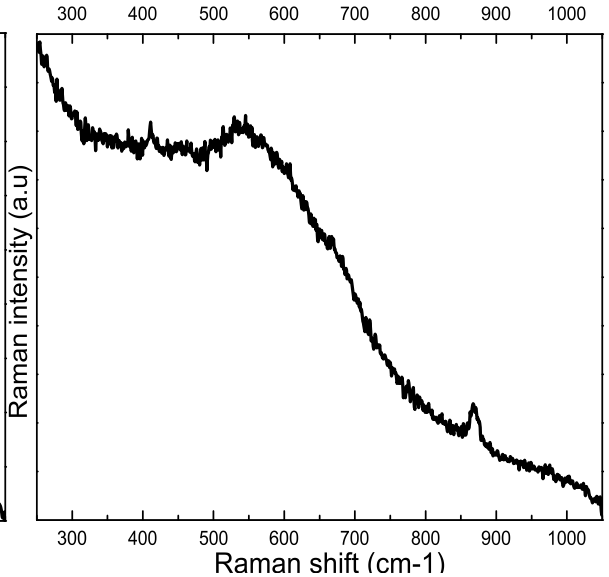

SERS Spectrum for Alloy 600
At E = -0.65V and pH=7.2

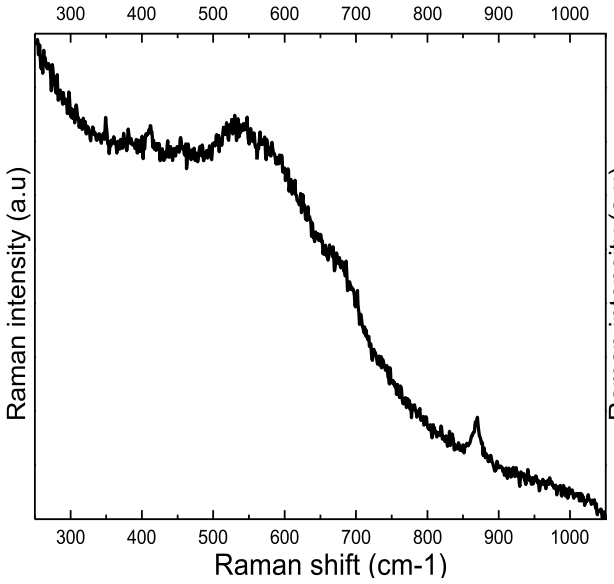

SERS Spectrum for Alloy 600
At E = -0.6V and pH=7.2

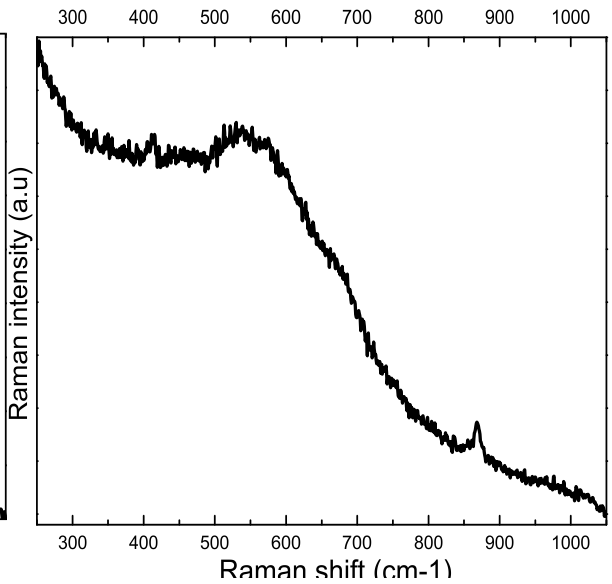

SERS Spectrum for Alloy 600
At E = -0.55V and pH=7.2

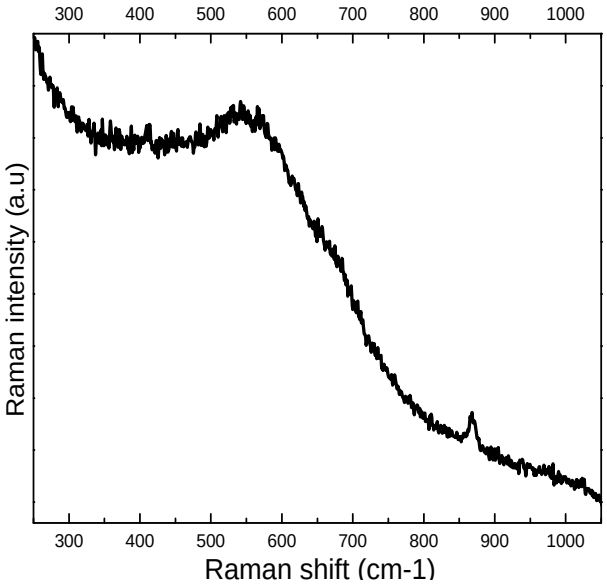

SERS Spectrum for Alloy 600
At E = -0.5V and pH=7.2

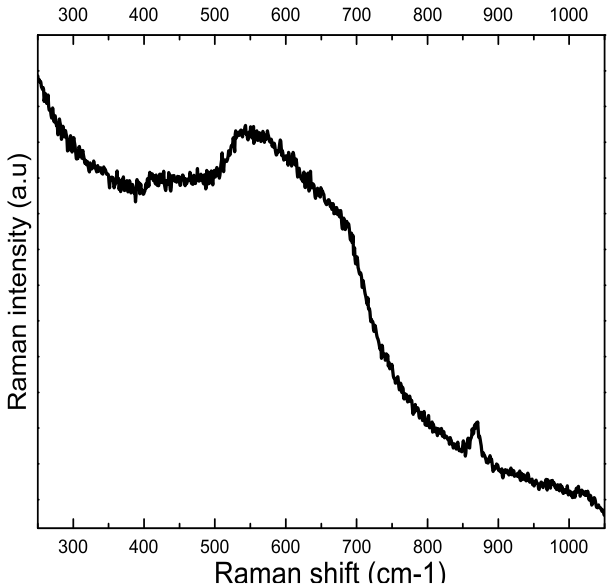

SERS Spectrum for Alloy 600
At E = -0.9V and pH=6.2

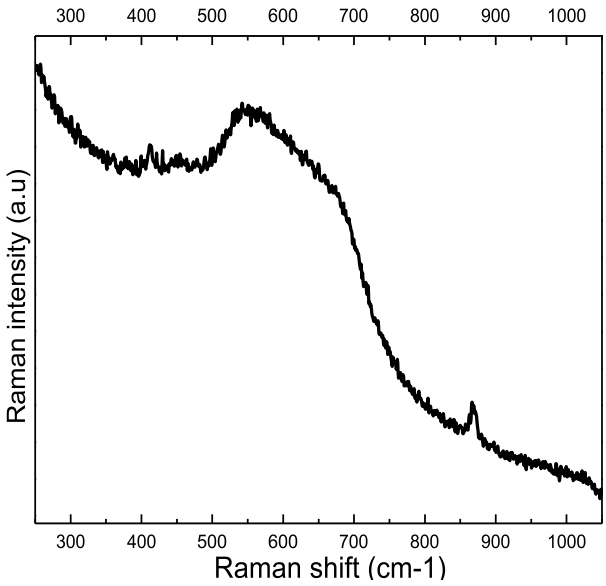

SERS Spectrum for Alloy 600
At E = -0.85V and pH=6.2

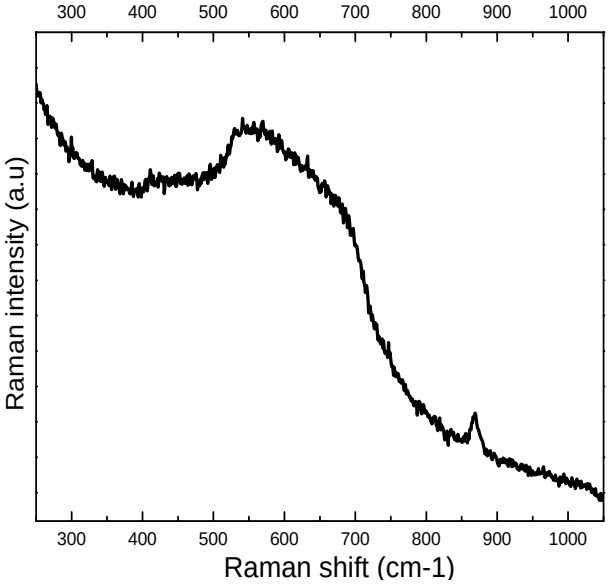

SERS Spectrum for Alloy 600
At E = -0.8V and pH=6.2

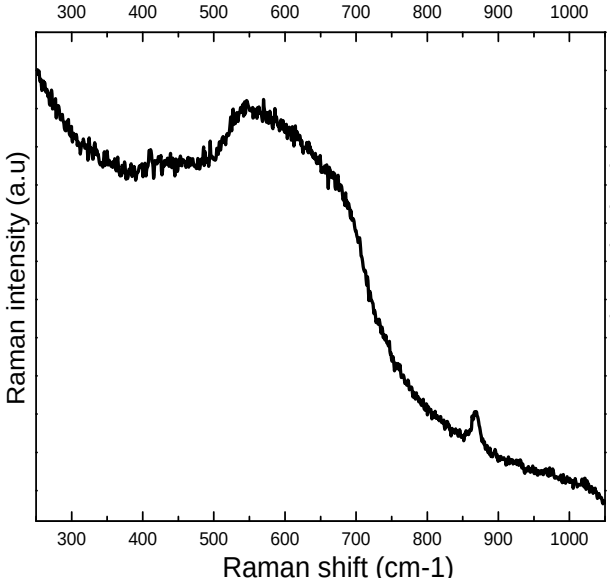

SERS Spectrum for Alloy 600
At E = -0.75V and pH=6.2

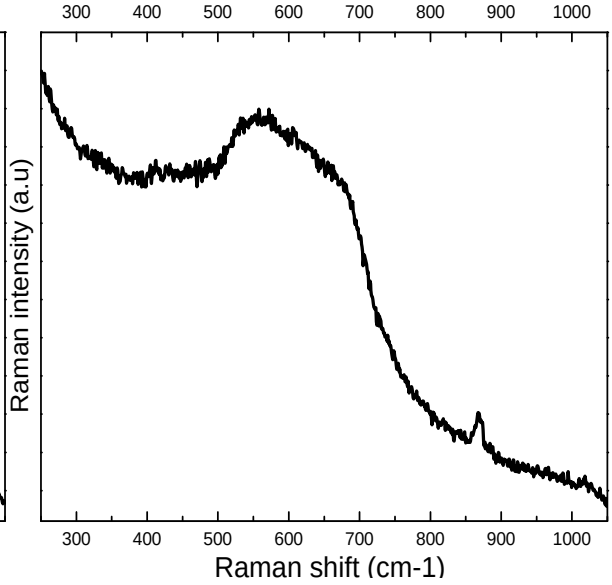

SERS Spectrum for Alloy 600
At E = -0.7V and pH=6.2

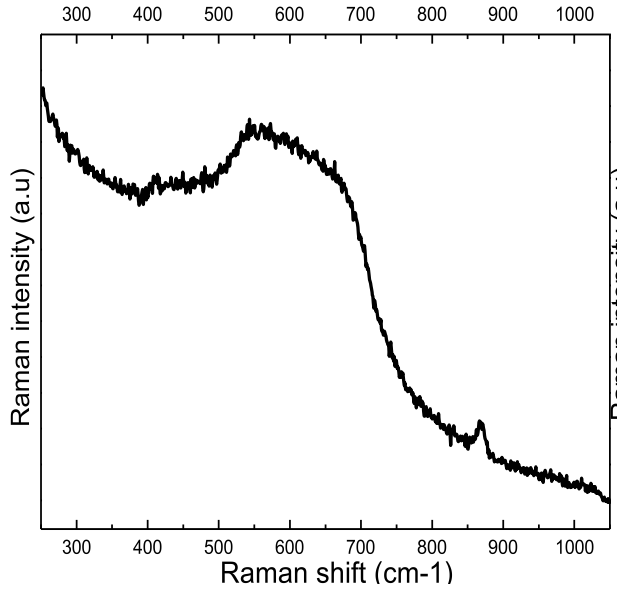

SERS Spectrum for Alloy 600
At E = -0.65V and pH=6.2

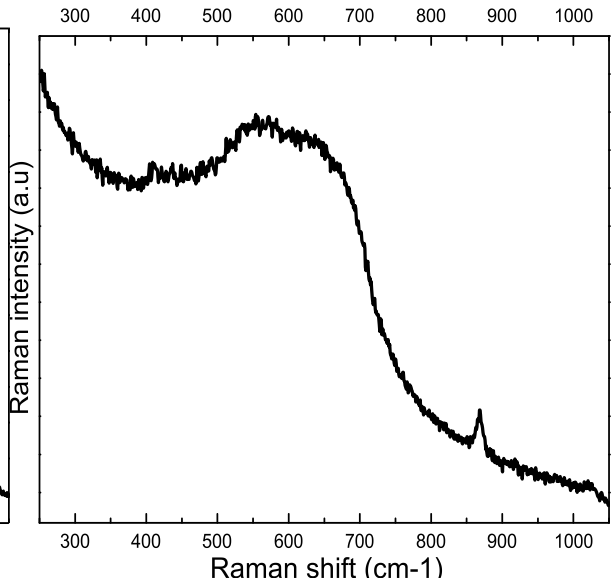

SERS Spectrum for Alloy 600
At E = -0.6V and pH=6.2

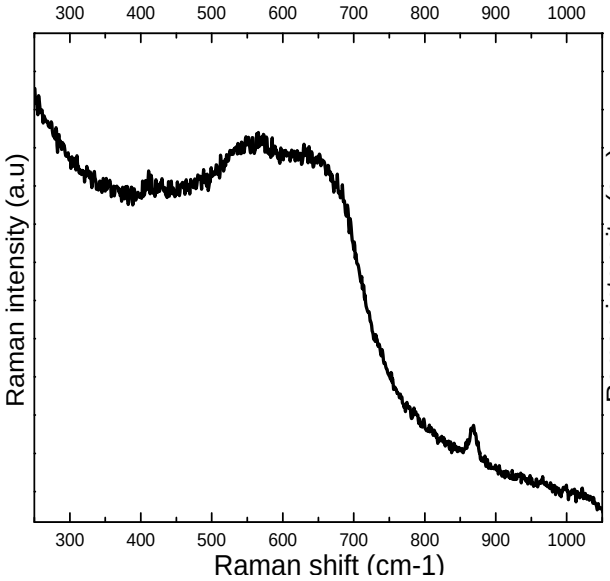

SERS Spectrum for Alloy 600
At E = -0.55V and pH=6.2

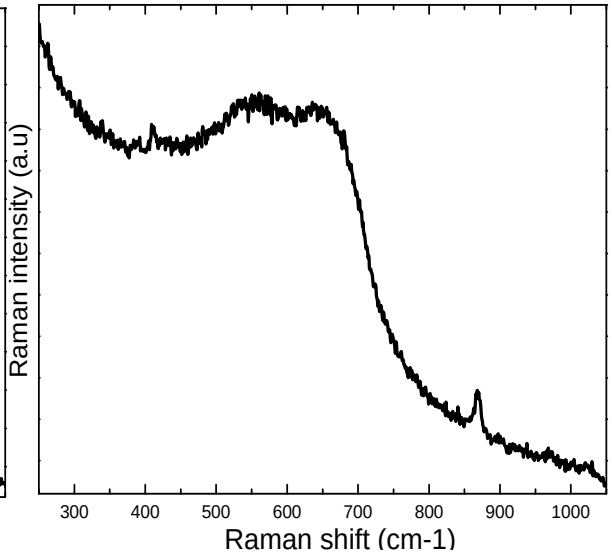

SERS Spectrum for Alloy 600
At E = -0.5V and pH=6.2

Appendix II. SERS spectra of Alloy 600 that were cathodically polarized during the heat-up from room temperature to 320 °C

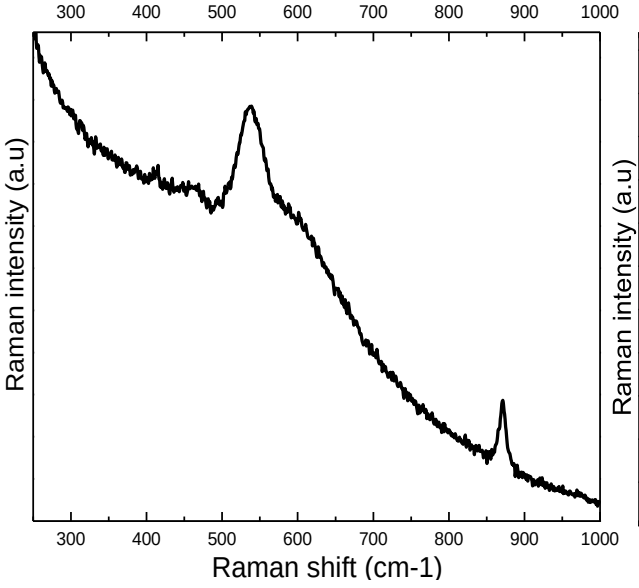

SERS Spectrum for Alloy 600
At E = -0.9V and pH=7.2

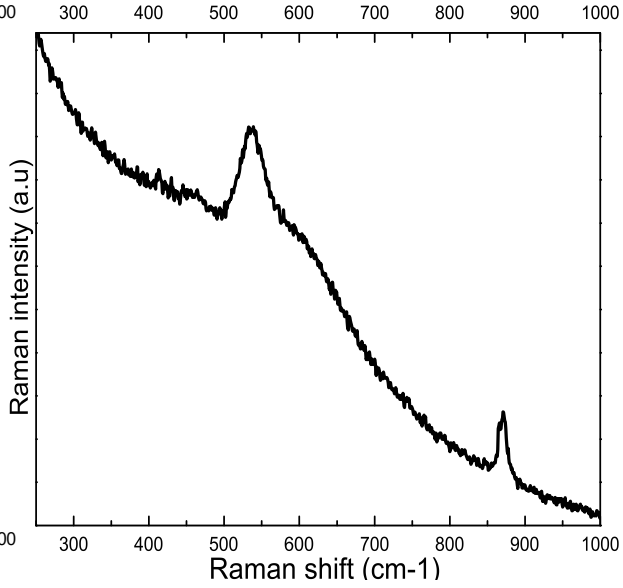

SERS Spectrum for Alloy 600
At E = -0.85V and pH=7.2

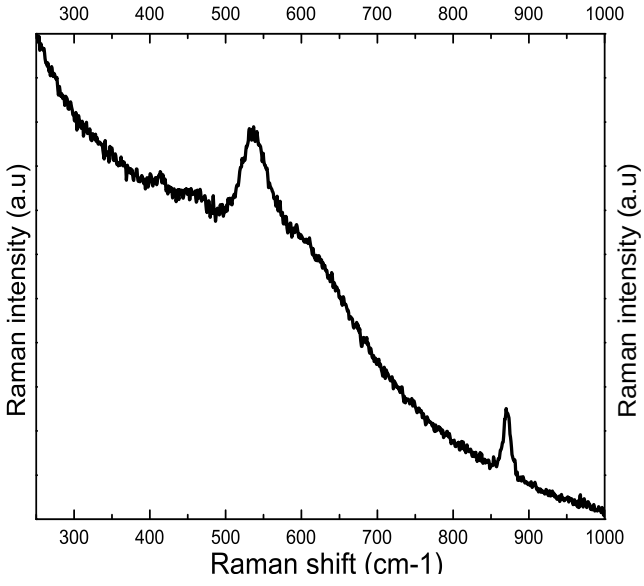

SERS Spectrum for Alloy 600
At E = -0.8V and pH=7.2

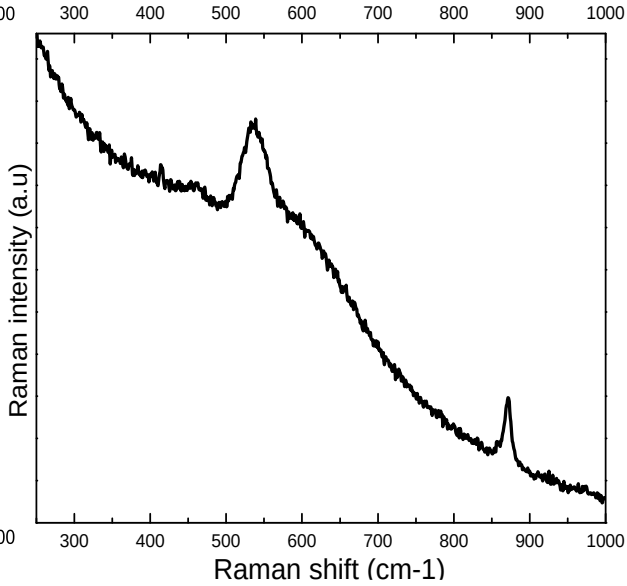

SERS Spectrum for Alloy 600
At E = -0.75V and pH=7.2

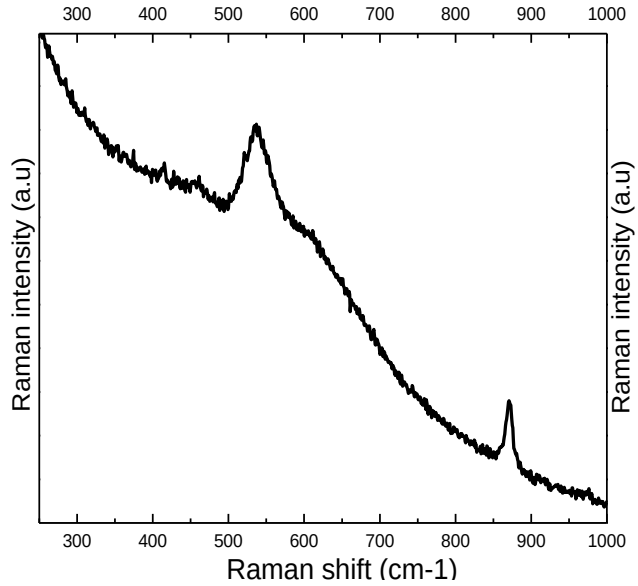

SERS Spectrum for Alloy 600
At E = -0.7V and pH=7.2

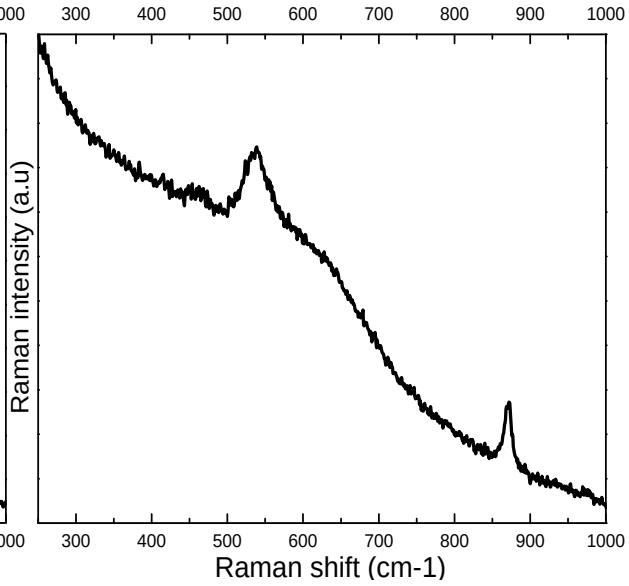

SERS Spectrum for Alloy 600
At E = -0.65V and pH=7.2

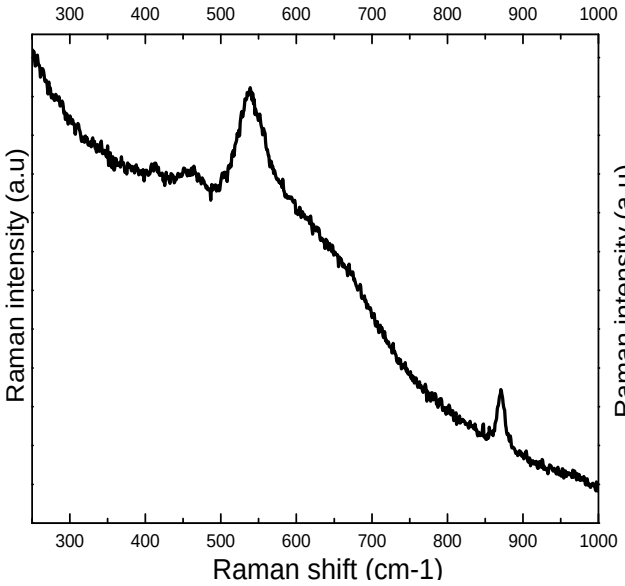

SERS Spectrum for Alloy 600
At E = -0.6V and pH=7.2

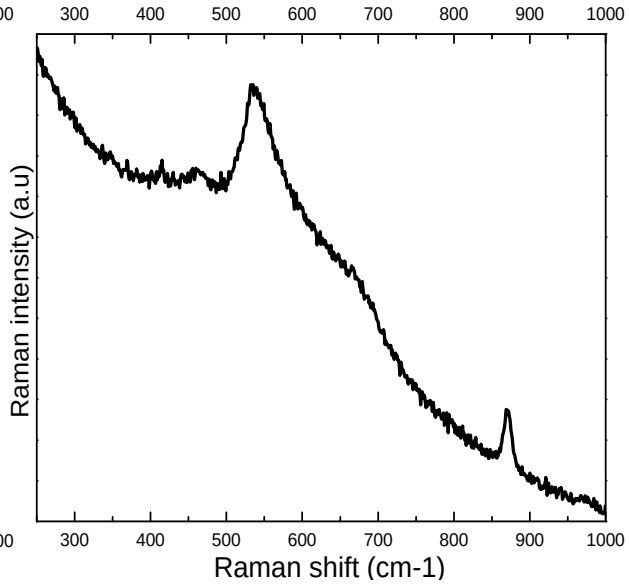

SERS Spectrum for Alloy 600
At E = -0.55V and pH=7.2

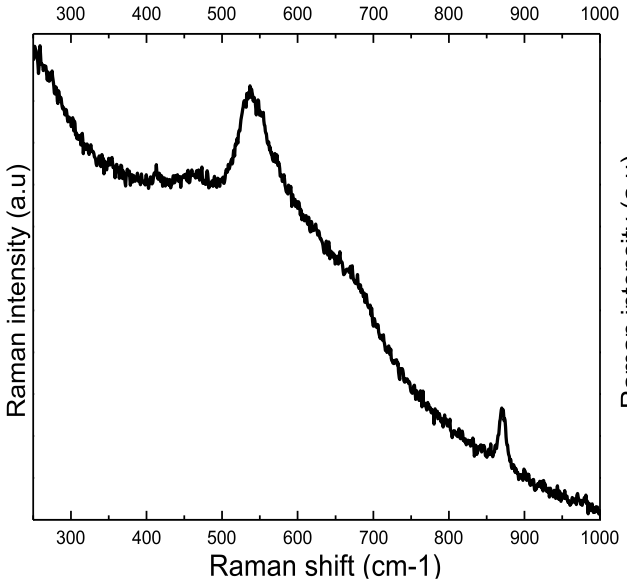

SERS Spectrum for Alloy 600
At E = -0.5V and pH=7.2

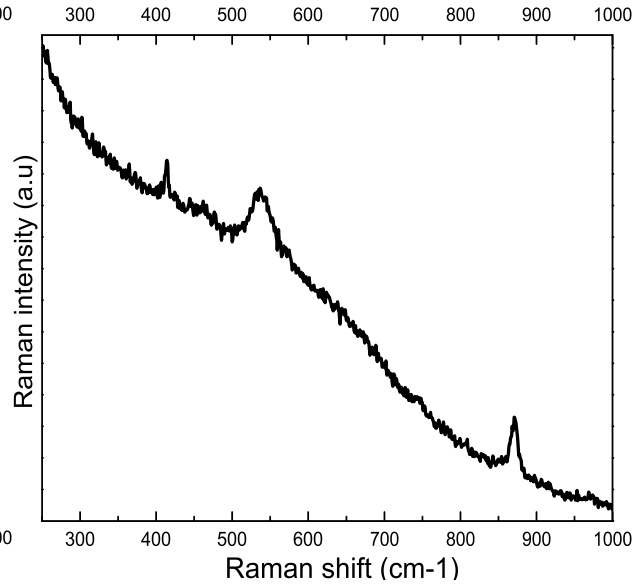

SERS Spectrum for Alloy 600
At E = -0.9V and pH=6.2

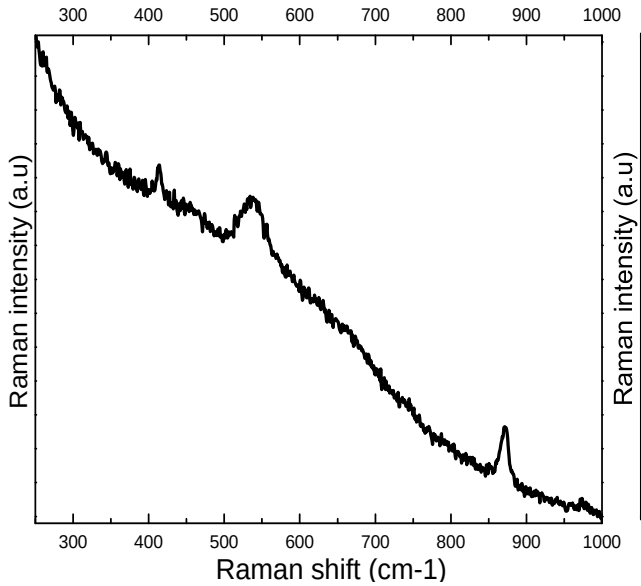

SERS Spectrum for Alloy 600
At E = -0.85V and pH=6.2

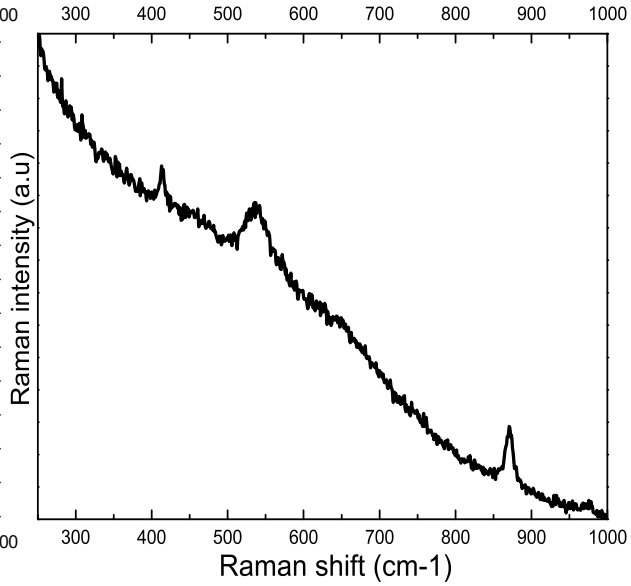

SERS Spectrum for Alloy 600
At E = -0.8V and pH=6.2

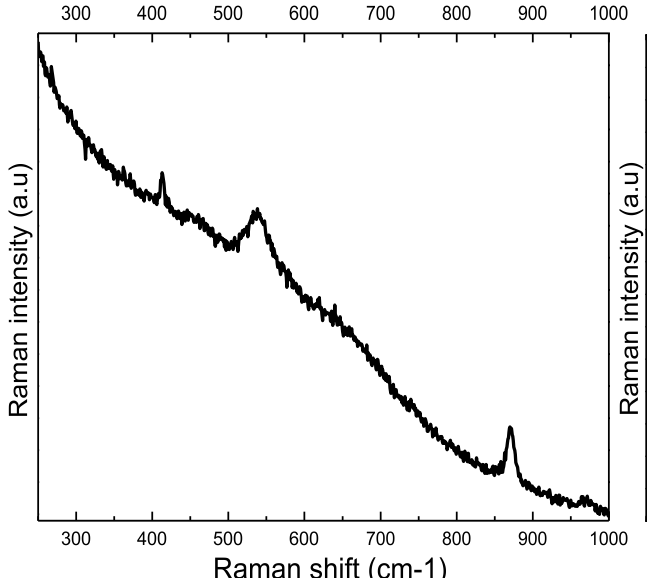

SERS Spectrum for Alloy 600
At E = -0.75V and pH=6.2

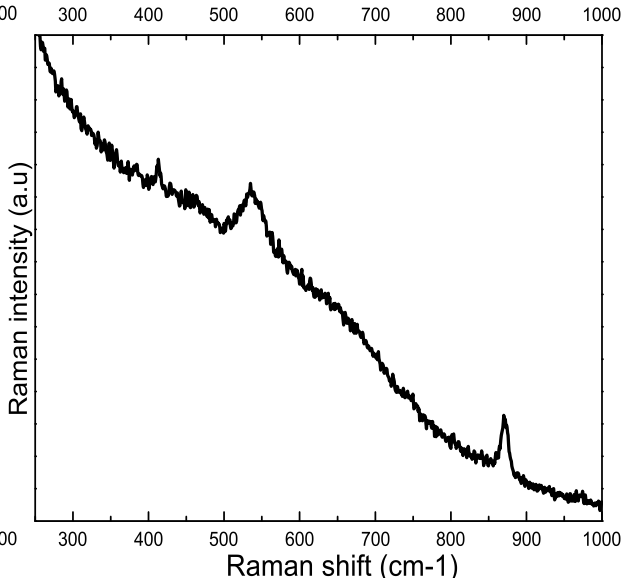

SERS Spectrum for Alloy 600
At E = -0.7V and pH=6.2

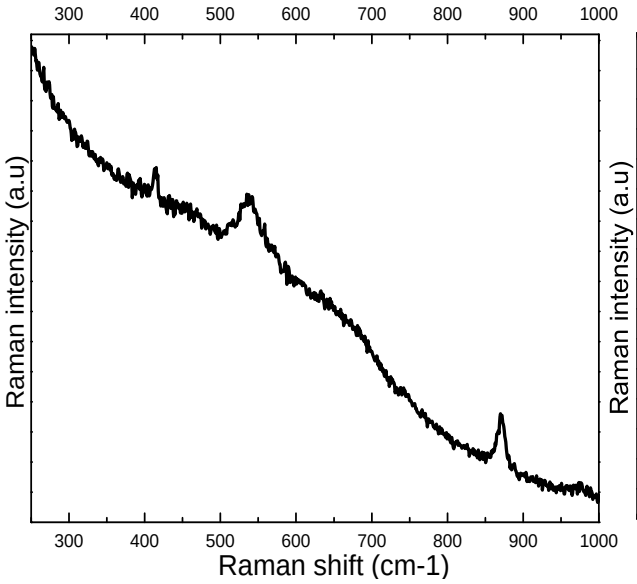

SERS Spectrum for Alloy 600
At E = -0.65V and pH=6.2

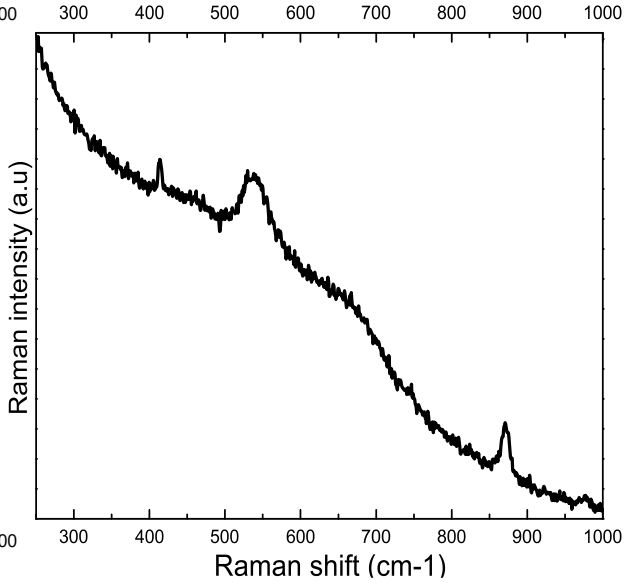

SERS Spectrum for Alloy 600
At E = -0.6V and pH=6.2

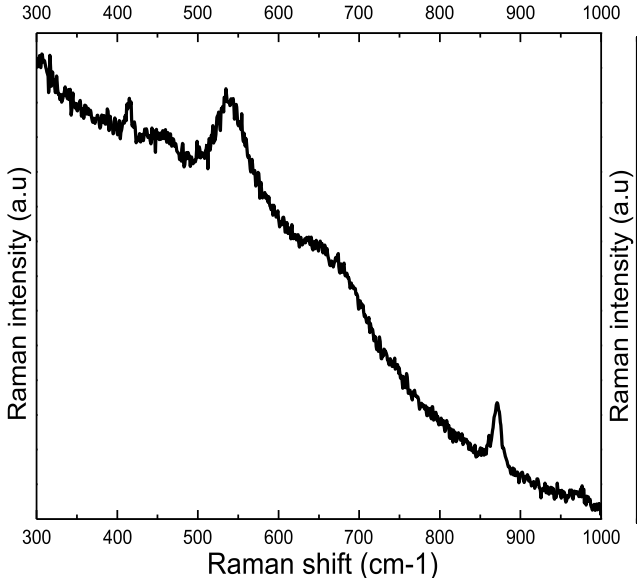

SERS Spectrum for Alloy 600
At E = -0.55V and pH=6.2

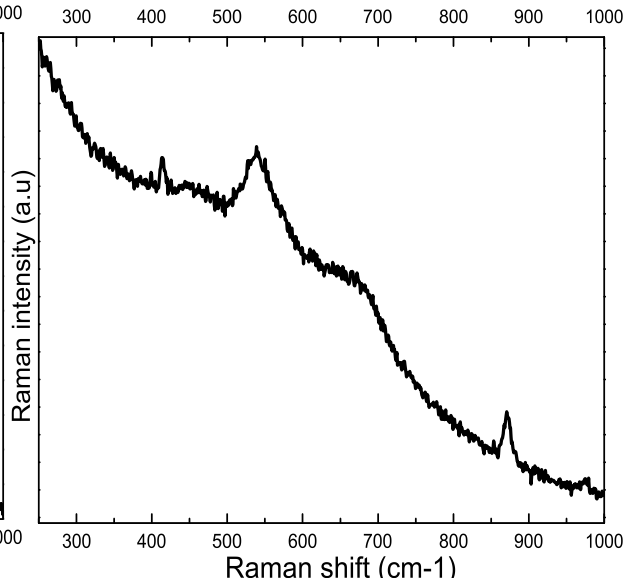

SERS Spectrum for Alloy 600
At E = -0.5V and pH=6.2

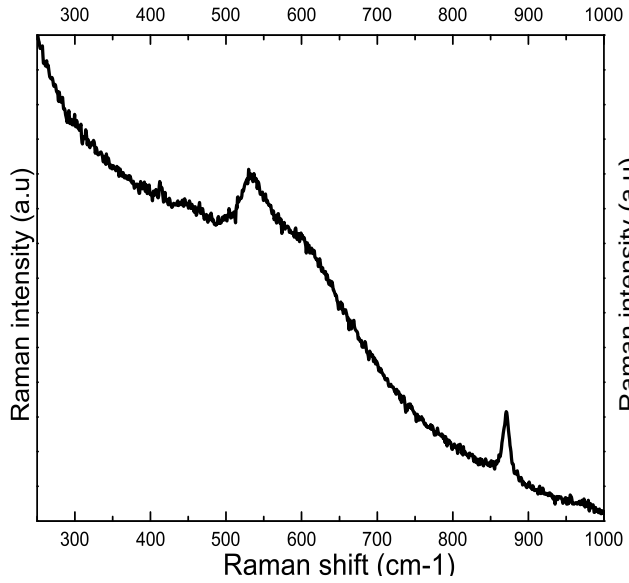

SERS Spectrum for Alloy 600
At E = -0.9V and pH=7.2

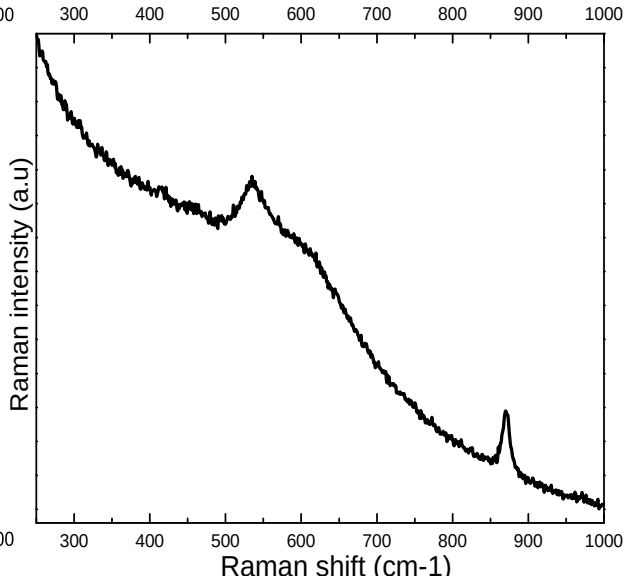

SERS Spectrum for Alloy 600
At E = -0.85V and pH=7.2

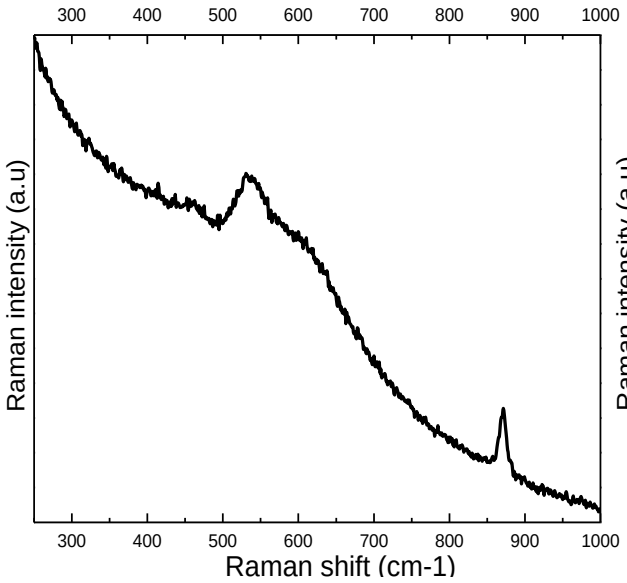

SERS Spectrum for Alloy 600
At E = -0.8V and pH=7.2

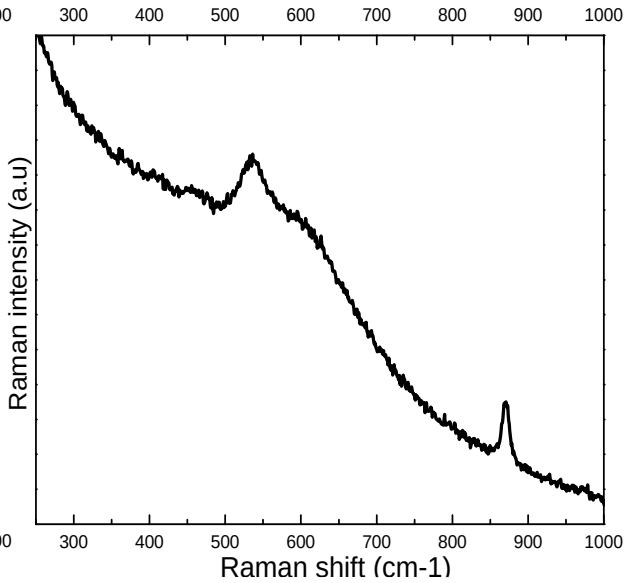

SERS Spectrum for Alloy 600
At E = -0.75V and pH=7.2

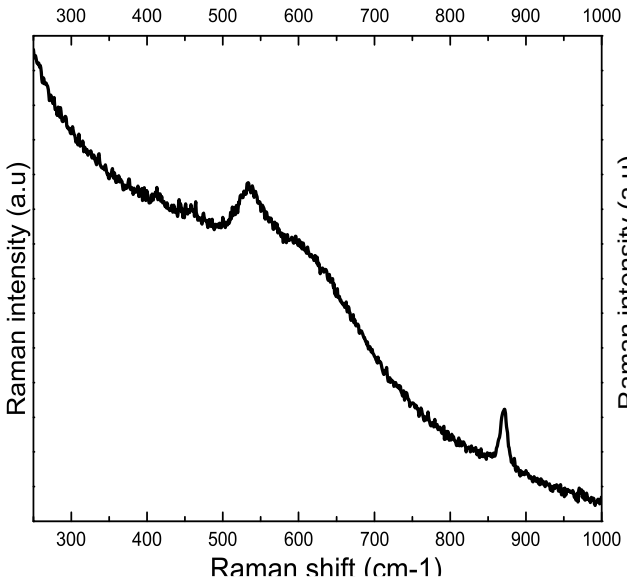

SERS Spectrum for Alloy 600
At E = -0.7V and pH=7.2

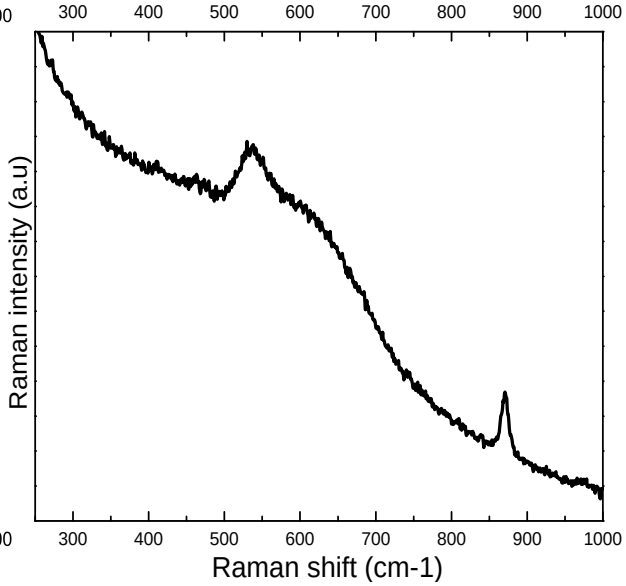

SERS Spectrum for Alloy 600
At E = -0.65V and pH=7.2

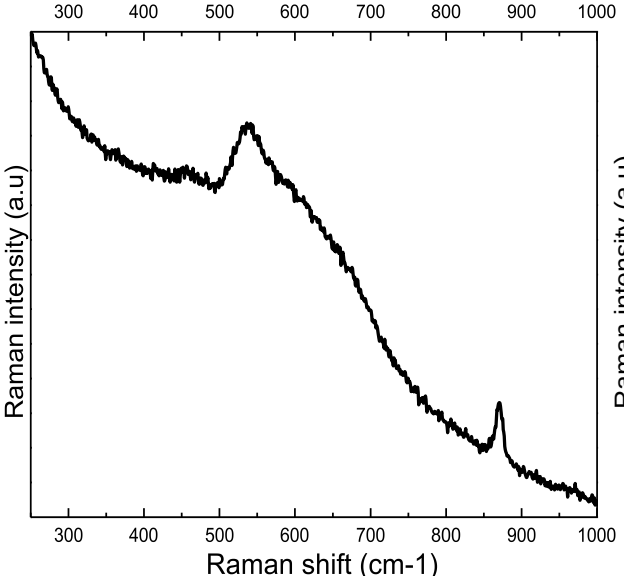

SERS Spectrum for Alloy 600
At E = -0.6V and pH=7.2

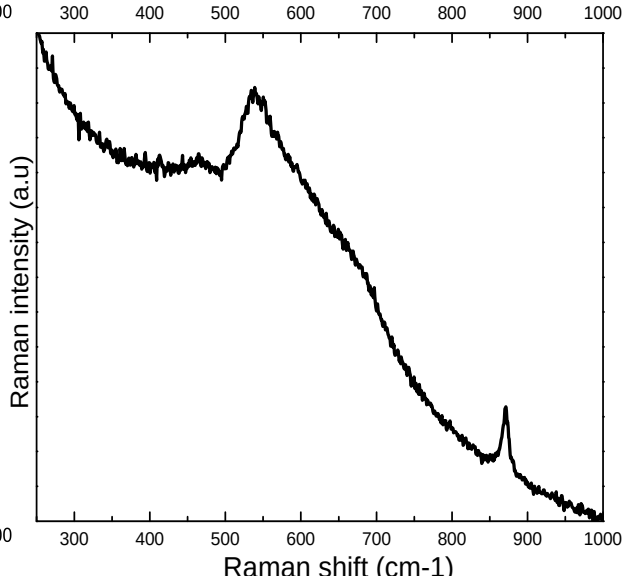

SERS Spectrum for Alloy 600
At E = -0.55V and pH=7.2

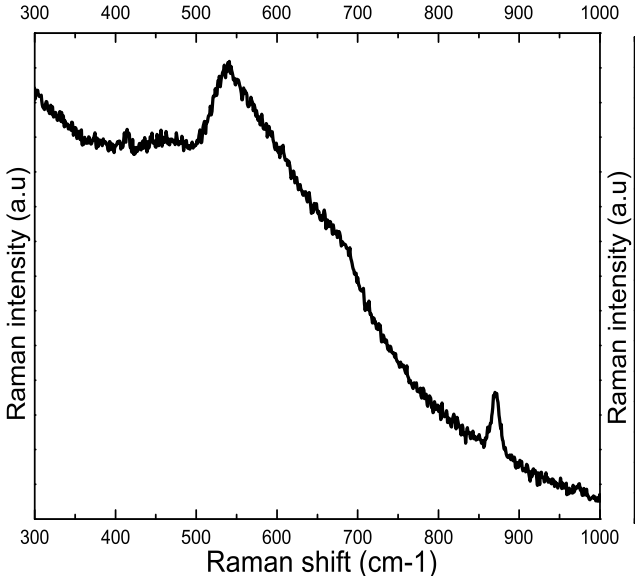

SERS Spectrum for Alloy 600
At E = -0.5V and pH=7.2

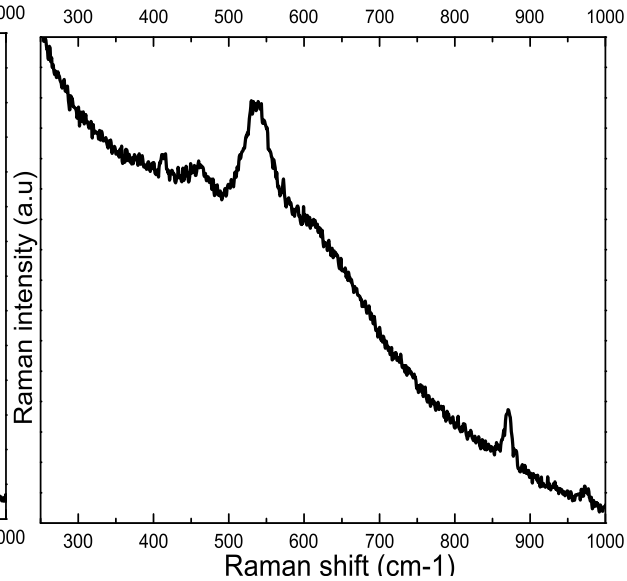

SERS Spectrum for Alloy 600
At E = -0.9V and pH=6.2

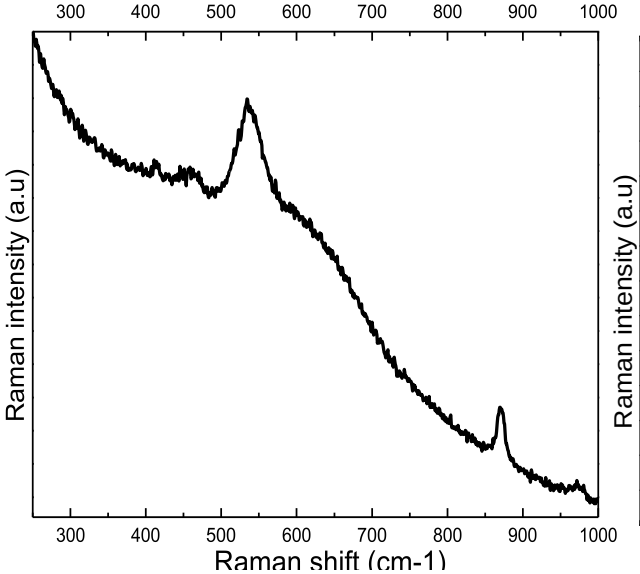

SERS Spectrum for Alloy 600
At E = -0.85V and pH=6.2

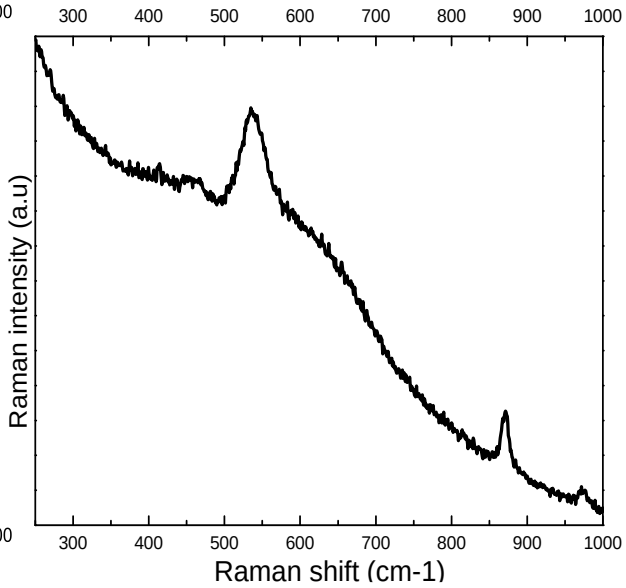

SERS Spectrum for Alloy 600
At E = -0.8V and pH=6.2

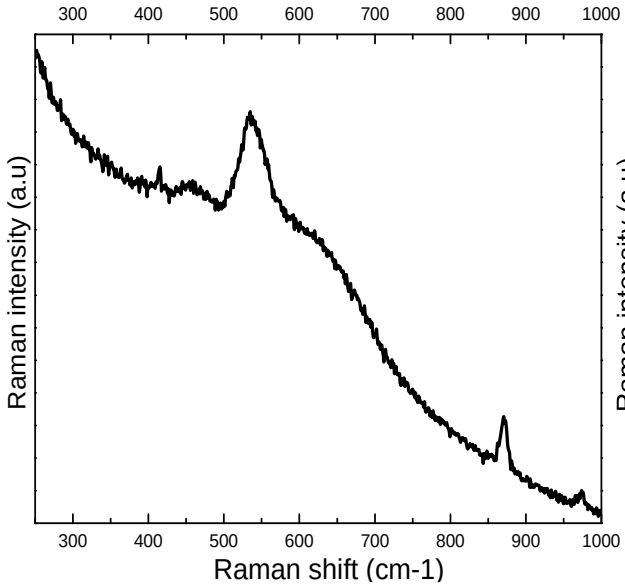

SERS Spectrum for Alloy 600
At E = -0.75V and pH=6.2

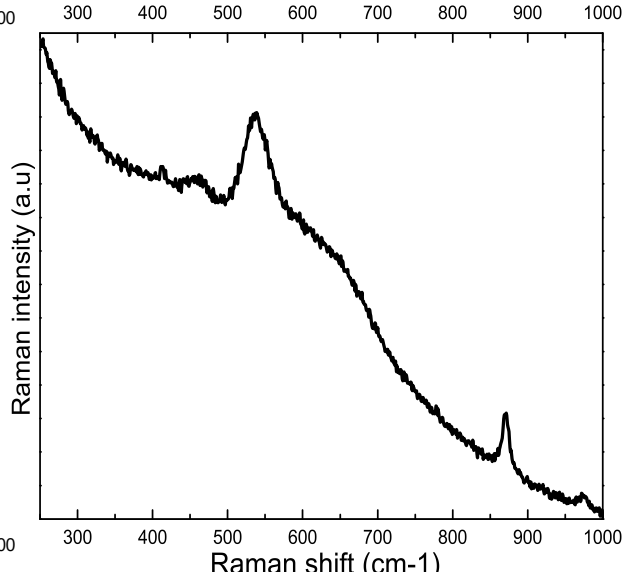

SERS Spectrum for Alloy 600
At E = -0.7V and pH=6.2

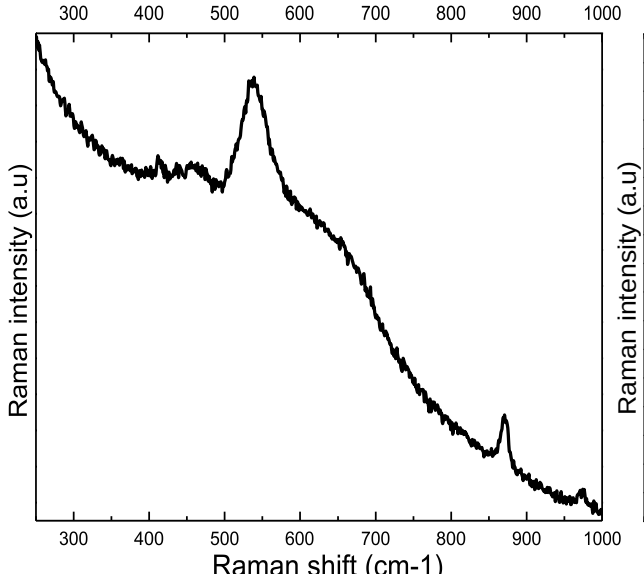

SERS Spectrum for Alloy 600
At E = -0.65V and pH=6.2

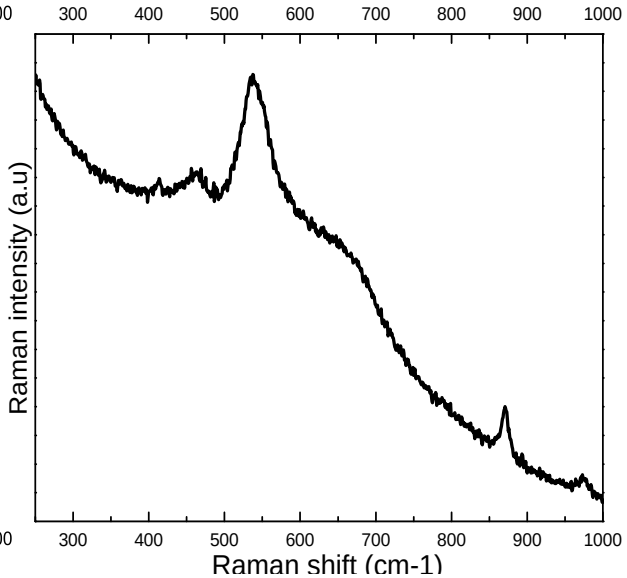

SERS Spectrum for Alloy 600
At E = -0.6V and pH=6.2

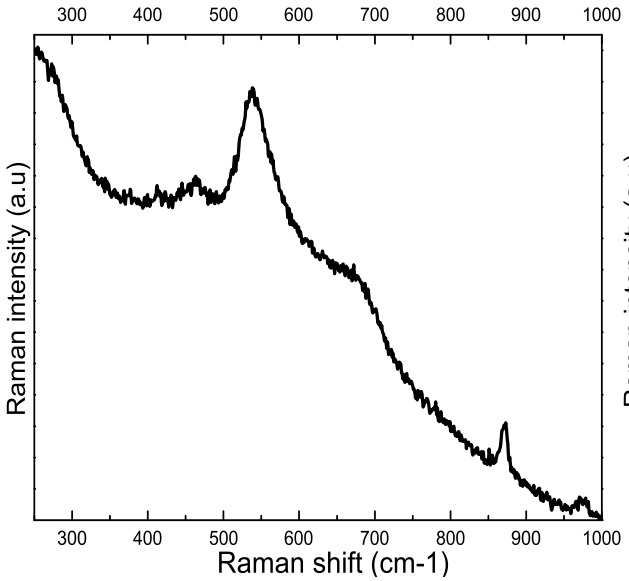

SERS Spectrum for Alloy 600
At E = -0.55V and pH=6.2

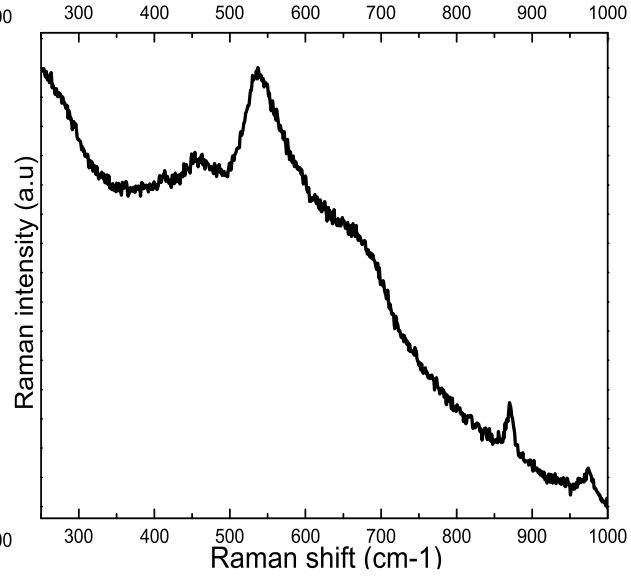

SERS Spectrum for Alloy 600
At E = -0.5V and pH=6.2

Appendix III. SERS spectra of Alloy 690 that were cathodically polarized during the heat-up from room temperature to 320 °C

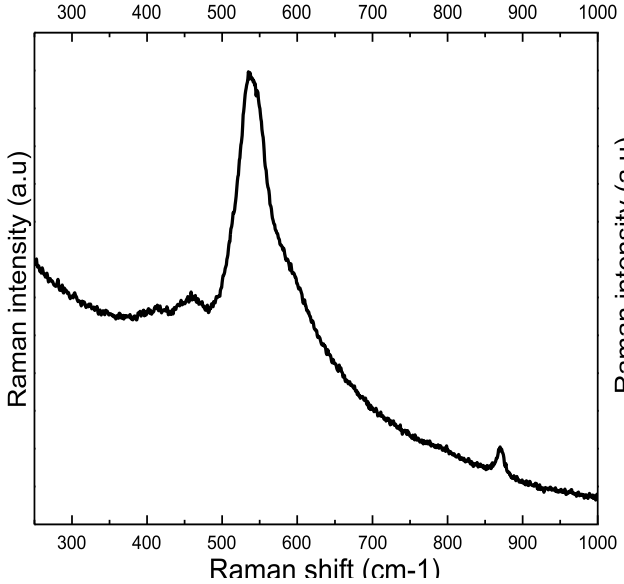

SERS Spectrum for Alloy 690
At E = -0.9V and pH=7.2

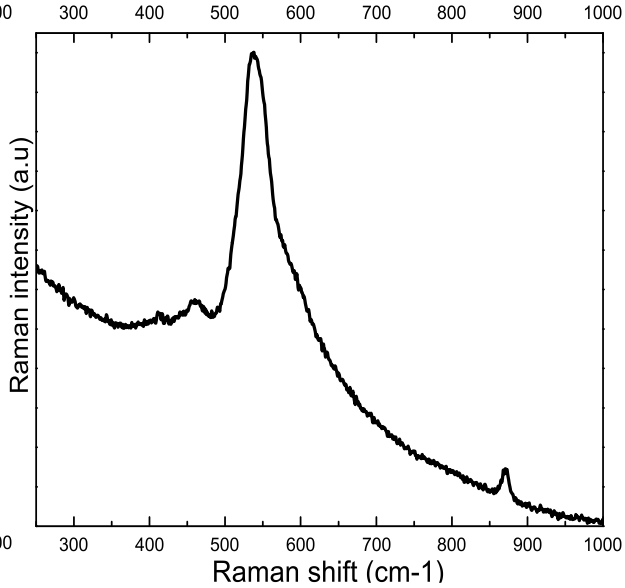

SERS Spectrum for Alloy 690
At E = -0.85V and pH=7.2

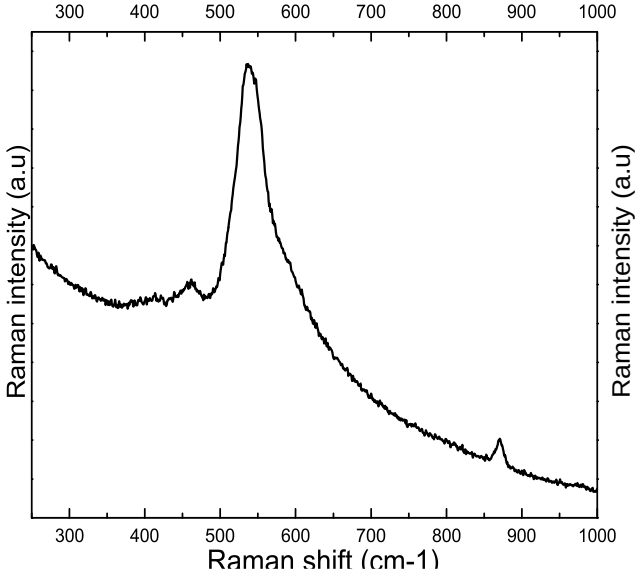

SERS Spectrum for Alloy 690
At E = -0.8V and pH=7.2

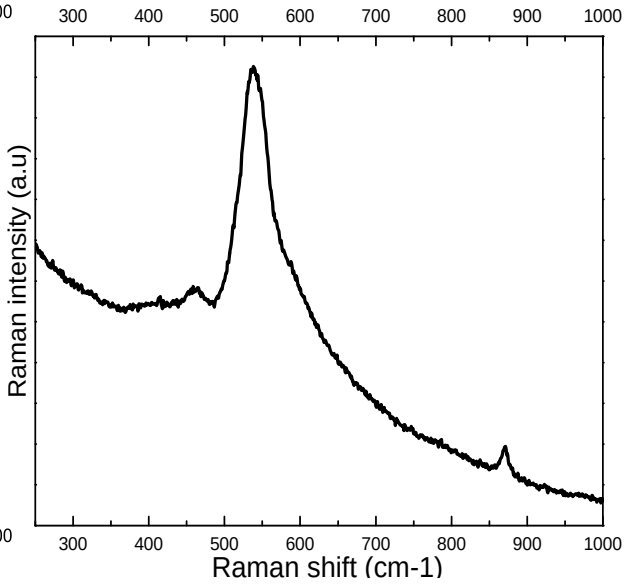

SERS Spectrum for Alloy 690
At E = -0.75V and pH=7.2

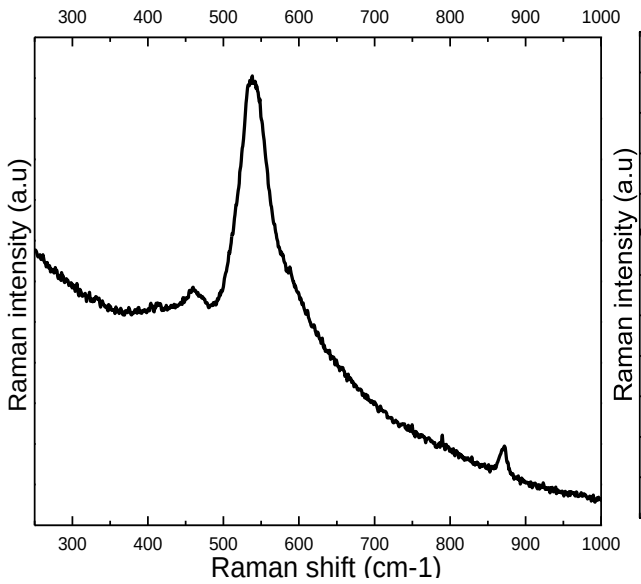

SERS Spectrum for Alloy 690
At E = -0.7V and pH=7.2

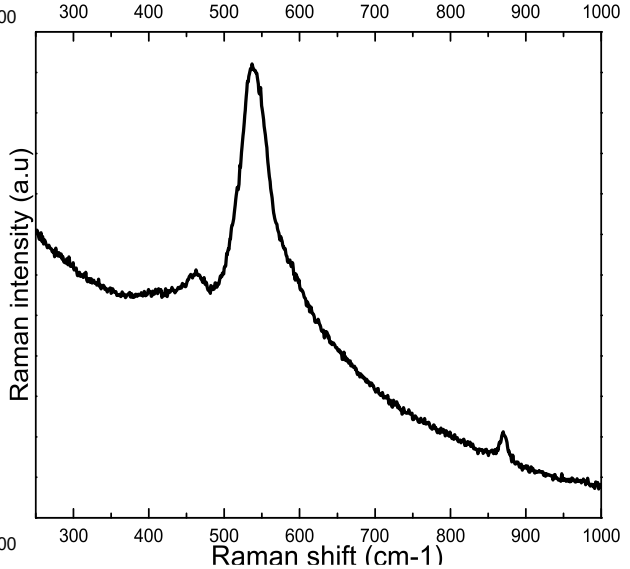

SERS Spectrum for Alloy 690
At E = -0.65V and pH=7.2

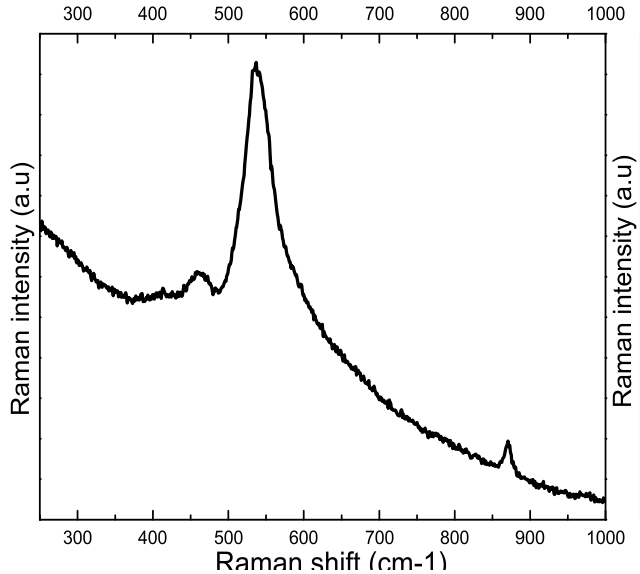

SERS Spectrum for Alloy 690
At E = -0.6V and pH=7.2

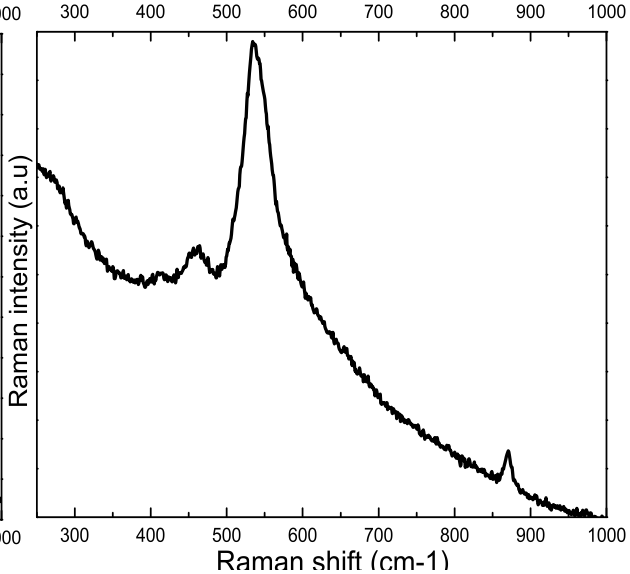

SERS Spectrum for Alloy 690
At E = -0.55V and pH=7.2

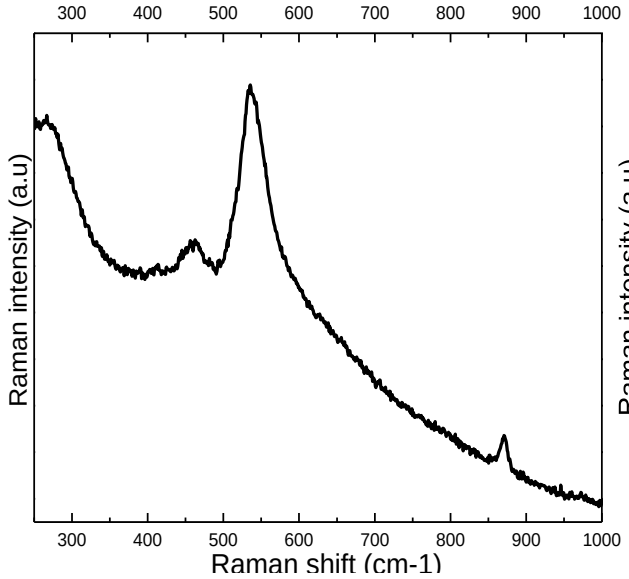

SERS Spectrum for Alloy 690
At E = -0.5V and pH=7.2

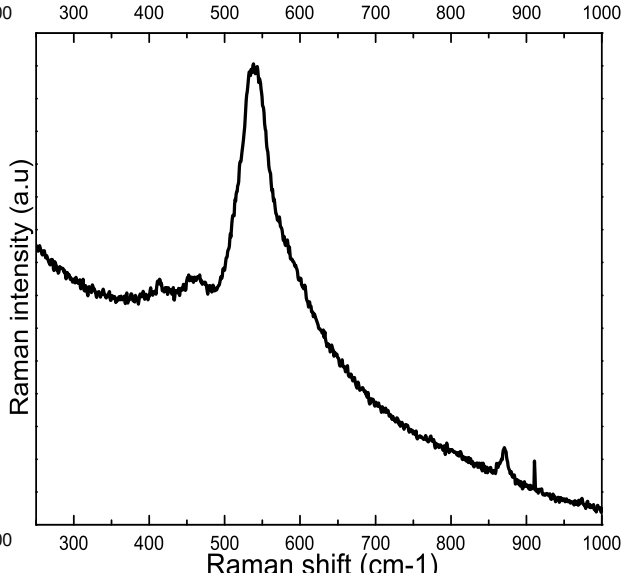

SERS Spectrum for Alloy 690
At E = -0.9V and pH=6.2

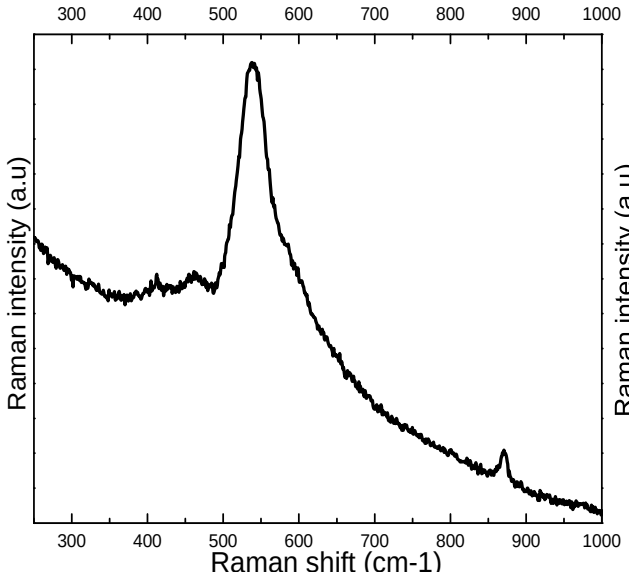

SERS Spectrum for Alloy 690
At E = -0.85V and pH=6.2

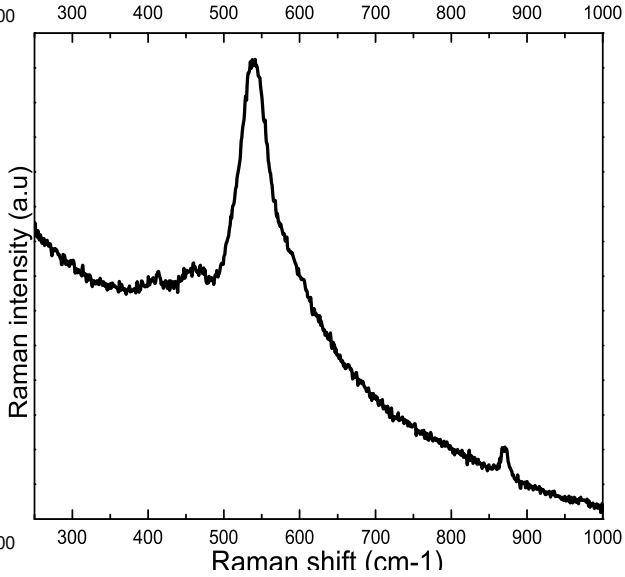

SERS Spectrum for Alloy 690
At E = -0.8V and pH=6.2

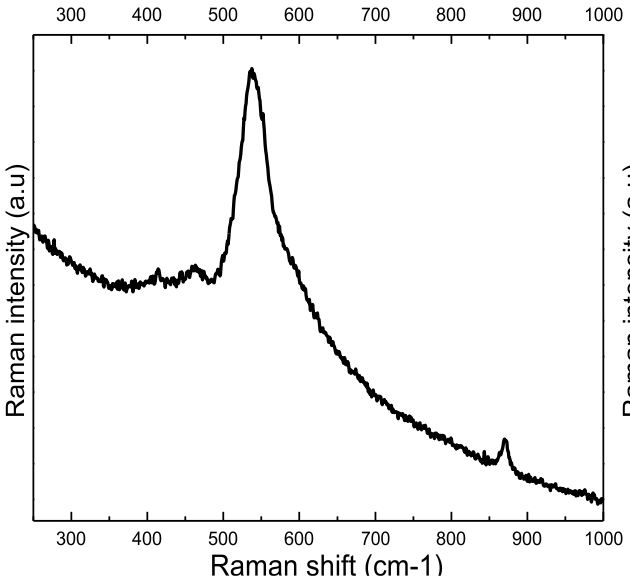

SERS Spectrum for Alloy 690
At E = -0.75V and pH=6.2

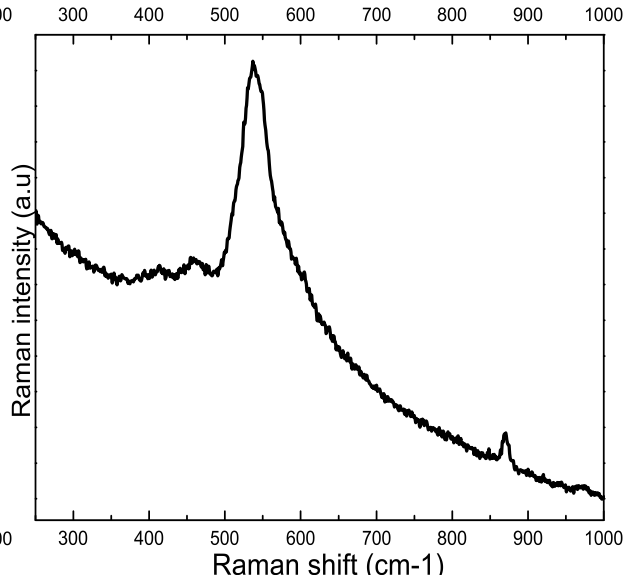

SERS Spectrum for Alloy 690
At E = -0.7V and pH=6.2

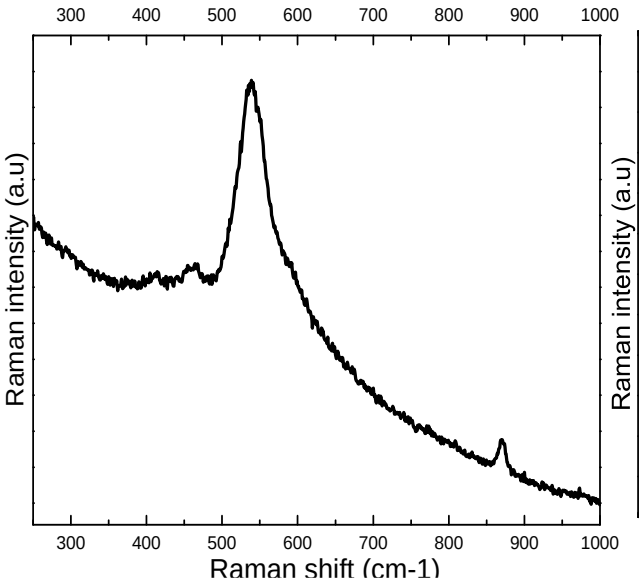

SERS Spectrum for Alloy 690
At E = -0.65V and pH=6.2

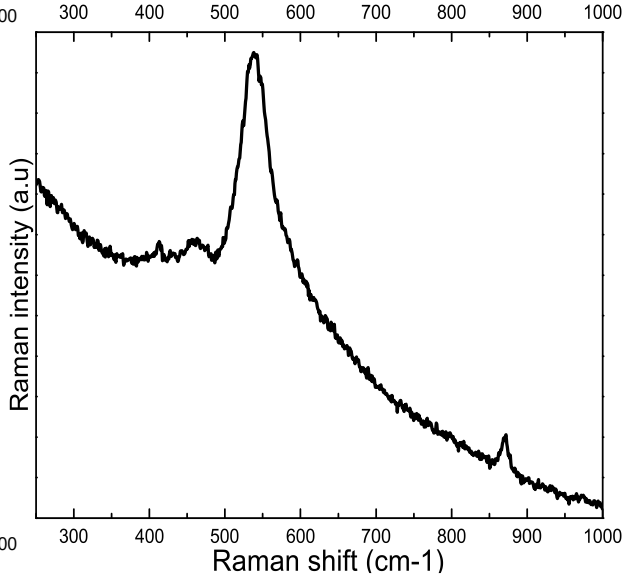

SERS Spectrum for Alloy 690
At E = -0.6V and pH=6.2

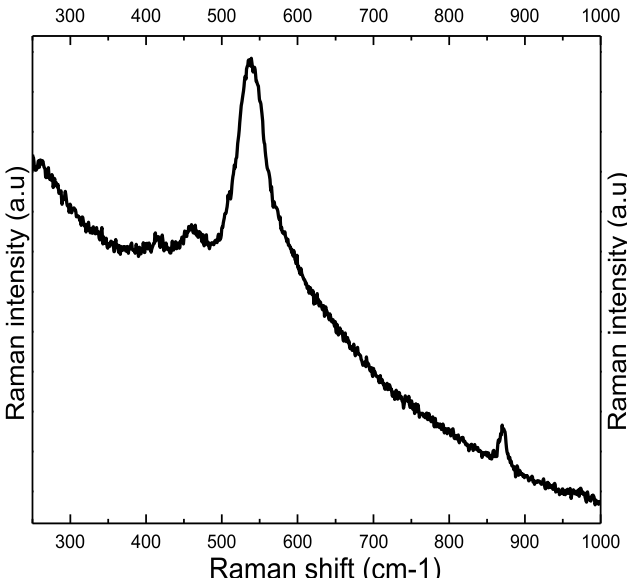

SERS Spectrum for Alloy 690
At E = -0.55V and pH=6.2

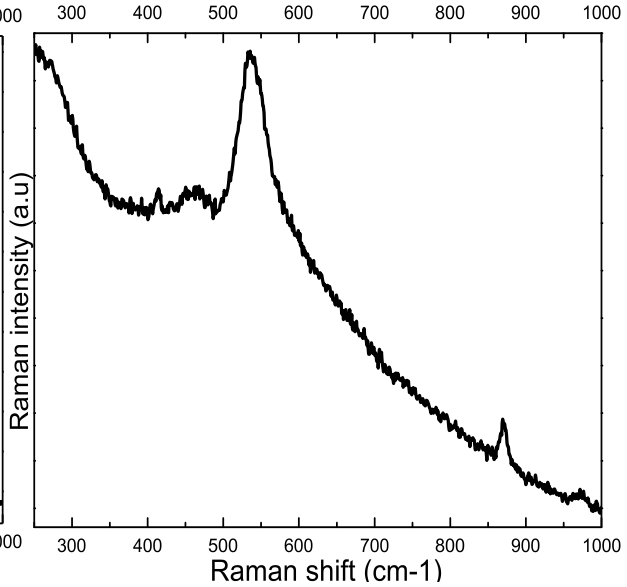

SERS Spectrum for Alloy 690
At E = -0.5V and pH=6.2

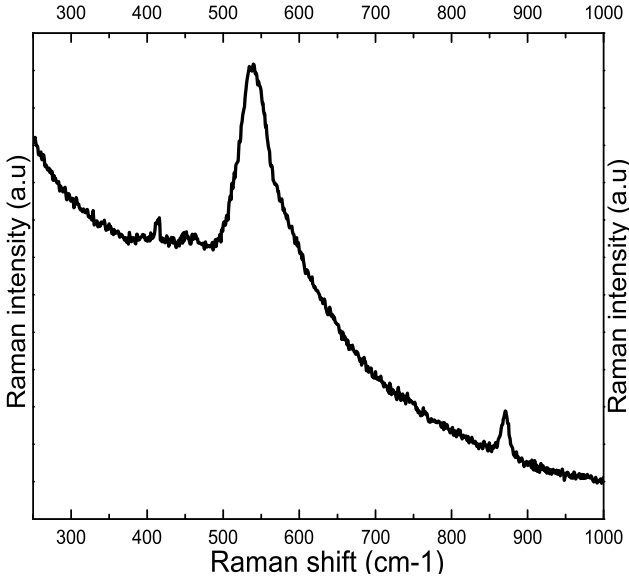

SERS Spectrum for Alloy 690
At E = -0.9V and pH=7.2

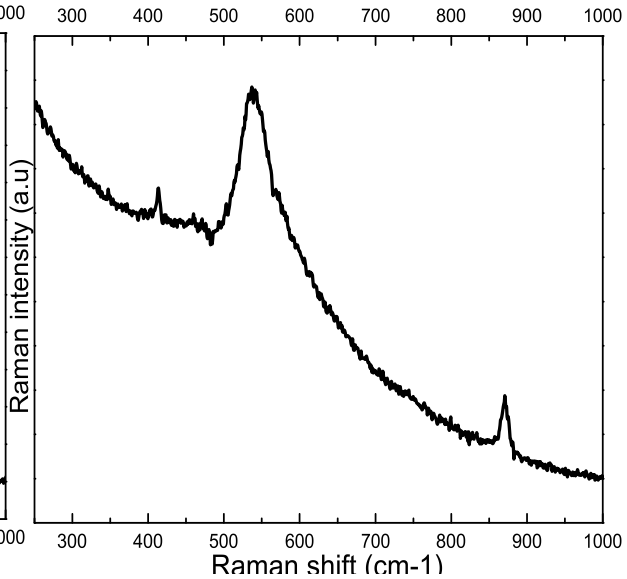

SERS Spectrum for Alloy 690
At E = -0.85V and pH=7.2

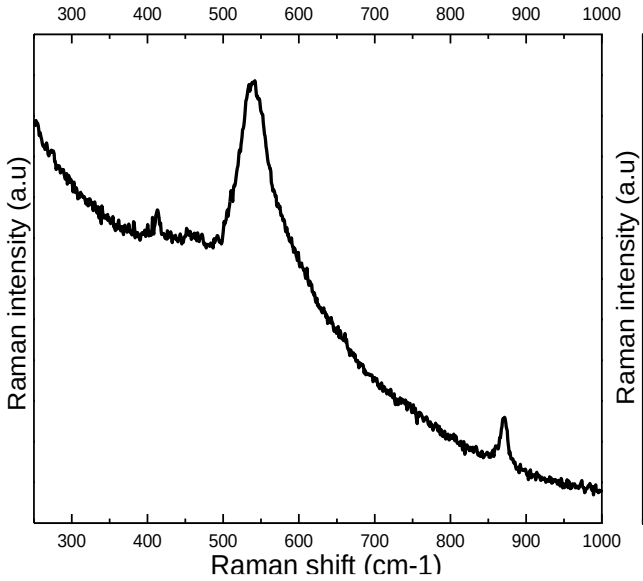

SERS Spectrum for Alloy 690
At E = -0.8V and pH=7.2

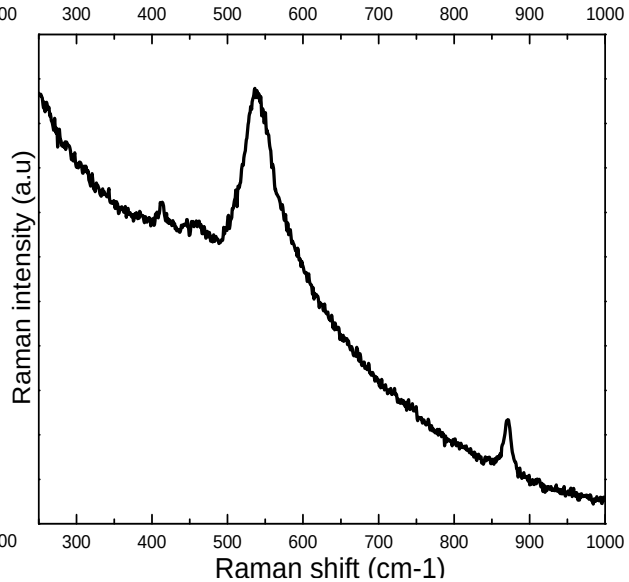

SERS Spectrum for Alloy 690
At E = -0.75V and pH=7.2

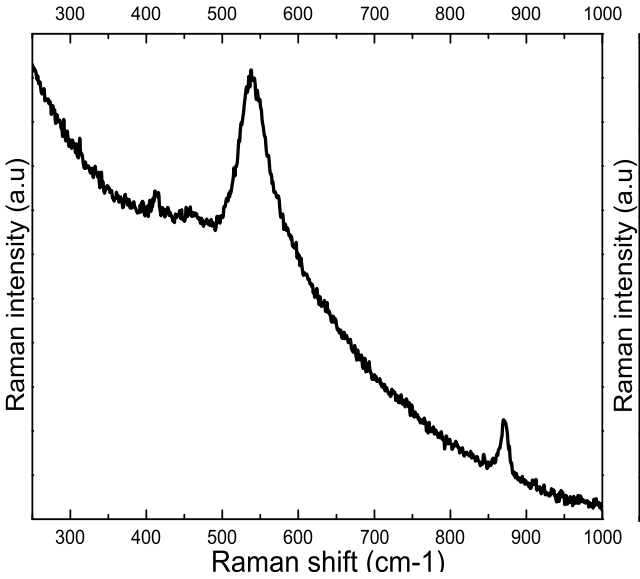

SERS Spectrum for Alloy 690
At E = -0.7V and pH=7.2

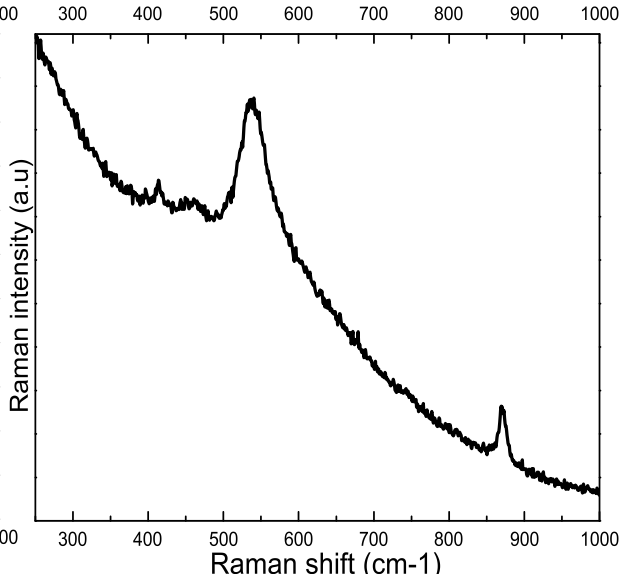

SERS Spectrum for Alloy 690
At E = -0.65V and pH=7.2

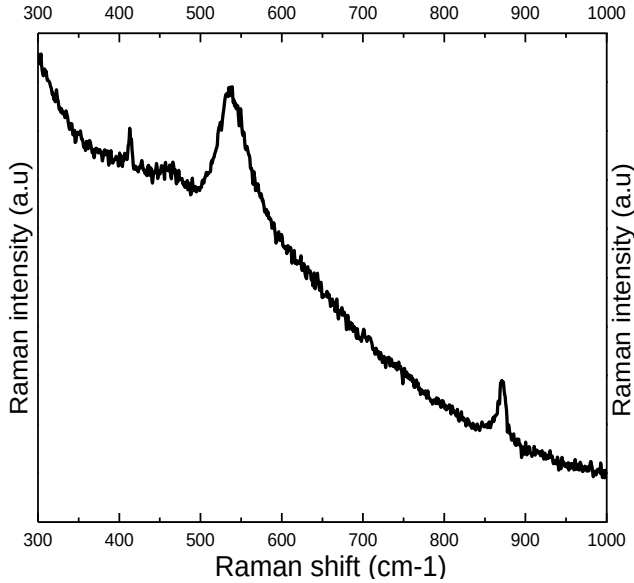

SERS Spectrum for Alloy 690
At E = -0.6V and pH=7.2

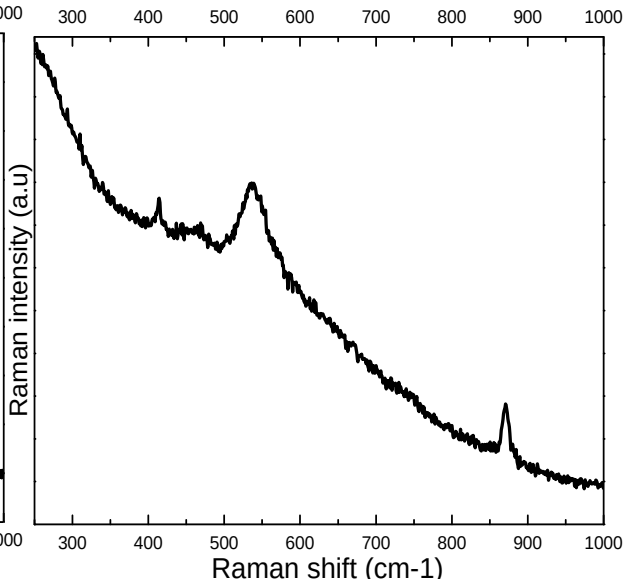

SERS Spectrum for Alloy 690
At E = -0.55V and pH=7.2

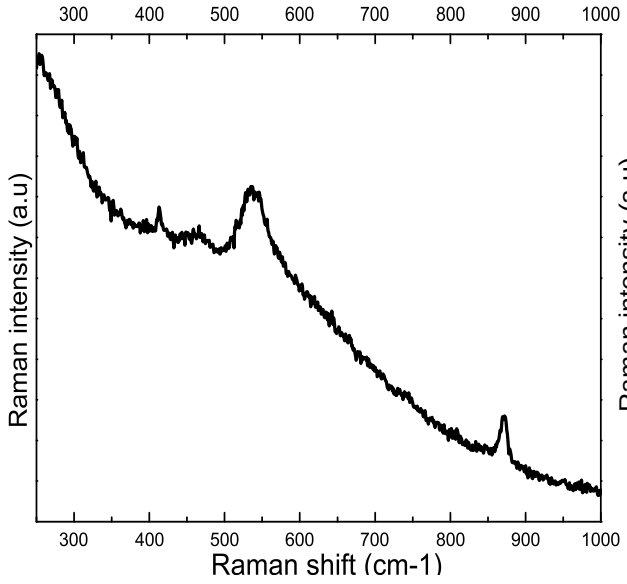

SERS Spectrum for Alloy 690
At E = -0.5V and pH=7.2

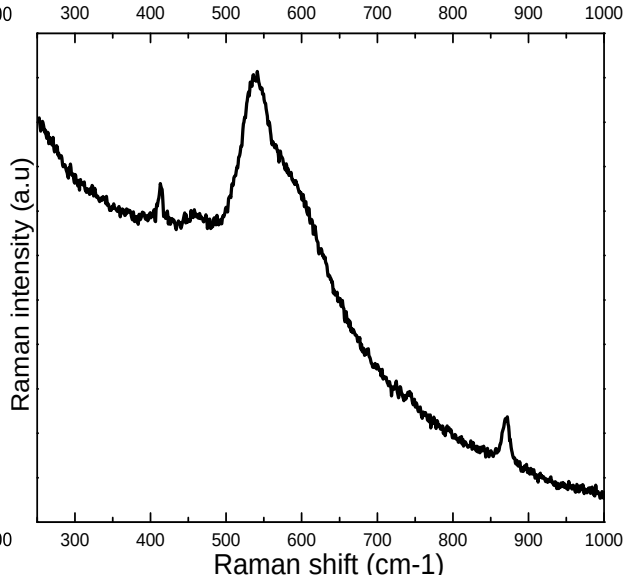

SERS Spectrum for Alloy 690
At E = -0.9V and pH=6.2

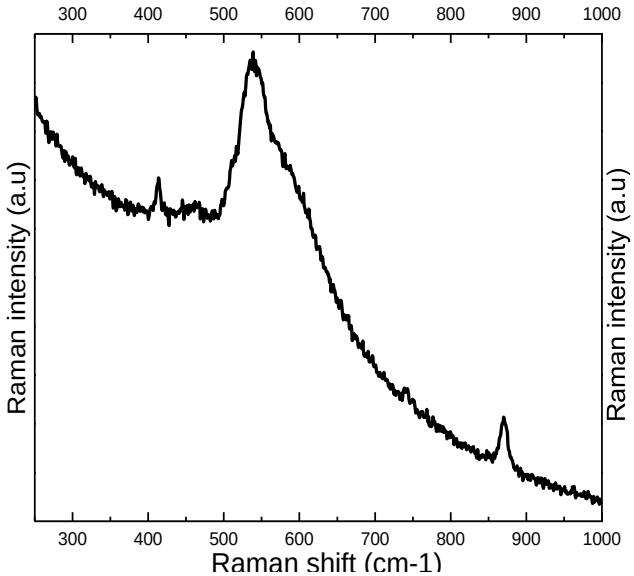

SERS Spectrum for Alloy 690
At E = -0.85V and pH=6.2

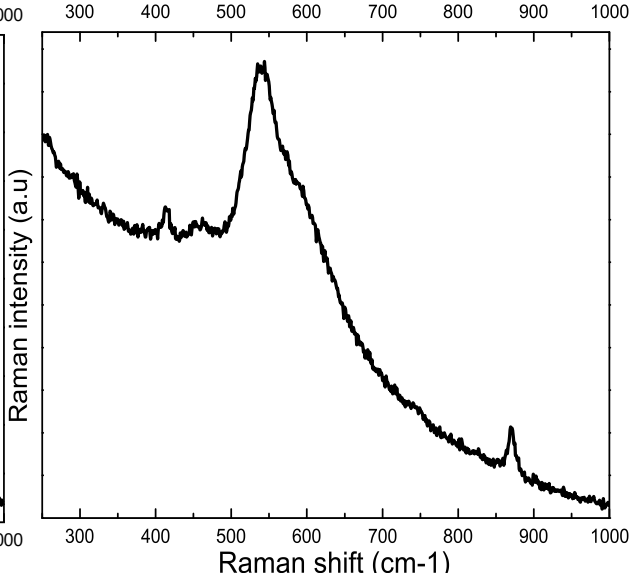

SERS Spectrum for Alloy 690
At E = -0.8V and pH=6.2

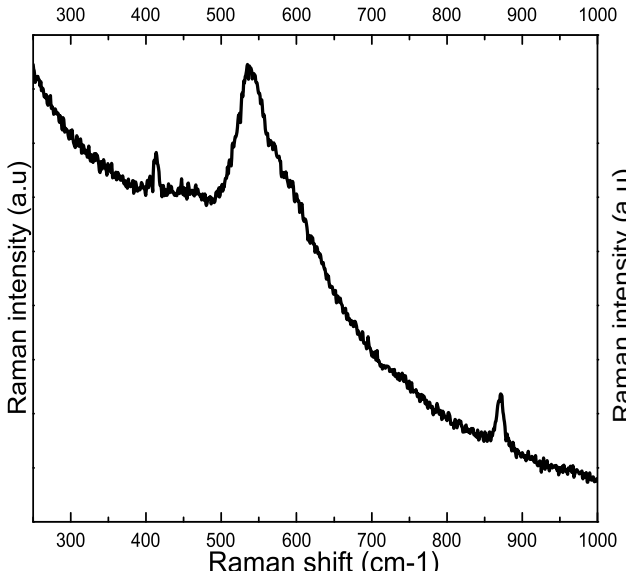

SERS Spectrum for Alloy 690
At E = -0.75V and pH=6.2

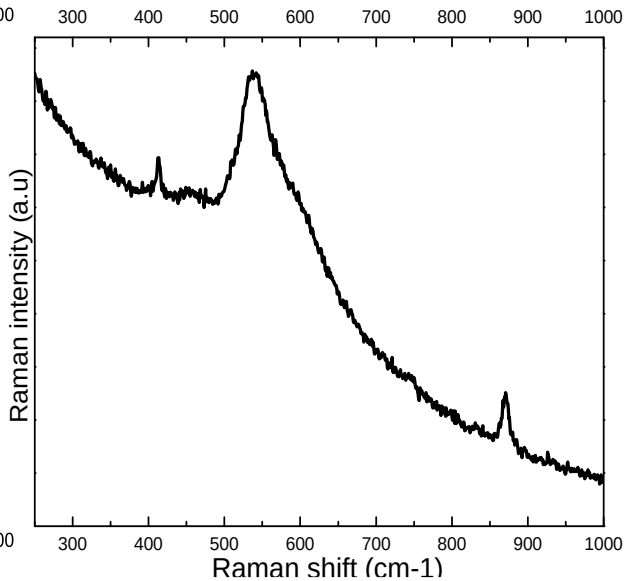

SERS Spectrum for Alloy 690
At E = -0.7V and pH=6.2

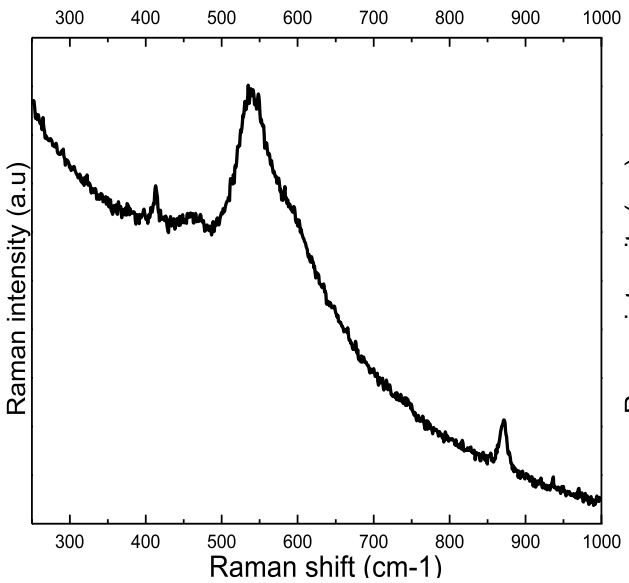

SERS Spectrum for Alloy 690
At E = -0.65V and pH=6.2

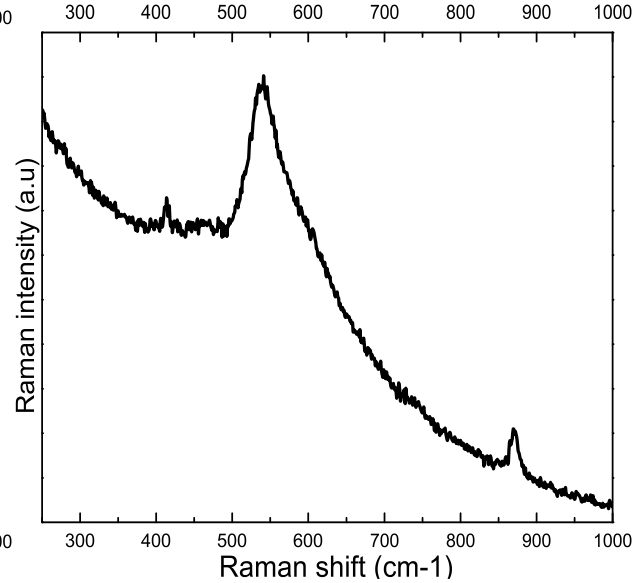

SERS Spectrum for Alloy 690
At E = -0.6V and pH=6.2

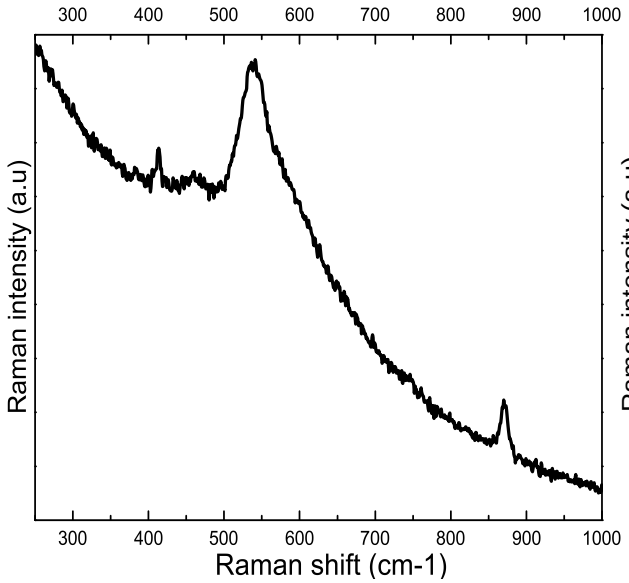

SERS Spectrum for Alloy 690
At E = -0.55V and pH=6.2

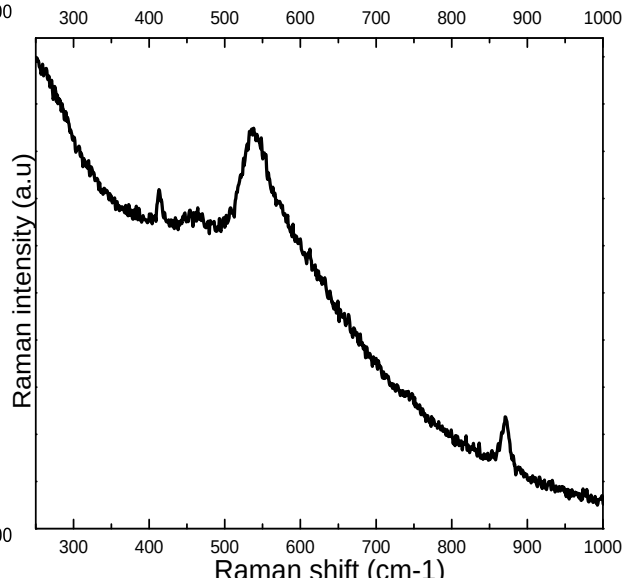

SERS Spectrum for Alloy 690
At E = -0.5V and pH=6.2

Appendix IV. SERS spectra of Ni, Cr, Ni-5Cr-8Fe, Ni-10Cr-8Fe, Ni-10Cr, and Ni-20Cr

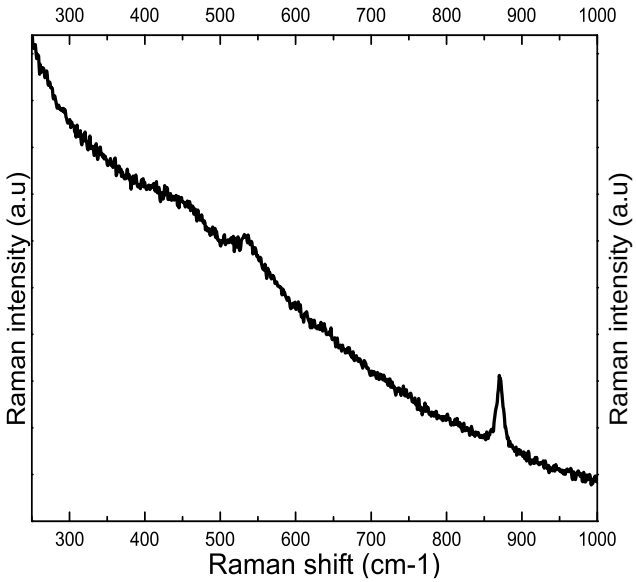

SERS Spectrum for Nickel at E = -0.9V

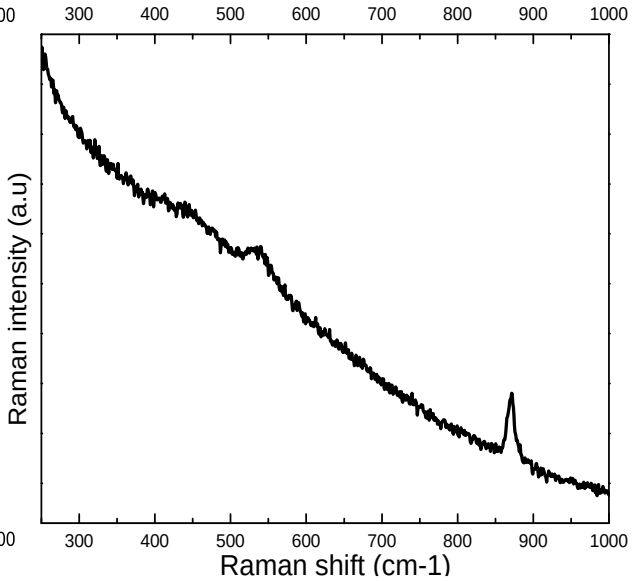

SERS Spectrum for Nickel at E = -0.85V

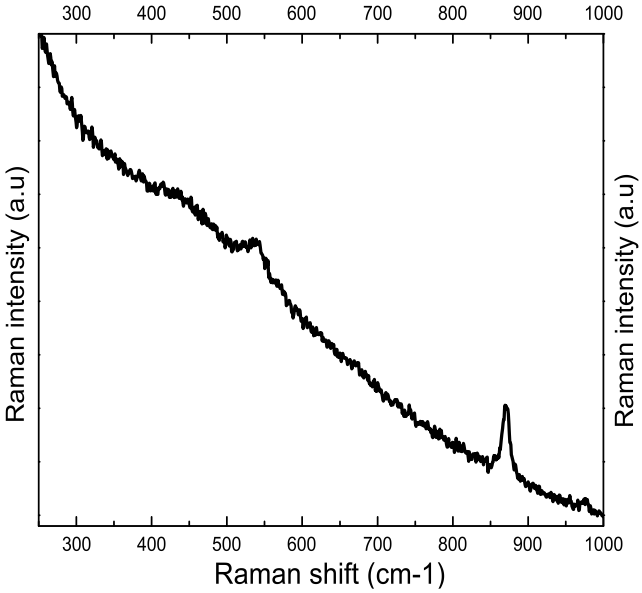

SERS Spectrum for Nickel at E = -0.8V

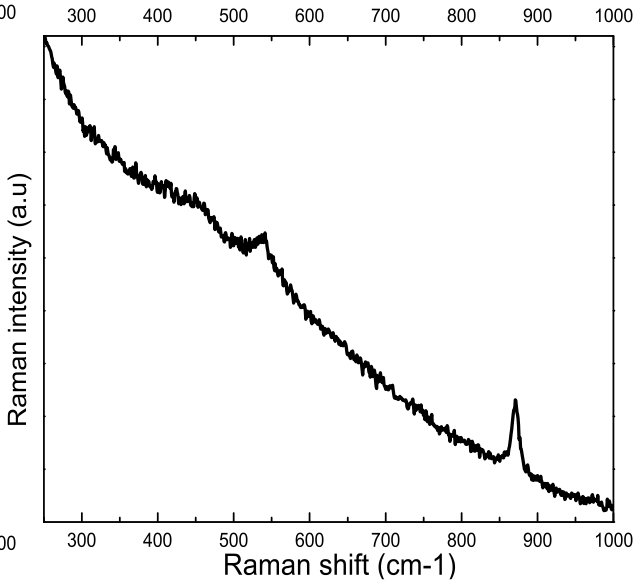

SERS Spectrum for Nickel at E = -0.75V

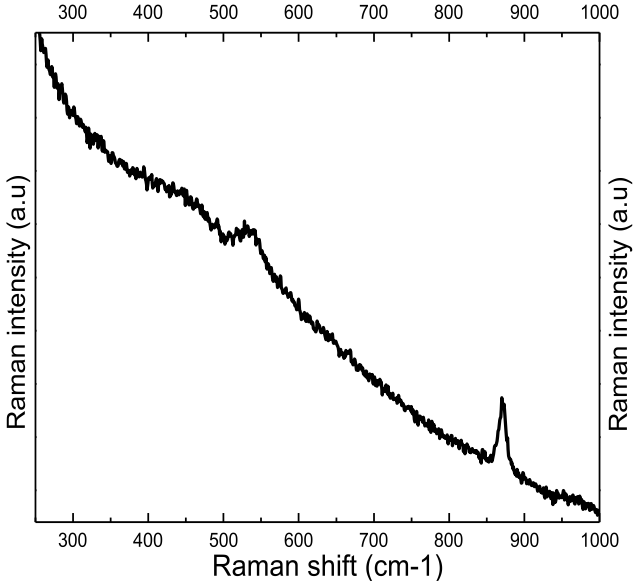

SERS Spectrum for Nickel at E = -0.7V

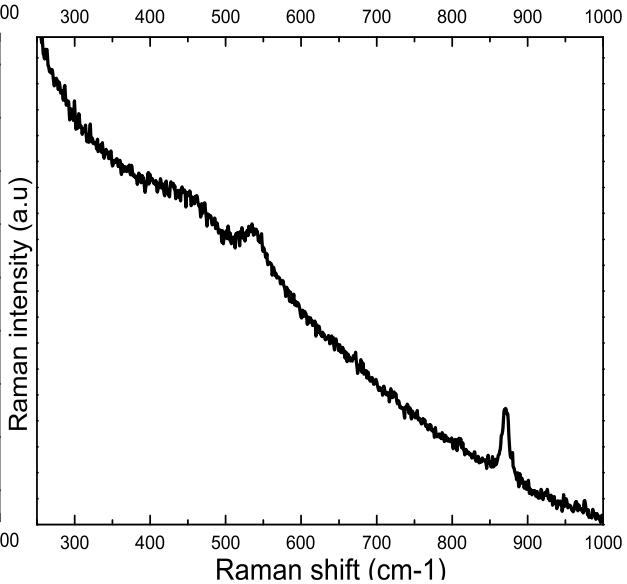

SERS Spectrum for Nickel at E = -0.65V

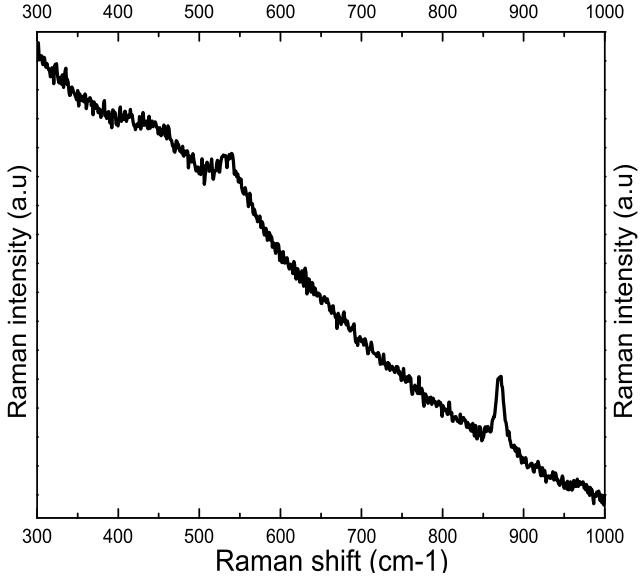

SERS Spectrum for Nickel at E = -0.6V

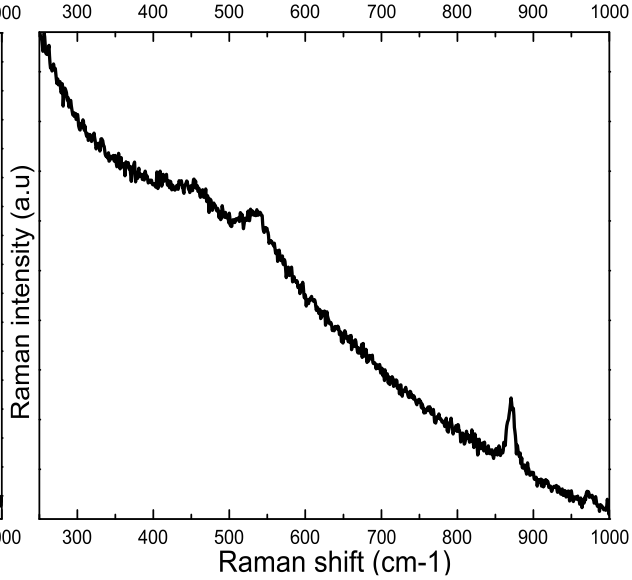

SERS Spectrum for Nickel at E = -0.55V

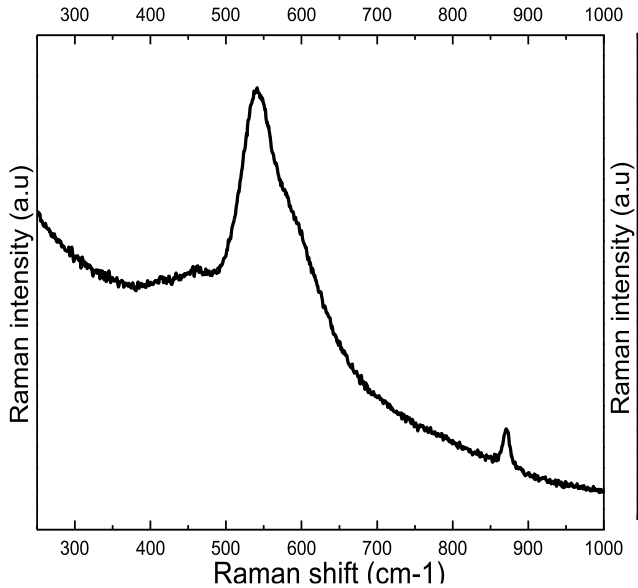

SERS Spectrum for Chromium at E = -0.9V

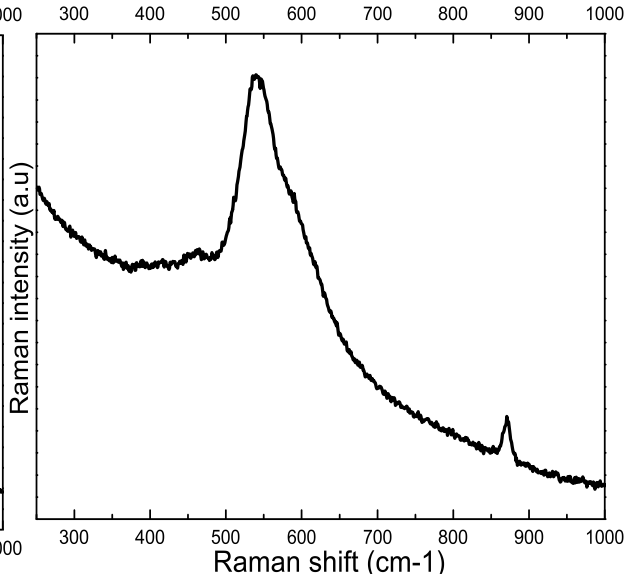

SERS Spectrum for Chromium at E = -0.85V

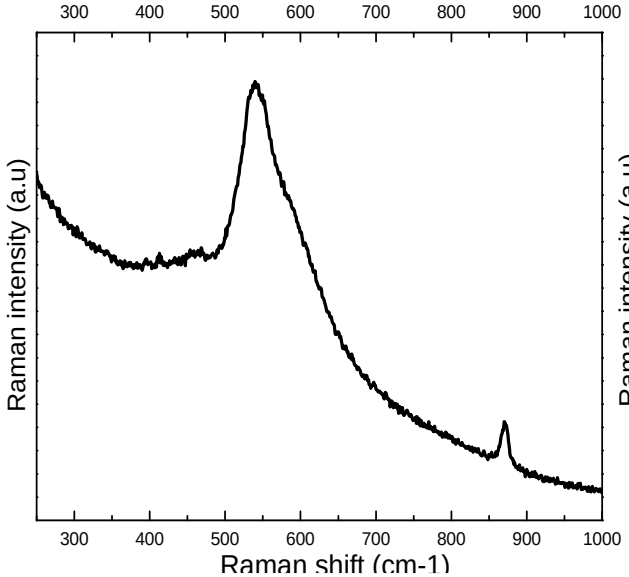

SERS Spectrum for Chromium at E = -0.8V

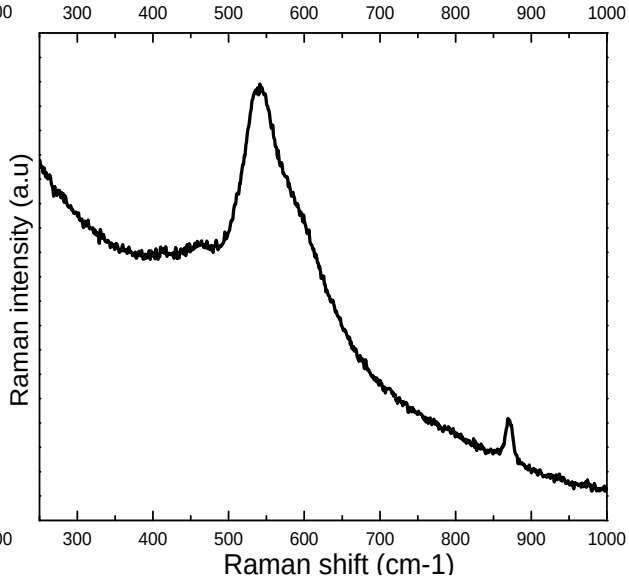

SERS Spectrum for Chromium at E = -0.75V

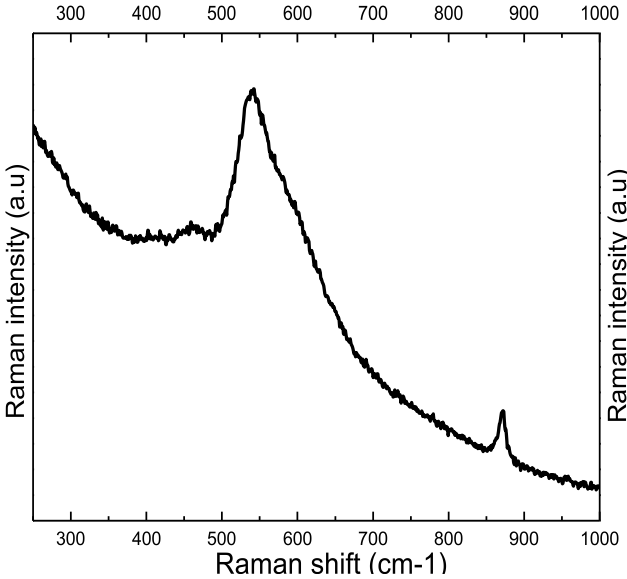

SERS Spectrum for Chromium at E = -0.7V

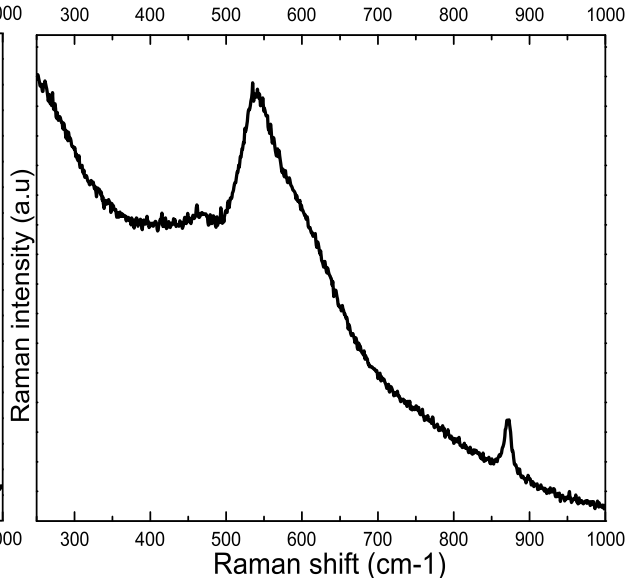

SERS Spectrum for Chromium at E = -0.65V

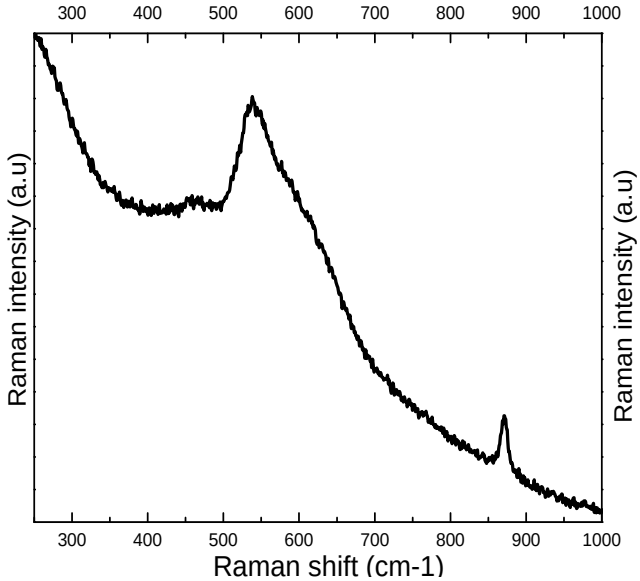

SERS Spectrum for Chromium at E = -0.6V

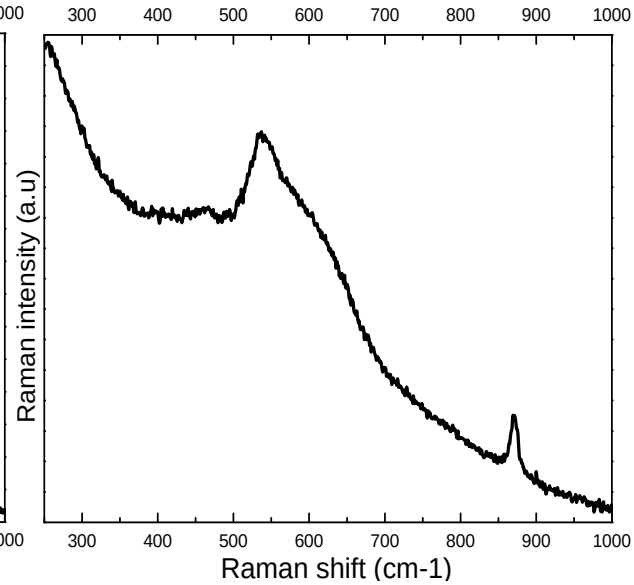

SERS Spectrum for Chromium at E = -0.55V

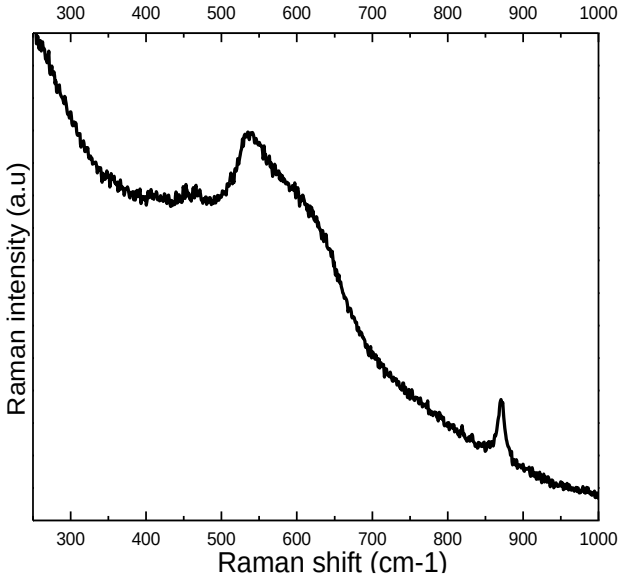

SERS Spectrum for Chromium at E = -0.5V

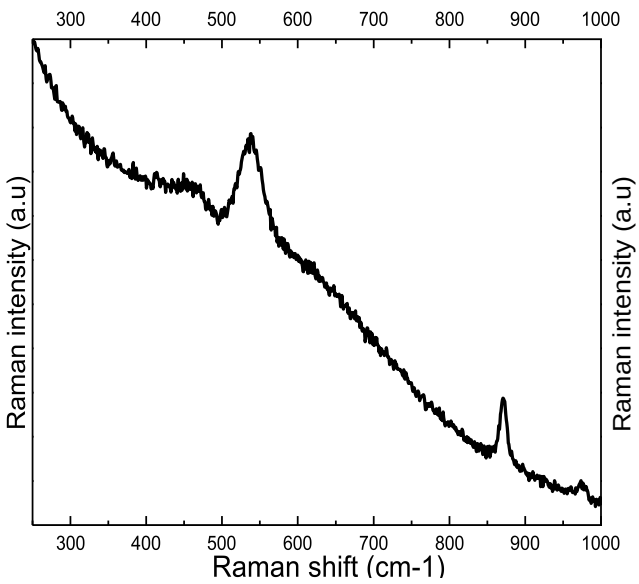

SERS Spectrum for Ni-5Cr-8Fe at E = -0.9V

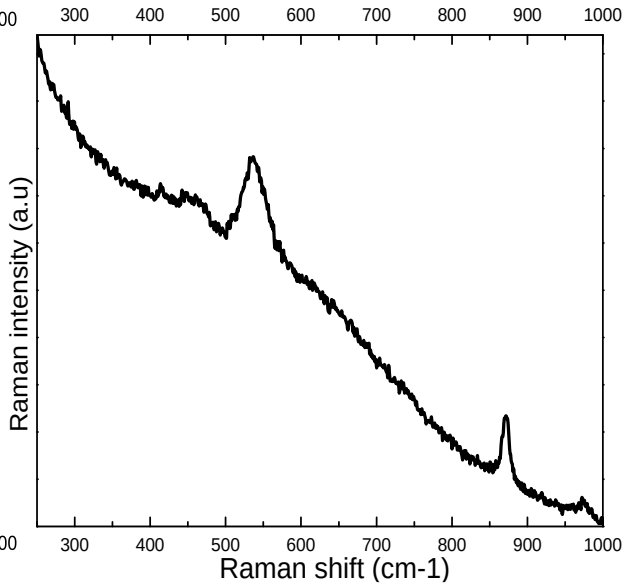

SERS Spectrum for Ni-5Cr-8Fe at E = -0.85V

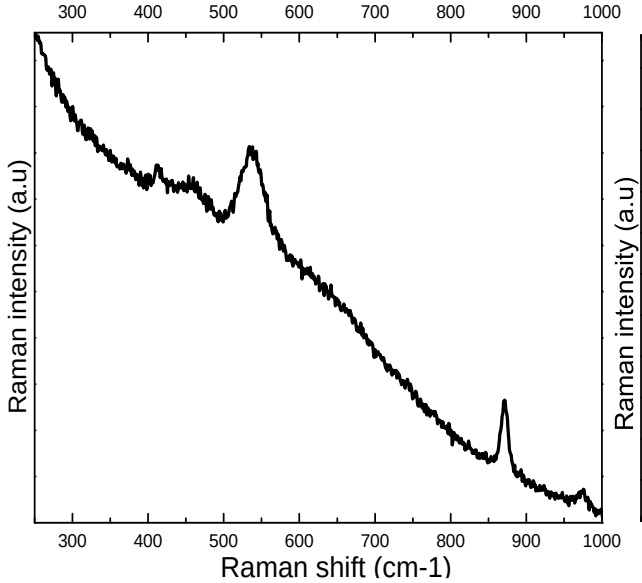

SERS Spectrum for Ni-5Cr-8Fe at E = -0.8V

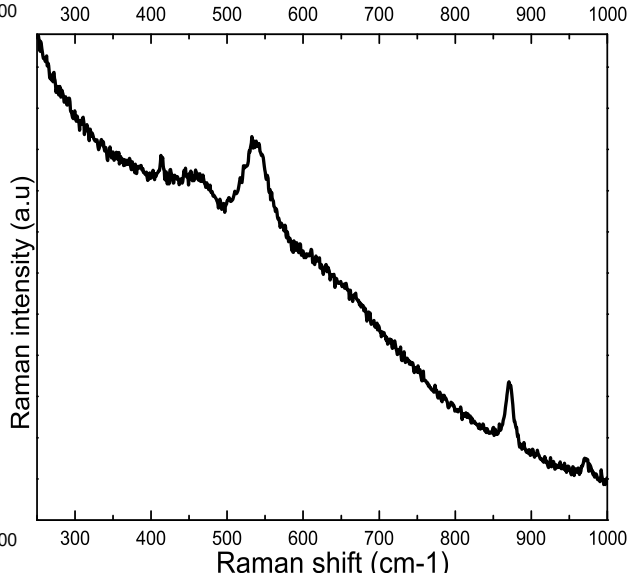

SERS Spectrum for Ni-5Cr-8Fe at E = -0.75V

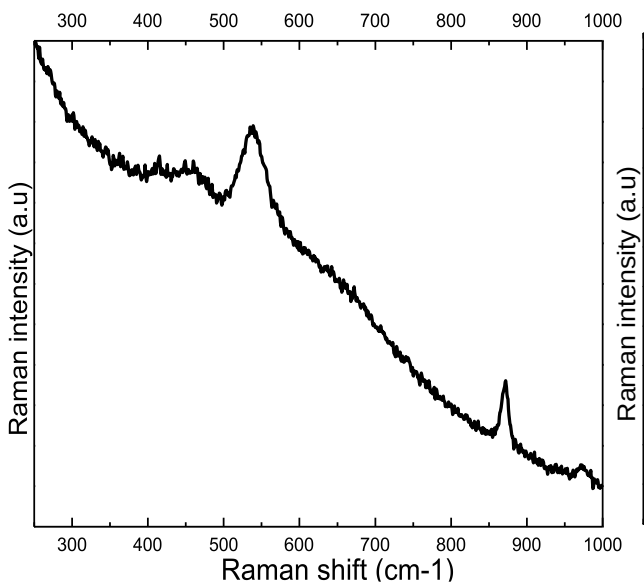

SERS Spectrum for Ni-5Cr-8Fe at E = -0.7V

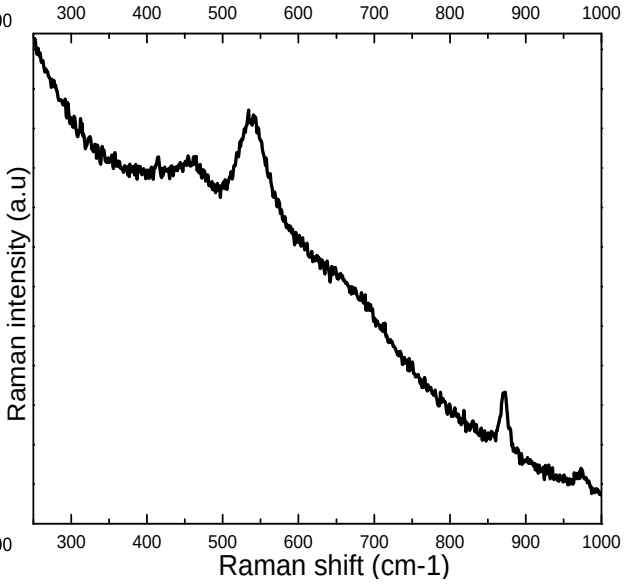

SERS Spectrum for Ni-5Cr-8Fe at E = -0.65V

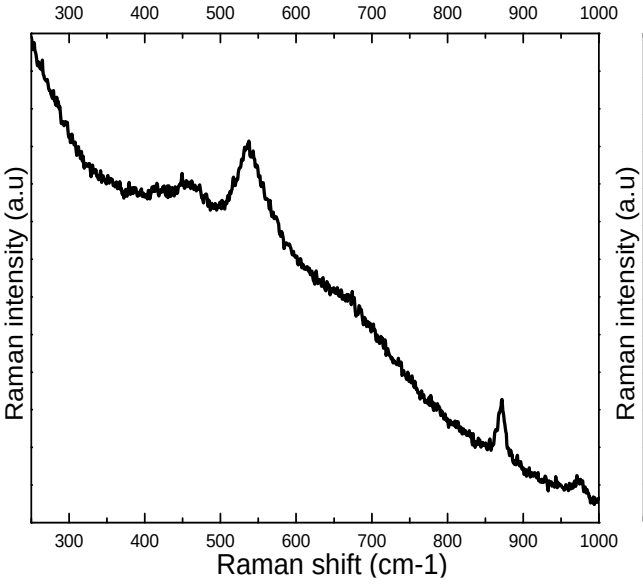

SERS Spectrum for Ni-5Cr-8Fe at E = -0.6V

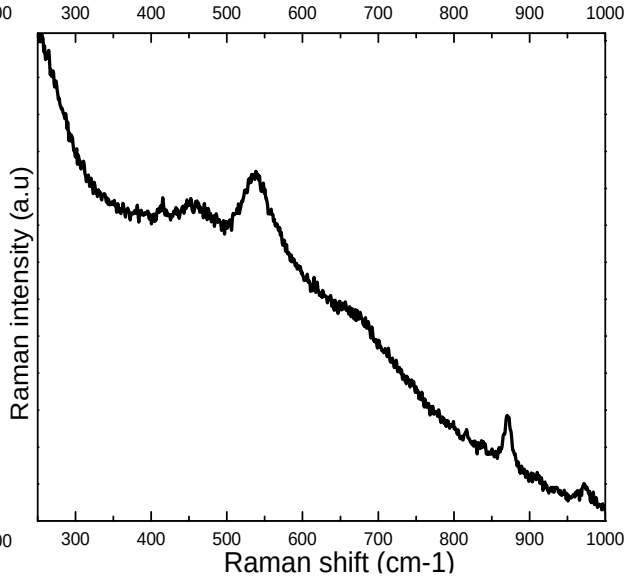

SERS Spectrum for Ni-5Cr-8Fe at E = -0.55V

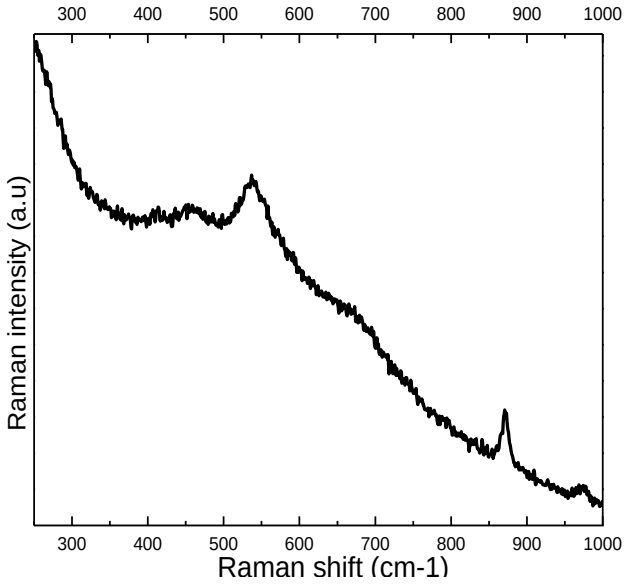

SERS Spectrum for Ni-5Cr-8Fe at E = -0.5V

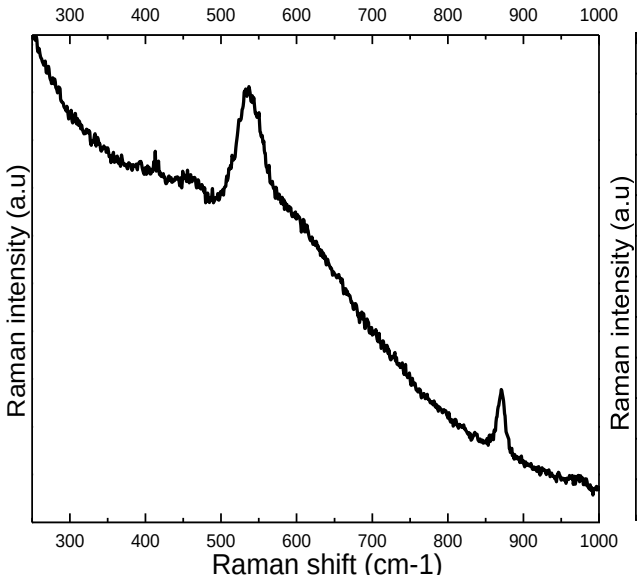

SERS Spectrum for Ni-10Cr-8Fe at E = -0.9V

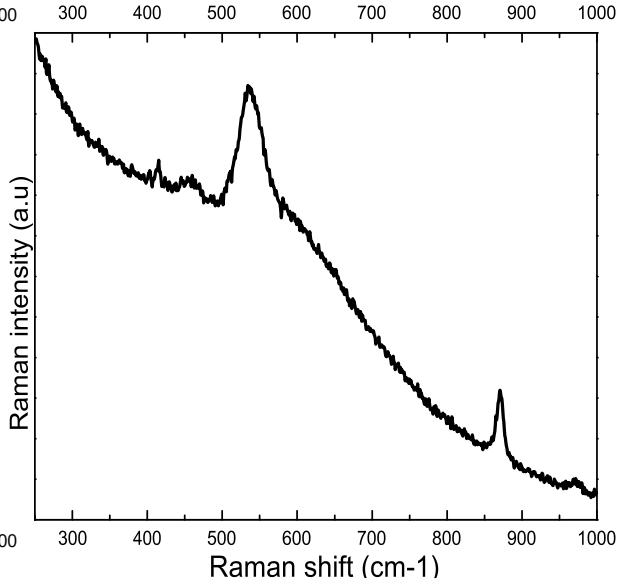

SERS Spectrum for Ni-10Cr-8Fe at E = -0.85V

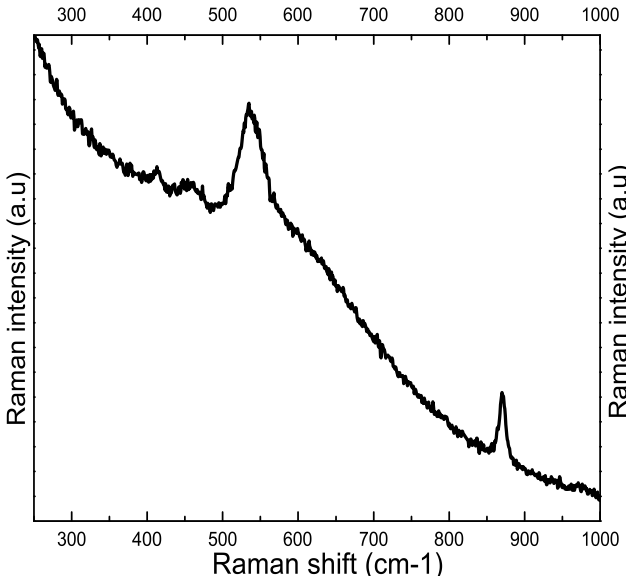

SERS Spectrum for Ni-10Cr-8Fe at E = -0.8V

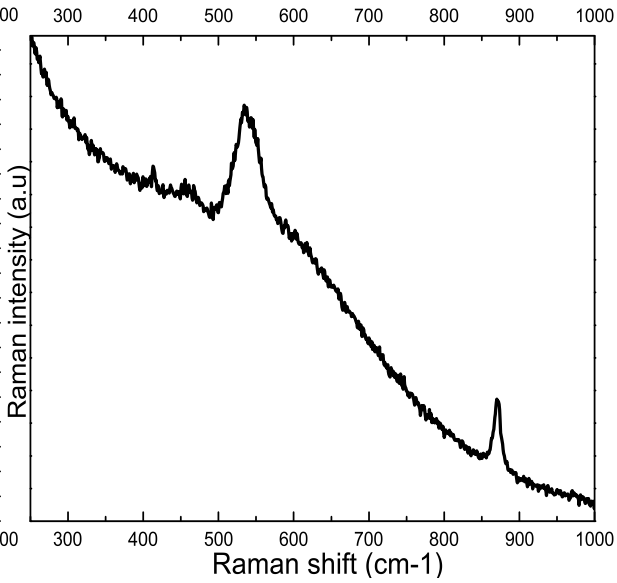

SERS Spectrum for Ni-10Cr-8Fe at E = -0.75V

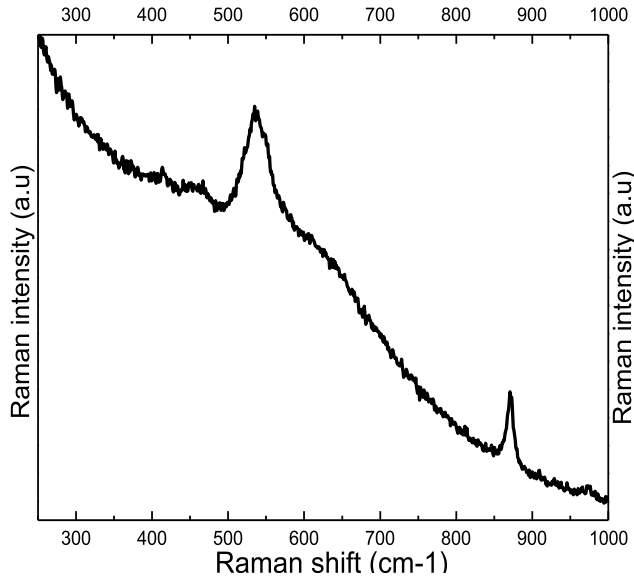

SERS Spectrum for Ni-10Cr-8Fe at E = -0.7V

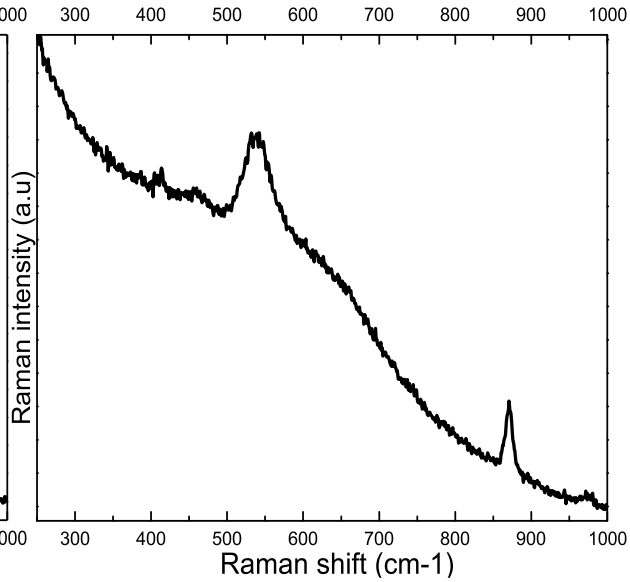

SERS Spectrum for Ni-10Cr-8Fe at E = -0.65V

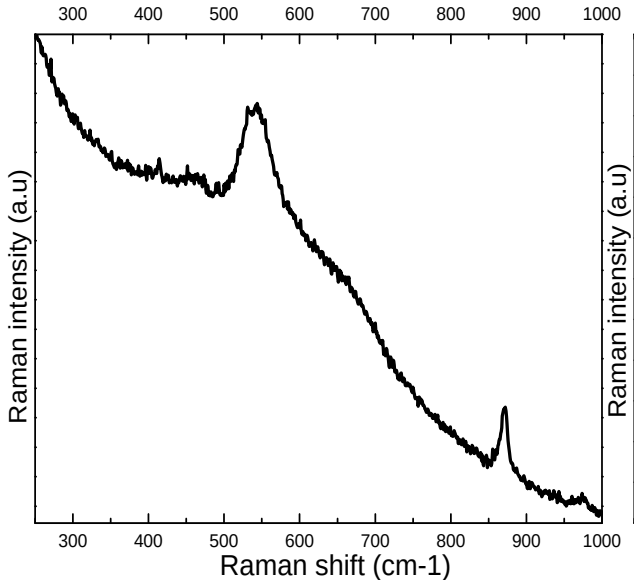

SERS Spectrum for Ni-10Cr-8Fe at E = -0.6V

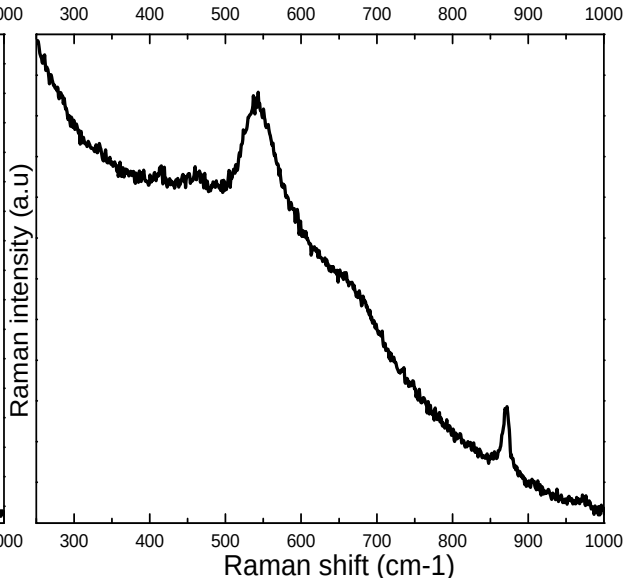

SERS Spectrum for Ni-10Cr-8Fe at E = -0.55V

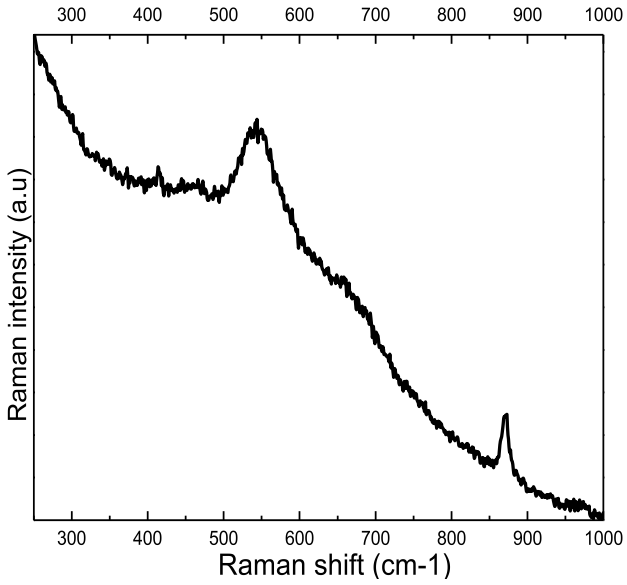

SERS Spectrum for Ni-10Cr-8Fe at E = -0.5V

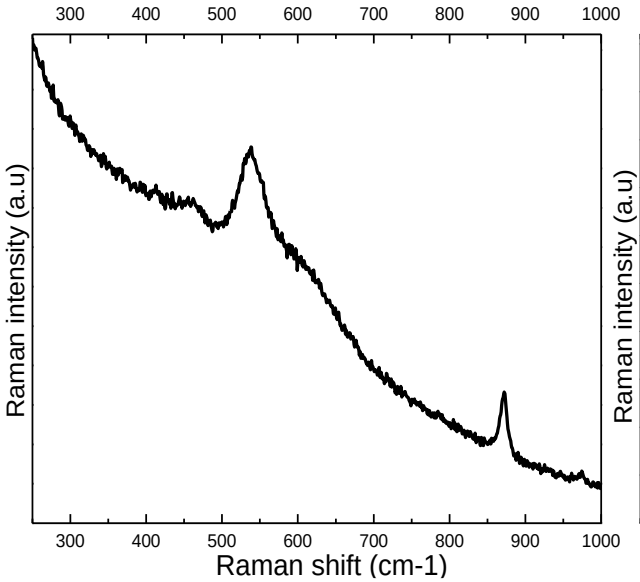

SERS Spectrum for Ni-10Cr at E = -0.9V

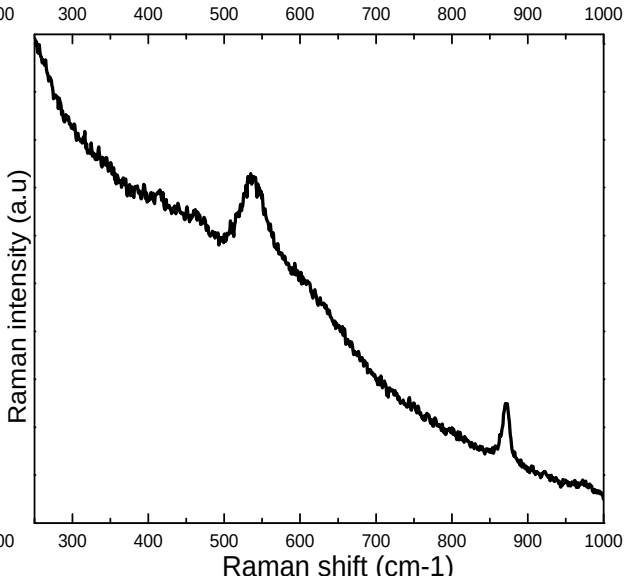

SERS Spectrum for Ni-10Cr at E = -0.85V

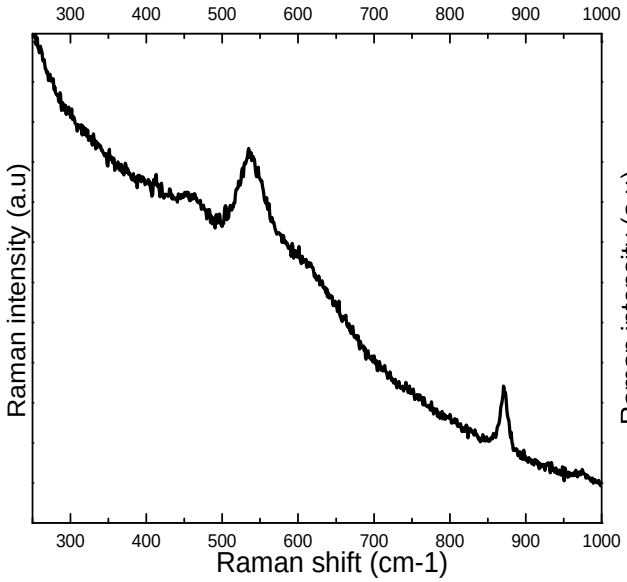

SERS Spectrum for Ni-10Cr at E = -0.8V

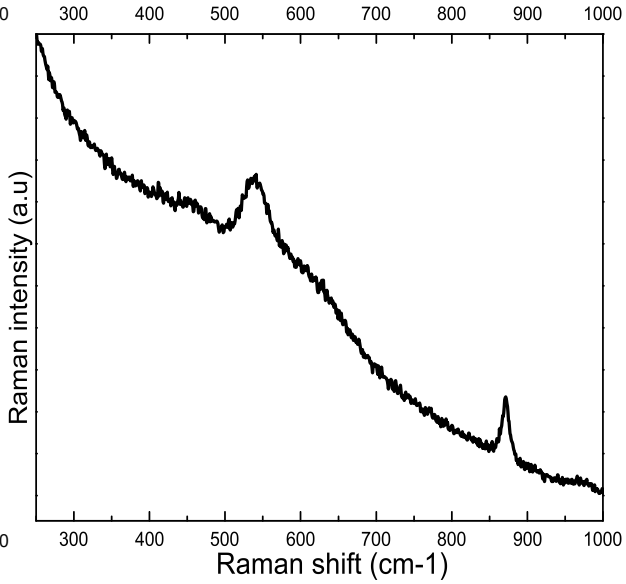

SERS Spectrum for Ni-10Cr at E = -0.75V

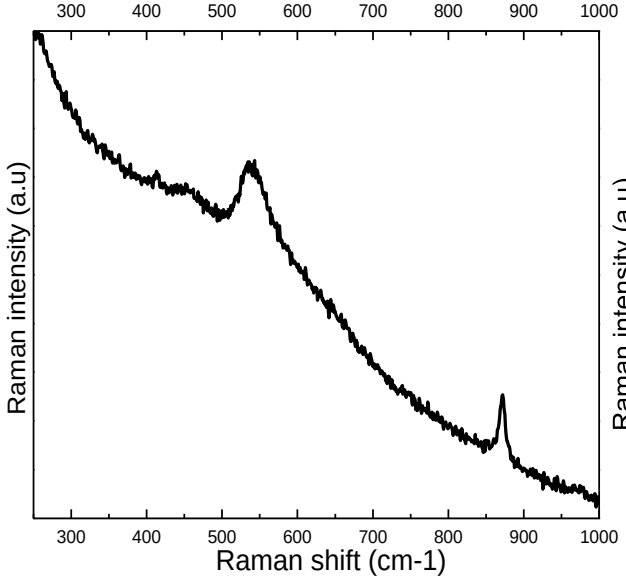

SERS Spectrum for Ni-10Cr at E = -0.7V

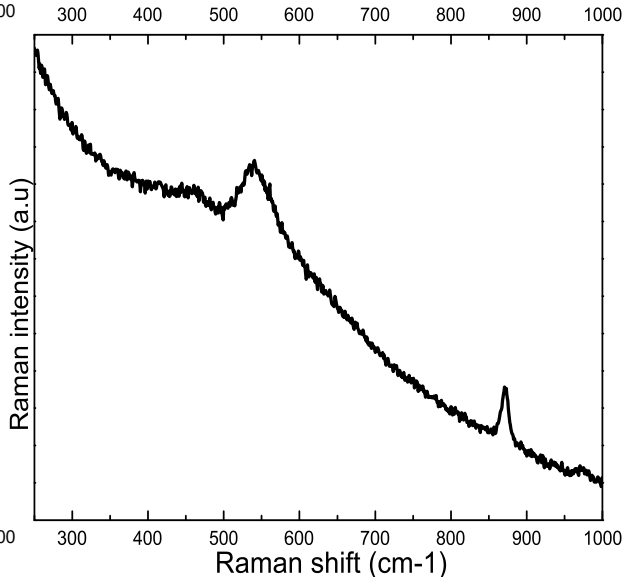

SERS Spectrum for Ni-10Cr at E = -0.65V

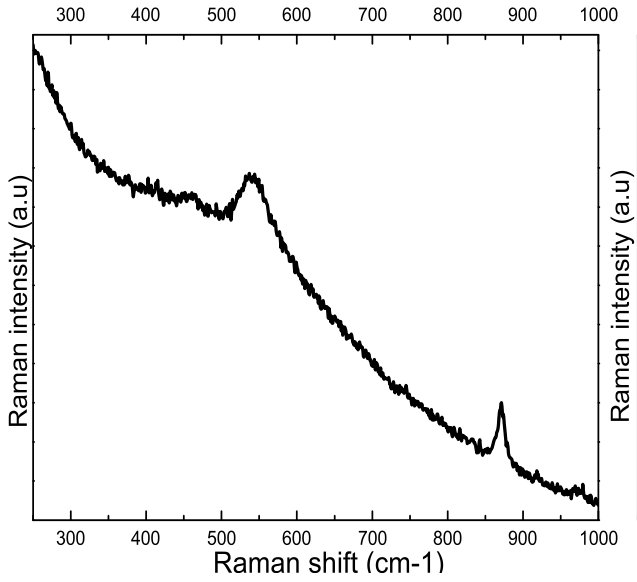

SERS Spectrum for Ni-10Cr at E = -0.6V

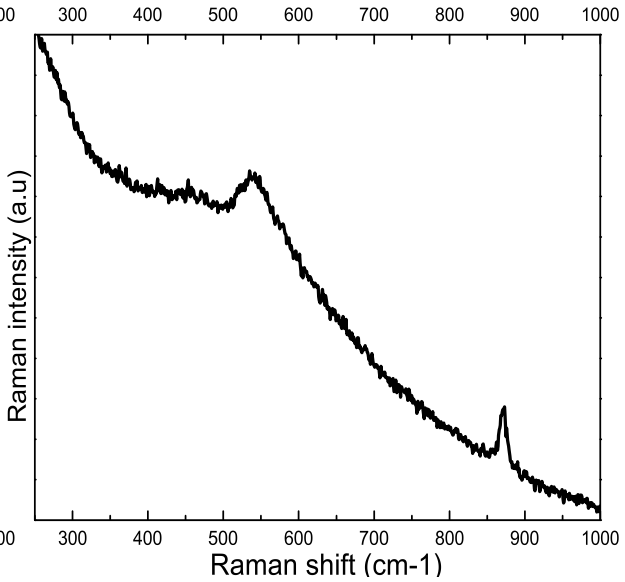

SERS Spectrum for Ni-10Cr at E = -0.55V

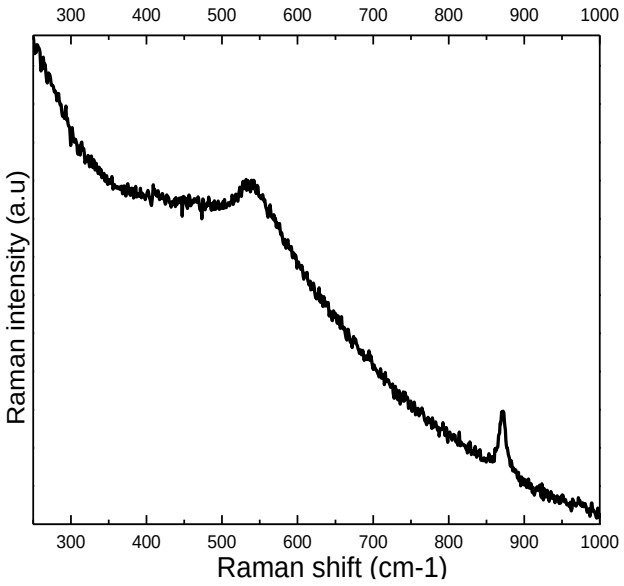

SERS Spectrum for Ni-10Cr at E = -0.5V

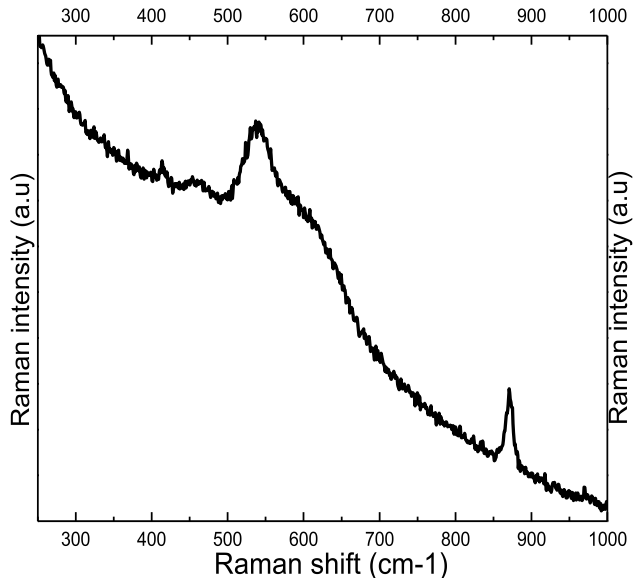

SERS Spectrum for Ni-20Cr at E = -0.9V

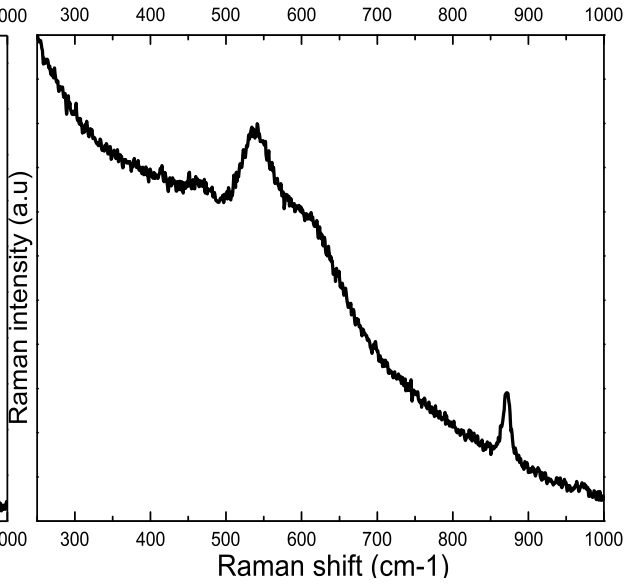

SERS Spectrum for Ni-20Cr at E = -0.85V

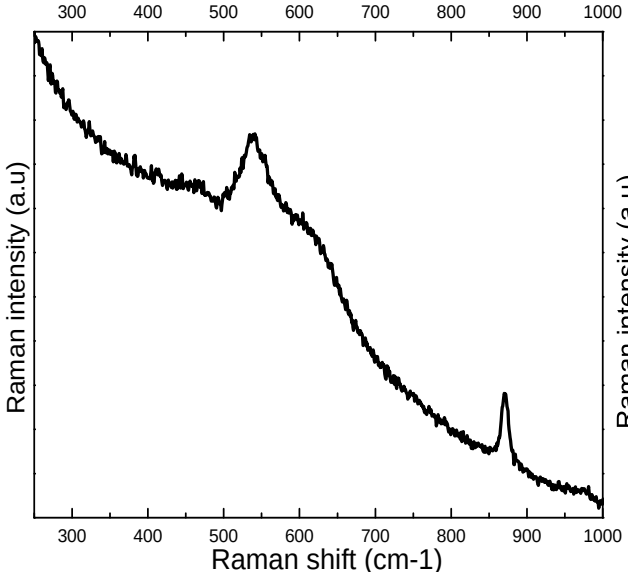

SERS Spectrum for Ni-20Cr at E = -0.8V

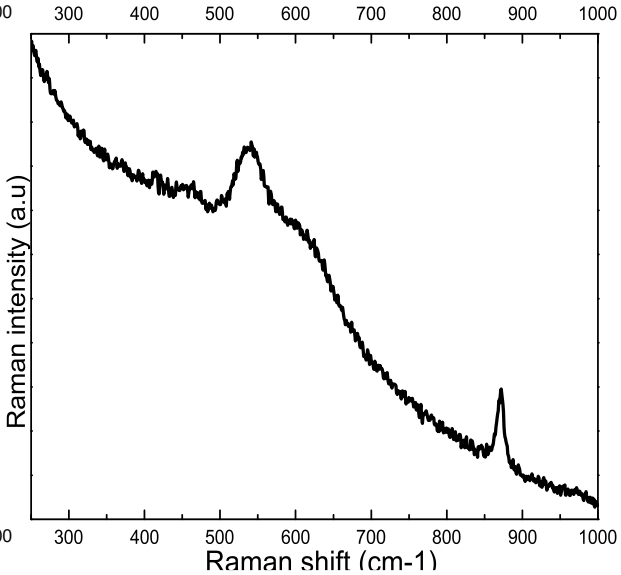

SERS Spectrum for Ni-20Cr at E = -0.75V

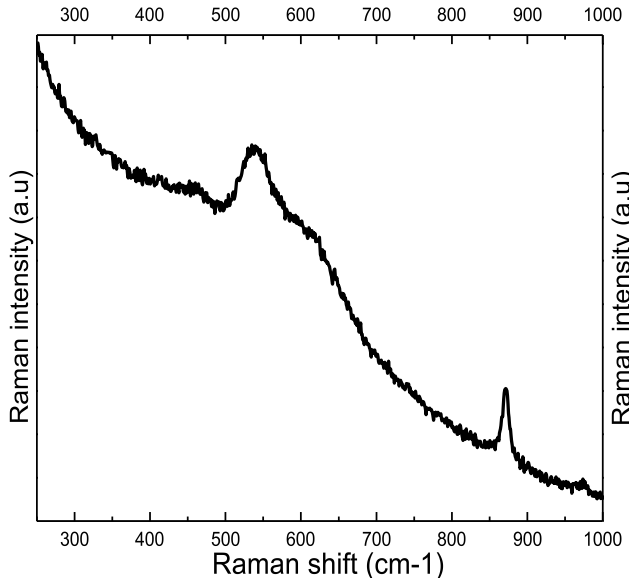

SERS Spectrum for Ni-20Cr at E = -0.7V

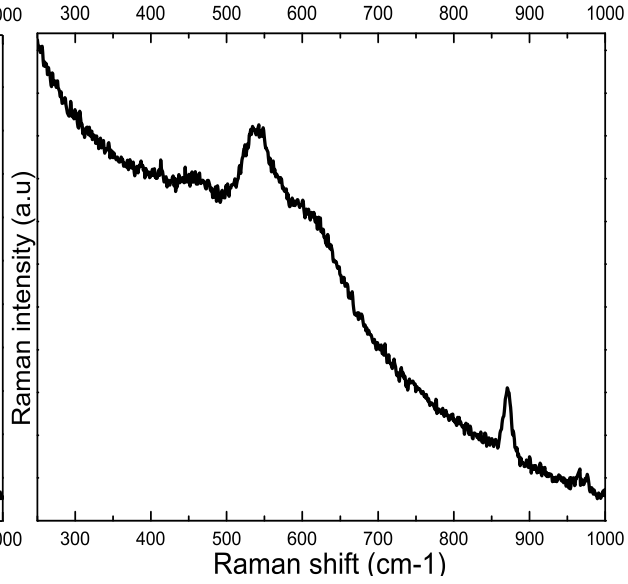

SERS Spectrum for Ni-20Cr at E = -0.65V

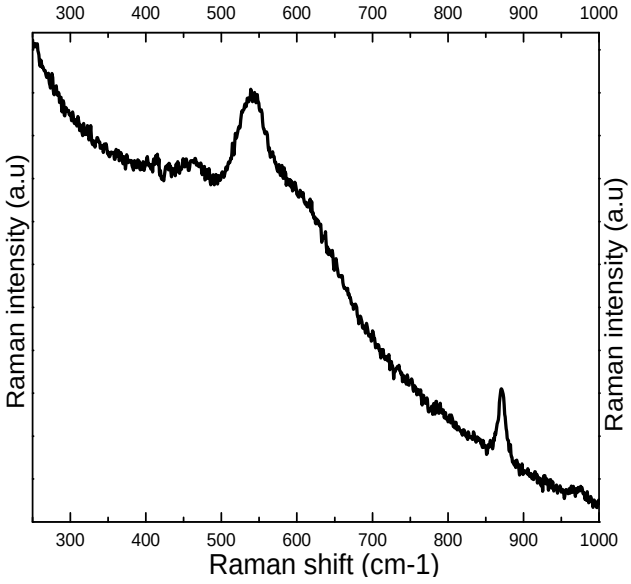

SERS Spectrum for Ni-20Cr at E = -0.6V

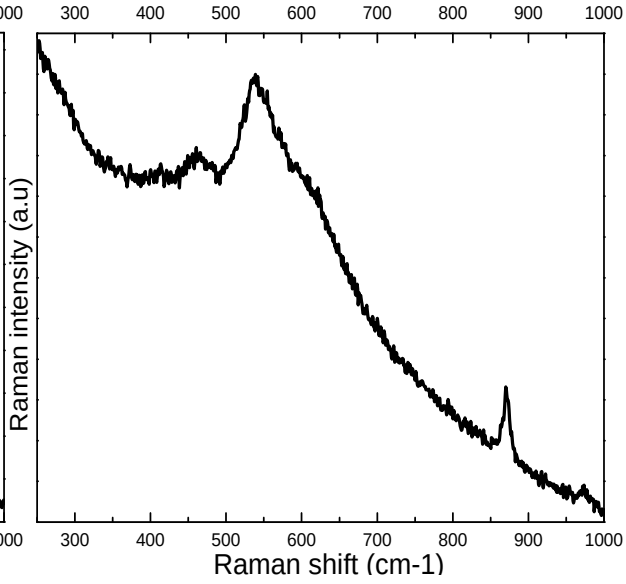

SERS Spectrum for Ni-20Cr at E = -0.5V

Appendix V. SERS Result of Ni, Cr, Ni-5Cr-8Fe, Ni-10Cr-8Fe, Ni-10Cr, and Ni-20Cr (After Background Subtraction and Peak Fitting)

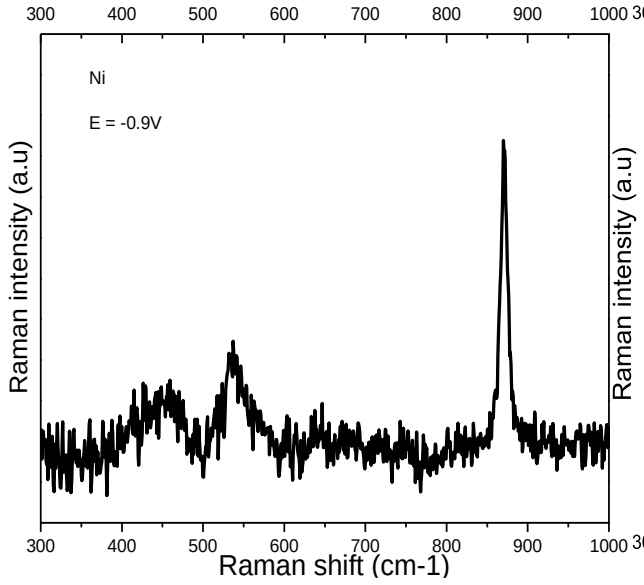

SERS Result for Nickel at E = -0.9V

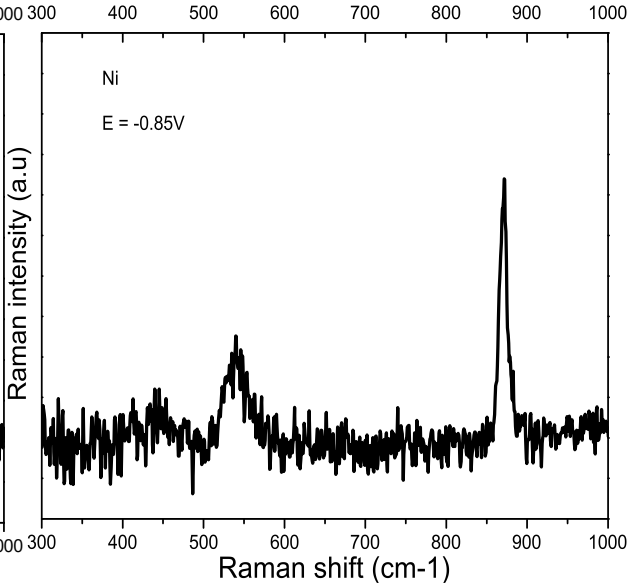

SERS Result for Nickel at E = -0.9V

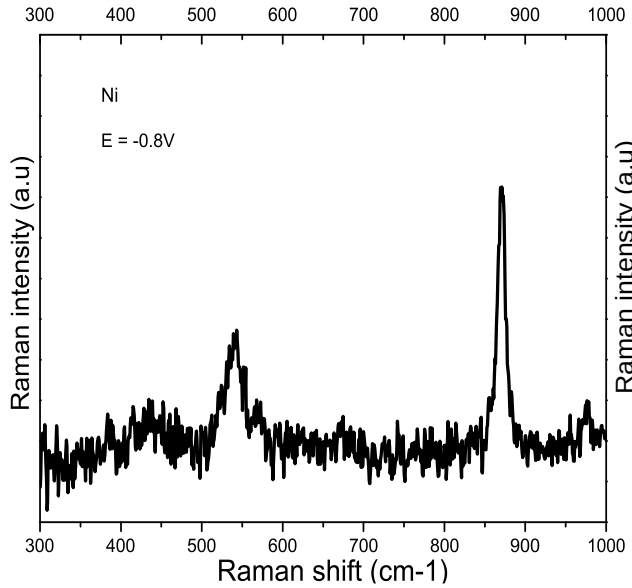

SERS Result for Nickel at E = -0.8V

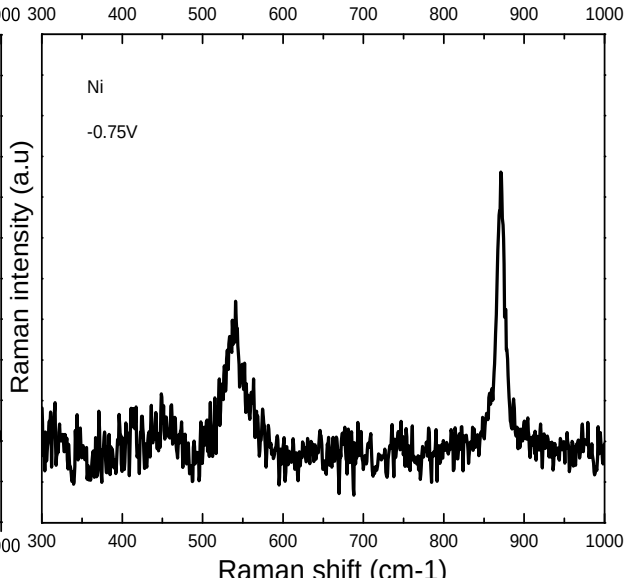

SERS Result for Nickel at E = -0.75V

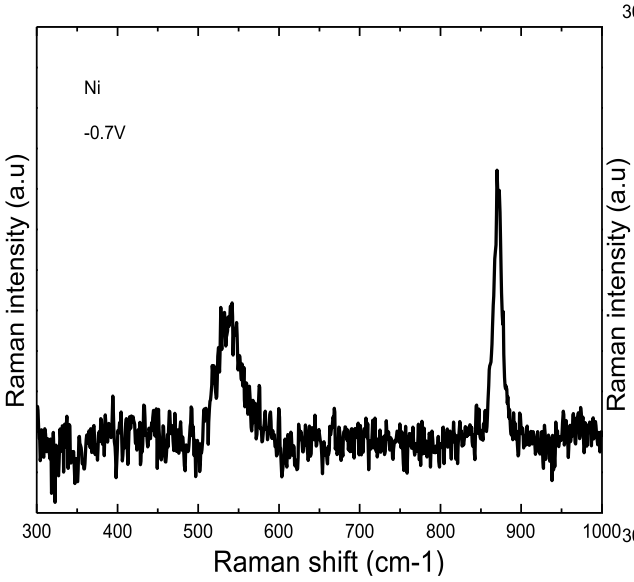

SERS Result for Nickel at E = -0.7V

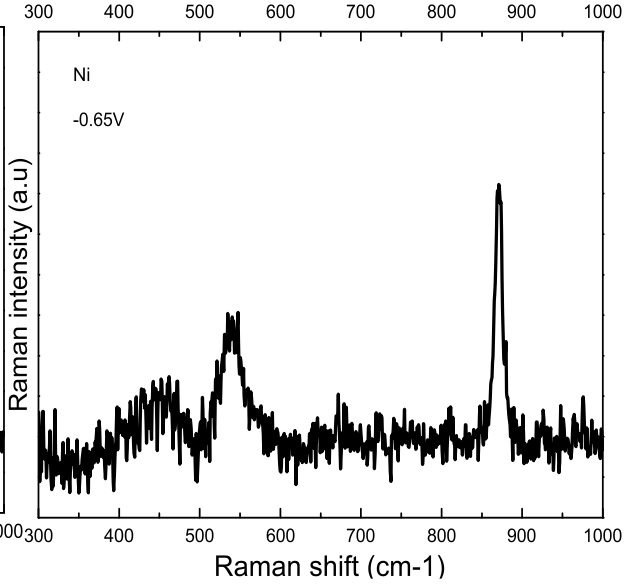

SERS Result for Nickel at E = -0.65V

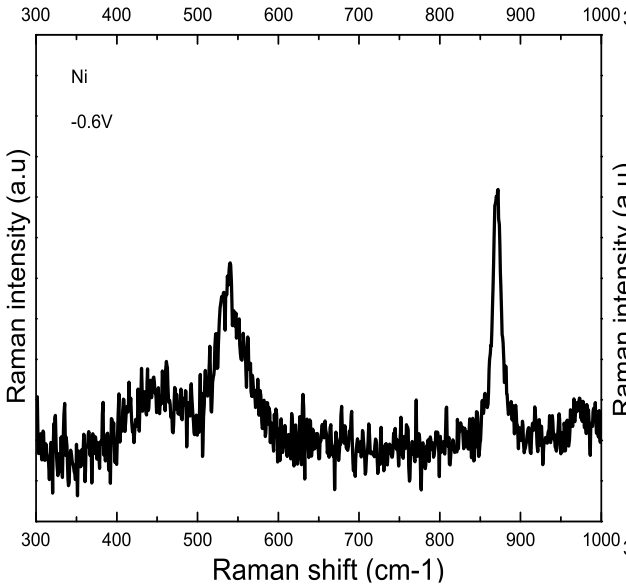

SERS Result for Nickel at E = -0.6V

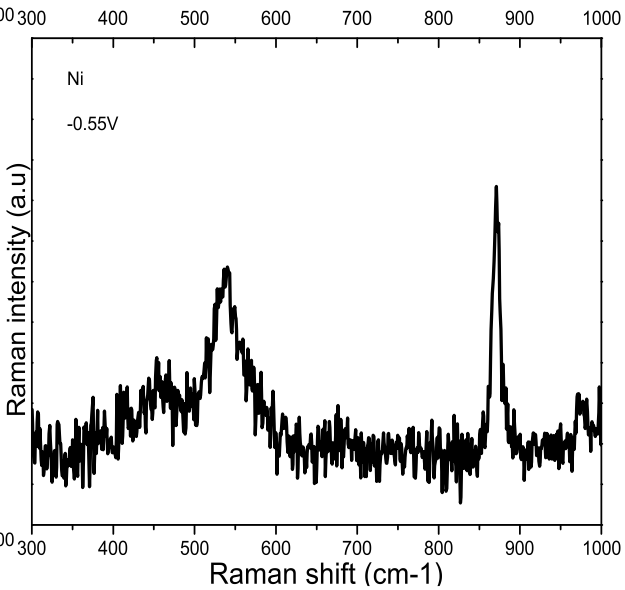

SERS Result for Nickel at E = -0.55V

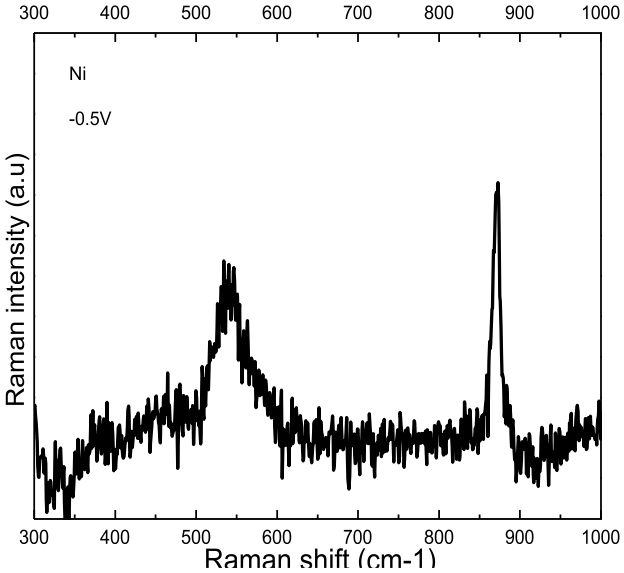

SERS Result for Nickel at E = -0.5V

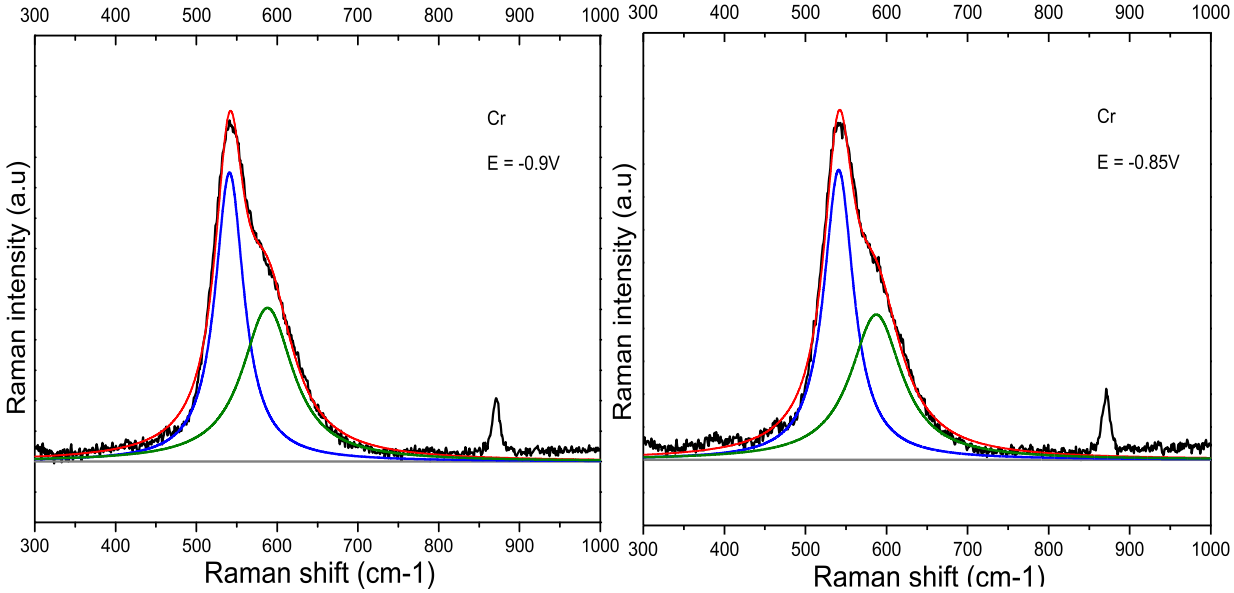

SERS Result for Chromium at E = -0.9V

SERS Result for Chromium at E = -0.85V

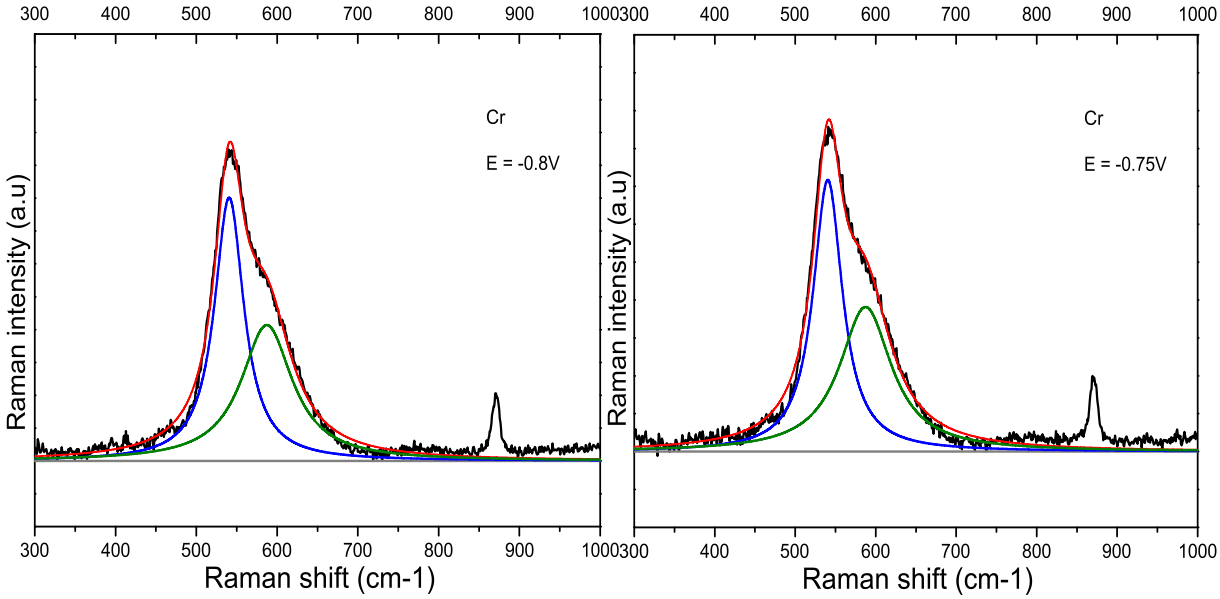

SERS Result for Chromium at E = -0.8V

SERS Result for Chromium at E = -0.75V

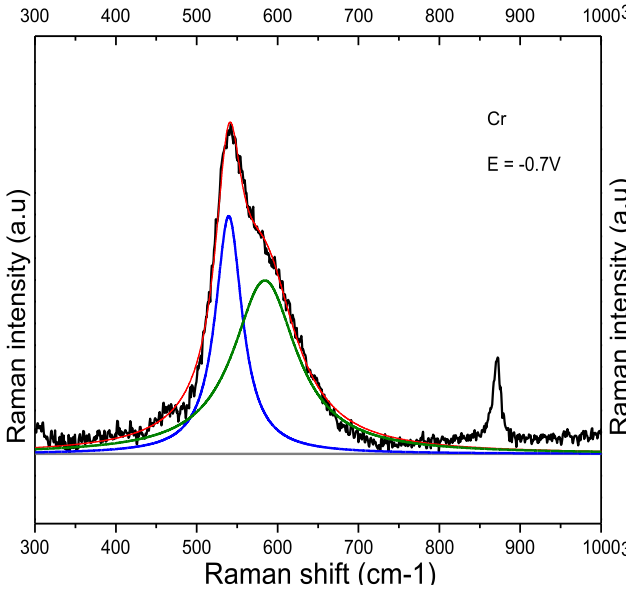

SERS Result for Chromium at E = -0.7V

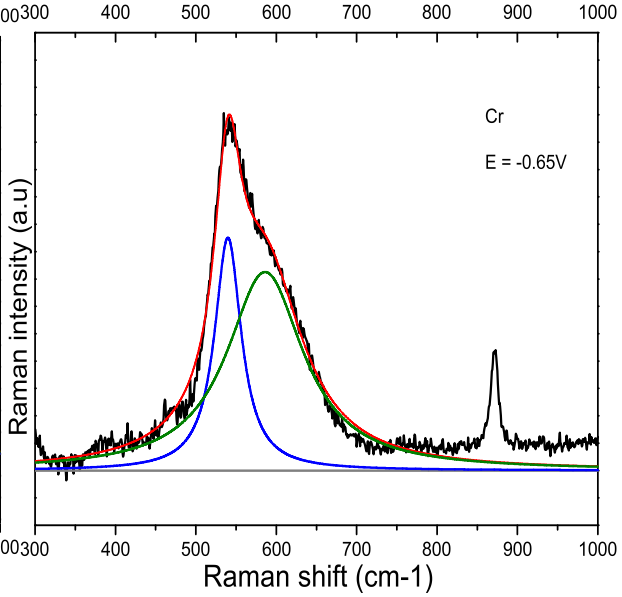

SERS Result for Chromium at E = -0.65V

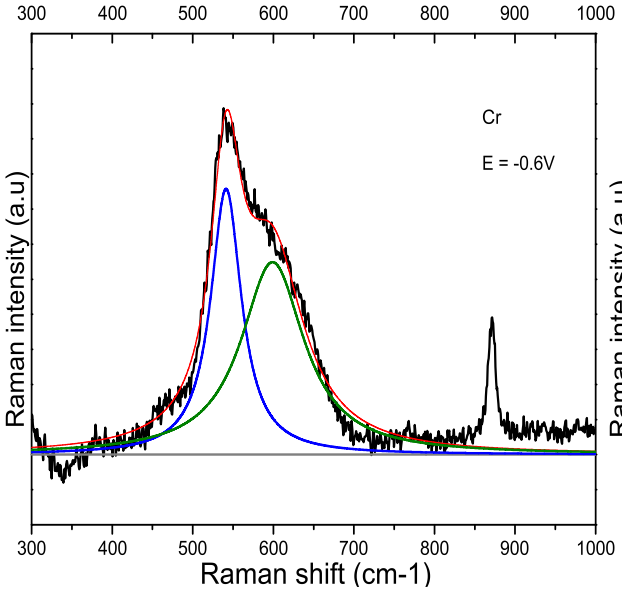

SERS Result for Chromium at E = -0.6V

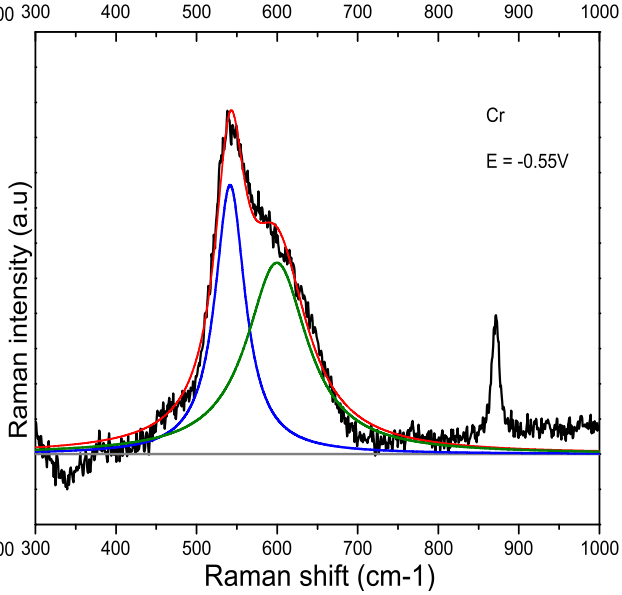

SERS Result for Chromium at E = -0.55V

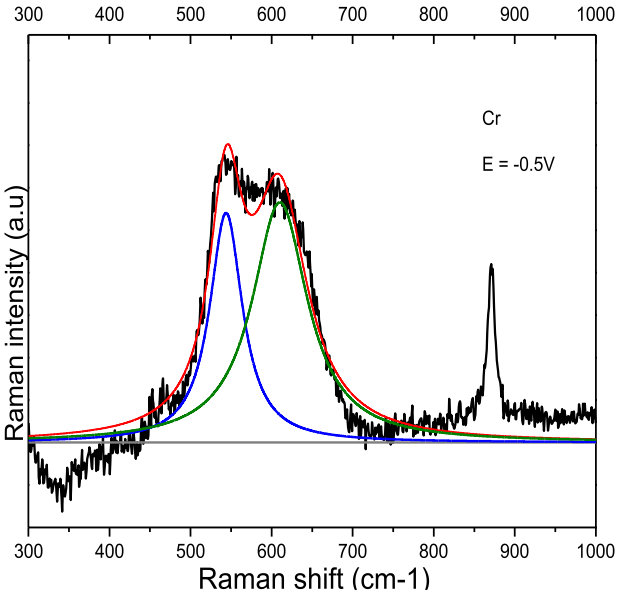

SERS Result for Chromium at E = -0.5V

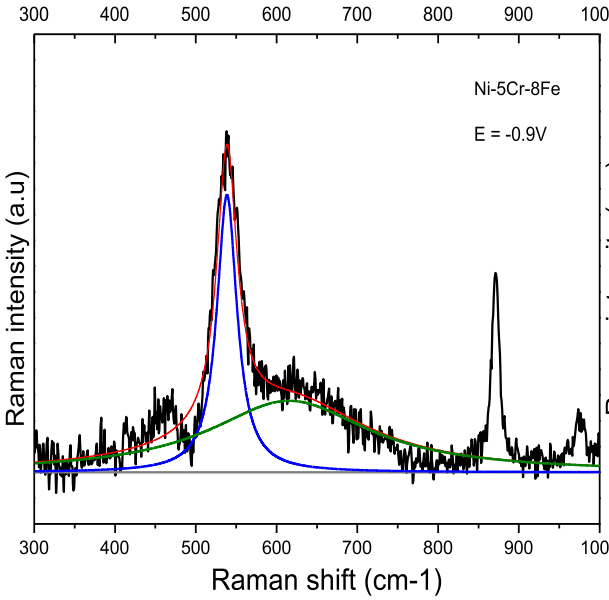

SERS Result for Ni-5Cr-8Fe at E = -0.9V

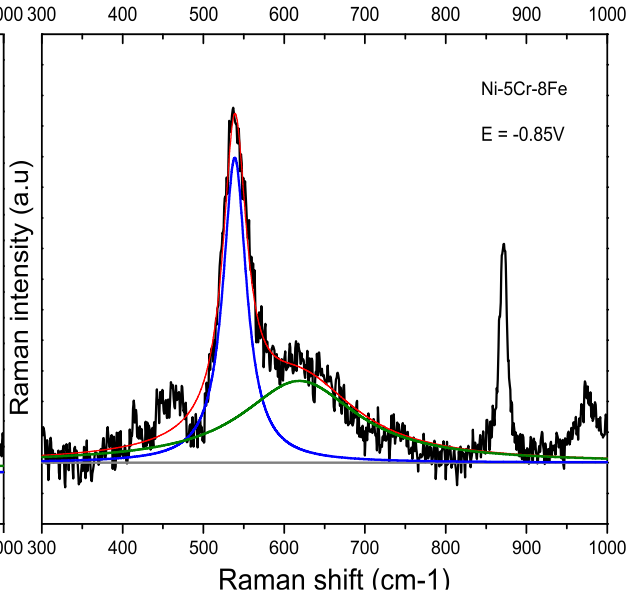

SERS Result for Ni-5Cr-8Fe at E = -0.85V

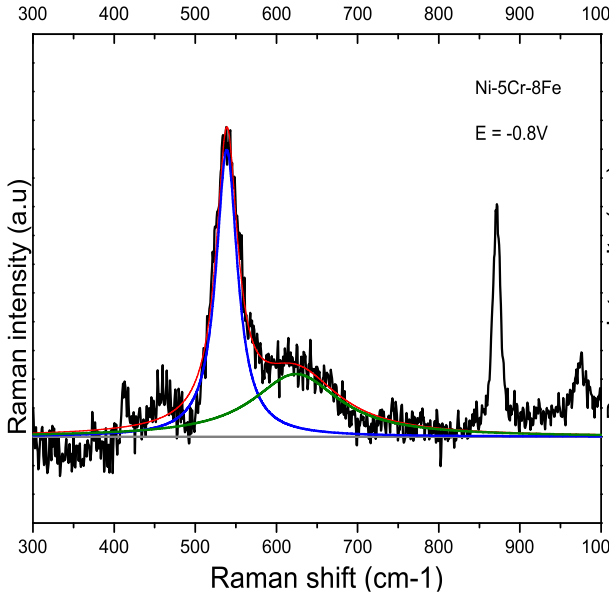

SERS Result for Ni-5Cr-8Fe at E = -0.8V

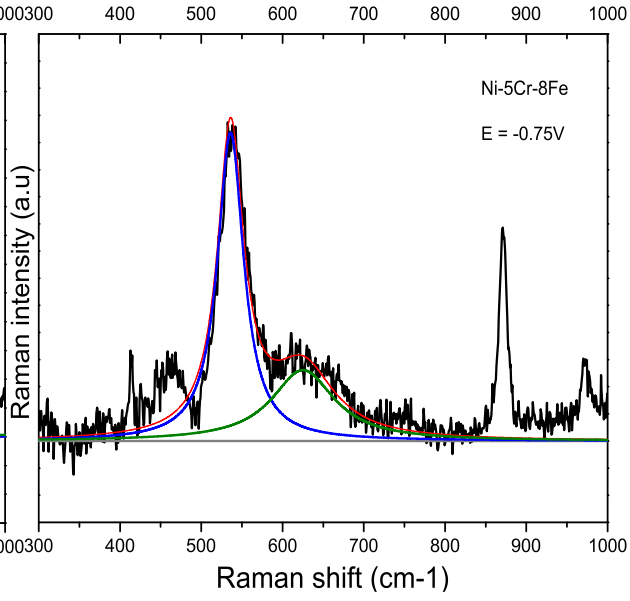

SERS Result for Ni-5Cr-8Fe at E = -0.75V

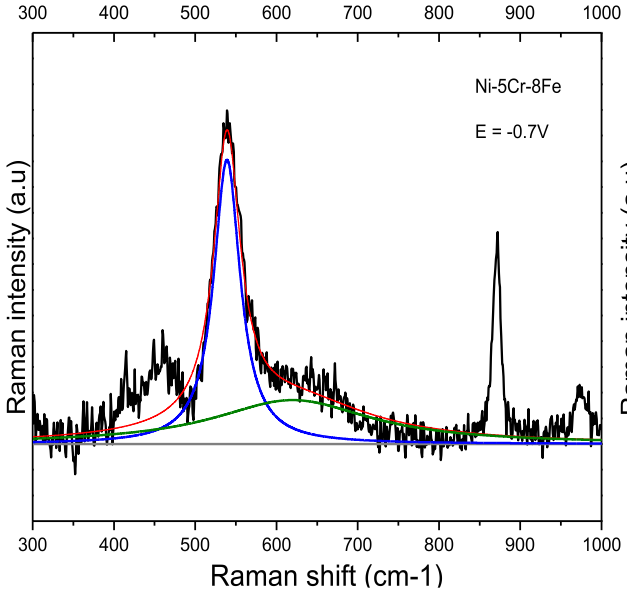

SERS Result for Ni-5Cr-8Fe at E = -0.7V

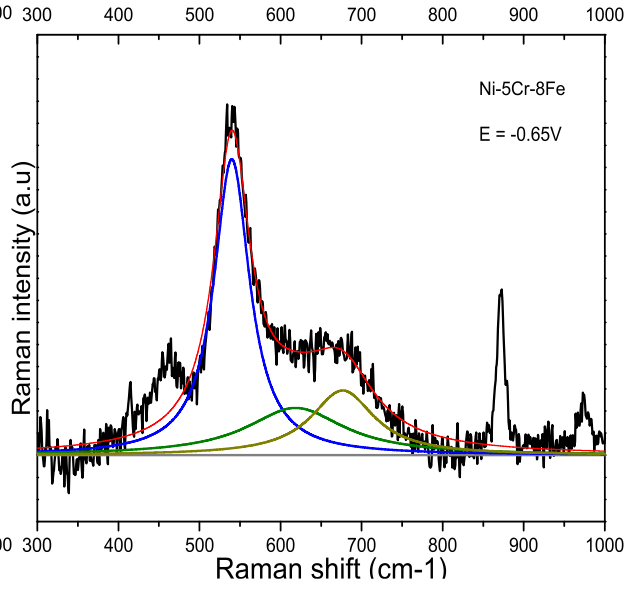

SERS Result for Ni-5Cr-8Fe at E = -0.65V

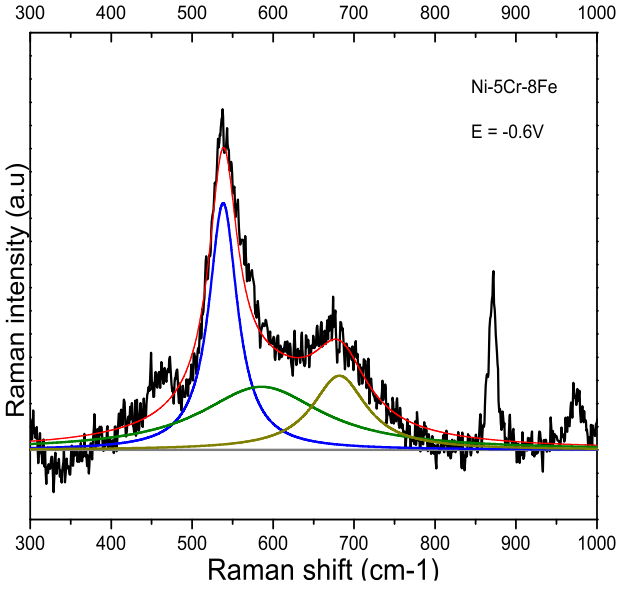

SERS Result for Ni-5Cr-8Fe at E = -0.6V

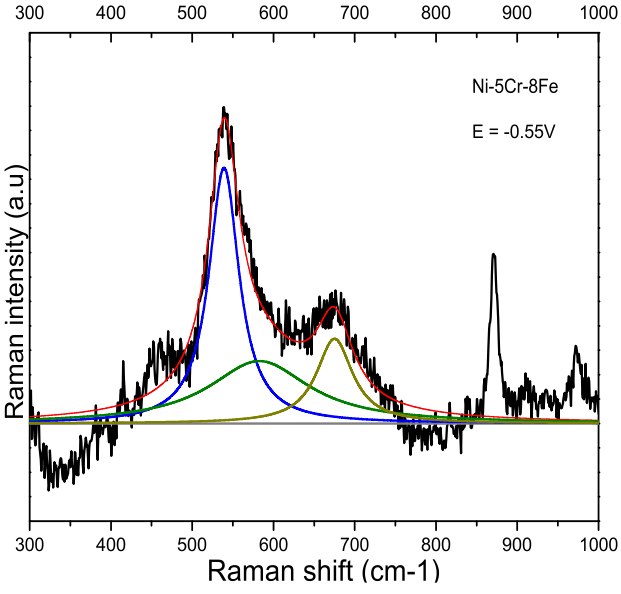

SERS Result for Ni-5Cr-8Fe at E = -0.55V

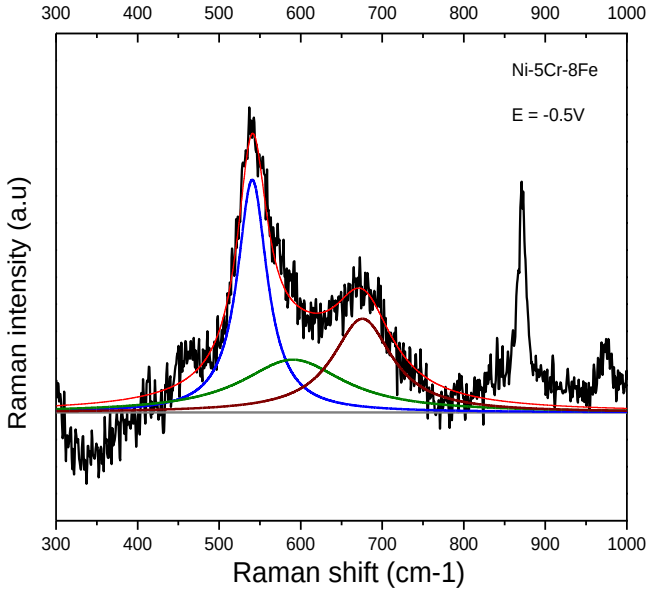

SERS Result for Ni-5Cr-8Fe at E = -0.5V

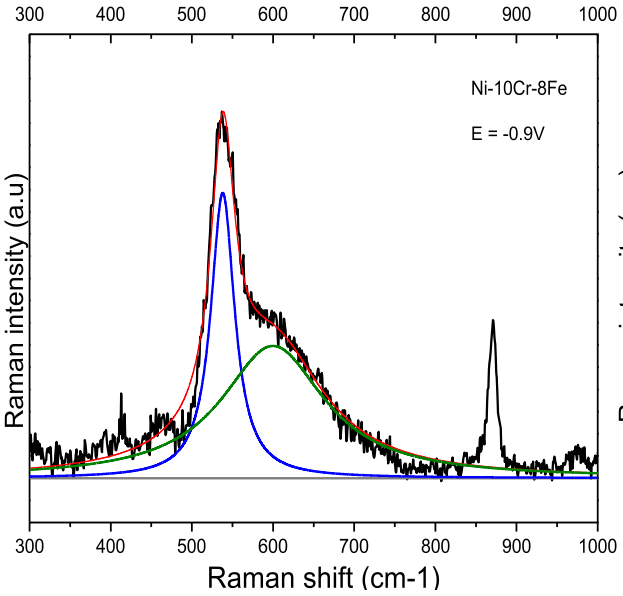

SERS Result for Ni-10Cr-8Fe at E = -0.9V

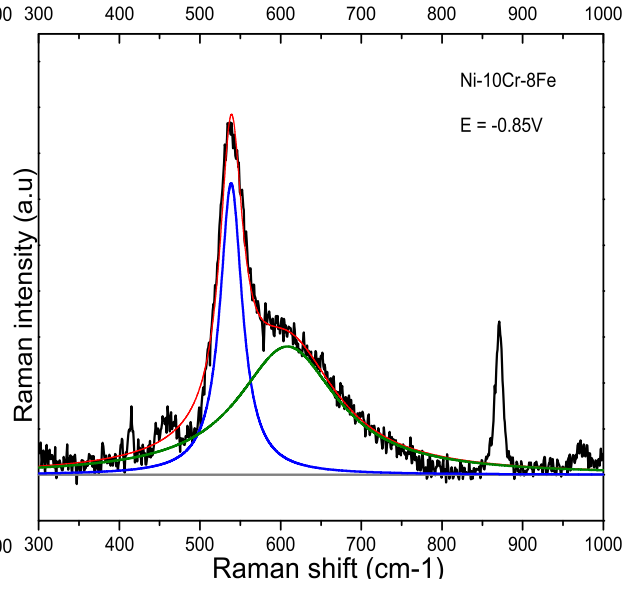

SERS Result for Ni-10Cr-8Fe at E = -0.85V

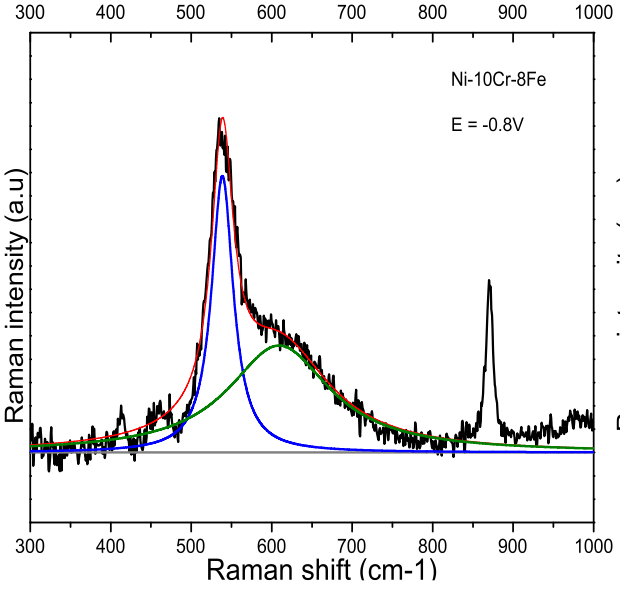

SERS Result for Ni-10Cr-8Fe at E = -0.8V

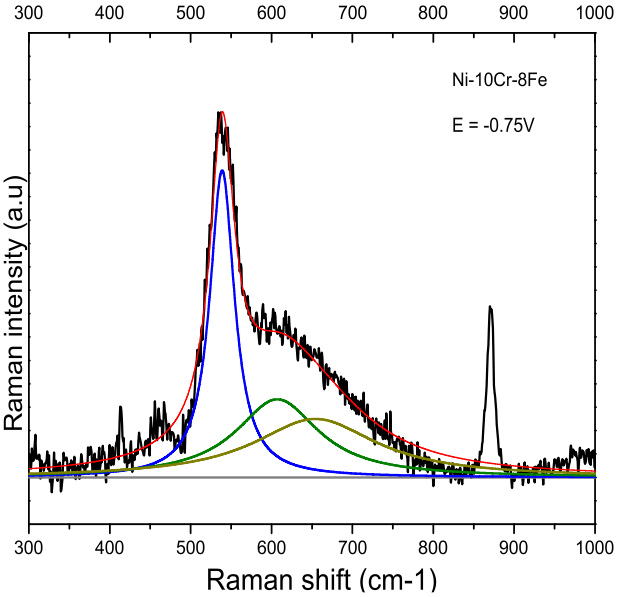

SERS Result for Ni-10Cr-8Fe at E = -0.75V

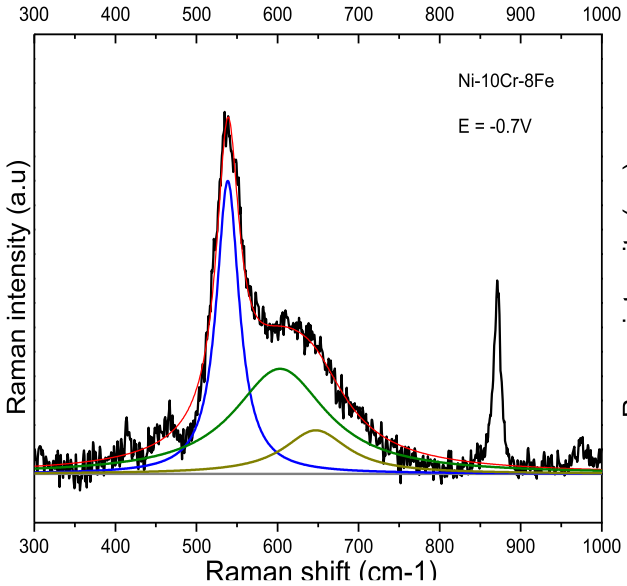

SERS Result for Ni-10Cr-8Fe at E = -0.7V

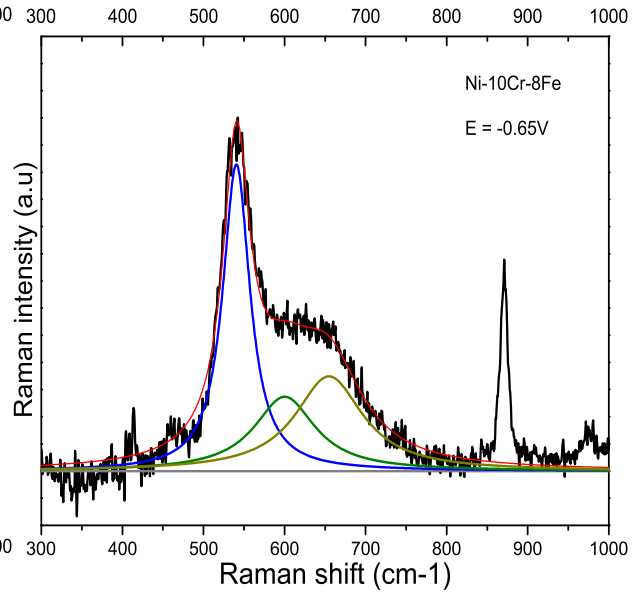

SERS Result for Ni-10Cr-8Fe at E = -0.65V

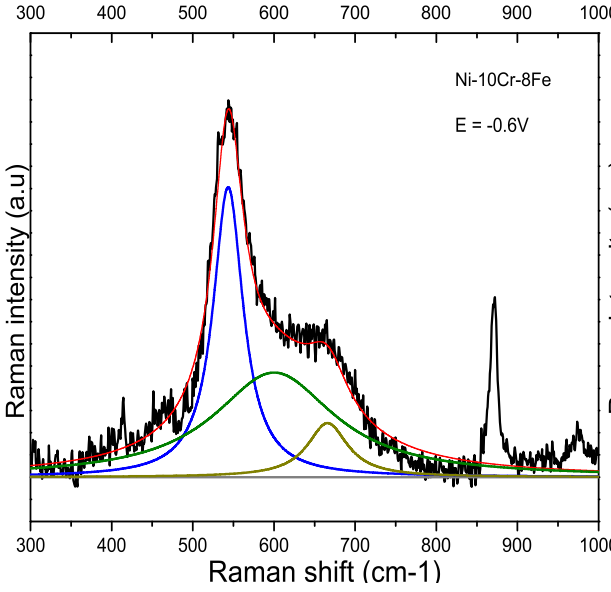

SERS Result for Ni-10Cr-8Fe at E = -0.6V

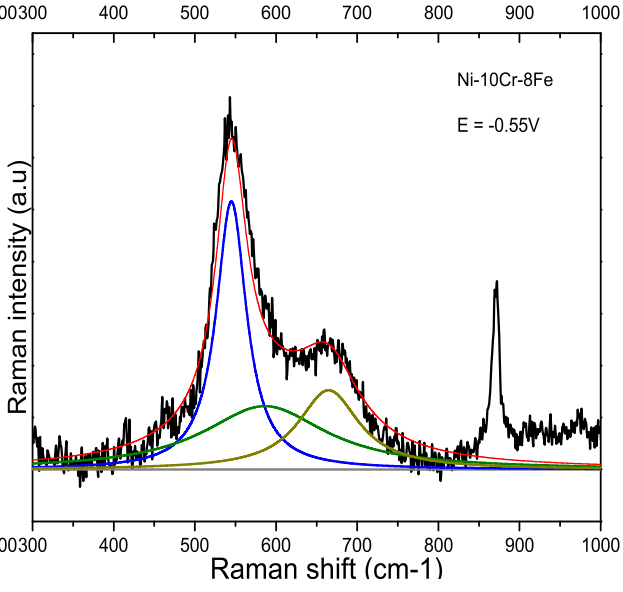

SERS Result for Ni-10Cr-8Fe at E = -0.55V

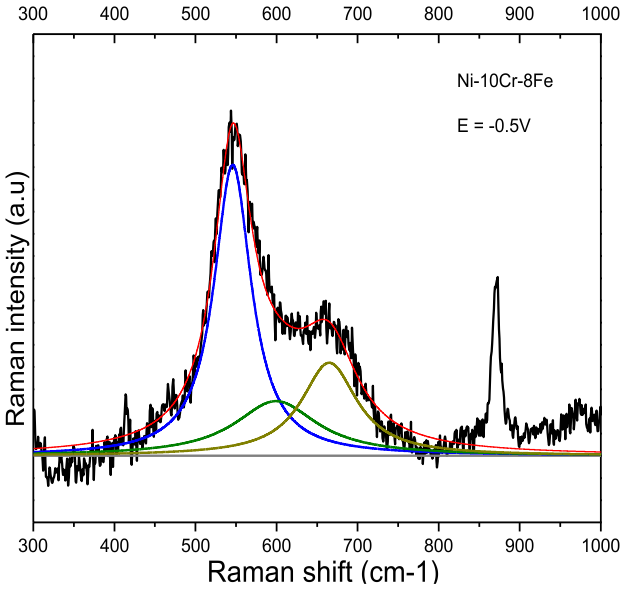

SERS Result for Ni-10Cr-8Fe at E = -0.5V

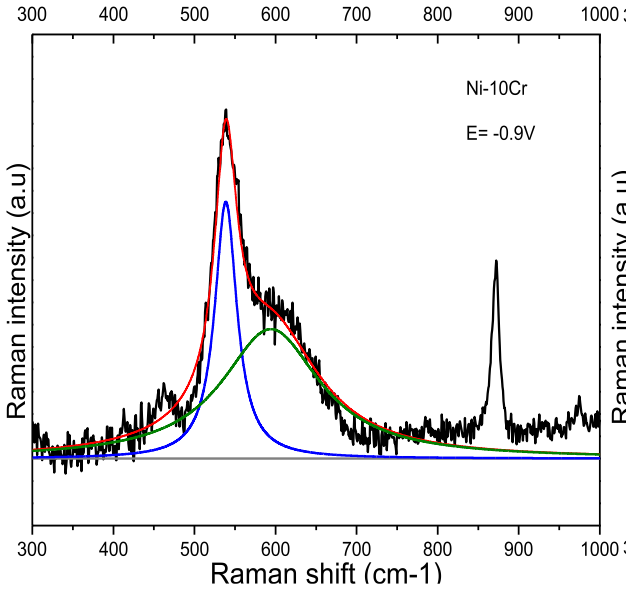

SERS Result for Ni-10Cr at E = -0.9V

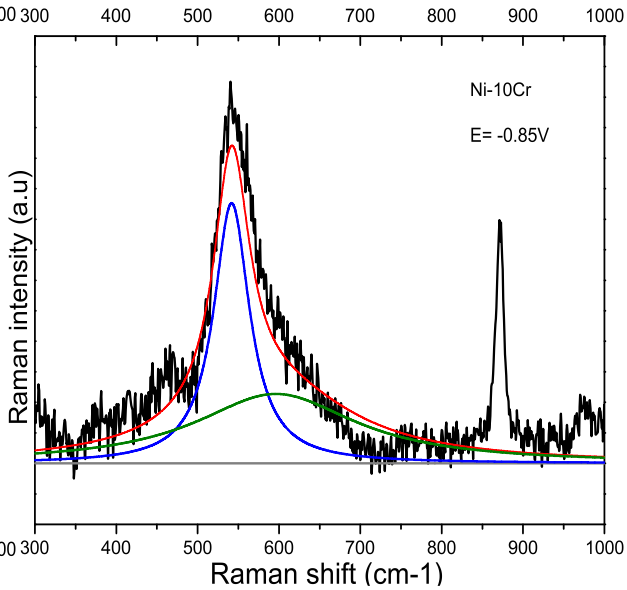

SERS Result for Ni-10Cr at E = -0.85V

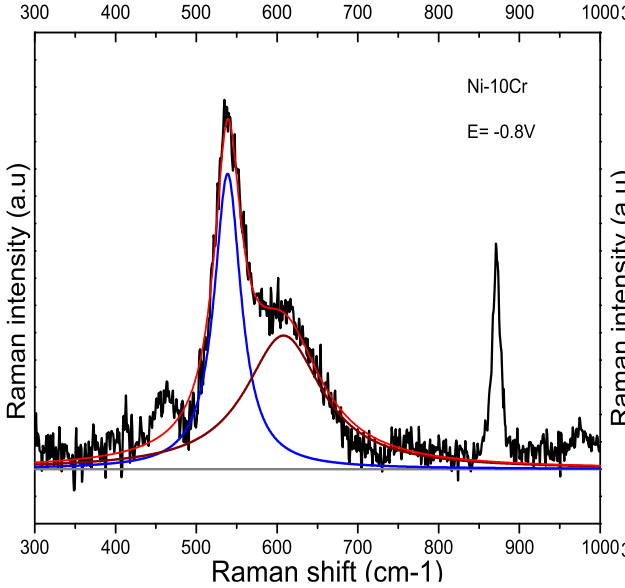

SERS Result for Ni-10Cr at E = -0.8V

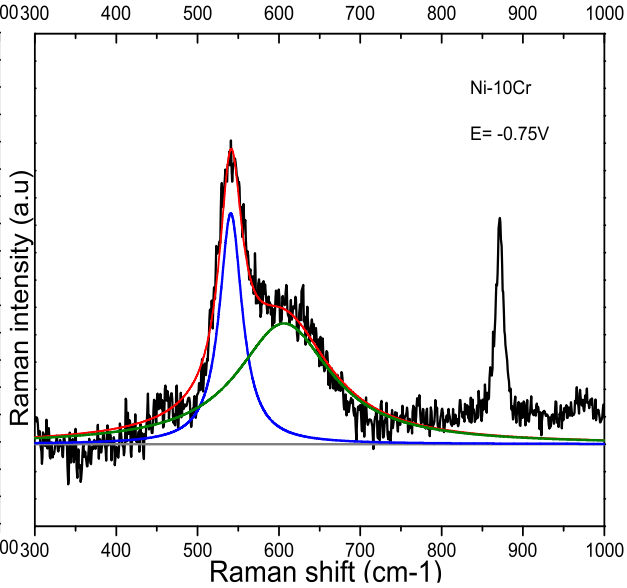

SERS Result for Ni-10Cr at E = -0.75V

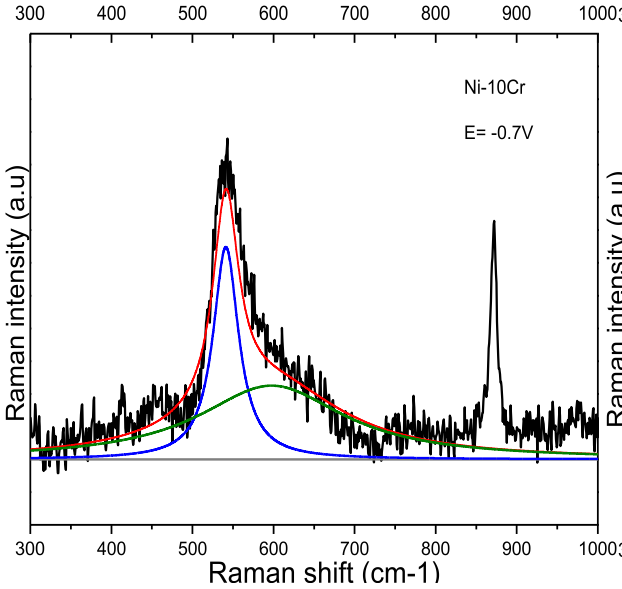

SERS Result for Ni-10Cr at E = -0.7V

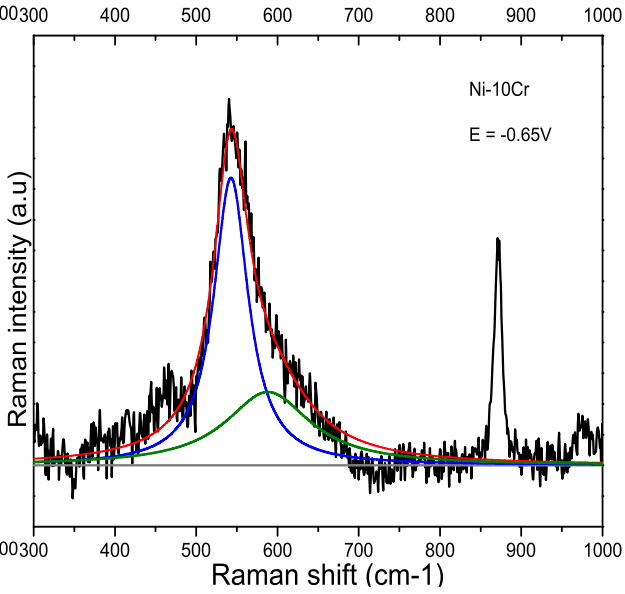

SERS Result for Ni-10Cr at E = -0.65V

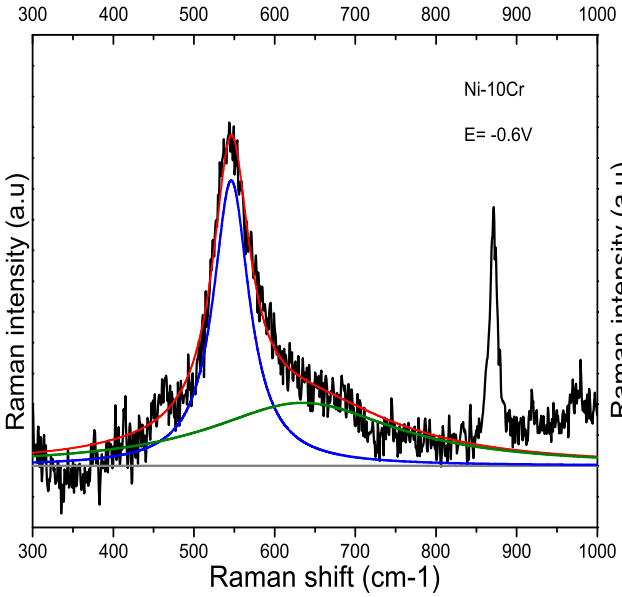

SERS Result for Ni-10Cr at E = -0.6V

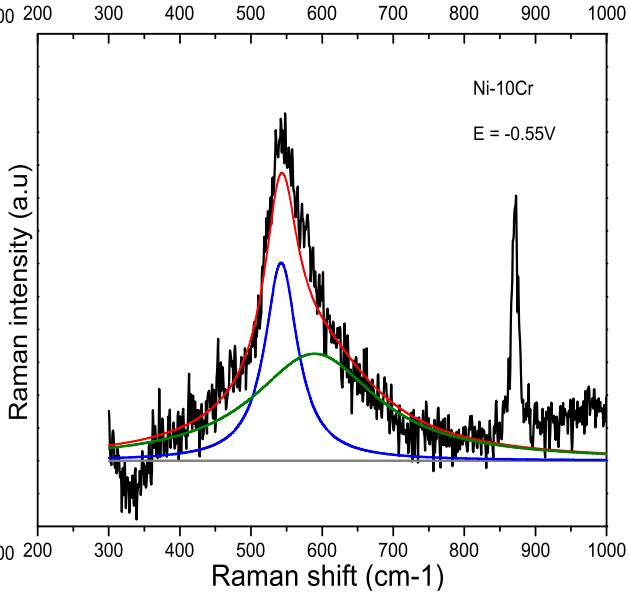

SERS Result for Ni-10Cr at E = -0.55V

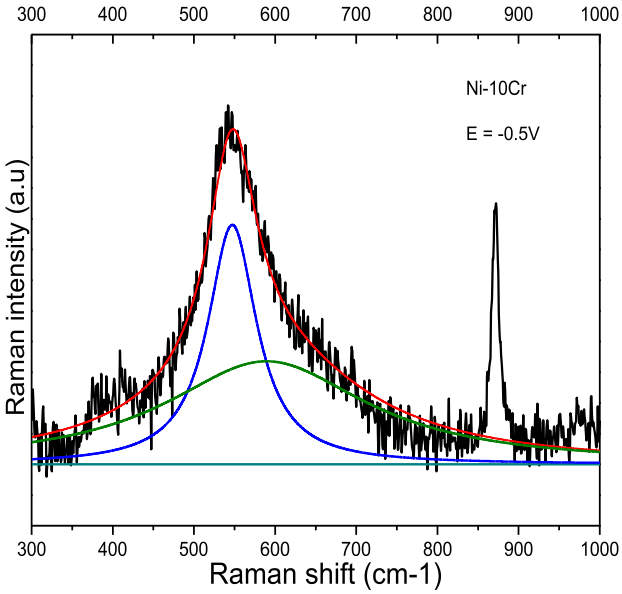

SERS Result for Ni-10Cr at E = -0.5V

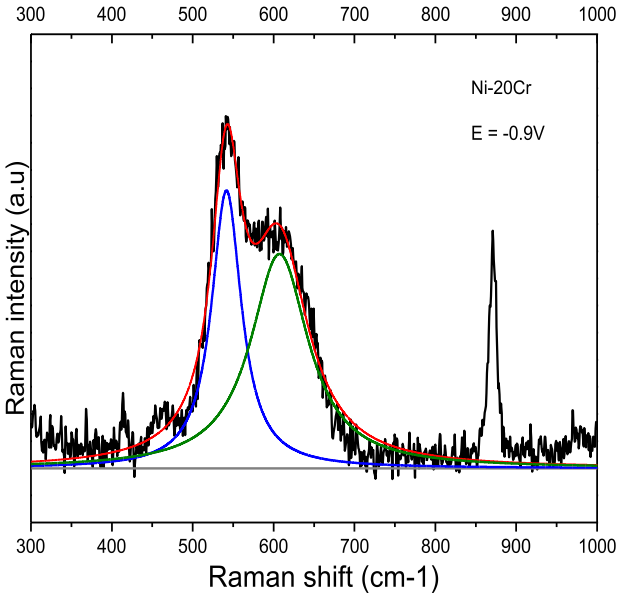

SERS Result for Ni-20Cr at E = -0.9V

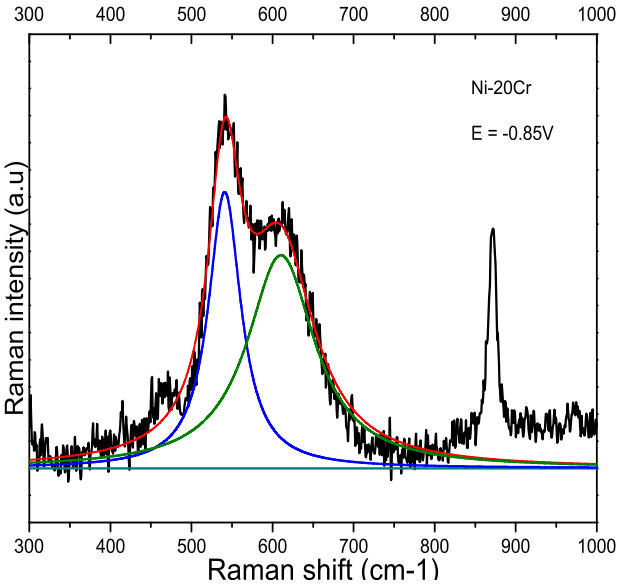

SERS Result for Ni-20Cr at E = -0.85V

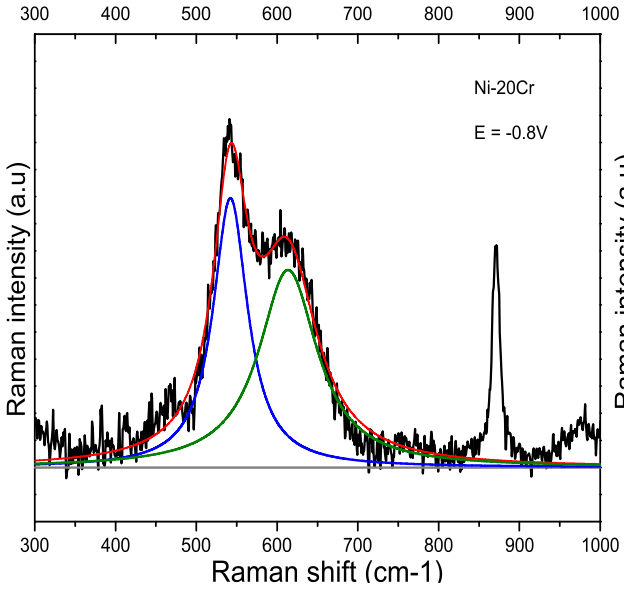

SERS Result for Ni-20Cr at E = -0.8V

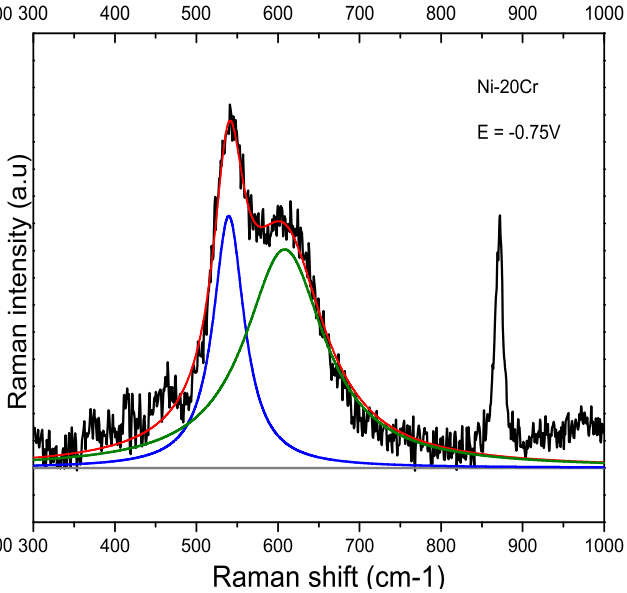

SERS Result for Ni-20Cr at E = -0.75V

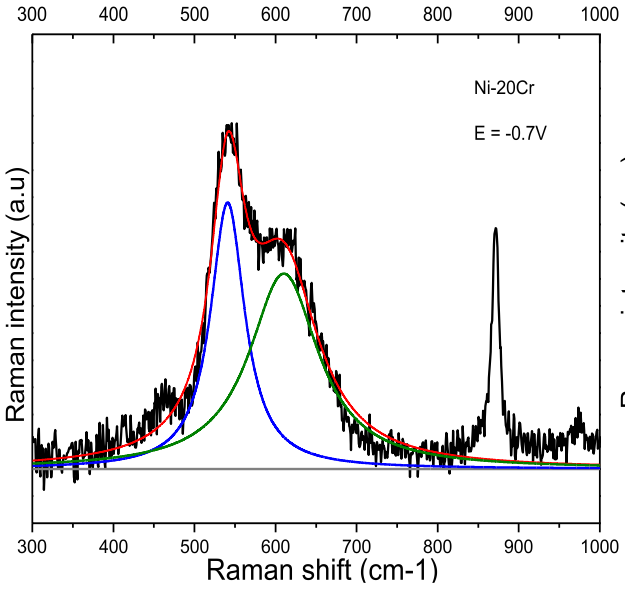

SERS Result for Ni-20Cr at E = -0.7V

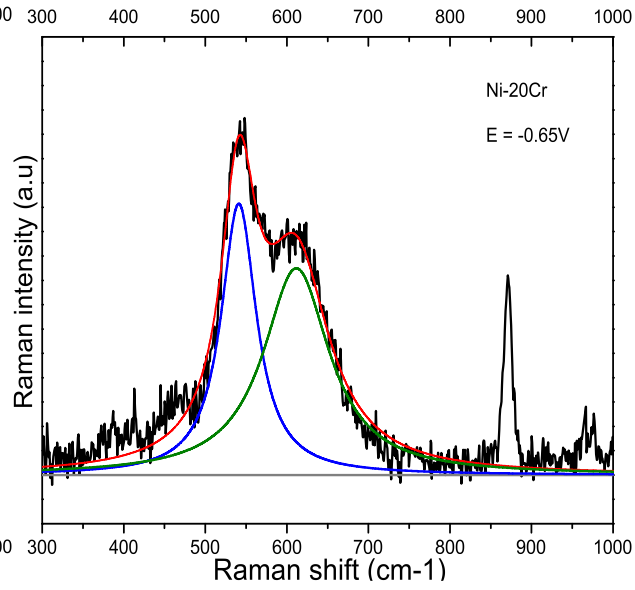

SERS Result for Ni-20Cr at E = -0.65V

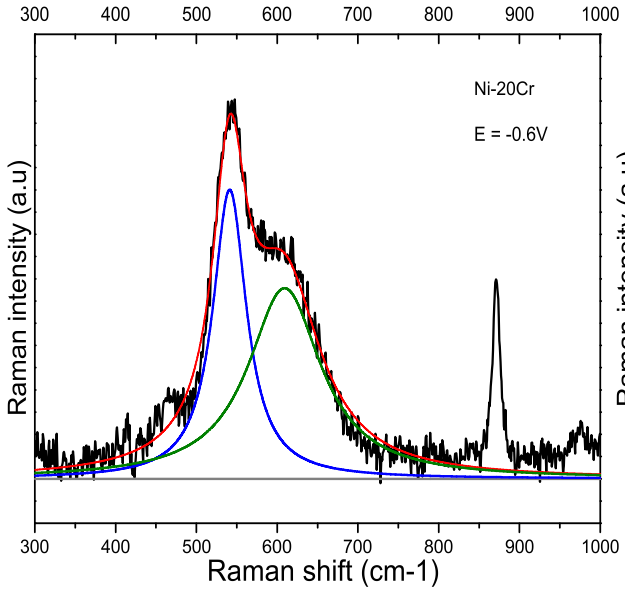

SERS Result for Ni-20Cr at E = -0.6V

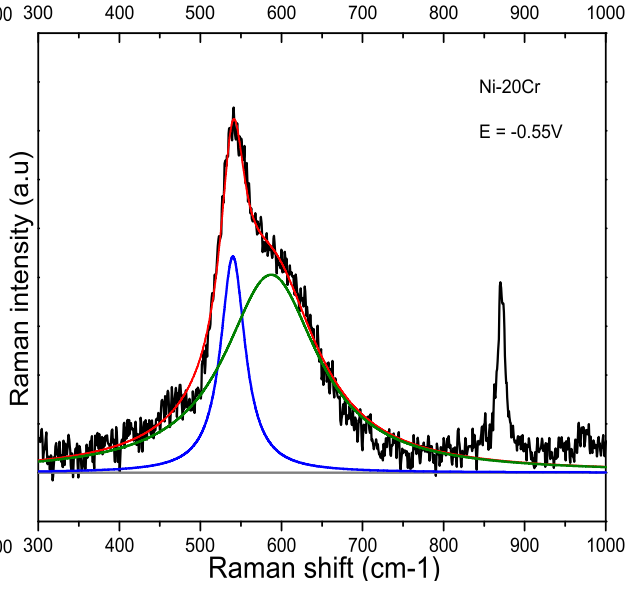

SERS Result for Ni-20Cr at E = -0.55V

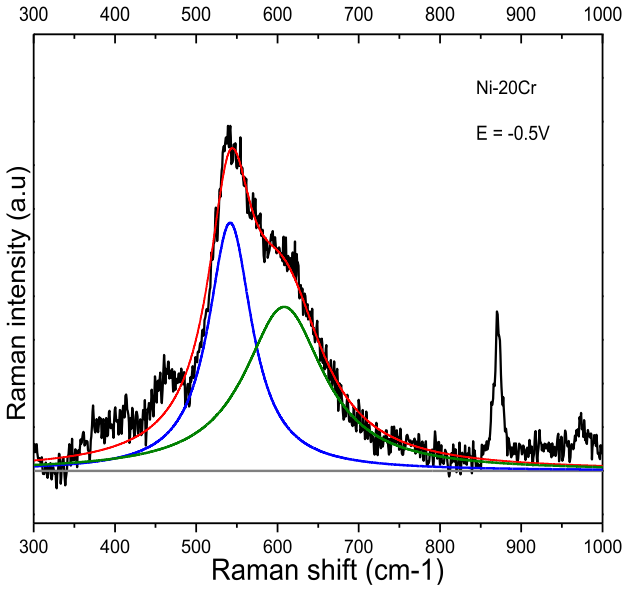

SERS Result for Ni-20Cr at E = -0.5V

Appendix VI. Diffusion Path Analysis Model

We have found that Cr_2O_3 films are formed on both Alloy 600 and Alloy 690. Are there any differences between Cr_2O_3 film on Alloy 600 and Cr_2O_3 film on Alloy 690? Why the surface film of Alloy 600 consists of Cr_2O_3 inner layer and $FeCr_2O_4$ outer layer, while the surface film on Alloy 690 is entirely Cr_2O_3 film?

A few years ago, T.M. Devine proposed a model, called Diffusion Path Analysis, to describe the formation mechanism of surface films on Alloy 600 and Alloy 690 in PWR primary water.

Alloy 690 has a higher resistance to SCC than Alloy 600. It is thought to be correlated with the formation of Cr_2O_3 on the surface of Alloy 690. However, this explanation is not complete because Alloy 600 also forms a continuous and protective Cr_2O_3 inner layer. As a result, one possible additional aspect of the mechanism is that the Cr_2O_3 on Alloy 600 is different with the Cr_2O_3 on Alloy 690.

F. Delabrouille analyzed the composition of surface films on Alloy 600 and Alloy 690 by TEM (as shown in Figure 1 and Figure 2) [106]. The compositions in Cr_2O_3 inner layer were different. For Alloy 600, the weight percent for Cr is 45%, Fe is 30% and Ni is 25%. For Alloy 690, the weight percent for Cr is 68%, Fe is 14% and Ni is 18% [106]. Therefore, a more Cr-enriched protective film is formed on Alloy 690 than on Alloy 600. There is a lower concentration of chromium and higher iron concentration in Cr_2O_3 layer of Alloy 600. As a result, there is a higher concentration of oxygen vacancies in the Cr_2O_3 layer of Alloy 600, which causes higher oxygen diffusivity through the inner layer. T.M. Devine was aimed to interpret the differences of the surface films on Alloy 600 and Alloy 690 based on film growth kinetic considerations.

Most models of passivity assume that equilibrium exists at the Alloy/film interface and at the film/electrolyte interface. Ion diffusion through the film is assumed to be the rate determining step of film growth. The same two assumptions are invoked when using the Diffusion Path concept to analyze the oxidation films formed on binary Alloys.

In the following discussion, the identities of the films that form on Alloy 600 and Alloy 690 are explained by Diffusion Path analyses, which consist of plotting on the appropriate ternary phase diagram (1) the composition of the Alloy, (2) the composition of the film, and (3) the composition of the environment. The Diffusion Path describes the variation of composition with distance across the diffusion couple composed of the Alloy and the environment.

The Diffusion Path concept has been employed in the analysis of the high temperature oxidation of binary Alloys in gaseous environments. The key assumptions of the method are: (1) equilibrium at interfaces between phases and (2) diffusion of oxygen and/or metal is the rate-determining step of oxidation. In addition to equilibrium at the interface between Alloy and

oxide, and between the oxide and the environment, the diffusing species are conserved at the interfaces. The main consequence of the assumptions is the interdependence of diffusion in the Alloy and diffusion in the oxide. There is a coupling between thermodynamics and kinetics (diffusion).

The interdependence of thermodynamics and diffusion during oxidation of the binary Alloy AB is most efficiently represented by the diffusion path plotted on the A-B-O ternary phase diagram.

There are 17 rules that govern the construction of the appropriate diffusion path. A few of the main characteristics of the diffusion path of a binary Ni-Cr Alloy undergoing oxidation are as follows. (1) One end of the diffusion path on the ternary phase diagram starts at the composition of the Alloy, located on the Ni-Cr axis and then veers toward the nickel rich end of the diagram on account of the preferential oxidation of chromium. (2) When the diffusion path crosses a two-phase region along a tie-line, the two end points of the tie line are the compositions of the two phases at the interface. (3) If the diffusion path enters one corner of a three-phase region, it exits by crossing the line opposite the corner. The position along the line represents the relative fraction of the two phases that make up one side of an interface. The corner represents the composition of the phase that forms the other side of the interface. (4) In the unlikely situation in which the two Alloy components, e.g., Ni and Cr, have the same diffusivities and the same reactivities, the diffusion path will be a straight line drawn from the Alloy's composition to the composition of the environment, which is given by the corner of the phase diagram opposite to the line representing the binary Alloy compositions. The actual diffusion path will cross the straight line at least once, consistent with the requirement of conservation of mass. In fact, most diffusion paths cross the straight line only once.

We propose to adopt the Diffusion Path concept to the analysis of the surface films that form on Alloys 600 and Alloy 690 in PWR primary water. In principle, it is possible to compute the diffusion path related to the oxidation of a binary Alloy, however, calculation of the diffusion path in the case of surface films formed in aqueous environments is not possible at this time due to insufficient information about the ternary phase diagrams and about the mobilities of metals and oxygen in the Alloy and oxide phases.

Consequently, our approach consists of plotting on a hypothetical ternary phase diagram the known compositions of the Alloy and the environment, along with the experimentally determined composition of the surface film. If the film's composition at its interface with the Alloy and at its interface with the environment were available as well as the composition of the Alloy at the interface with the oxide, they would also be plotted on the ternary phase diagram. The diffusion path consists of the path formed by connecting together the various plotted compositions. As mentioned above, there are 17 specific rules that must be obeyed in connecting the various compositions. The Diffusion Path concept provides formalism for understanding the microstructure of the Alloy's surface film. The value of the experimentally determined diffusion path is that it helps to explain how the Alloy's composition and the diffusivities of different components affect the film's microstructure.

The diffusion path for the oxidation of Alloy 600 and Alloy 690 should be plotted in a tetrahedon, which provides the four coordinates needed to map the composition of the ternary

Alloy's components (Ni, Cr and Fe) as well as the environment's composition. In the interest of simplicity, we employ a ternary diagram and ignore the relatively small amount of iron that is present in Alloys 600 and Alloy 690.

In the ternary diagram, the environment is represented by the activity of O/O^{2-}, which is present either in the form of (1) H_2O in the environment, as well as O_2 (if any oxygen is dissolved in the water, which is not the case in our experiments), (2) O^{2-} in the solid oxides, and (3) atomic oxygen in the Alloy.

The ternary Ni-Cr-Water diagram is valid for one particular value of temperature, which in our case is 320°C.

Two possible diffusion paths associated with the oxidation of Alloy 600 in PWR primary water, as determined by our SERS measurements are presented in Figure 3 and Figure 4. Each diffusion path is defined by three points on the phase diagram: the Alloy composition, the water's composition, and the film's composition, as determined by in situ SERS, and microstructure, as determined by ex situ TEM. The three points are then connected by the lines, which define the diffusion path. The diffusion path is the composition profile one would measure along a straight line that starts in the unoxidized Alloy, crosses into the Alloy that is immediately underneath the film, crosses through the film, and terminates in the bulk solution, well away from the solution/film interface.

Note that as required, each diffusion path crosses the straight line connecting the Alloy's composition and the environment's composition. According to SERS, the composition of the film is a mixture of $CrOOH/Cr_2O_3$ and spinel. The two diffusion paths in Figures 3 and 4 both indicate the film consists of a mixture of $CrOOH/Cr_2O_3$ and spinel. The two diffusion paths correspond to different film microstructures. The diffusion path in Figures 3 passes through the ternary region composed of spinel, $CrOOH/Cr_2O_3$, and the Alloy, and crosses the side along which the relative amounts of spinel and $Cr_2O_3/CrOOH$ vary from 0 to 100%. Accordingly, the diffusion path needs to enter the three phase region at the opposite corner. The diffusion path in Figures 3 indicates that the film of $CrOOH/Cr_2O_3$ and spinel do not form a layered structure but, rather, the film consists of homogeneous mixture of $CrOOH/Cr_2O_3$ and spinel. That is, both $CrOOH/Cr_2O_3$ and spinel are in contact with the Alloy at the Alloy/film interface, and are in contact with the electrolyte at the electrolyte/film interface (see the sketch of the cross-section of the Alloy-Water interface at the bottom of Figures 3).

The diffusion path through the two phase $CrOOH/Cr_2O_3$ + spinel region crosses tie-lines. Each point on this portion of the path indicates the average composition of the two-phase microstructure. The tie-line that passes through a point on this part of the diffusion path denotes the compositions of the spinel and $Cr_2O_3/CrOOH$ at that point. The location of the point on the tie-line specifies the relative amounts of the two phases. Finally, the diffusion path enters the three phase, $CrOOH/Cr_2O_3$ + spinel + water region. The lower endpoint of the dashed line defines the relative amounts of $CrOOH/Cr_2O_3$ and spinel at the oxide/water interface. The upper endpoint of the dashed line identifies the composition of the water in contact with the oxide.

According to TEM studies, the mixed oxide of $CrOOH/Cr_2O_3$ and spinel that forms on Alloy 600 forms a layered structure. Consequently, the diffusion path of Figures 8 does not represent the oxide film formed on Alloy 600 in PWR Primary Water.

As shown in the sketch of the cross-section of the Alloy/film/water at the bottom of Figures 4, the diffusion path presented in Figures 4 indicates a duplex, layered film forms on Alloy 600. The inner layer consists of $Cr_2O_3/CrOOH$ and the outer layer is composed of spinel. The layered film microstructure is in agreement with TEM observations and the diffusion path of Figure 4 describes the oxidation of Alloy 600 in PWR Primary Water.

To create the layered structure, the diffusion path is curved through the two single phase regions of $Cr_2O_3/CrOOH$ and spinel, and travels along the tie-line of the two phase $Cr_2O_3/CrOOH$ + spinel region. The right-side endpoint of the tie line indicates the composition of the $Cr_2O_3/CrOOH$ phase at the interface with the spinel phase, and the left-side endpoint of the tie-line specifies the composition of the spinel phase at the interface with $Cr_2O_3/CrOOH$. The sections of the curved portions of the tie lines that are nearly parallel to the Ni-Cr axis correspond to portions of the film in which the oxygen concentration profile is nearly flat and the chromium concentration is decreasing. These regions correspond to high diffusivity of the oxygen anion relative to the diffusivity of chromium.

The diffusion path describing the oxidation of Alloy 690 in 320°C water is presented in Figures 5. SERS indicates the films of Alloy 690 consist solely of $CrOOH/Cr_2O_3$ and so the diffusion path must pass through the single phase $CrOOH/Cr_2O_3$ region. That is, the diffusion path travels along a tie-line through the two phase $CrOOH/Cr_2O_3$ + Alloy region. The end points of the tie line give the compositions of the Alloy and $CrOOH/Cr_2O_3$ at the Alloy/film interface.

The diffusion path through the single phase $CrOOH/Cr_2O_3$ region describes the change in composition through the thickness of the film of $CrOOH/Cr_2O_3$.

At this point it is important to emphasize that there is only one diffusion path for a given combination of Alloy composition and environment. Accordingly, the different films are a consequence of either different Alloy compositions or different environments. It appears that the main consequence of different Alloy and aqueous compositions is a change in the relative diffusivity of O and Cr. In our analyses, sections of the diffusion path that are parallel to the Ni-Cr axis, correspond to portions of the microstructure in which the chromium concentration is decreasing while the oxygen concentration is approximately constant. A near-constant oxygen concentration would result from a much faster diffusivity of oxygen compared to chromium.

Briefly, the difference of surface films formed on Alloy 600 and Alloy 690 is a consequence of a change in the relative diffusivity of O and Cr. The relative diffusivity of oxygen to chromium in Alloy 600 is significantly higher than that in Alloy 690, which causes a formation of different surface films on the two Alloys.

The Cr_2O_3 film formed on Alloy 690 has a higher resistance to the transportation of oxygen through the film, while the mobility of oxygen is higher in the Cr_2O_3 film on Alloy 600. As a consequence, $FeCr_2O_4$ external layer is formed on the top of $Cr_2O_3/CrOOH$ inner layer of Alloy 600, but $FeCr_2O_4$ does not form on the top of Cr_2O_3 film of Alloy 690.

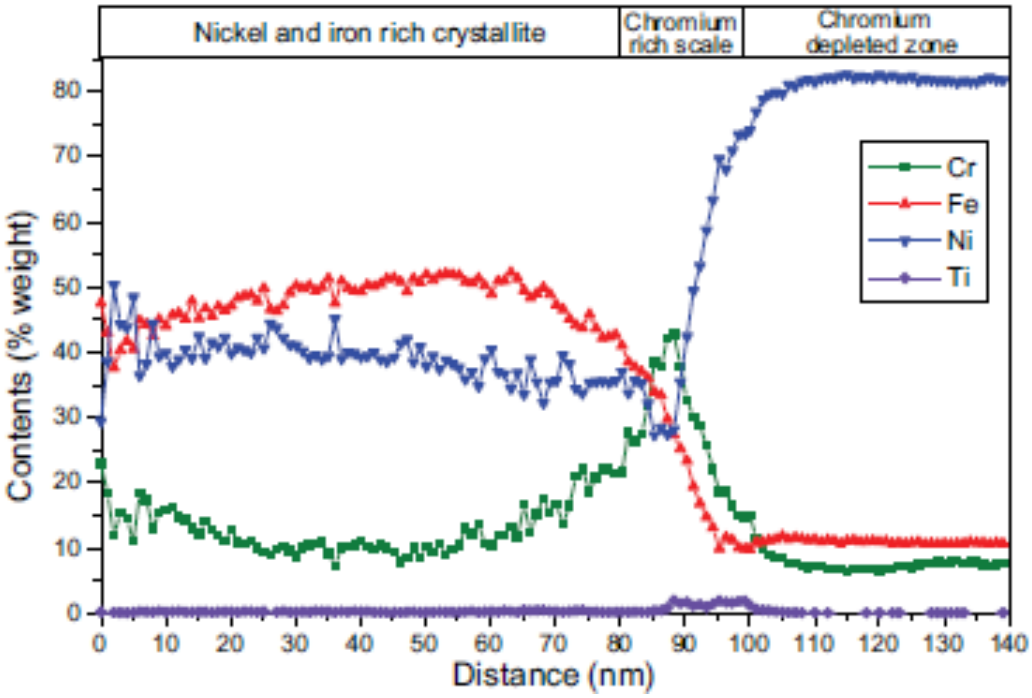

Appendix: Figure 1. TEM cross-section of the oxide scale formed on the 15% Cr alloy in simulated primary water. *After F. Delabrouille et.*

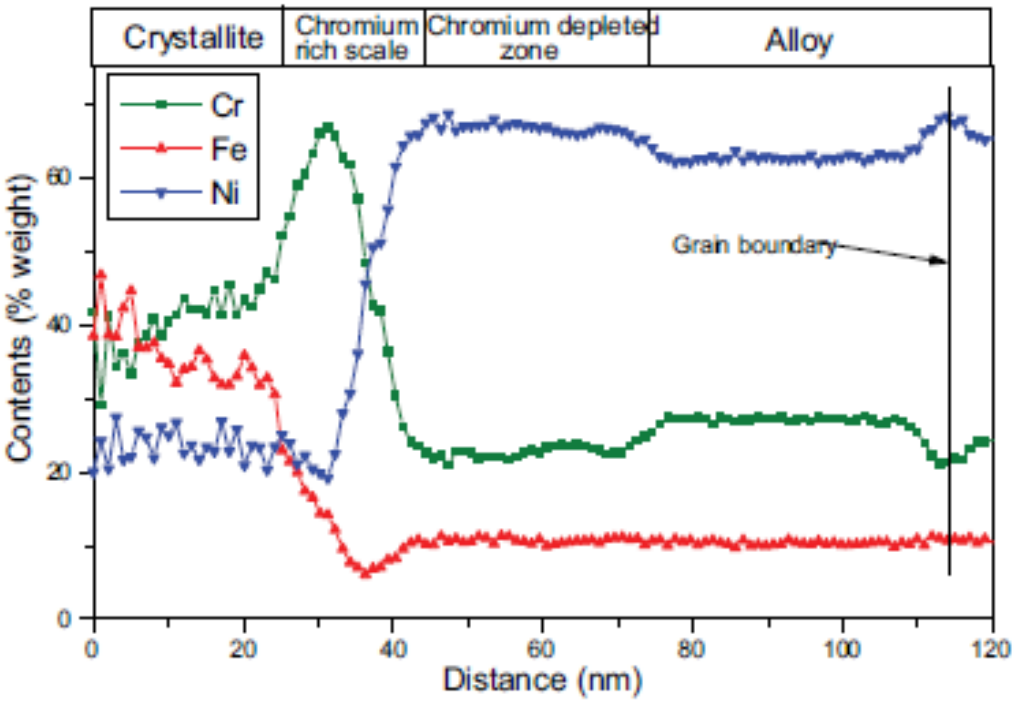

Appendix: Figure 2. TEM cross-section of the oxide scale formed on the 30% Cr alloy in simulated primary water. *After F. Delabrouille*

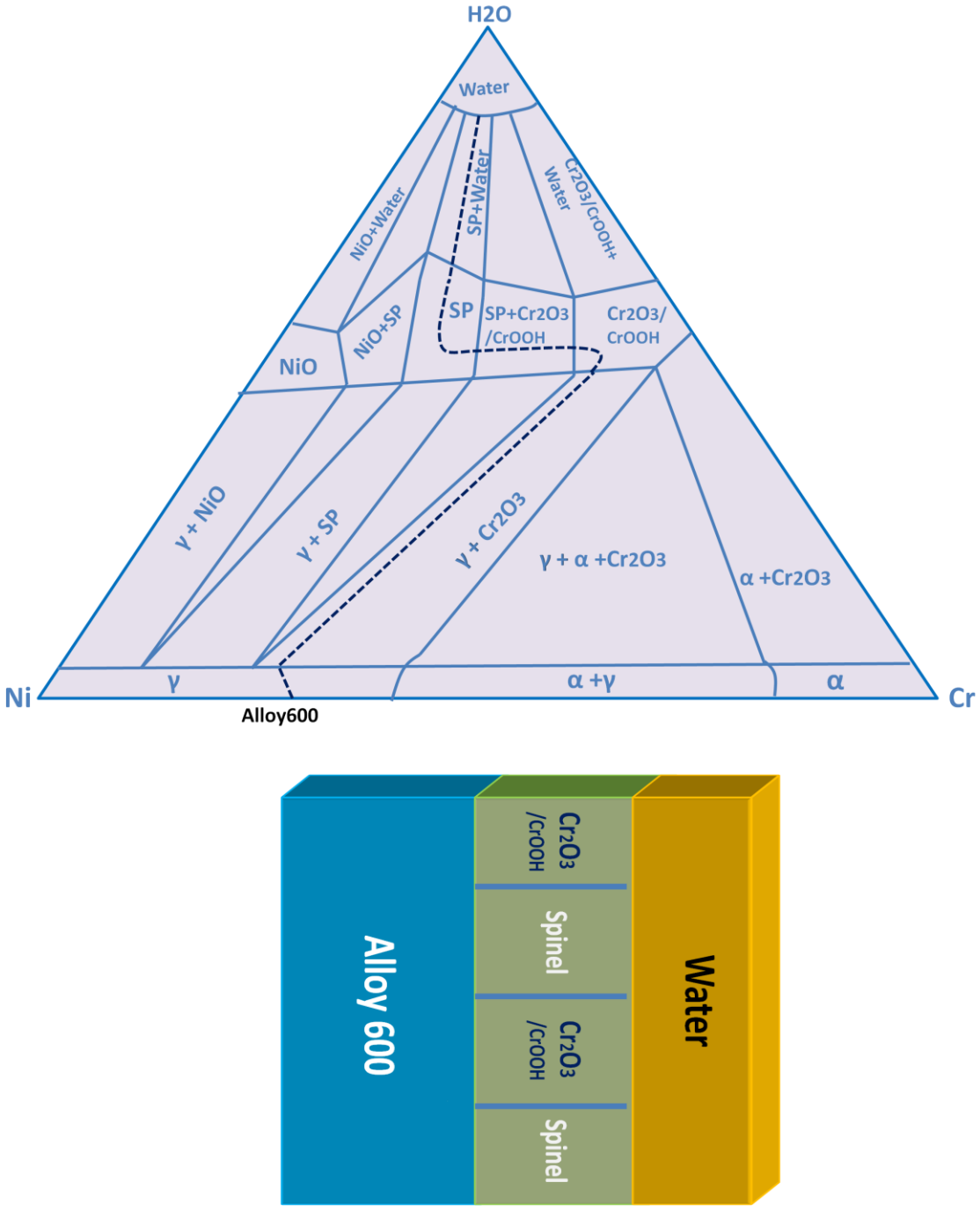

Appendix: Figure 3. Diffusion Path (qualitative) associated with oxidation of Alloy 600 in PWR Primary Water. The film consists of homogeneous mixture of CrOOH/Cr_2O_3 and spinel.

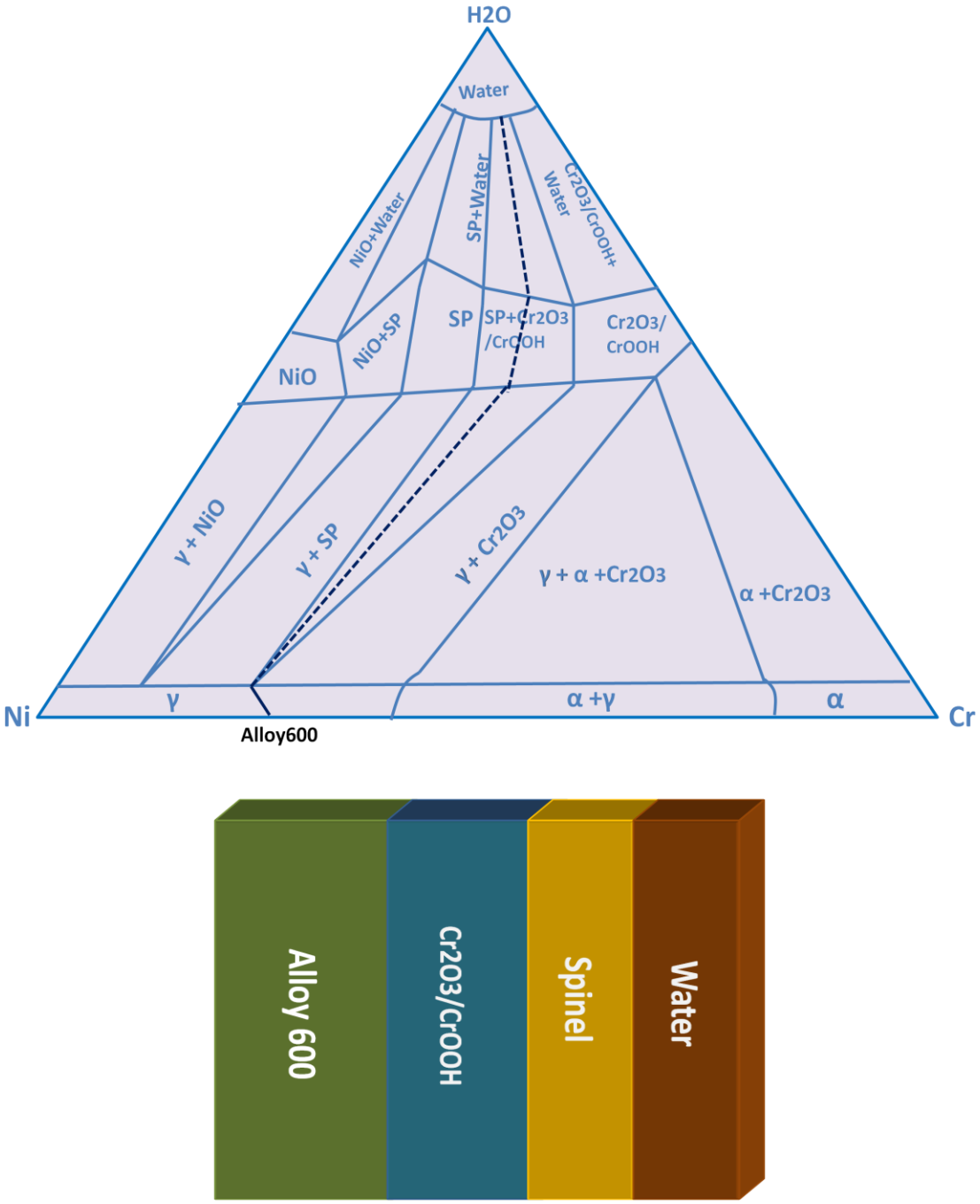

Appendix: Figure 4. Diffusion Path (qualitative) associated with oxidation of Alloy 600 in PWR Primary Water. The layered-film consists of an inner layer of Cr_2O_3/CrOOH layer and an outer layer of spinel.

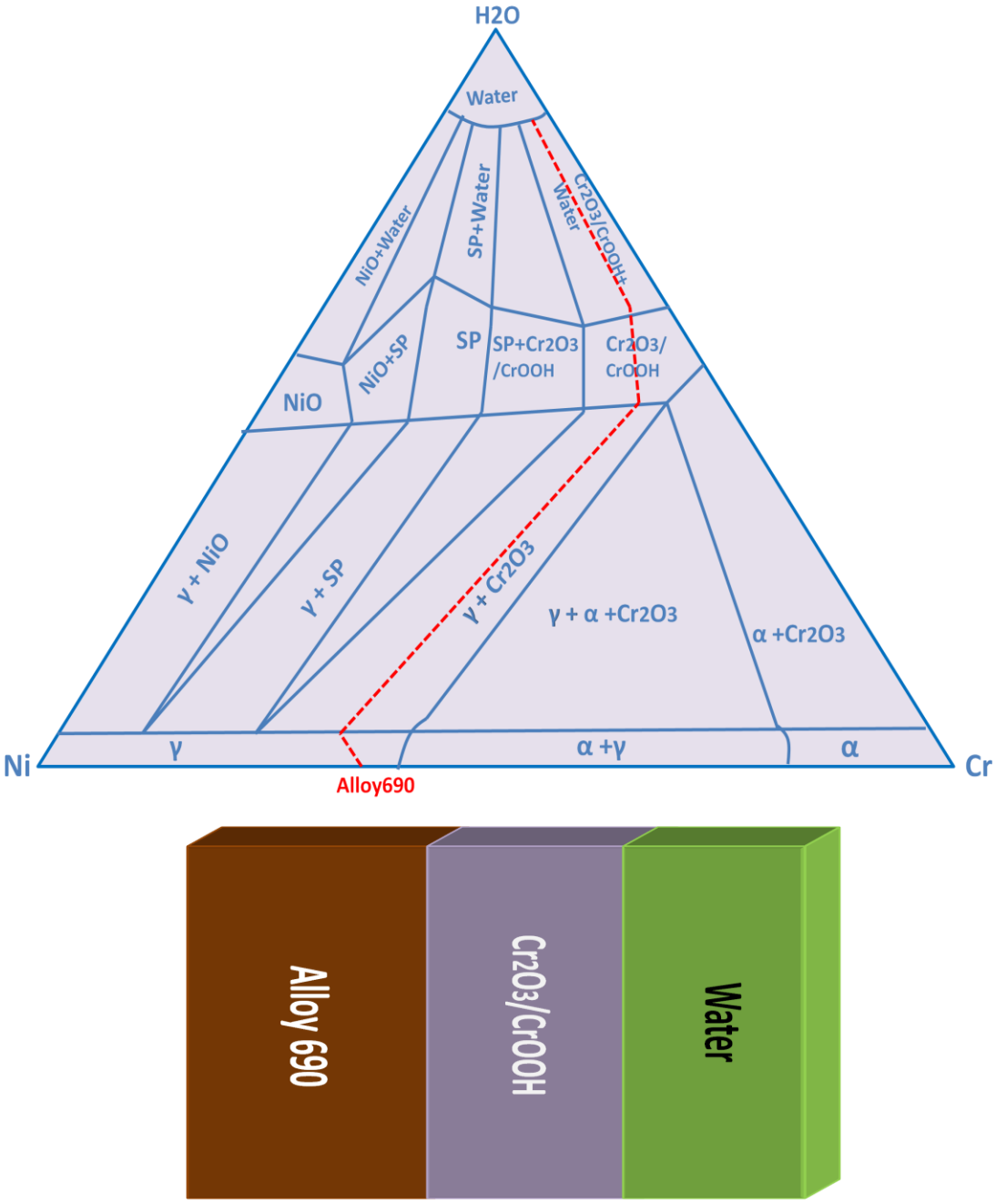

Appendix: Figure 5. Diffusion Path (qualitative) associated with oxidation of Alloy 690 in PWR Primary Water. The film of Alloy 690 consists solely of $CrOOH/Cr_2O_3$.